University of Louisville

ThinkIR: The University of Louisville's Institutional Repository

Electronic Theses and Dissertations

8-2022

Role of machine learning in early diagnosis of kidney diseases.

Mohamed Nazih Mohamed Ibrahim Shehata
University of Louisville

Recommended Citation

ROLE OF MACHINE LEARNING IN EARLY DIAGNOSIS OF
KIDNEY DISEASES

By

Mohamed Nazih Mohamed Ibrahim Shehata
M.Sc., Department of Electrical and Computer Engineering,
University of Louisville, Louisville, KY, USA, 2016

A Dissertation
Submitted to the Faculty of the
J. B. Speed School of Engineering of the University of Louisville
in Partial Fulfillment of the Requirements
for the Degree of

Doctor of Philosophy in Computer Science and Engineering

Department of Computer Science and Engineering
University of Louisville
Louisville, Kentucky

August 2022

ROLE OF MACHINE LEARNING IN EARLY DIAGNOSIS OF
KIDNEY DISEASES

By

Mohamed Nazih Mohamed Ibrahim Shehata
M.Sc., Department of Electrical and Computer Engineering,
University of Louisville, Louisville, KY, USA, 2016

A Dissertation Approved on

July 28, 2022

by the Following Dissertation Committee:

_____

Adel Elmaghraby, Ph.D., Co-advisor

_____

Ayman El-Baz, Ph.D., Co-advisor

_____

Ibrahim Imam, Ph.D.

_____

Juw Park, Ph.D.

_____

Amy Dwyer, M.D.

DEDICATION

This dissertation is dedicated to my beloved family.

ACKNOWLEDGMENTS

In the name of Allah the most Merciful, the most Compassionate. All the praises and deepest thanks are due to Almighty Allah for the uncountable gifts given to me.

I would like to express my deepest gratitude to my thesis co-advisors, Dr. Adel El-maghraby and Dr. Ayman El-Baz, for their continuous encouragement, guidance, advice, and support during my Ph.D. studies. Their discussions, comments, and feedback were valuable and helped me a lot to surpass many challenges towards building my scientific career.

My appreciation towards the valuable dissertation committee members, Dr. Ibrahim Imam, Dr. Juw Park, and Dr. Amy Dwyer for being enthusiastic in my research in the midst of many other responsibilities and commitments.

I also would like to thank Dr. Mohamed Abou El-Ghar, Dr. Mohamed Badawy, and Dr. Rasha T. Abouelkheir of the Radiology Department, Urology and Nephrology Center, University of Mansoura, Mansoura, Egypt, for being helpful and letting me gain from their radiological wide experience. They all spent much of their valuable time in medical discussions and validating the different analyses and obtained results.

I also express my deepest thanks to all members of the research group in the BioImaging Laboratory at the University of Louisville. They have been a tremendous source of support and a lot of fun to work with. Their encouragement, help, and support during hard times were especially valuable.

Last but not least, I am especially grateful to all of my family members: my dad Dr. Nazih Shehata, my mom Dr. Mervat Nouh, my beloved wife Yasmin Moustafa, my little princesses Kenzi Shehata, Carla Shehata, and Kenda Shehata and my sisters Sara Shehata and Manar Shehata for their great patience and encouragement with me all of these years during my Ph.D. journey. All of that would not be accomplished without their unconditional support and love.

Finally, I would like to send a brief message to my very close friends who supported and encouraged me during my study journey, "I value your friendship and I missed you very much."

ABSTRACT

ROLE OF MACHINE LEARNING IN EARLY DIAGNOSIS OF KIDNEY DISEASES

Mohamed Nazih Mohamed Ibrahim Shehata

July 28, 2022

Machine learning (ML) and deep learning (DL) approaches have been used as indispensable tools in modern artificial intelligence-based computer-aided diagnostic (AI-based CAD) systems that can provide non-invasive, early, and accurate diagnosis of a given medical condition. These AI-based CAD systems have proven themselves to be reproducible and have the generalization ability to diagnose new unseen cases with several diseases and medical conditions in different organs (e.g., kidneys, prostate, brain, liver, lung, breast, and bladder). In this dissertation, we will focus on the role of such AI-based CAD systems in early diagnosis of two kidney diseases, namely: acute rejection (AR) post kidney transplantation and renal cancer (RC).

A new renal computer-assisted diagnostic (Renal-CAD) system was developed to precisely diagnose AR post kidney transplantation at an early stage. The developed Renal-CAD system perform the following main steps: *(1)* auto-segmentation of the renal allograft from surrounding tissues from diffusion weighted magnetic resonance imaging (DW-MRI) and blood oxygen level-dependent MRI (BOLD-MRI), *(2)* extraction of image markers, namely: voxel-wise apparent diffusion coefficients (ADCs) are calculated from DW-MRI scans at 11 different low and high b-values and then represented as cumu-

lative distribution functions (CDFs) and extraction of the transverse relaxation rate (R2*) values from the segmented kidneys using BOLD-MRI scans at different echotimes, *(3)* integration of multimodal image markers with the associated clinical biomarkers, serum creatinine (SCr) and creatinine clearance (CrCl), and *(4)* diagnosing renal allograft status as nonrejection (NR) or AR by utilizing these integrated biomarkers and the developed deep learning classification model built on stacked auto-encoders (SAEs). Using a leave-one-subject-out cross-validation approach along with SAEs on a total of 30 patients with transplanted kidney (AR = 10 and NR = 20), the Renal-CAD system demonstrated 93.3% accuracy, 90.0% sensitivity, and 95.0% specificity in differentiating AR from NR. Robustness of the Renal-CAD system was also confirmed by the area under the curve value of 0.92. Using a stratified 10-fold cross-validation approach, the Renal-CAD system demonstrated its reproduciblity and robustness with a diagnostic accuracy of 86.7%, sensitivity of 80.0%, specificity of 90.0%, and AUC of 0.88.

In addition, a new renal cancer CAD (RC-CAD) system for precise diagnosis of RC at an early stage was developed, which incorporates the following main steps: *(1)* estimating the morphological features by applying a new parametric spherical harmonic technique, *(2)* extracting appearance-based features, namely: first order textural features are calculated and second order textural features are extracted after constructing the gray-level co-occurrence matrix (GLCM), *(3)* estimating the functional features by constructing wash-in/wash-out slopes to quantify the enhancement variations across different contrast enhanced computed tomography (CE-CT) phases, *(4)* integrating all the aforementioned features and modeling a two-stage multilayer perceptron artificial neural network (MLP-ANN) classifier to classify the renal tumor as benign or malignant and identify the malignancy subtype. On a total of 140 RC patients (malignant = 70 patients (ccRCC = 40 and nccRCC = 30) and benign angiomyolipoma tumors = 70), the developed RC-CAD system was validated using a leave-one-subject-out cross-validation approach. The developed

RC-CAD system achieved a sensitivity of 95.3% ± 2.0%, a specificity of 99.9% ± 0.4%, and Dice similarity coefficient of 0.98 ± 0.01 in differentiating malignant from benign renal tumors, as well as an overall accuracy of 89.6% ± 5.0% in the sub-typing of RCC. The diagnostic abilities of the developed RC-CAD system were further validated using a randomly stratified 10-fold cross-validation approach. The results obtained using the proposed MLP-ANN classification model outperformed other machine learning classifiers (e.g., support vector machine, random forests, and relational functional gradient boosting) as well as other different approaches from the literature.

In summary, machine and deep learning approaches have shown potential abilities to be utilized to build AI-based CAD systems. This is evidenced by the promising diagnostic performance obtained by both Renal-CAD and RC-CAD systems. For the Renal-CAD, the integration of functional markers extracted from multimodal MRIs with clinical biomarkers using SAEs classification model, potentially improved the final diagnostic results evidenced by high accuracy, sensitivity, and specificity. The developed Renal-CAD demonstrated high feasibility and efficacy for early, accurate, and non-invasive identification of AR. For the RC-CAD, integrating morphological, textural, and functional features extracted from CE-CT images using a MLP-ANN classification model eventually enhanced the final results in terms of accuracy, sensitivity, and specificity, making the proposed RC-CAD a reliable noninvasive diagnostic tool for RC. The early and accurate diagnosis of AR or RC will help physicians to provide early intervention with the appropriate treatment plan to prolong the life span of the diseased kidney, increase the survival chance of the patient, and thus improve the healthcare outcome in the U.S. and worldwide.

TABLE OF CONTENTS

LIST OF TABLES

LIST OF FIGURES

LIST OF ALGORITHMS

CHAPTER I

INTRODUCTION

Machine learning (ML) and deep learning (DL) approaches are sub-fields of arti-
ficial intelligence (AI) that have shown significant success in many diverse medical imag-
ing applications, such as image segmentation, registration, and classification [1]. They
have been used as indispensable tools in modern AI-based computer-aided diagnostic (AI-
based CAD) systems that assist in making decisions regarding medical diagnosis. These
systems can automate the diagnosis, reduce the subjectivity between different radiological
assessments, and improve the diagnostic performance. Traditional ML approaches mainly
depend on hand-crafted features to convert the input data into suitable patterns that could
be used for diagnostic problems [2]. These kind of AI-based CAD systems encompass
segmentation of the intended organ/region of interest, hand-crafted feature extraction, and
classification. Traditional ML classification algorithms that have been widely used in AI-
based CAD systems include, but are not limited to: k-nearest neighbors (k-NN), support
vector machine (SVM), linear discriminant analysis (LDA), logistic regression (LR), ran-
dom forest (RF), Naive Bayes (NB), decision tree (DT), multi-layer perceptron artificial
neural networks (MLP-ANN), and Adaboost. During the last 5-10 years, DL has evolved
as an exciting field through adaptation of MLP-ANN in which the network has many hid-
den layers [2]. This technique builds a hierarchical data representation (i.e. from less
to more abstracted representations), and thus has the power of learning high-level fea-
tures from the underlying data [3]. Stacked-auto encoder (SAE) [4, 5] is an example of
DL techniques that has the ability to process thousands of hand-crafted features extracted

1

from input images to obtain a final diagnosis of a given medical condition. Other examples of DL techniques are convolution neural network (CNN), deep neural networks (DNN), and generative adversarial networks (GAN), which have been shown to be efficient in AI-based CAD systems dealing with large datasets are . Although they can automatically extract thousands of features from input images data for classification purposes and avoid the burden of the hand-crafted features, they are limited by the need for large datasets to be well-trained. In addition, the automated extracted features are not readily explainable and need much effort for correlation and interpretation [3, 6]. Those AI-based CAD systems have proven themselves to be reproducible and have the generalization ability to diagnose new unseen cases with several diseases and medical conditions in different organs (e.g., kidneys, prostate, brain, liver, lung, breast, and bladder). In this dissertation, we will focus on the role of such AI-based CAD systems in early diagnosis of kidney diseases.

Several kidney diseases might rise up and badly affect the kidneys, which hinder them from performing their functions in a normal way. These kidney diseases [7] include, but are not limited to: chronic kidney disease (CKD), acute kidney injury (AKI), acute tubular necrosis (ATN), kidney stones, acute rejection (AR) post kidney transplantation, and renal cancer (RC). Early and precise diagnosis of kidney diseases is crucial to provide an appropriate and timely intervention plan to prevent or mitigate kidney failure. This dissertation will focus on two of the most contributing kidney diseases, namely: AR and RC. Chronic kidney disease (CKD) is the 10th leading cause of mortality in the United States. Approximately 37 million patients are suffering from CKD [8], which if it remains untreated, will result in progressive damage of the kidney until it develops a fatal condition called end stage kidney disease (ESKD). In 2022, the estimated number of ESKD patients in the U.S. is $\approx$ 780,000 [8]. ESKD is treated by blood dialysis and eventually by kidney transplant. While dialysis helps the patient stay alive, it performs only 10% of the kidney's function which leads to dangerous health conditions. Meanwhile, transplan-

tation is considered a long-term treatment as it prolongs patients' lives. However, organ procurement and transplantation is a challenging process. Each month, more than 3,000 patients are added to the kidney transplant waiting list while only 17,500 renal transplants are performed each year due to the paucity of donor organs [9–11]. In addition, during the first five years after transplantation, there is a 15% - 27% chance that the immune system will reject the foreign organ, leading to AR [12]. AR is considered the leading cause of kidney transplant dysfunction with two main types, including T-cell mediated rejection (TMR) and antibody-mediated rejection (AMR) [13]. Given the dearth of living or cadaveric donors, routine clinical follow-up, assessment, and functionality evaluation of the kidney transplant is crucial to minimize the chance of kidney damage [14]. Chapter II will provide a comprehensive survey about AR diagnosis. This will be followed by Chapter III, which will discuss the developed AI-based CAD system for early and precise diagnosis of AR.

In addition, RC is the 10th most prevalent cancer among men and women. It is a heterogeneous disease in which the renal cells become malignant (cancerous) and form tumors called renal masses. These renal tumors, if not detected early and treated promptly, will lead to mortality [15, 16]. For the past several decades, an increasing number of new patients have been diagnosed with RC. In the year 2022, approximately 79,000 new cases are expected to be diagnosed with RC in the United States, and 14,000 patients are expected to die from RC in that same time period [15]. Roughly two thirds of the time, RC is diagnosed before it has metastasized, in which case the 5-year survival rate is 93%. Once it has spread to the lymph nodes or the surrounding abdominal organs or tissues, the 5-year survival rate falls to 72%. In the worst case of metastasis to distant parts of the body, the 5-year survival rate falls to 15% [15]. Renal cell carcinomas (RCCs) are the most common and aggressive malignant tumors ($\approx$ 70%). The World Health Organization (WHO) states that most common RCC subtypes are clear cell RCC (ccRCC), and

non-ccRCC including papillary RCC (paRCC) and chromophobe RCC (chrRCC), representing 70%, 15%, and 5% of all RCCs, respectively. These malignant tumors have different grades (I-IV) which specify how aggressive the tumor is as well as different stages (I-IV), which help specifying the size of the tumor and how far it has spread to veins, lymph nodes, or other abdominal structures (i.e. metastasis). This RCC taxonomy is crucial for handling different prognosis [15, 17]. In addition, angiomyolipoma (AML) and oncocytoma (ONC) are benign renal tumors that can be easily misclassified as RCC ($\approx$ 15% - 20%) using traditional diagnostic methods such as physical examination and/or visual qualifications, particularly if these AML are fat-poor tumors, which might lead to unneeded surgeries [18]. Therefore, early and accurate diagnosis of RC is essential to provide the appropriate timely intervention and management plans. Chapter IV will provide a comprehensive survey about RC diagnosis. This will be followed by Chapter V that will discuss the developed AI-based CAD system for early and precise diagnosis of RC.

This dissertation is given in six chapters with their scopes summarized below:

Chapter I: This chapter gives an overview about different ML and DL techniques that had been utilized to build AI-based CAD systems to early diagnose different diseases that might affect many organs in human body with the focus on two of the most critical kidney diseases. Namely; AR and RC are discussed with their fast facts, consequences, and different types.

Chapter II: This chapter provides a comprehensive survey about most of the related studies in the literature that have used ML and/or DL to develop an AI-based CAD system to early diagnose AR using magnetic resonance images (MRIs). It starts with the basic anatomy of the kidney, the gives fast facts about the AR post transplantation and the traditional diagnostic techniques of AR.

Chapter III: This chapter details the developed AI-based CAD system with its novel-

ties and contributions for early and accurate diagnosis of AR using multimodal MRIs and clinical biomarkers. The developed AI-based CAD system performs kidney segmentation, followed by the estimation of best hand-crafted discriminating functional markers from multimodal MRIs. These markers are then integrated with their associated clinical biomarkers. The integrated biomarkers were then used to train and test a deep learning-based classifier; namely, SAEs to differentiate non-rejection (NR) from AR. Then, the diagnostic performance of developed AI-based CAD system is evaluated and discussed to draw a final take-home message.

Chapter IV: This chapter provides a comprehensive survey on most of the related studies in the literature from the last decade that have utilized ML and/or DL along with Radiomic markers extracted from multi-phasic contrast enhanced computed tomography (CE-CT) images to build an AI-based CAD system for early diagnosis of RC, including identifying the malignancy status, subtyping, grading, and staging. It starts with fast facts about RC, then discusses briefly the traditional diagnostic techniques of RC, different Radiomic markers, and possible treatment plans.

Chapter V: This chapter introduces a novel AI-based CAD system to early and precisely diagnose RC. The developed AI-based CAD system extracts the best discriminating hand-crafted morphological, textural, and functional markers from CE-CT images. These markers are then integrated and used to train and test a two-stage MLP-ANN classifier to differentiate malignant from benign RCC renal tumors and identify the malignancy subtype. Then, the diagnostic performance of developed AI-based CAD system is evaluated and discussed to draw a final conclusion.

Chapter VI: This chapter concludes the work that has been done in this dissertation, highlights the main contributions and obtained results, and spots the lights on possible future avenues to be handled.

Main contributions of this dissertation can be summarized as follows:

- A new AI-based CAD system was developed to precisely diagnose AR post kidney transplantation at an early stage. The developed system was named Renal-CAD and encompasses the following contributions:

  - Extraction of DW-MR image markers, namely: voxel-wise apparent diffusion coefficients (ADCs) are calculated from the segmented kidneys at 11 different low and high b-values and then mapped to their cumulative distribution functions (CDFs) for better representation.

  - Extraction of BOLD-MR image markers, namely: the transverse relaxation rate (R2*) values from the segmented kidneys at four different echotimes and then R2* curves were constructed for better representation.

  - Integrating the extracted multimodal MR image markers with the associated clinical biomarkers serum creatinine (SCr) and creatinine clearance (CrCl). These integrated biomarkers are then fed to the developed DL classification model built on SAEs to diagnose the kidney transplant as NR or AR.

- A new AI-based CAD system for precise diagnosis of RC at an early stage was developed. The developed system was named RC-CAD and incorporates the following major contributions:

  - Integrating the morphological features the best describe the surface complexity of a given renal tumor, with first and second order appearance-based features that can capture the texture heterogeneity of a given renal tumor, and with the functional features by constructing wash-in/wash-out slopes to quantify the enhancement variations across different CE-CT phases.

6

– Modeling a two-stage MLP-ANN classifier using the aforementioned integrated features to diagnose the renal tumor as benign or malignant and identify the malignancy subtype.

CHAPTER II

KIDNEY DIAGNOSIS SURVEY

A.   Background on Acute Rejection

Kidneys are important organs that are acting as a filtration system in human bod-
ies. Kidneys are able to keep nutrients like salts, sugar, and protein, while at the same
time they are responsible for removing waste products, removing excess fluids, balancing
minerals and chemicals, producing red blood cells, controlling blood pressure, and main-
taining healthy bones [19]. Although most humans are born with two kidneys, one nor-
mally functioning kidney should be enough to live in a healthy manner. However, several
diseases might rise up and badly affect the kidneys, which hinder them from performing
their functions in a normal way. As shown in Figure 1, the kidney is bean shaped and is
composed of an outer "shell" known as renal cortex; an inner layer known as medulla; and
a hollow area known as renal pelvis, where the urine is collected [20]. Inside the cortex
and medulla are the filtration units known as the nephrons (see Figure 1), which are then
made up of smaller subunits such as the glomerulus, vasa recta, and loop of Henle [20].
Since the kidneys must filtrate the blood, they must be connected to veins and arteries. The
kidneys are connected to the renal artier and vein which are connected to the iliac artery
and vein, respectively. It is clear that kidney has a very complex structure and is associated
with many diseases and medical conditions that might arise (e.g., Chronic kidney disease
(CKD)).
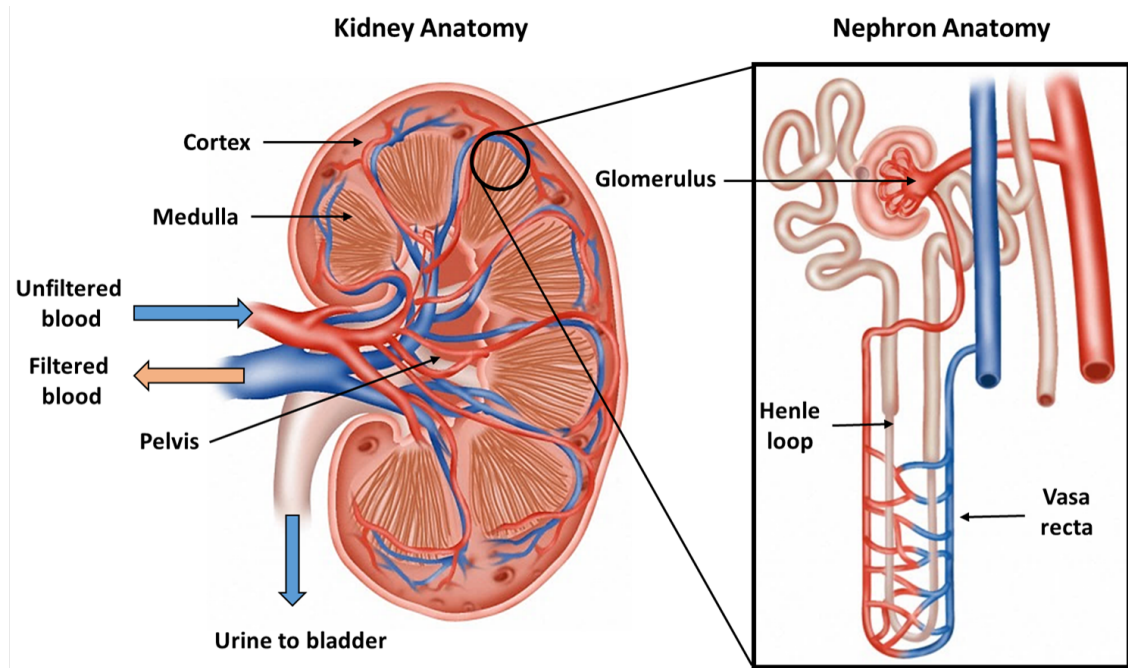
FIGURE 1: Anatomy of the kidney

CKD is the 10th leading cause of mortality in the United States. Approximately, 15% that is 37 million of the population in the USA suffer from CKD with more than 780,000 patients diagnosed with end-stage renal disease (ESRD) [8]. Over \$114 billion is spent annually on diagnosis and treatment of CKD or ESRD [21]. Although renal transplantation provides the best outcome for ESRD patients, only 17,500 renal transplants are performed in the USA each year due to the paucity of donor organs [10, 11]. In addition, during the first 5 years after transplantation, there is a 15% - 27% chance that the immune system will reject the foreign organ, leading to acute rejection (AR) post kidney transplantation [12]. AR is considered the leading cause of kidney transplant dysfunction with two main types including T-cell mediated rejection (TMR) and antibody-mediated rejection (AMR) [13]. AR of renal allografts has to be detected and treated promptly at an early stage, to minimize permanent damage and failure of the transplanted kidney [10, 11]. Given the dearth of living or cadaveric donors, routine clinical follow-up, assessment, and functionality evaluation of the renal allograft post-transplantation is crucial to minimize

allograft loss [14]. The diagnostic technique that is currently recommended by the National Kidney Foundation (NKF) for assessing renal allograft function is the glomerular filtration rate (GFR). The GFR has low sensitivity and is a late indicator for renal allograft dysfunction as major/noticeable changes can only be observed after>60% of renal allograft function is lost [22]. Renal biopsy, the gold standard, is used as a conclusive AR diagnostic tool. However, it cannot be used as a screening or early detection tool due to high invasiveness, high cost, long time for recovery/report, and associated adverse events (infection, bleeding, etc.). Therefore, there is a significant unmet clinical need for a non-invasive diagnostic tool that can provide a precise and early identification of AR renal allograft. In this chapter, we will discuss most of the related studies that have utilized magnetic resonance imaging (MRI) to early diagnosis AR post kidney transplantation.

B.   Related Work

Dynamic contrast enhanced (DCE) MRI provides, high contrast, low signal-to-noise (SNR) ratio, and thus; provide sufficient anatomical and functional information about the kidney [23–26]. Therefore, it had been investigated by researchers to develop AI-based CAD systems for renal function assessment [24–33]. For example, Farag et al. [27] developed an AI-based CAD system for early diagnosis of AR. Their CAD was evaluated on 30 patients and classified kidney status of each patient using four indexes: the peak signal intensity, the time-to-peak, the wash-in slope, and the wash-out slope, calculated from the MRI signal for the kidney cortex. Bayesian classifier was used and their CAD classified 13 out 15 and 15 out of 15 correctly for both training and testing, respectively. They extended their studies in [34] by constructing perfusion curves from the whole kidney rather than only the cortex. On a larger cohort of 100 patients, their modified CAD achieved a 94% accuracy using Bayesian classifier as well. Zikic et al. [25] eval-

uated kidney kinetic parameters as the contrast-invariant similarity measure. However, the evaluation of perfusion parameters (plasma volume and tubular flow) was performed visually by trained physicians for 10 data sets of healthy volunteers. De Senneville et al. [26] evaluated renal function for both native and transplanted kidneys. The renal cortex was segmented manually and the GFR was estimated with Patlak-Rutland tracer kinetic model. The study demonstrated a significant uncertainty reduction on the computed GFR for native kidneys (10 healthy volunteers), but not the transplanted ones (10 transplant patients). Aslan et al. [28] developed an automated CAD system to classify NR from AR renal allografts using DCE-MRI. Following kidney segmentation, three classification methods (least square support vector machines (LS-SVMs), Mahalanobis distance, and the Euclidean distance) were compared to assess transplant status based on medullary perfusion curves. On a cohort of 55 clinical data sets, they a achieved a diagnostic accuracy, sensitivity, and specificity of 84%, 75%, and 96%, respectively using the Mahalanobis distance-based classifier. Zöllner et al. [24] extracted functional parameters using k-means clustering. This system was tested on only 4 DCE-MRI datasets and the evaluation of kidney regions was assessed qualitatively according their mean signal intensity time courses. Wentland et al. [29] utilized MRI-based intrarenal perfusion measurement to differentiate between NR, ATN, and AR on a cohort of 24 renal allografts. The study concluded that the cortical and medullary blood flow is significantly reduced in grafts experiencing AR, as compared with NR. Additionally, AR patients demonstrated medullary blood flow reduction as compared with ATN patients. Abou El-Ghar et al. [30] explored the feasibility of DCE-MRIevaluated the functionality on 55 patients using the mean medullary intensity a achieved sensitivity, specificity and accuracy of 75%, 96% and 84%, respectively, to separate NR from AR. Yamamoto et al. [31] utilized DCE-MRI to identify the cause of acute graft dysfunction. Their study included 60 patients (NR = 31 and AR = 29). Their study employed a multi-compartmental tracer kinetic model to estimate the GFR and mean transit time (MTT) at different compartments of the kidney. The study

document differences in the fractional MTT values between NR and AR groups; however, substantial overlaps among these groups and with normal kidneys were observed. Khalifa et al. [32] included 26 data sets, and a K-nearest neighbor classifier was used. Their CAD system achieved a 92.31% correct classification using the time-to-peak and wash-out slope empirical parameters that are estimated from the agent kidney kinetic curves. Their framework was extended in [33] by using four augmented empirical parameters (peak intensity value, time-to-peak, up-slope and average plateau). Unlike [32], the parameters were derived from the cortex rather than from the whole kidney and the system was tested on 50 patients, and the overall diagnostic accuracy increased to 96%

Although AI-based CAD systems that utilized DCE-MRI have shown promising results to assess the status of the renal allograft post-transplantation, the use contrast agents may adversely affect the kidney and cause nephrogenic systemic fibrosis [35] when GFR < 30 $ml/min/1.73m^2$. Thus, medical centers are reluctant to use DCE-MRI anymore in patients with renal disease [13, 23, 35]. To overcome these limitations, researchers started to investigate other modalities of MRIs. Diffusion-weighted MRI (DW-MRI) [36–41] and blood oxygen level-dependent MRI (BOLD-MRI) [37, 42–49] have been widely used to assess the status of the renal allograft post-transplantation at an early stage. These modalities provide both anatomical and functional information about the kidney while avoiding the use of contrast agents. DW-MRI enables non-invasive, *in-vivo* mapping of the diffusion of water molecules in tissues. These *in-vivo* diffusion maps are known as apparent diffusion coefficients (ADC) and can be obtained at different magnetic field strengths and duration (*b*-value) [50]. Thus, they can reveal the functional status of the kidney (normal or diseased) [13, 37]. While BOLD-MRI estimates the amount of oxygen diffused blood (i.e. oxygen bioavailability) in the kidney to determine whether it is functioning properly. Specifically, the amount of deoxyhemoglobin is measured by the apparent relaxation rate (R2*) parameter [13, 37].

Eisenberger et al. [41] assessed the function of kidney transplants using DW-MRIs. Scans were collected at 10 different b-values (0, 10, 20, 50, 100, 180, 300, 420, 550, 700 s/mm^2) for 15 patients with renal allografts (NR = 10, AR = 4, acute tubular necrosis (ATN) = 1). After placing manual ROIs, means and standard deviations of the ADC values were estimated from all b-values. The NR renal allografts demonstrated significantly higher ADC values in both cortex and the medulla compared to AR and ATN patients. The ADCs were directly correlated with the creatinine levels. Hueper et al. [36] investigated the role of DW-MRIs in assessing the function of transplanted kidneys. Their study consisted of 64 participants (NR = 33 patients, AR = 31 patients) and DW-MRIs were acquired at b0 and b600 s/mm^2. Manual ROIs were placed in the medulla and cortex of the allograft, and the associated ADCs were estimated from these ROIs. AR allografts had a significant decrease in ADC values, which conformed with biopsy reports. A total of 69 renal allograft patients (non-rejection (NR) = 43, AR= 26) were enrolled in a study conducted by Xu et al. [51]. Manual regions of interest (ROI) were placed on renal cortex and medulla and the ADCs were estimated. Renal allografts with AR demonstrated lower ADCs than NR kidneys. The b_{800} had the highest sensitivity and specificity of all measured b-values. Palmucci et al. [52] evaluated functionality of 21 transplanted kidneys by comparing the estimated ADCs and true diffusion (TD) with renal function indices. Patients were divided into three groups by their CrCl values. The cortical ADC and TD were evaluated in a user-defined ROI of the transplanted kidney for the three groups. A moderate positive correlation between the CrCl and both the ADC and TD, as well as no difference between the ADC and TD values for the adjacent groups, has been found. The subsequent extension [53] of these evaluations to 35 patients revealed a slightly smaller positive correlation than the previously reported one [52]. However, acute rejection responses after transplantation could not be detected. Abou-El-Ghar et al. [38] conducted a study to assess renal transplants function. Their study included 70 renal allograft patients. Using only two b-values of 0 and 800 s/mm^2, DW-MRI scans were conducted for

21 patients with acute graft impairment (group 1) and 49 normal renal allografts (group 2). A user-defined ROI was placed in the middle portion of the kidney in a selected cross-section, and a pixie-wise ADCs were calculated. Their study revealed that group 1 had significantly higher ADC values than group 2. Katarzyna et al. [54] investigated possible relations between the diffusion parameters and selected laboratory results in the early stage after kidney transplantation. The measurements were conducted in kidneys over multiple user-defined ROIs at b-values of 600 and 1000 s/mm^2 only. According to the relative variability in the results and SNR, the optimum ADC value in the renal cortex was at b_{1000} s/mm^2 with a strong dependency between the ADC measured at the same b-value and the estimated GFR. Kaul et al. [39] evaluated the allograft function using the ADC values of cortex and medulla. There were a significant reduction in ADC values of the medulla compared to the cortex in normally functioning donor and transplanted kidneys. They reported that in case of AR, the ADC values decreased in the cortex and medulla. Remarkably, they found that when the patients recovered from the AR using anti-rejection treatments, these values increased significantly. Thus, this method can be used in therapy follow-up of AR patients. Park et. al. [55] investigated the potential of DW-MRI in early detection of allograft dysfunction. 24 patients with early dysfunction and 10 with normal transplants were enrolled in the study. The medullary and the cortical ADC values were calculated for the patients. They found a moderate correlation between cortical or medullary ADC values and estimated GFR. Moreover, the ADC values were higher in normal allografts than the AR patients. Steiger et. al. [56] investigated the utilization of DW-MRI to classify kidney allograft biopsies by the seriousness of its pathological conditions. Renal DW-MRI and biopsy were performed on 40 kidney recipients. The patients were divided by biopsy results to one group of 15 patients with normal or simple pathological conditions and to a second group of 25 patients with sever conditions. Classification based on the ADC resulted in a sensitivity of 84.0% and specificity of 73.3%. When ADC was combined with intravoxel incoherent motion parameter, an accuracy of 80% was achieved. Xie et.

14

al. [57] investigated the ability of DW-MRI to detect the difference in function of renal allografts. The study included 40 kidney recipients who were assigned to three groups based on their eGFR with a unit of $ml/min/1.73m^2$. Groups 1, 2, and 3 had 16, 16, and 8 subjects with eGFR $\geq$ 60, 60 > eGFR $\geq$ 30, eGFR < 30, respectively. Also, 18 volunteers who had eGFR $\geq$ 60 were added as group 4. Cortical total ADC of group1 was higher than the group3. Also, total ADC and F_p had positive correlation with the eGFR. Their ROC analysis achieved 97.1% sensitivity and 66.7% specificity based on F_p values.

In addition to diffusion studies, BOLD-MRI has been used by researchers to quantify renal allograft function by estimating the transverse relaxation rate R2*, which correlates with the relative proportion of deoxy- to oxyhemoglobin. Djamali et al. [44] assessed early-stage renal allograft dysfunction (the first four months post-transplantation) using BOLD-MRI. In their study 23 renal allografts (NR = 5, AR = 13, ATN = 5). After manual placements of cortical and medullary ROIs, cortical and medullary R2* were estimated. Their study reported that AR allografts had the lowest medullary R2* values as well as the lowest medullary to cortical R2* ratios. Han et al. [42] explored the potential of BOLD-MRI in demonstrating significant differences between normal and dysfunctional renal allografts. A total of 110 patients (NR = 82, AR = 21, ATN = 7) who underwent renal transplants were enrolled in their study. After manual placement of ROIs in cortices and medullas, mean cortical and medullary R2* values were estimated. Their study demonstrated higher cortical and medullary R2* values in ATN group compared to both AR and NR groups. The NR group had higher cortical R2* values than the AR group. No correlations were found between R2* values and the creatinine level. Sadowski et al. [43] conducted a study on 20 renal allografts (NR = 6, AR = 8, ATN = 6) using BOLD-MRIs. Their study demonstrated lower medullary R2* values in AR patients compared to NR and ATN patients. Xiao et al. [58] conducted a study to differentiate between AR and NR kidneys post-transplantation using BOLD-MRIs. Their study included a total of 122 pa-

15

tients (AR = 21, NR = 72, and 20 normal functioning kidneys). After placing 2D manual ROIs, they estimated the R2* values for all participants. They reported significantly lower medullary and cortical R2* values in AR than other normal groups. Mendes et al. [59] investigated the potential power of BOLD-MRI to assess renal allograft post transplantation. Their study included 19 patients (AR = 4, ATN = 10, and other dysfunction = 5). Using 2D ROIs, they estimated the R2* values to differentiate between different groups of patients. Although they failed to find significant differences in cortical R2* values, they found that the medullary R2* values were significantly higher in the AR group.

Studies that utilized both DW-MRI and BOLD-MRI in assessing renal allografts post-transplantation have been performed [37, 60]. Vermathen et al. [60] followed up renal allograft patients for 3-years post transplantation. Nine renal allografts were scanned twice using both DW- and BOLD-MRIs to determine the changes in functional parameters (i.e., ADC and R2*) as an indication of the allograft rejection. They reported only small and non-significant changes for NR allografts. ADC values were reduced significantly and R2* values were higher in the second scan for AR allografts. A study by Liu et al. [37] included 50 patients with renal transplants (NR = 35 AR = 10, and ATN = 5). Lower ADC values were reported for AR compared to NR. Medullary R2* values were significantly higher for ATN group compared to NR and AR groups.

C. Discussion and Conclusions

Early detection of AR can help physicians with early intervention with appropriate treatment and thus prolong the renal graft function and improve patient outcomes. Generally, there are multiple types of AR, and the selection of the appropriate treatment depends on the rejection type. For example, acute cellular rejection is treated with a high dose of corticosteroids, administrated intravenously as the first line treatment [61, 62].

The most popular regimen is the administration of methylprednisolone for three successive days [61]. In the case of persistent kidney deficiency with the steroid and/or antithymocyte globulin or the presence of a new defect in renal function after treatment of AR, another biopsy is recommended to discover additional causes of renal dysfunction. T-cell depleting antibodies are suggested for aggressive vascular cellular rejection and AR episodes that do not respond to steroid treatments [63]. On the other hand, if antibody mediated rejection is the resulting diagnosis, the following alternatives are suggested for treatment: plasmapheresis, immunoadsorption, intravenous immunoglobulin, or monoclonal antibodies [64].

DCE-MRI had been efficient imaging modality to assess the status of the renal allograft post-transplantation by estimating perfusion parameters. However, medical centers are reluctant to use DCE-MRI anymore in patients with renal disease [13, 23, 35] as the contrast agent might adversely affect the kidney [35], especially when GFR < 30 $ml/min/1.73m^2$. DW-MRI and BOLD-MRI have been used by researcher as good replacement that is safer and suitable for all kind of patients regardless the value of GFR. It is worth mentioning that most of the clinical research estimates the ADC at a few select b-values [36–39, 51, 54–57, 65], typically one of the lower b-values and one of the higher b-values along with the baseline (b0). Perfusion is measurable at low b-values $\leq$ 200 s/mm^2 [66, 67], while the high b-values account for the water diffusion [66–69]. Most of these studies agreed on that AR patients usually demonstrates reduced values of ADCs. On the other hand, contradictions were found in the values of R2* to be higher or lower in AR patients. At the end, these studies suggested that DW-MRIs and BOLD-MRIs are valuable imaging tools to be used for the early evaluation of AR post kidney transplantation [37, 38, 42–44, 70, 71].

The related work studies, discussed in this Chapter, had several limitations that need to be addressed: (1) most of the studies investigated only significant differences and

correlations among different renal transplant groups, and (2) none of these studies investigated the integration of image markers from different MRI modalities with clinical biomarkers to enhance the diagnostic performance, and (3) none of these studies investigated the power of deep learning (DL) to produce a comprehensive, AI-based CAD system to identify AR at an early stage. To overcome these limitations, in the next Chapter III, a novel fully automated AI-based CAD system, named Renal-CAD, is developed to provide an early and precise diagnosis of AR post kidney transplantation.

CHAPTER III

KIDNEY REJECTION COMPUTER-AIDED DIAGNOSIS

A.   Materials

Forty seven patients who underwent renal transplantation were enrolled in this study after providing consent. DW-MRI scans (n = 47 patients), BOLD-MRI scans (n = 30 patients), and renal biopsies (n = 47, M = 31, F = 16, age = 35 ± 16.13 years, age range = 12–65 years) were obtained (June 2016 to June 2019) from two geographically diverse countries (USA and Egypt). For the DW-MRI and biopsy data, two groups were identified: NR group (30 patients) and AR group (17 patients). BOLD-MRI data included 20 NR patients and 10 AR patients. Kidney function for all patients participating in this study, as a part of post-transplantation routine medical care, were assessed with their laboratory values, namely; creatinine clearance (CrCl) and serum creatinine (SCr). The NR group (30 patients) had an average SCr value of 1.20 ± 0.36 mg/dl and CrCl value of 74.83 ± 26.26 ml/min. The AR group (17 patients) had a mean SCr value of 1.63 ± 0.57 mg/dl and CrCl value of 54.05 ± 22.28 ml/min. Renal biopsies and coronal MRI data were acquired within 48 hours of each other. The biopsy results were used as the ground truth for comparison with the classification algorithm. The 47 DW-MRI scans (30 in Egypt and 17 in the USA) were acquired using two similar 3T Ingenia MRI scanners (Philips Medical Systems, Best, The Netherlands) using a body coil and a gradient single-shot spin-echo echoplanar sequence. However, data acquisition protocols were slightly different and are

summarized in Table 1. For both DW-MRI acquisition protocols, water signals were acquired at different b-values of b_0, b_{50}, and b_{100}–b_{1000} s/mm^2 at 100 increments, see Fig. 2. Thirty BOLD-MRI scans were acquired in Egypt using the same 3T scanner; TR: 140 ms, TE: 2 ms, Flip angle: 25°, Bandwidth: 150 kHz, slice size: 384×384, number of signals acquired: 1, FOV: 14.4 cm, thickness: 6.0 mm. For each subject, the middle/largest coronal image was selected and obtained at five different echo-times (TE = 2, 7, 12, 17, and 22 ms), see Fig. 2. Both biopsy reports and MRI scans were included in the final analysis and were examined by two clinicians, a radiologist and a nephrologist.
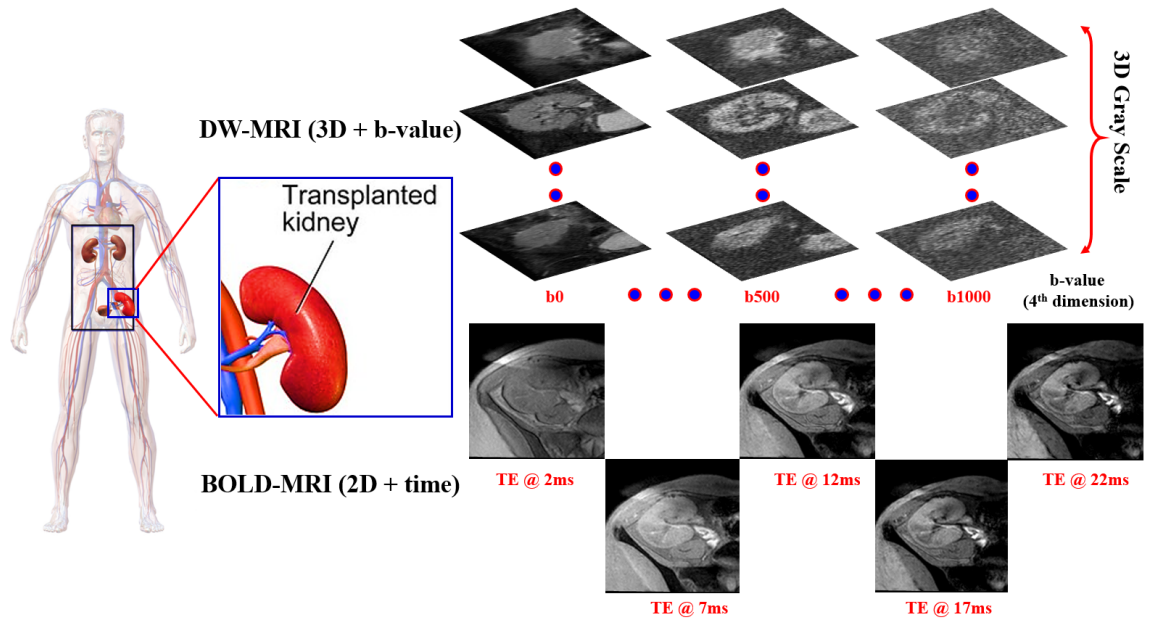
FIGURE 2: Data collection process demonstration for transplanted kidneys. DW-MRI data are collected at 11-different gradient field strengths and duration (b-values) of (b0, b50, b100, ..., b1000 s/mm^2), while BOLD-MRI data are collected at 5-different TEs (2, 7, 12, 17, 22 ms).

TABLE 1: Summary of the DW-MRI acquisition protocols of the data collected in USA and Egypt. Note that TR/TE: repetition time/echo time, SZ: slice size, STH: slice thickness, IG: intersection gap, FOV: field of view, NCS: number of cross-sections.

	Acquisition Protocol Metric					
	TR/TE	SZ (*pixels*)	STH (*mm*)	IG (*mm*)	FOV (*cm*)	NCS
Egypt (30)	4400/82	176×176	4	0	22	24
USA (17)	8000/93.7	256×256	4	0	36	38

B.   Methods

In this chapter, a novel fully automated AI-based computer-aided diagnostic system, named Renal-CAD (Fig. 15), is developed to provide a precise diagnosis of AR post kidney transplantation at an early stage. The developed Renal-CAD system performs the following major steps: (1) auto-segmentation of the renal allograft from surrounding tissues from DW-MRI and BOLD-MRI, (2) extraction of multimodal MR image markers, namely: voxel-wise apparent diffusion coefficients (ADCs) are calculated from DW-MRIs at 11 different low and high *b*-values and then represented as cumulative distribution functions (CDFs) and the transverse relaxation rate (R2*) values are estimated from the BOLD-MRIs at different echotimes and then R2* curves were constructed for better representation, (3) integration of multimodal MR image markers with the associated clinical biomarkers, serum creatinine (SCr) and creatinine clearance (CrCl), and (4) diagnosing renal allograft status as nonrejection (NR) or AR by utilizing these integrated biomarkers and the developed deep learning classification model built on stacked auto-encoders (SAEs). Details of the developed Renal-CAD are discussed below.
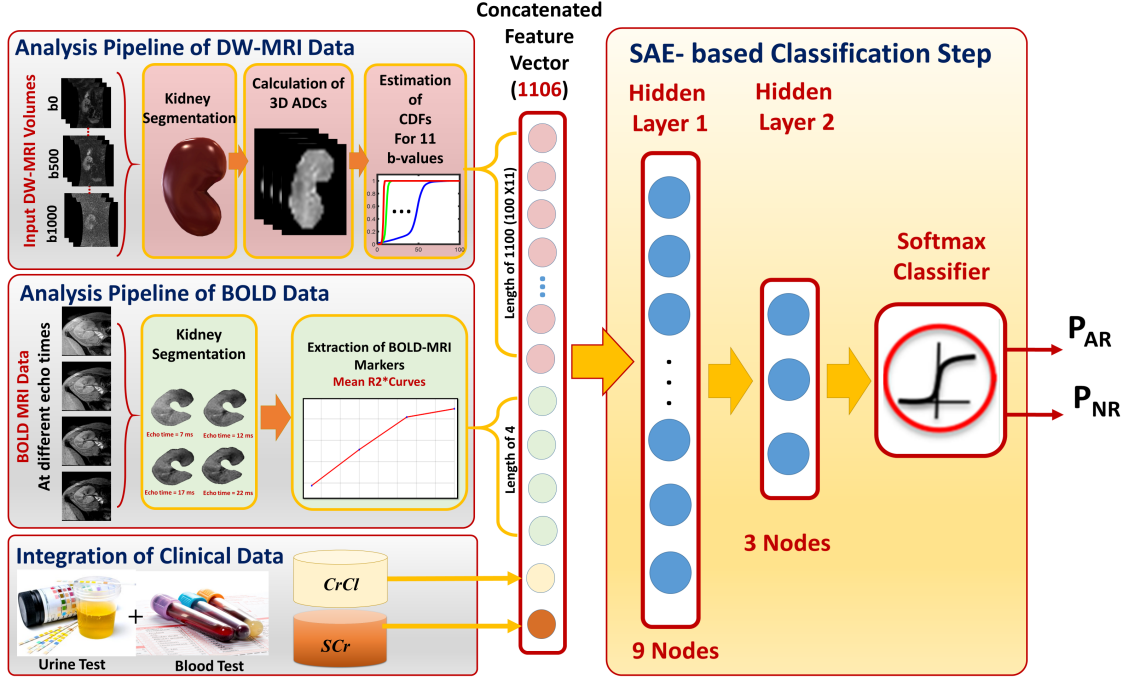
FIGURE 3: The proposed Renal-CAD system for early diagnosis of acute renal transplant rejection (AR). The input diffusion-weighted (DW) and blood oxygen level-dependent (BOLD) MRI data acquired at 11-different *b*-values and 5-different echo-times are first segmented. Then, the DW-MR image markers (cumulative distribution function (CDF) of the voxel-wise apparent diffusion coefficients (ADCs)) and the BOLD-MR image markers (mean R2* curve) are constructed. These image markers are then integrated with clinical biomarkers (creatinine clearance (CrCl) and serum creatinine (SCr)) and are fed into a stacked auto-encoder (SAE) with a softmax classifier to obtain the final diagnosis as AR or non-rejection (NR).

1. Kidney Segmentation

Providing a fully-automated and precise segmentation of the renal allograft is a key step in the Renal-CAD system. Precise extraction of imaging features for accurate final diagnosis requires high segmentation accuracy. To improve segmentation accuracy, data preprocessing was performed prior to applying the previously developed segmenta-
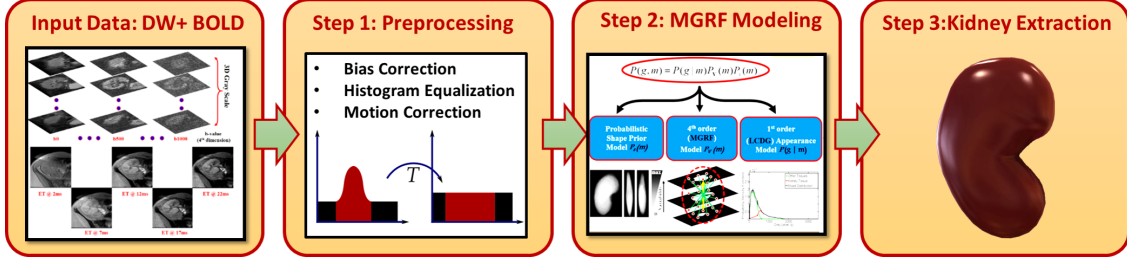
FIGURE 4: Block diagram illustrating the kidney segmentation approach's steps. The raw DW- and BOLD-MRI data are first pre-processed to suppress noise and motion effects. Then, a joint Markov-Gibbs random field (MGRF) image model that accounts for the shape, intensity, and spatial features is employed. Finally, a level-set segmentation guided by the MGRF model is applied to get the final segmented kidney.

tion approach [72], see Fig. 16. Briefly, histogram equalization was first applied on the bias corrected [73] MR images to suppress noise effects and image inconsistencies. Then, a nonrigid registration using B-splines approach [74] was employed to handle kidney motion and to reduce MRI anatomical variability among different patients to improve segmentation accuracy. Subsequently, renal segmentation based on the level-sets method [72] was performed. To enhance kidney segmentation accuracy, a joint Markov-Gibbs random field (MGRF) image model that combines three different components: shape, grey level, and spatial MRI features was employed. Renal segmentation approach accuracy was evaluated on all DW- and BOLD-MRIs for a more precise estimation of the discriminatory features. Two examples for the segmentation approach's results for both DW- and BOLD-MRIs are shown in Figs. 5 and 6, respectively. Details of this approach has been described in the published work [72].
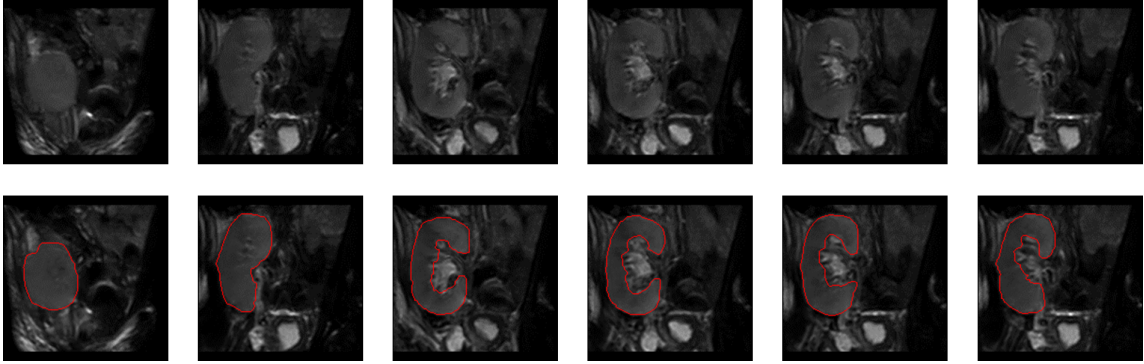
FIGURE 5: Segmentation results example for a DW-MRI subject. The upper raw shows different DW-MRI coronal cross-sections raw data, while the lower raw shows the corresponding segmentation results with red edges.

Kidney Segmentation for BOLD Data
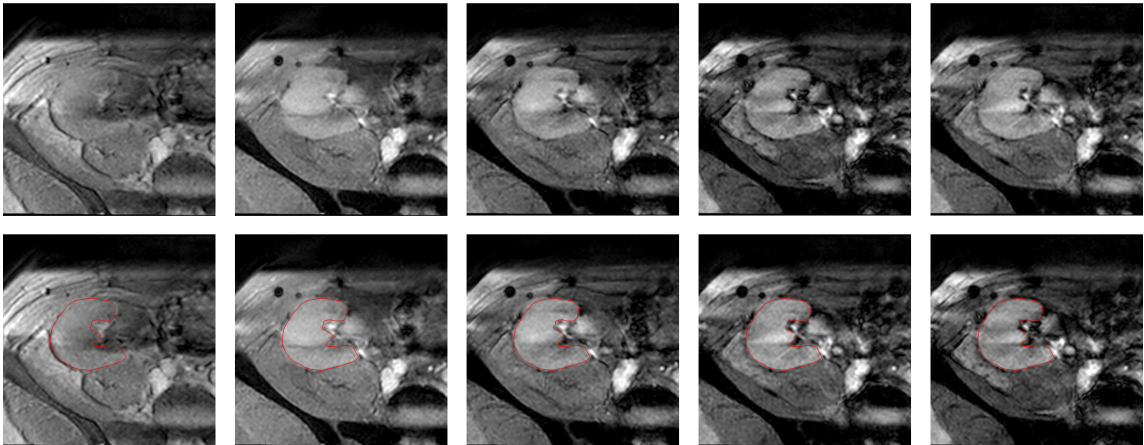
FIGURE 6: Segmentation results example for a BOLD-MRI subject. The upper raw shows different BOLD-MRI coronal cross-sections raw data at different echo times (from left to right: 2, 7, 12, 17, and 22 ms), while the lower raw shows the corresponding segmentation results with red edges.

2. Feature Extraction

Diffusion Weighted Imaging Markers: The significant advantages of DW-MRI is high-lighted by its ability to quantify local characteristics of blood diffusion and to interrelate them with the transplant status, due to DW-MRI's ability to measure the unique charac-teristics of inner spatial water behavior in the soft tissue (e.g., kidney). This behavior is quantified by apparent diffusion coefficients (ADCs) [37, 40, 55], which can be utilized to evaluate the kidney transplant status. Following the accurate segmentation of the kid-ney, the DW-MR image-markers (i.e. voxel-wise ADCs) are estimated precisely using the following equation [50, 75] as:

$$\mathrm{ADC_{vx}} = \frac{\ln g_{0:vx} - \ln g_{b:vx}}{b} \tag{1}$$

vx : A voxel with its 3D Cartesian location (x, y, z).

g$_0$: T2-weighted signal intensity obtained at $b = 0$.

g$_b$: Diffusion-weighted signal intensity obtained at the given b-value.

The voxel-wise ADCs were estimated at the 11-different b-values to be used as dis-criminatory features to assess kidney transplant. However, using such voxel-wise ADCs as discriminatory features has the following limitations: (1) varying input data size that might lead to data truncation and/or zero padding for smaller and/or larger kidney volumes, re-spectively and (2) considerable training and classification time is needed, especially, in the case of large data volumes. In order to overcome these limitations, these voxel-wise ADCs were characterized at the 11 different b-values, using the cumulative distribution functions (CDFs) of the ADCs. To construct such CDFs, the minimum and maximum ADCs were calculated for all input datasets. Then, CDFs of the voxel-wise ADCs were constructed at the 11-different b-values (100 steps for each CDF) resulting in a DW-MR image markers (D_{mrks}) vector of size 1100×1. Please see Fig. 7.

25
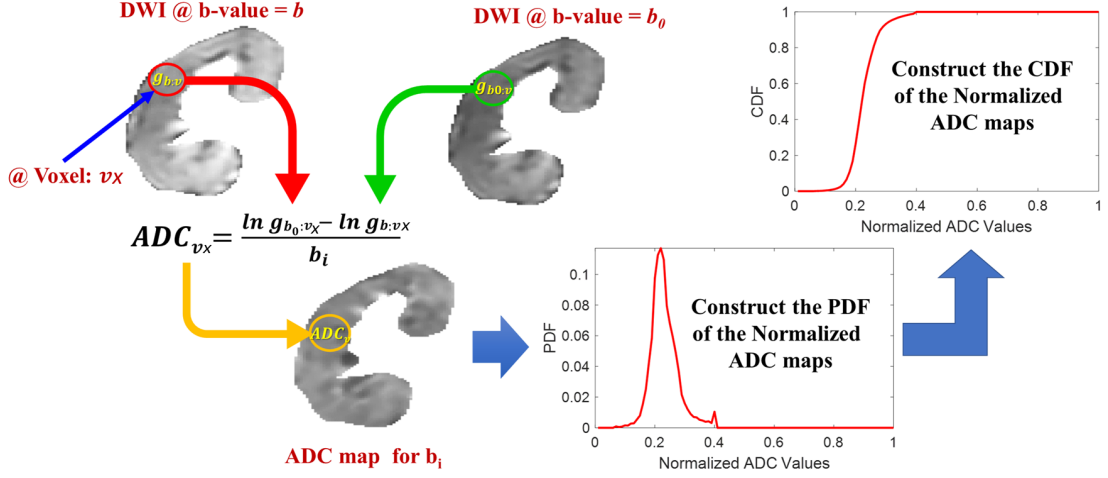
FIGURE 7: Demonstration of DW-MRI features construction procedure. First, the apparent diffusion coefficients (ADCs) are estimated from the segmented kidneys at 11-different *b*-values. Then, probability distribution functions (PDFs) and cumulative distribution functions (CDFs) are constructed consequently from the estimated ADCs at all *b*-values.

BOLD-MR Imaging Markers: BOLD-MRI estimates the amount of the renal allograft content of deoxygenated hemoglobin (R2*). By measuring T2* (i.e., the amount of oxygenated hemoglobin [49]) in the allograft, one can calculate the R2* by taking the reciprocal of T2*. The mean R2* values were estimated from the delineated allograft using four different TE (7, 12, 17, 22 ms) resulting in a 4×1 vector of mean R2* values (Fig. 8). This vector was used as the combined discriminatory BOLD-MR image-markers (B_{mrks}) to assess renal allograft status. The BOLD-MRI data acquired at 2 ms was used as the baseline. The pixel-wise T2* and R2* maps can be estimated using the following equations [48]:

$$\text{T2}^*_{\mathbf{px}} = \frac{t_0 - t}{\ln S\,I_{t:\mathbf{px}} - \ln S\,I_{t_0:\mathbf{px}}} \tag{2}$$

$$\text{R2}^*_{\mathbf{px}} = \frac{1}{\text{T2}^*_{\mathbf{px}}} \tag{3}$$

26
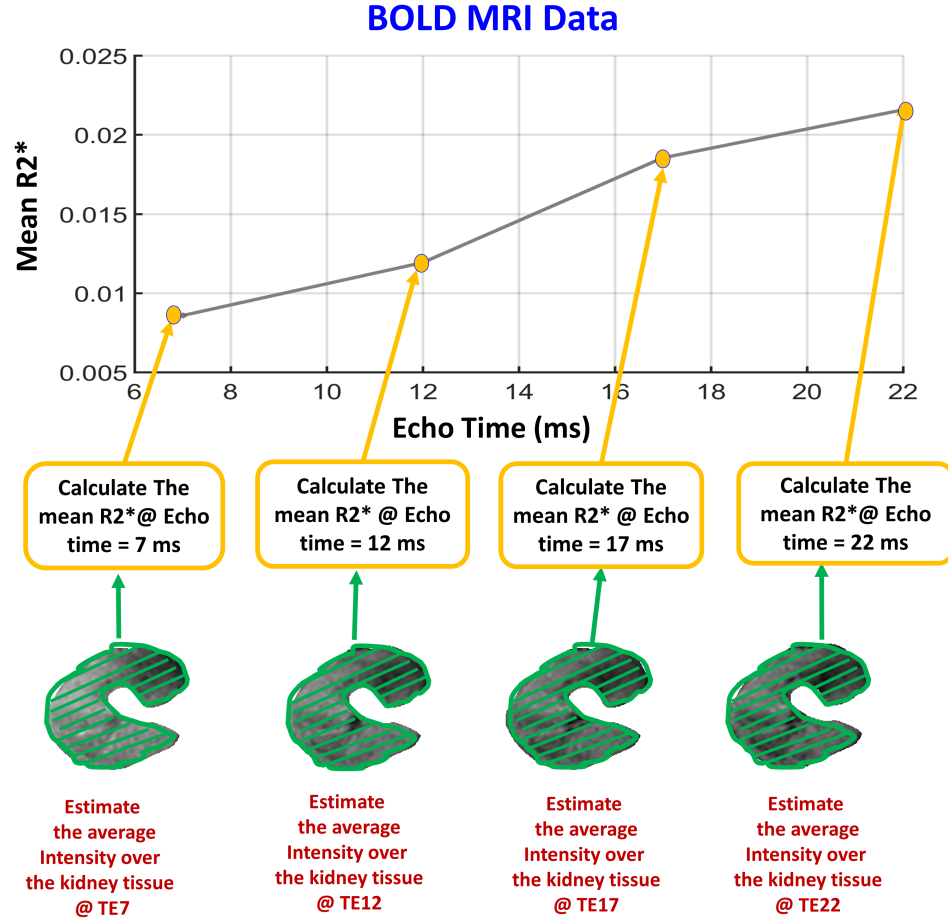
FIGURE 8: Demonstrating the procedure of constructing BOLD-MRI features, where the mean T2* values are estimated from the segmented allograft at 4-different echo-times (TE = 7, 12, 17, 22 ms). Then, the mean R2* values are estimated by taking the reciprocal of the estimated T2* values.

px: a pixel with its 2D Cartesian location (x, y).

$\mathbf{SI}_t$: signal intensity obtained at TE = t and extracted from the segmented image.

$\mathbf{SI}_{t_0}$: signal intensity obtained at the baseline TE = 2 ms and extracted from the segmented image.

3. Deep Learning-based Stacked Autoencoders

Deep learning is a machine learning approach that is widely used in many applications, including in the medical domain (e.g., detection, diagnosis, prediction, etc.) for specific diseases. An autoencoder (AE) is an artificial neural network (ANN) that employs an unsupervised deep learning/training approach followed by a supervised backpropagation-based refinement algorithm to provide a better classification performance [4, 5, 76]. The main structure of an AE, shown in Fig. 9, can be basically defined as three main types of layers: an input layer, a hidden layer, and an output layer. The AE training procedure can be classified into encoding and decoding processes. In the encoding process, the input data is mapped into a hidden representation through the hidden layer. In the decoding process, the input data are reconstructed from the hidden-layer representation. Both encoding and decoding processes are primarily used to learn an approximation to the identity function, which implies that the reconstructed input $\widehat{X}$ (i.e., decoding process output) is almost identical to the input X, see Fig. 9. The main purpose of this identity function is to force the AE to learn a compressed representation of the input, especially when the number of hidden nodes is less than the input size. Conversely, the AE is forced to reconstruct the input back given only the hidden features/activations.

Given the unlabeled training input dataset $\{X_n : n = 1 \ldots N\}$, such that each $X_n \in \mathbb{R}^m$, $H_n \in \mathbb{R}^k$ represents the hidden layer's features/activations resulting from the encoding process of the input vector X_n, this encoding process can be described by the following equation:

$$H_n = f_e \left(W_e X_n + B_e \right), \tag{4}$$

where f_e represents the encoder activation function, which in this study is a sigmoid func-

28
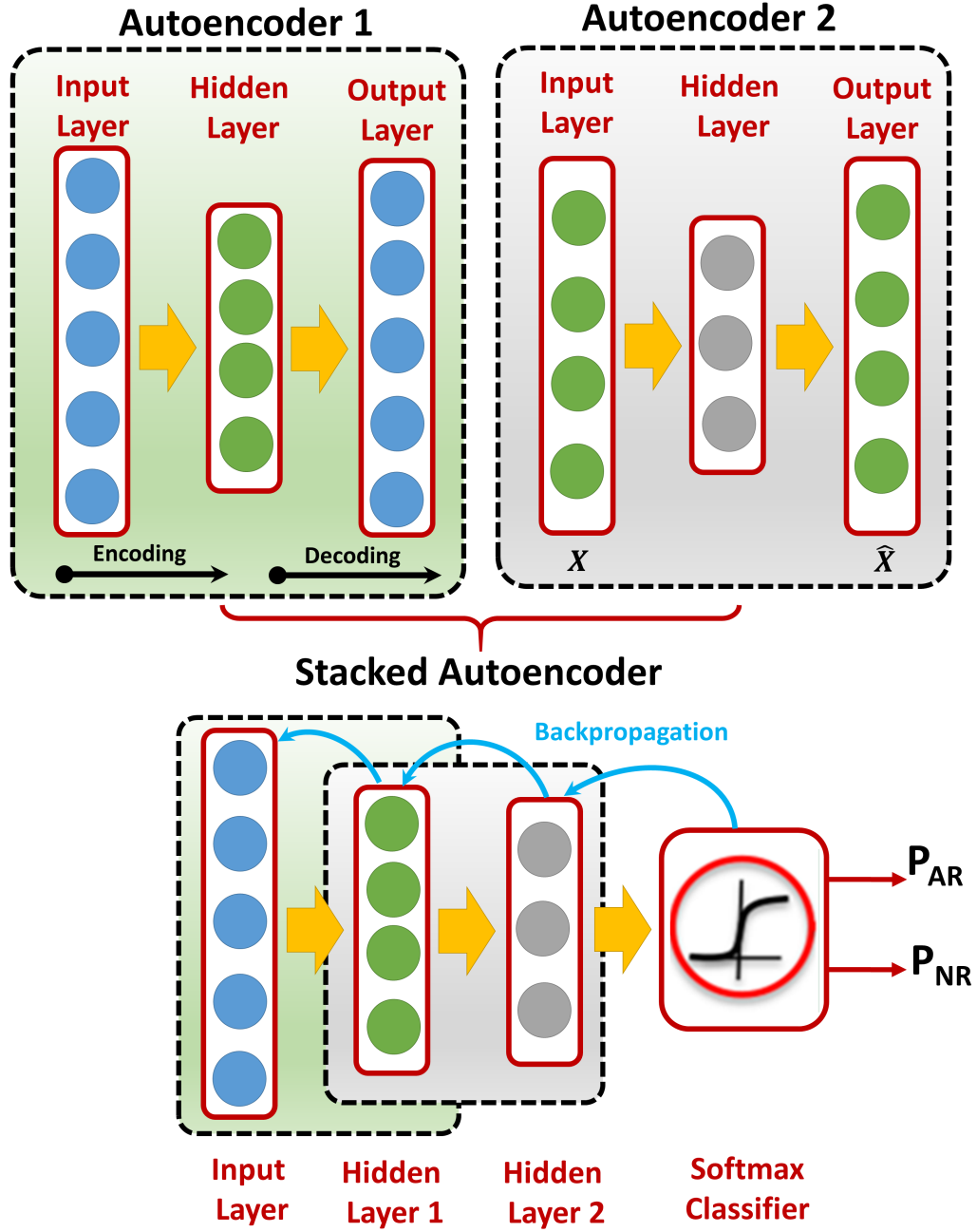
FIGURE 9: A demonstrative figure for the basic structure of the autoencoder (AE), where each AE consists of an input layer, a hidden layer, and an output layer. After training each AE separately, AE_1 is stacked with AE_2 and a softmax classifier on the top of them to obtain a stacked AE (SAE). Then, a backprobagation-refinement algorithm is used to update the hidden weights of the SAE.

tion, i.e. a differentiable, monotone scalar function with range $(0, 1)$. $W_e \in \mathbb{R}^{k \times m}$ and $B_e \in \mathbb{R}^k$ are the weight matrix and the bias vector of the encoder, which are randomly initialized. Given the hidden layer's features/activations H_n obtained from the aforementioned encoding process, the following equation describes the decoding process to obtain the reconstructed input $\widehat{X}$:

$$\widehat{X}_n = f_d \left(W_d H_n + B_d \right), \tag{5}$$

where f_d represents the decoder function, while W_d and B_d are the weights and biases of the decoder, respectively. The optimal set of hyper-parameters of the AE can be tuned based on the compression/decompression reconstruction error minimization criteria as follows:

$$J_{AE}(W, B) = \frac{1}{2n} \sum_{i=1}^{n} \left\| \widehat{X}_{W:i} - X_i \right\|^2, \tag{6}$$

where $\|\widehat{X}_{W:i} - X_i\|^2$ represents the loss function that needs to be minimized, which in turn will lead to the reduction of the reconstruction error $J_{AE}(W, B)$ at the end. To obtain the final stacked AEs (SAEs) that will be used in the Renal-CAD system for the early detection of AR, two autoencoders (AE_1 and AE_2) followed by a softmax classifier were trained and stacked together, see Fig. 10. Algorithm summarizes building and optimizing the SAE classification model.

Overfitting and Dropout Technique: Deep neural networks (DNNs) are known with their complex structure, which makes them prone to overfitting. A DNN is overfitted when it fails to generalize or provide a correct analysis/output given a new set of input data. Overfitting typically occurs when the training set is not large enough. Dropout technique is a proven methodology for its ability to reduce overfitting in the training phase [77, 78]. Using dropout technique, one can obtain various representations for the relationships between the training data. Some of the hidden neurons can be randomly deactivated, while

30
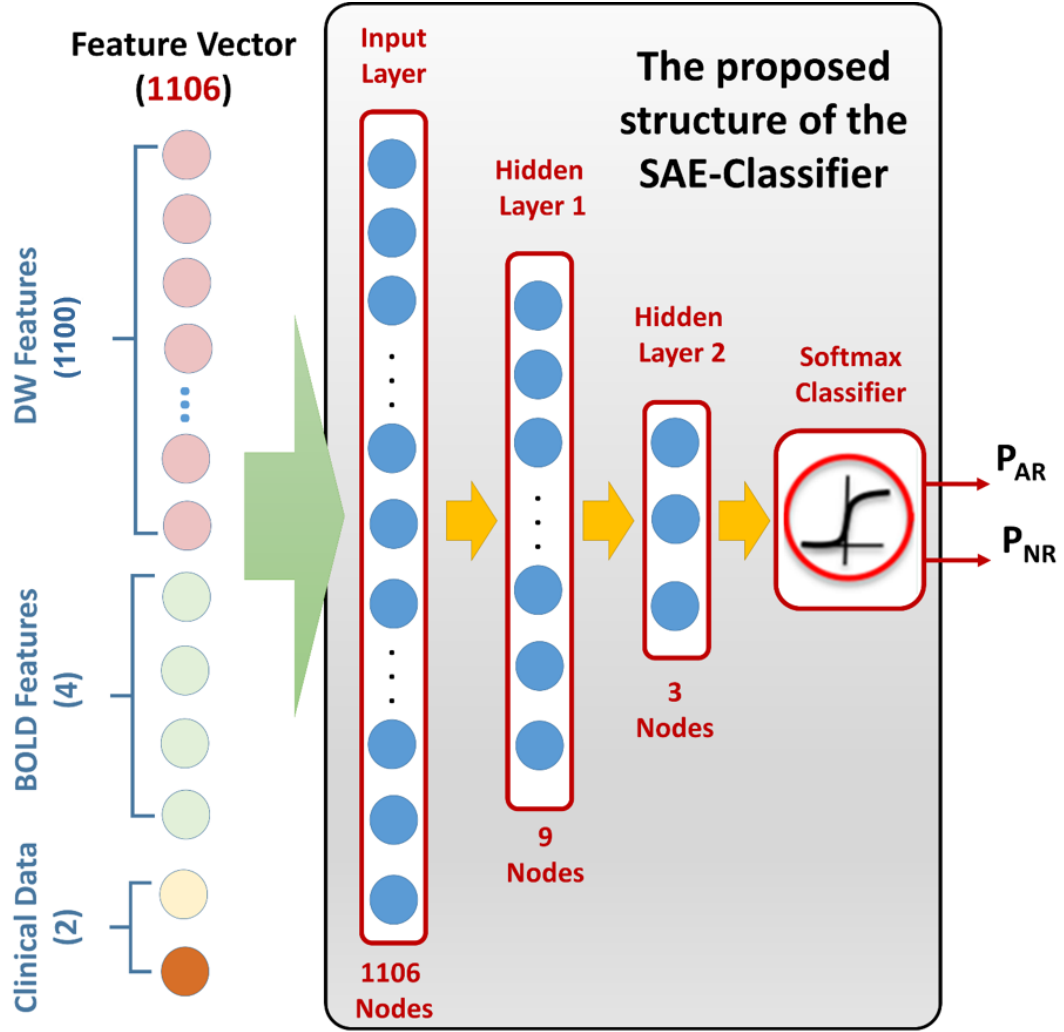
FIGURE 10: An illustrative figure showing the structure of the proposed SAE classifier. The feature vector uses the concatenation criteria to integrate diffusion markers with BOLD markers and clinical biomarkers. This vector is used as the SAE's input and processed through two hidden layers and a softmax classifier to get the final probability of being an AR or NR renal allograft.

Algorithm 1 Building, Stacking, and Optimizing The Developed SAE

1 Train the first autoencoder AE_1, separately, by using the input data X_1 to obtain the learned features/activations H_1.

2 Use the features/activations (H_1) obtained from AE_1 as an input to train the second AE_2.

3 Use the features/activations (H_2) obtained from the second AE_2 as an input to train a softmax classifier to compute the plausibility of being assigned to class 1 or 2.

4 Stack AE_1, AE_2, and the softmax classifier together to get your SAEs, and use a supervised backpropagation-based refinement algorithm to minimize the conventional error in the SAEs and update the hidden weights.

5 Finally, fine tune the hyper-parameters by using a grid search criteria that minimizes the cost function as an optimization metric to provide a better classification performance.

preserving their corresponding weights and biases, in each iteration during the training phase. In the next iteration, these deactivated neurons could be re-activated and some other different neurons might be deactivated. These permutating deactivation process leads to reduction in the total number of the activated neurons and thus hinder the complex co-adaptations between training data. In this chapter, the dropout technique was used to suppress the overfitting effect by extracting meaningful features and to improve the final diagnostic accuracy of the developed Renal-CAD system.

4.   Kidney Diagnosis by Integrating Diffusion, BOLD, and Clinical Biomarkers

To obtain an accurate assessment of the kidney transplant, the following different sources of information were integrated: (*i*) the estimated D_{mrks} vector of size 1100×1 to interrelate local blood diffusion characteristics with the transplant status; (*ii*) the estimated B_{mrks} vector of size 4×1 to quantify the amount of the renal allograft content of deoxygenated hemoglobin and interrelating it with the transplant status; and (*iii*) the combined

clinical biomarkers (SCr and CrCl) resulting in C_{bmrks} vector of size 2×1 to measure the creatinine levels in both blood and urine, and thus; the filtration ability for renal transplant assessment. These three sources of information were integrated using the concatenation method resulting in an integrated biomarkers (I_{bmrks}) vector of size 1106×1 that will be used as the final discriminatory features between the AR and NR groups.

After obtaining the I_{bmrks}, a classification process based on using a leave-one-subject-out cross-validation (LOSOCV) approach was employed using SAEs to obtain the final diagnosis. The I_{bmrks} of size 1106×1 were fed as an input vector to SAEs to build the classification model. A grid search algorithm minimizing the cost function as an optimization metric was employed to find the optimal-set of hyper-parameters. The two-layer SAEs with the first hidden layer (n = 9 nodes), second hidden layer (n = 3 nodes), output softmax layer (n = 2 nodes), weight decay parameter = 0.0022, weight of sparsity penalty term = 20, desired average activation of the hidden units = 0.2421, and dropout fraction = 0.5, provided the optimal diagnostic accuracy using LOSOCV approach and was selected for the proposed Renal-CAD system (Fig. 10).

C.   Experimental Results

Two methods were used for train, test, and validation purposes. The first one is known as K-fold (i.e., LOSOCV) and is depending on training the network with all data while leaving only one subject outside for testing purpose. Then, in the next iteration, the network was reinitialized, and the subject that was left in the previous iteration was included back in the training data and the next subject was left outside for testing purpose. This procedure was repeated by the number of the subjects (N = 30, Training Data = 29, Testing Data = 1) and the diagnostic results were reported. The second validation is known as stratified 10-fold cross-validation in which 90% of the data were used for the

training and 10% of the data were randomly selected and kept for testing. Then, in the next iteration, the network was reinitialized and that 10% was included back in the training set and another randomly selected 10% was kept for testing. This process was repeated for 10 times (N = 30, Training Data = 27, Testing Data = 3).

It is worth mentioning that stratification was assured in the 10-fold cross-validation to help reduce both bias and variance. Stratification technique does not only allow for randomization but also ensures that the training/testing spilt percentages of each class in the entire data will be similar within each individual fold. In this case, NR = 20 subjects (67%) and AR = 10 subjects (33%), stratification ensures that 67% of the training data will be derived from NR subjects and 33% will be derived from AR subjects and the same percentages will be maintained for the test data too.

Renal-CAD software is primarily implemented in Matlab (The MathWorks, Natick, Massachusetts), with time-critical subroutines developed in C using the Matlab Mex API. Cross-validation experiments were performed on a Dell Precision workstation with Intel Xeon eight-core CPU running at 2.1 GHz and 256 GiB RAM.

The developed Renal-CAD system with SAEs classifier was tested using the I_{bmrks} constructed for the 30 datasets that had both DW- and BOLD-MRI scans based on the LOSOCV approach. To demonstrate the effect of integrating D_{mrks} with B_{mrks} and C_{bmrks} and highlight its advantages, six additional scenarios were performed and compared with the Renal-CAD system using accuracy, sensitivity, and specificity as performance evaluation metrices, see Table 2. The first scenario (S_1) utilized the D_{mrks} alone on the 47 datasets along with the same SAEs classifier and the LOSOCV approach. The second scenario (S_2) employed the B_{mrks} alone on the 30 datasets along with the same LOSOCV approach. However, because the B_{mrks} are of smaller size (i.e. 4×30), SAEs were replaced with a conventional multi-layer preceptron artificial neural network (MLP-ANN) classi-

34

fier with two hidden layers (hl_1, n = 3 nodes and hl_2, n = 1 node). The third scenario (S_3) used the C_{bmrks} alone on the 47 datasets along with the same LOSOCV approach. However, because the C_{bmrks} are of smaller size (i.e. 2×47), the SAEs were replaced by a linear discriminant analysis (LDA) classifier. The fourth scenario (S_4) integrated both D_{mrks} with B_{mrks} resulting in DB_{mrks} on the 30 datasets along with the same SAEs classifier and the LOSOCV approach. The fifth scenario (S_5) integrated both D_{mrks} with C_{mrks} resulting in DC_{mrks} on the 47 datasets along with the same SAEs classifier and the LOSOCV approach. The sixth scenario (S_6) integrated both B_{mrks} with C_{mrks} resulting in BC_{mrks} on the 30 datasets along with the same LOSOCV approach. However, because the BC_{mrks} are of smaller size (i.e. 6×30), SAEs were replaced with a MLP-ANN classifier with two hidden layers (hl_1, n = 5 nodes and hl_2, n = 1 node). Results in Table 2 suggests that the utilization of the I_{bmrks} had a positive effect on the final diagnostic accuracy. This can be justified in part by the different abilities of each individual marker (i.e. D_{mrks}, B_{mrks}, and C_{bmrks}) to evaluate renal allograft function, which are complementary to each other.

To ensure that the developed Renal-CAD system is not prone to overfitting (i.e., after using the dropout technique) and to validate the reproducibility and robustness of the Renal-CAD system, a stratified 10-fold cross-validation approach was performed on the same dataset (N = 30) using the same integrated biomarkers I_{bmrks} and the same SAEs with its previously defined structure and hyper-parameters. Results are reported in Table 3 and compared with the results obtained earlier using the LOSOCV approach in terms of accuracy, sensitivity, specificity, and area under the curve (AUC). In addition, the LOSOCV experiment was repeated 100 times with different randomly selected network initialization to ensure that the Renal-CAD system would be able to produce consistent diagnostic results. The Renal-CAD system produced the following diagnostic results: 91.65 ± 1.74 (% accuracy), 90.0 ± 0.0 (% sensitivity), and 92.5 ± 2.64 (% specificity). These validation experiments demonstrated the reproducibility and robustness of the Renal-CAD system.

TABLE 2: Diagnostic performance comparison between the proposed Renal-CAD system using the integrated biomarkers (I_{bmrks}) and six other scenarios S_1, S_2, S_3, S_4, S_5, and S_6 using the individual DW-MR image markers (D_{mrks}), BOLD-MR image markers (B_{mrks}), clinical biomarkers (C_{bmrks}), integrated diffusion and BOLD markers DB_{mrks}, integrated diffusion and clinical biomarkers DC_{mrks}, and integrated BOLD and clinical biomarkers BC_{mrks} respectively. Let Acc: accuracy, Sens: sensitivity, Spec: specificity, and AUC: area under the curve.

	Classification Performance (NR vs. AR)						
	$S_1(D_{mrks})$	$S_2(B_{mrks})$	$S_3(C_{bmrks})$	$S_4(DB_{mrks})$	$S_5(DC_{mrks})$	$S_6(BC_{mrks})$	**Renal-CAD(I_{mrks})**
Acc%	80.9	86.7	70.2	90.0	87.2	90.0	**93.3**
Sens%	76.5	80.0	80.0	90.0	82.4	80.0	**90.0**
Spec%	83.3	90.0	52.9	90.0	90.0	95.0	**95.0**
AUC	0.84	0.84	0.71	0.90	0.88	0.88	**0.92**

TABLE 3: Diagnostic performance of the developed Renal-CAD system using the integrated biomarkers (I_{bmrks}) using LOSOCV approach vs. 10-fold cross-validation approach. Let Acc: accuracy, Sens: sensitivity, Spec: specificity, and AUC: area under the curve.

	Classification Performance (NR vs. AR)			
	Acc%	**Sens%**	**Spec%**	**AUC**
Renal-CAD (LOSOCV)	93.3	90.0	95.0	92.0
Renal-CAD (10-fold)	86.7	80.0	90.0	0.88

Statistical analysis was performed using R version 3.6. Differences in ADC or R2* between groups (AR/NR) were analyzed using MANOVA. Statistical significance was estimated from Pillai's trace, converted into its approximately equivalent F statistic. MANOVA was performed using the individual imaging parameters by themselves, combined imaging parameters, and also in combination with lab values (CrCl and SCr). Follow up comparisons of ADC or R2* at each individual b-value or time point, respectively, were made using t-tests.

From Tables 4 and 5, renal allografts without AR had a slightly higher, albeit not significantly, mean ADCs at individual b-values, particularly with higher gradients ≥ 200, compared to AR. When all gradients were combined together, NR group had significantly higher ADCs than the AR group. The AR renal allografts had a higher, but not significant, mean R2* at the different echo-times (i.e. lower T2* values, which means lower amount of oxygen supply). Similarly, the combined R2* model did not reach significant differences. Table 6 demonstrates the statistical significance between the two groups (AR vs. NR) using the individual clinical biomarkers, all of the possible pair-wise multivariate combinations, and the combination of the imaging modalities with the clinical biomarkers (All). As reported in Table 6, the CrCl and SCr have shown statistically significant differences between the two groups (the NR group demonstrated higher CrCl values and lower SCr values than the AR group). In addition, all possible pair-wise combinations and the combined model (All) demonstrated statistical significance between the two groups.

The performance of the developed Renal-CAD system was evaluated by constructing the receiver operating characteristics (ROC) [79], see Fig. 11. Furthermore, the performance of Renal-CAD system was compared to the six scenarios (S_1, S_2, S_3, S_4, S_5, and S_6) in terms of area under the curve (AUC). The Renal-CAD demonstrated the highest AUC of 0.92, as shown in Table 2 and Fig. 11. In addition, reproducibility and robustness of the Renal-CAD system was confirmed by comparing the performance of the

TABLE 4: A comparison in terms of means and standard deviations (stds) of the ADC maps at 11-individual b-values between the non-rejection (NR) group and the acute rejection (AR) group. Statistic is t with approximately 31 effective degrees of freedom in univariate case, F with 11 degrees of freedom in the numerator and 35 in the denominator in the multivariate case.

ADC Maps at Individual b-values: mean(std) $\approx$											
b (s/mm^2)	50	100	200	b300	400	500	600	700	800	900	1000	Combined
NR(30)	4.0(0.66)	3.31(0.48)	2.86(0.31)	2.62(0.25)	2.48(0.20)	2.35(0.18)	2.25(0.15)	2.17(0.13)	2.09(0.12)	2.01(0.12)	1.94(0.11)	$-----$
AR(17)	3.99(0.71)	3.37(0.48)	2.81(0.36)	2.53(0.32)	2.37(0.25)	2.26(0.23)	2.17(0.23)	2.07(0.22)	2.00(0.20)	1.93(0.19)	1.87(0.18)	$-----$
Statistics	-0.016	0.368	-0.465	-1.00	-1.52	-1.40	-1.36	-1.62	-1.65	-1.61	-1.56	2.49
p-value	0.987	0.715	0.645	0.326	0.139	0.173	0.188	0.119	0.113	0.120	0.133	**0.020**

TABLE 5: A comparison in terms of means and standard deviations (std) of the R2* maps at 4-individual echo-times between the non-rejection (NR) group and the acute rejection (AR) group. Statistic is t with approximately 13 effective degrees of freedom in univariate case, F with 4 degrees of freedom in the numerator and 25 in the denominator in the multivariate case.

R2*/s Values at Individual Echo-times: mean(std) $\approx$					
Echo-time	**7 ms**	**12 ms**	**17 ms**	**22 ms**	**Combined**
NR(20)	23.6(18.0)	19.9(5.8)	19.9(7.2)	19.4(4.7)	$-----$
AR(10)	25.1(16.8)	20.3(9.3)	23.7(11.3)	23.3(10.3)	$-----$
Statistics	0.244	0.149	0.974	1.14	1.95
p-value	0.810	0.884	0.348	0.277	0.133

Renal-CAD using a 10-fold cross-validation to the LOSOCV approach in terms of ROC (Fig. 12) and AUC (Table 3).
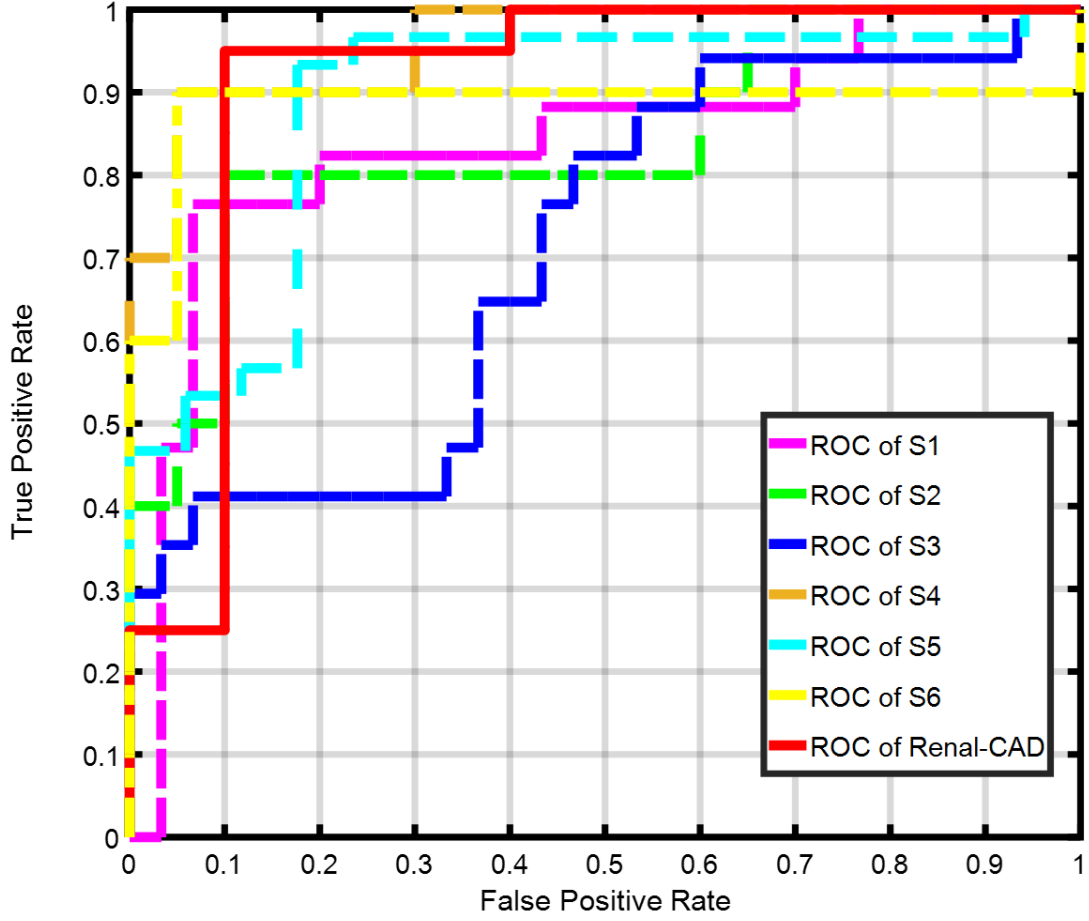
FIGURE 11: Receiver operating characteristics (ROC) curve for the proposed Renal-CAD system vs. six other different scenarios, namely; S_1, S_2, S_3, S_4, S_5, and S_6 using the individual DW-MR image markers (D_{mrks}), BOLD-MR image markers (B_{mrks}), clinical biomarkers (C_{bmrks}), the combined DW- and BOLD-MR image markers (DB_{mrks}), the combined DW-MR image markers and clinical biomarkers (DC_{mrks}), and the combined BOLD-MR image markers and clinical biomarkers (BC_{mrks}), respectively. The Renal-CAD area under the curve (AUC) is almost approaching the unity, demonstrating the feasibility and robustness of the developed system.
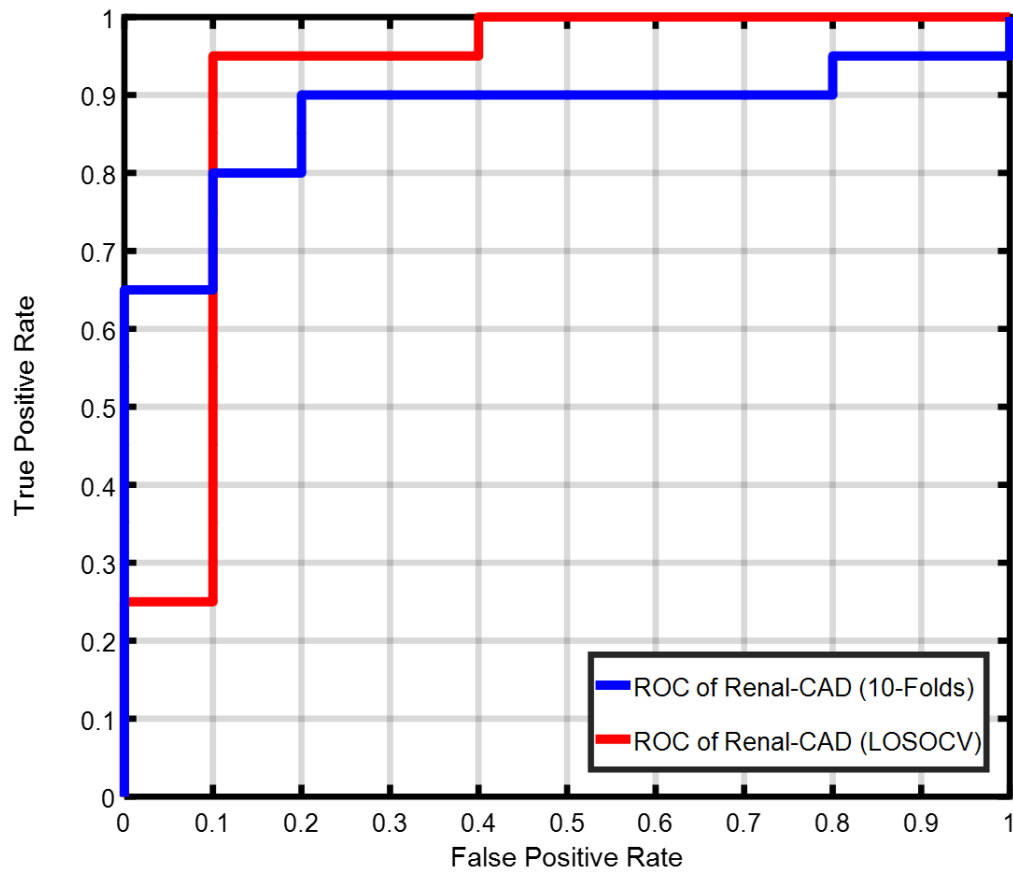
FIGURE 12: Receiver operating characteristics (ROC) curve for the proposed Renal-CAD system using the leave-one-subject-out cross-validation (LOSOCV) approach with an area under the curve (AUC) of 0.92 vs. using the 10-fold cross-validation approach with an AUC of 0.88. A reduction of only 0.04 in the AUC demonstrates the reproduciblity and robustness of the developed system.

TABLE 6: A comparison in terms of means and standard deviations (stds) of the clinical biomarkers (CrCl and SCr) between the non-rejection (NR) group and the acute rejection (AR) group. Note: d.f. denotes degree of freedom with different values depending on the combined variables.

Data	CrCl	SCr	D_{mrks}+C_{mrks}	B_{mrks}+C_{mrks}	D_{mrks}+B_{mrks}	All
NR	74.8(26.3)	1.2(0.4)	– – ––	– – ––	– – – – –	– – – – –
AR	54.1(22.3)	1.63(0.6)	– – ––	– – ––	– – – – –	– – – – –
Statistics	−2.88	2.81	2.51	3.78	3.00	3.57
d.f.	38.1	23.4	13/33	6/23	15/14	17/12
p-value	**0.007**	**0.010**	**0.016**	**0.009**	**0.023**	**0.015**

D.   Discussion and Conclusions

The classification results of the Renal-CAD system that integrated multi-modal imaging markers and clinical biomarkers demonstrated high accuracy, sensitivity, and specificity. These results demonstrated the feasibility and efficacy of the Renal-CAD system to precisely and non-invasively identify renal allograft status at an early stage. Classification results obtained using individual imaging modalities (DW-MRI or BOLD-MRI) had lower accuracy, sensitivity, specificity, and area under the curve compared to the Renal-CAD system. The estimated diffusion markers (D_{mrks}) has the potential to interrelate local blood perfusion and water diffusion characteristics with the transplant status and thus, provide a good discriminator between AR and NR renal transplants. Most of the clinical studies estimated the ADC values at two selected *b*-values. Usually, they select one with a low gradient strength *b*-values < 200 to be able to measure blood perfusion [66, 67]

and one with a high gradient strength > 200 to be able to measure water diffusion inside the kidney [66–69]. This study utilized 11-different gradients to estimate both blood perfusion and water diffusion to enhance diagnostic accuracy. The obtained results are in line with the findings of other clinical studies [36, 38–41, 51, 56, 57, 65] in that the NR renal transplants demonstrated higher ADC values than AR transplants (*b*-value > 200).

The estimated BOLD-MRI markers (B_{mrks}) can quantify the amount of the renal allograft content of deoxygenated hemoglobin to interrelate with the transplant status. There is no consensus regarding whether NR or AR has higher R2* values. Further, the threshold R2* values to distinguish AR from NR are not known [43, 44, 49]. The findings of this study suggest that AR renal allografts demonstrate higher values of R2* at the different echo-times as previously reported [42, 60]. This can be physiologically justified in part by the fact that the change in oxygenation in the medulla may be associated with an almost hypoxic condition that makes it vulnerable to a further decrease in oxygen supply.

Clinicians are able to measure the creatinine levels in both blood and urine, and thus; the filtration ability for renal transplant assessment. However, these clinical biomarkers are imprecise and usually a later stage indication of rejection, when the damage to the kidney and the loss of renal function can be substantial. The developed Renal-CAD system integrates all available information to enhance diagnostic accuracy (93.3%), sensitivity (90.0%), specificity (95.0%), and AUC (0.92). This improved diagnostic ability is due to the integration of each individual marker (i.e. D_{mrks}, B_{mrks}, and C_{bmrks}) that can capture different aspects of renal allograft dysfunction that are complementary. The Renal-CAD system is robust to handle missing data, while still providing reasonable accuracy, as evidenced by Table 2.

In conclusion, the developed Renal-CAD system demonstrated a high classification accuracy (93.3%), sensitivity (90.0%), specificity (95.0%), and AUC (0.92) for early

stage diagnosis of AR post-transplantation. Renal-CAD integrates individual biomarkers (i.e. clinical biomarkers with DW-MR and BOLD-MR image markers) for a better characterization of renal allograft function and accurate identification of AR.

CHAPTER IV

RENAL CANCER DIAGNOSIS SURVEY

Renal cancer (RC) is considered the 10th most prevalent cancers in men and women worldwide. Early and accurate diagnosis of renal tumors, specifically, grading and staging of malignant tumors help identifying the aggressiveness and the spread of such tumors, respectively. This can potentially help in administering a timely intervention with the optimal management plan. Although biopsy remains the gold standard for diagnosing renal tumors, it is late, invasive, expensive, and has adverse affects such as bleeding and infection. In addition, it cannot assess the treatment response. Artificial intelligence (AI) when paired with Radiomic markers resulted in developing AI-based computer-aided diagnostic (AI-based CAD) systems, which have shown promising results for early diagnosis of renal tumors (i.e., specifying malignancy status, subtyping, grading, and staging). Definitely, this will help reducing diagnosis time, enhancing diagnostic performance, reducing the need for invasive procedures, and provide the guidance for proper management to avoid the burden of unresponsive treatment plans. This main goal of this chapter is to spot the lights on the recent technical diagnostic studies from the last decade, with their pros and cons, that have utilized AI and Radiomics markers extracted from computed tomography (CT) and magnetic resonance (MR) images to produce AI-based CAD systems for precise diagnosis of RC at an early stage.

A. Background on Renal Cancer

Renal cancer is 10th most common cancer among men and women. For the past several decades, an increasing number of new patients have been diagnosed with renal cancer. In the year 2022, approximately 79,000 new cases are expected to be diagnosed with RC in the United States [15, 80], and 14,000 patients are expected to have died from renal cancer in that same time period [15, 80]. Roughly two thirds of the time, renal cancer is diagnosed before it has metastasized, in which case the 5-year survival rate is 93%. Once it has spread to the lymph nodes or the surrounding abdominal structures (i.e., other organs or tissues), the 5-year survival rate falls to 72%. In the worst case of metastasis to distant parts of the body, the 5-year survival rate is a mere 15% [15, 80]. In addition, the National Cancer Institute had an approximated cost estimate of $5.1 billion for renal cancer care in the United States by the end of 2022 [81]. Renal cancer is a heterogeneous disease in which the renal cells become malignant (cancerous) and form tumors called renal masses. These renal masses, if not detected early and treated promptly, will lead to mortality. The most common, and also the most aggressive, renal cancer is renal cell carcinoma (RCC), accounting for 70% of all cases [82, 83]. In turn, 70% of RCC are clear cell renal cell carcinoma (ccRCC), and of the remaining non-clear cell subtypes (nccRCC), the most prevalent are papillary (paRCC) and chromophobe (chrRCC) renal cell carcinomas, accounting for 15% and 5% of all RCC, respectively [84]. The World Health Organization (WHO) taxonomy of RCC [84] has clinical significance because the various subtypes can have very different prognoses [84–86]. Differential diagnosis of RCC must look out for the benign tumors angiomyolipoma (AML) and oncocytoma (ONC), which are easily confused with RCC using conventional diagnostic techniques [87–91]. AMLs with low fat content are particularly prone to misdiagnosis [92]. Diagnostic error leads to unnecessary surgical intervention for benign lesions, to the point where 15–20% of surgically resected "RCC" may actually be AML [93]. Therefore, accurate characterization of such renal

masses at an early stage is crucial to the identification of appropriate treatment plan.

Evidence of renal cancer can be found in complete blood count (CBC) to check for the number of red blood cells; urine tests to look for blood, bacteria, or cancerous cells in urine; and blood chemistry tests to quantify renal function by checking the levels of certain chemicals in the blood. These signs are suggestive at best, and inadequate for diagnosis or typing of renal cancer. Only biopsy, performed by interventional radiologists and/or nephrologists, can provide a definite diagnosis of renal cancer, and thus remains the gold standard [15, 80]. However, it can only be used as the last resort due to its high invasiveness, cost, and turnaround and recovery times (approximately a week). Therefore, the investigation of noninvasive diagnostic techniques to provide an early, reliable, accurate, cost-effective, and rapid diagnosis of renal tumors is ongoing [94–97].

B.   Related Work

Contrast-enhanced computed tomography (CECT) [98, 99], contrast-enhanced magnetic resonance imaging (CEMRI) [100], and diffusion weighted MRI (DW-MRI) [101] are the most commonly used imaging modalities for the accurate diagnosis of renal tumors. Different contrast phases of CECTs or CEMRIs are: pre-contrast/unenhanced phase (Phase 1), corticomedullary/arterial phase (Phase 2), nephrographic/portal-venous phase (Phase 3), and excretory/delayed phase (Phase 4). CECT and CEMRI can specify the location, shape, and size of a given tumor and can distinguish malignant from benign lesions with high accuracy based on their different uptake of the contrast agent [96, 102, 103]. For DW-MRI, apparent diffusion coefficients (ADCs) are the most discriminating parameter that quantify the Brownian motion of water molecules inside the soft tissue and thus, reveals the status of that tissue if it is normal or diseased [37, 40, 55]

For this purpose, Radiomics are quantitative techniques that have been widely performed on CTs and MRIs to extract discriminatory markers/features for better interpretation [104, 105]. Texture, morphology, and functionality, are different aspects that could be captured by various types of Radiomic markers, which in turn improve both the diagnostic and prediction capabilities of RC [106] at an early stage. Different types of Radiomic markers that could be extracted from either CTs or MRIs are shown in Fig. 13. Meanwhile, recent advances in artificial intelligence (AI), machine learning (ML), and deep learning (DL) have accelerated the application of Radiomics in clinical practice. A typical example of AI-based computer-aided diagnostic (AI-based CAD) system to diagnose RC is shown in Fig. 14. It could be either hand-crafted-based pipeline or a deep learning-based one. In both pipelines, region of interest (ROI) containing renal tumors is defined from input CT or MR images. Then, different types of Radiomic markers are extracted, reduced, and selected to be further processed using ML classification model. After that, diagnosis of renal tumor is then obtained and assessed using different evaluation metrics (e.g., accuracy, sensitivity, specificity, and area under the curve (AUC)). The higher diagnostic capabilities will help physicians to early intervene with the optimal treatment plan.

In this chapter, we will review the studies that were performed in the last decade utilizing AI and Radiomic markers extracted from CECT, multi-parametric MRIs, CEMRI, or DW-MRI scans to develop an AI-based CAD systems for accurate diagnosis of RC at an early stage. In particular, identifying the malignancy status of a given renal tumor [92, 107–113], specifying the associated subtype [100, 113–116], grading and staging of malignant tumors (I-IV) [100, 117–121]. For example, Deng et al. [122] utilized texture analysis (TA) techniques along with CECT to discriminate malignant from benign renal tumors. Their study included 501 renal tumors of which 354 were RCCs and 147 were benign lesions. From the portal-venous phase, they manually placed a 2D ROI in the largest CECT cross-section of the tumor volume. Then, they extracted four textural
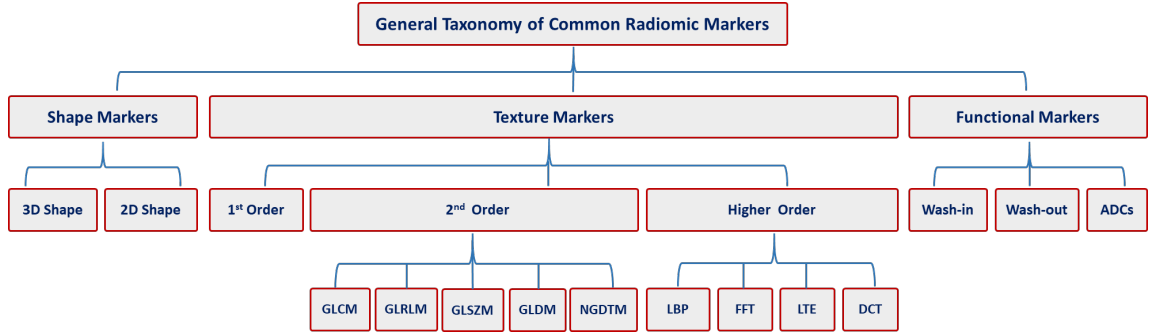
FIGURE 13: A typical taxonomy for the different types of Radiomics. Note that ADCs, GLCM, GLRLM, GLSZM, GLDM, NGDTM, LBP, FFT, LTE, and DCT denote apparent diffusion coefficients, grey-level co-occurrence matrix, grey-level run length matrix, grey-level size zone matrix, grey-level dependence matrix, neighboring gray tone difference matrix, local binary pattern, fast Fourier transform, Law's texture energy, and discrete Cosine transform, respectively.
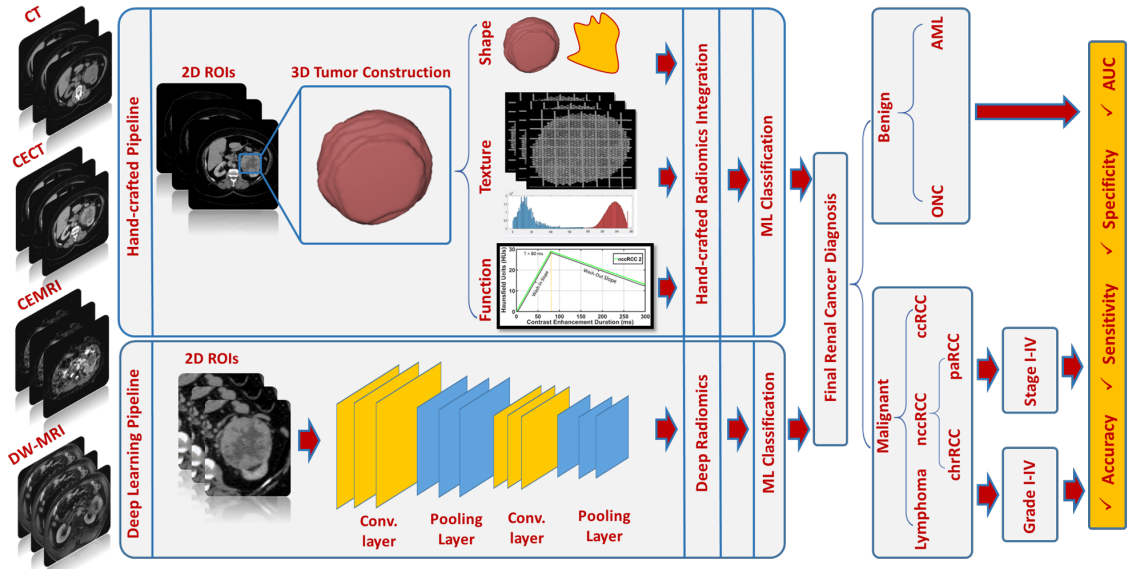
FIGURE 14: A typical pipeline for an AI-based CAD system for early diagnosis of renal tumors using CT or MR images.

features, namely entropy, kurtosis, mean positive pixel density, and skewness. Utilizing logistic regression, they found that higher values of entropy were significantly associated with a greater likelihood of malignancy ($p = 0.022$). As a diagnostic indicator of RCC, the entropy feature had high specificity (85.5%), but quite low sensitivity (31.3%) [122]. Kunapuli et al. [123] conducted a study to explore the potential of CECT along with TA to identify malignant renal tumors. Their dataset included images of 100 malignant (70 ccRCC, 20 paRCC, and 10 chrRCC) and 50 benign (20 AML and 30 ONC) tumors. After segmenting renal tumors manually using image-rendering software, 2D and 3D TAs were performed on tumor with the largest diameter and the entire tumor volume, respectively. They extracted 51 2D and 3D textural features from each of four different CT phases, yielding a total of two-hundred and four features per subject. These comprised 8 histogram features (i.e., first-order textural features), 40 second-order textural features (20 grey-level co-occurrence matrix (GLCM) and 20 grey-level difference matrix (GLDM)), and 3 spectral features derived from the 2D Fourier transform. Recursive feature elimination [124] was used to reduce the number of features to 10 per phase, or a total of 40. Their classification algorithm incorporating these features, using relational functional gradient boosting, had a reported 82% accuracy and an 0.83 area under the curve. The classifier was developed to discriminate between malignant and benign tumors only, and the authors did not investigate the subtype classification of malignant RCC [123].

Kocak et al. [125] conducted a study to classify ccRCC renal tumors from nccRCC ones using CECT along with TA. A total of 68 RCCs were included for internal validation (N = 48 ccRCC and N = 20 nccRCC). For external validation purposes, they included an additional 26 RCC from a public dataset (N = 13 and N = 13 nccRCC). Their study utilized MaZda image-rendering software [126] to manually segment renal tumors on the largest/middle cross-section. This was followed by an extraction of 275 textural-related features from each subject in both the enhanced CT phase and the unenhanced phase. In

49

addition, a wrapper-based nested cross-validation approach was employed to select the reproducible features in both phases and to optimize their classification model. Artificial neural networks (ANNs) were used, and a classification accuracy of 86.7%, a sensitivity of 80%, and a specificity of 89.6% on internal data and an accuracy of 84.6%, a sensitivity of 69.2%, and a specificity of 100% on external data were reported in differentiating ccRCC from nccRCC. Although their study reported a good overall classification performance between ccRCC and nccRCC, they were limited by their low sensitivity. In addition, they reported a very poor diagnostic performance to differentiate chrRCC from paRCC and from ccRCC. They suggested that CECT is more powerful at providing useful textural features than the unenhanced CT. Sun et al. [127] performed a study to compare between the diagnostic performance of machine learning approaches and four expert radiologists in differentiating malignant from benign renal tumors, as well as ccRCC from nccRCC malignant tumors using CECT. Their study included 254 malignant tumors (ccRCC = 190, nccRCC = 64 (chrRCC = 38, paRCC = 26)), 26 AML benign tumors, and 10 ONCs. After performing manual delineation of the tumor lesions, they used open-source software packages to extract and analyze textural features and used another open-source software to complete their analysis. Then, they utilized a support vector machine (SVM) classifier with a radial basis function along with a 10-fold cross-validation approach to obtain the final diagnosis. They reported sensitivities of 90%, 86.3%, and 73.4% using SVM compared to 73.7–96.8%, 73.7–96.8%, and 28.1–60.9% obtained by the four expert radiologists in differentiating ccRCC from nccRCC, ccRCC from AML and ONC, and nccRCC from AML and ONC, respectively. Hence, they concluded that ML approaches along with textural features have potential power, as well as low-variance performance in diagnosing renal tumors.

Lee et al. [128] used TA and CECT in their study to differentiate between ccRCC malignant and AML benign renal tumors. Their study included 80 renal tumors (ccRCC =

41 and AML = 39). They combined several hand-crafted textural features extracted from a 2D manually annotated central image of the entire mass with automated deep features extracted by different ImageNet pretrained convolutional neural network (CNN) classification models, namely AlexNet [129], VGGNet [130], GoogleNet [131], and ResNet [132]. Then, they used the combined features to train and test a random forest (RF) classifier. Using a leave-one-out cross-validation approach, their combined model achieved a diagnostic accuracy of 76.6% ± 1.4%, outperforming the individual diagnostic results using either the hand-crafted features alone or the deep features alone. The reported results were not accurate enough to consider the developed an independent diagnostic tool. Oberai et al. [133] investigated the potential power of CNN along with multi-phasic CECT images to differentiate benign from malignant renal masses. Their study included 143 patients (malignant = 97 and benign = 46). After performing manual segmentation of the whole tumor volume, they selected the largest axial segmented tumor image from each CECT phase to fed to the CNN for training and validation. Using an 8-fold cross-validation approach, they reported an accuracy of 78%, a sensitivity of 70%, and a specificity of 81%. However, their dataset had class imbalance, which might contribute to the reduced diagnostic performance. Although their study included different types of malignant tumors, they did not investigate the subtyping of malignant class. Zhou et al. [134] conducted a study to distinguish malignant from benign renal tumors using CECT along with an ImageNet-pretrained InceptionV3 model. This model was then cross-trained using transfer learning on their own dataset of 192 renal tumors (malignant: ccRCC = 117 and nccRCC = 17, benign: renal cyst = 50 and AML = 8). Several image-level models were considered, using whole CT slices, ROIs, and rectangular subregions of the CT-CT data. Then, during the transfer learning, different number of layers were frozen, resulting in two-patient level models based on the optimal image-level models. Using a five-fold cross-validation approach, they reported a 69% accuracy using the slice dataset, a 97% accuracy using the ROI dataset, and a 93% accuracy using the RBR dataset. In spite of achieving a high

51

accuracy in differentiating malignant from benign renal tumors, 50 out of 58 benign cases were renal cysts, which are much easier to distinguish from RCC compared to AML. In addition, they did not investigate discriminating ccRCC from nccRCC renal tumors.

In differentiating benign from malignant renal tumors, [92, 107] found that first- and second-order texture features extracted from unenhanced CT achieved an accuracy range of (82% - 91%) and an AUC range of (0.73 - 0.90) using SVM classifiers. While [108, 135–137] reported that first- and second-order texture features extracted from multi-phasic CECT achieved an accuracy range of (72% - 94%) and an AUC range of (0.75 - 0.97) using SVM classifiers. Yan et al. [138], Ma et al. [139], and Tang et al. [140] agreed with their findings regarding the texture features from multi-phasic CECT. However, Yan et al. [138] rather suggested ANNs and achieved an accuracy of 97% on a slightly small unbalanced dataset (N = 50), while Ma et al. [139] and Tang et al. [140] reported an AUC range of (0.67 - 0.93) on logistic regression (LR) classifiers instead. An extended study by Ma et al. [139] suggested the superiority of phase 3 of CECT by an AUC range of (0.74 - 0.89). In addition to first and second order texture features, Nassiri et al. [141] integrated higher order texture features and shape features extracted from phase 3 of CECT and achieved an accuracy range of (74% - 79%) and an AUC range of (0.77 - 0.84) using RF and Adaboost classifiers. While Yap et al. [142] integrated the same features but from multi-phasic CECT and achieved an AUC range of (0.65 - 0.75). Uhlig et al. [116] achieved an accuracy of 84% and AUC of 0.83 using a RF classifier without the need for higher-order features. Using DL on multi-phasic CECT, Coy et al. [143] achieved the best diagnostic performance (74% accuracy) on phase 4 of CECT. Kim et al. [144] found that entropy as a first order texture feature extracted from unenhanced CT is statistically significant and can differentiate RCC from benign cysts using LR with an AUC of 0.92. Tanaka et al. [145] used DL approach based on Inception-V3 CNN with data augmentation and achieved an accuracy range of (41% - 88%) and an AUC range of (0.49 - 0.85) and

promoted phase 2 of CECT than over other contrast phases. Li et al. [146] differentiated malignant chrRCC from benign ONC using first and second order features extracted from multi-phasic CECT and achieved an accuracy of 0.95 and AUC of 0.85 using an SVM classifier. They suggested that phases 2 and 3 are superior to other contrast phases for the specified task. Then, they extended their studies [147, 148] for the same differentiation problem on bigger datasets and suggested that integrating some clinical factors enhanced the final diagnostic performance. Zabihollahy et al. [149] utilized 2D and 3D CNNs on ROIs around the tumor and reported an accuracy range of (77% - 84%).

For the subtyping of RCC tumors, studies [114, 150] suggested that first-order texture features such as mean, standard deviation (STD), kurtosis, skewness, entropy, and median extracted from phase 3 of CECT are of high significance for RCC subtyping. Deng et al. [114] reported a very low accuracy of 47% and an AUC of (0.80 - 0.84) using LR and Yu et al. [150] reported an AUC of range (0.86 - 0.92) using SVM. Zhang et al. [115] agreed with them on the significant features, however they extracted them from phase 2 rather than phase 3 of CECT and achieved an accuracy range of (78%-0.87%) and an AUC range of (0.94 - 0.96) using an SVM classification model. Verghase et al. [151] suggested that many of the first-, second-, and higher-order texture features extracted from multi-phasic CECT are of high importance and achieved an AUC range of (0.80 - 0.98) using stepwise LR as a statistical analysis method. On two consequent studies by Uhlig et al. [116, 152], they promoted first- and second-order texture features as well as shape features extracted from phase 3 of CECT. They demonstrated an accuracy range of (54% - 92%) and an AUC range of (0.45 - 0.85) using RF and XGBoost classifiers. Chen et al. [153] suggested that second-order texture features extracted from phase 3 of CECT achieved an accuracy range of (82% - 88%) and an AUC range of (0.86 - 0.90) using LR.

For grading and staging of RCC tumors, Feng et al. [117] found that entropy, STD, and kurtosis extracted from multi-phasic CT are statistically significant first-order texture

features and reported an accuracy range of (70% - 79%) and an AUC range of (0.74 - 0.83). Shu et al. [118] suggested that first- and second- order texture features and shape features extracted from phases 2 and 3 of CECT are useful Radiomic markers and reported an accuracy range of (72% - 78%) and an AUC range of (0.77 - 0.82) using LR classifier. They extended their study on a slightly larger dataset and excluded the shape features. In addition, they used SVM and RF classifiers instead of LR and reported an improved accuracy range of (92% - 94%) and AUC range of (0.96 - 0.98). Two studies [154, 155] extracted second order texture features from phases 2 and 3 of CECT. Ding et al. [154] reported an AUC $\geq$ 0.67 using LR classifier, while Yin et al. [155] reported an AUC of 0.86 using a SVM classifier. Bektas et al. [156] suggested that second- and higher-order texture features extracted from phase 3 of CECT are very useful evidenced by an accuracy of 85% and an AUC of 0.86 using a SVM classifier. Lin et al. [157] found that first- and second-order texture features extracted from multi-phasic CECT can grade renal tumors with an accuracy of 74% and an AUC of 0.87 using gradient boosting decision tree classifier. Momenian et al. [158] suggested that first-order texture features extracted from phase 2 of CECT can potentially grade ccRCC tumors using a RF classifier with an accuracy of 97%. Lai et al. [159] found that first-order texture features and shape features extracted from unenhanced CT can grade ccRCC tumors using a Bagging classifier with an AUC of 0.75. Luo et al. [160] reported that first-order texture features and shape features extracted from phases 1 and 4 of CECT demonstrated an accuracy of 81% and an AUC of 87% using a RF classifier. Yi et al. [161] suggested that using first-, second-, and higher-order texture features extracted from unenhanced CT can grade ccRCC tumors using SVM (accuracy = 90% and AUC = 0.91). He et al. [162] agreed with Yi et al. [161] on the type of features but contradict with him on the CECT phases where they should be extracted. He rather suggested phases 2 and 3 of CECT and achieved an accuracy range of (91% - 94%) using ANNs. Xu et al. [163] used an ensemble of different types of DL networks on 2D ROIs at phase 2 of CECT. They reported an accuracy of 82% and and AUC of

0.88. Demirjian et al. [119] conducted a study for both grading and staging of ccRCC tumors. For the grading, they extracted multiple second-order texture features as well as the mean intensity as a first order texture feature from multi-phasic CECT. While for the staging, they depended only on the second-order texture features. Using RF classifiers, they achieved an AUC of 0.73 and 0.77 for grading and staging, respectively.

Table 7 provides summary of the aforementioned AI-based CAD systems that have been developed, in the last decade, by utilizing multi-phasic CECT images. The Table encompasses the following details: study, main goal, Radiomics, methods, results, and findings.

TABLE 7: Summary of studies utilized CT for renal cancer diagnosis in the last decade.

Study	Main Goal	Radiomics	Method	Results	Findings

Yang et al. [107]	Differentiation of small (≤ 4 cm) AMLwvf and RCC renal tumors (N = 163) using multiphasic CECT images	• Shape: 12
		
		• 1st Order Statistics: 17
		
		• 2nd Order Statistics: 74
		
		  – GLCM: 23
		  – GLRLM: 16
		  – GLSZM: 16
		  – NGTDM: 5
		  – GLDM: 14
			• 2D ROI
			
			• SVM
			
			• 5-fold CV
				• Acc: 0.82
				
				• Sen: 0.83
				
				• Spe: 0.78
				
				• AUC: 0.90
					Radiomics extracted from unenhanced CT phase are sufficient to accurately differentiate AMLwvf from RCC using SVM

You et al. [108]	Differentiation of small (≤ 4 cm) AMLwvf and RCC renal tumors (N = 67) using four phases of CECT images	• 1st Order Statistics: 3
		
		  – Phase 1: 2
		  – Phase 4: 1
		
		• 2nd Order Statistics: 2
		
		  – Phase 2: 1 (GLCM)
		  – Phase 3: 1 (GLRLM)
			• 2D ROI
			
			• SFS
			
			• SVM
			
			• k-fold CV
				• Acc: 0.85
				
				• Sen: 0.82
				
				• Spe: 0.76
				
				• AUC: 0.85
					Radiomics of small renal masses extracted from multiphasic CECT can accurately differentiate AMLwvf from ccRCC using SVM

Coy et al. [143]	Differentiation of ccRCC from ONC renal tumors (N = 179) using four phases of CECT images	• RGB encoding of the entire tumor volume in Phase 4	• 3D ROI • TL of GTf • k-fold CV	• Acc: 0.74 • Sen: 0.86 • Spe: 0.44 • AUC: —	Radiomics extracted from 3D VOI of the entire tumor demonstrated the best diagnostic performance in Phase 4 of CECT using TL of GTf

Continued on next page

56

TABLE 7 – *Continued from previous page*

Study	Main Goal	Radiomics	Method	Results	Findings

Deng et al. [114] (Study 1)	Subtyping of RCC renal tumors and correlation with its grade (N = 298) using Phase 3 of CECT images	• 1st Order Statistics: 4
		  – mean
		  – entropy
		  – kurtosis
		  – skewness
			• 2D ROI
			• Holm-P
			• LR (Statistical analysis only)
				• Acc: 0.47
				• Sen: 0.31
				• Spe: 0.86
				• AUC: range (0.80 - 0.84)
					Entropy had shown higher statistically significant values in ccRCC (p < 0.05). High entropy is correlated with high grade RCC.

Deng et al. [122] (Study 2)	Differentiation of RCC from benign renal tumors (N = 501) using Phase 3 of CECT images	• 1st Order Statistics: 5
		  – entropy
		  – kurtosis
		  – skewness
		  – mean
		  – max
			• 2D ROI
			• LSSF
			• Binary LR (Statistical analysis only)
				• Acc: 0.47
				• Sen: 0.31
				• Spe: 0.86
				• AUC: 0.62
					Entropy had shown higher statistically significant values in RCC than benign tumors (p < 0.05) and could potentially be used as a discriminatory Radiomic marker

Zhou et al. [134]	Differentiation between RCC and benign renal tumors (N = 192) using at least one phase of CECT images	• Axial Multi-channel (RGB) 2D ROI images	• 2D ROI • TL of ImageNet-pretrained InceptionV3 model • softmax • 5-fold CV	• Acc: 0.97 • Sen: 0.95 • Spe: 0.97 • AUC: —	Deep learning has the potential to distinguish malignant from benign renal tumors using deep transfer learning

Kim et al. [144]	Differentiation between RCC and benign renal cysts (N = 286) using unenhanced CT images	• 1st Order Statistics: 3
		  – entropy
		  – kurtosis
		  – MGLA
			• 2D ROI, Threshold
			• 2D ROI, LR
				• Acc: 0.84
				• Sen: 0.81
				• Spe: 0.89
				• AUC: range (0.89 - 0.92)
					Entropy ≥ 4 differentiated RCC from benign renal tumors (AUC = 0.89). The combined model using Radiomics provided AUC of 0.92

TABLE 7 – *Continued from previous page*

Study	Main Goal	Radiomics	Method	Results	Findings
Nie et al. [164]	Differentiation of AMLwvf from ccRCC renal tumors (N = 99) using multi-phasic CECT images	• Shape: 2 – Phase 2: 1 – Phase 3: 1 • 1st Order Statistics: 3 – Phase 2: 1 – Phase 3: 2 • 2nd Order Statistics: 9 – Phase 2: 3 (GLCM), 3 (GLDM), 1 (GLRLM) – Phase 3: 2 (GLRLM)	• 3D ROI • LASSO • Nomogram • Rad-score ≥ 0.017 • 20% validation	• Acc: 0.84 • Sen: 0.85 • Spe: 0.83 • AUC: 0.85	Radiomics extracted from multi-phasic CT can differentiate AMLwvf from ccRCC. By integrating some clinical factors, a Nomo-score ≥ 1.451 demonstrated better diagnosis (Acc = 0.89, AUC = 0.95)
Varghese et al. [151]	Differentiation of malignant from benign renal tumors (N = 174) and their subtypes using multi-phasic CECT images	• 1st Order Statistics: 8 • 2nd Order Statistics: 20 – GLCM: 13 – GLDM: 7 • Higher Order Statistics: 3 – FFT: 3	• 3D ROI • Stepwise LR (Statistical analysis only)	• Acc: — • Sen: — • Spe: — • AUC: range (0.80 - 0.98)	With a significance level ($p < 0.05$), different Radiomics are very useful in differentiating benign from malignant renal tumors and their subtypes

TABLE 7 – *Continued from previous page*

Study	Main Goal	Radiomics	Method	Results	Findings
Tang et al. [140]	Differentiation between RCC and AMLwvf renal tumors (N = 115) using multi-phasic CECT images	• 1st Order Statistics: 24 • 2nd Order Statistics: 52 – GLCM: 23 – GLRLM: 11 – GLSZM: 13 – NGDTM: 5 • Higher Order Statistics: 120 – LTE: 120	• 2D ROI • 100% Data Augmentation • LASSO, LR	• Acc: range (0.8 - 0.92) • Sen: — • Spe: — • AUC: range (0.67 - 0.92)	Integrating different combinations of Radiomic markers can potentially provide preoperative diagnosis of AMLwvf and RCC renal tumors
Cui et al. [135]	Differentiation of AMLwvf from RCC renal tumors with its different subtypes (N = 168) using multi-phasic CECT images	• AMLwvf vs RCC: 17 • AMLwvf vs ccRCC: 21 • AMLwvf vs nccRCC: 12 • 1st Order Statistics: — • 2nd Order Statistics: — – GLCM: — – GLRLM: — – GLSZM: — – NGDTM: — – GLDM: —	• 3D ROI • RFE • SVM • SMOTE • 5-fold CV	• Acc: range (0.84 - 0.93) • Sen: range (0.83 - 0.95) • Spe: range (0.85 - 0.96) • AUC: range (0.89 - 0.97)	Machine learning-based Radiomics techniques can precisely distinguish AMLwvf from RCC, ccRCC, and nccRCC when compared to radiological assessment
Lee et al. [136] (Study 1)	Differentiation of AMLwvf from ccRCC renal tumors (N = 50) using multi-phasic CECT images	• 1st Order Statistics: 3 • 2nd Order Statistics: 1 – GLCM: 1	• 2D ROI • ReliefF • kNN, SVM • 5-fold CV	• Acc: 0.72 • Sen: 0.72 • Spe: 0.73 • AUC: 0.75	Proper selection and integration of optimal Radiomics and machine learning classification methods could potentially help distinguishing AMLwvf from ccRCC

TABLE 7 – *Continued from previous page*

Study	Main Goal	Radiomics	Method	Results	Findings

Lee et al. [128] (Study 2)	Differentiation of AMLwvf from ccRCC renal tumors renal tumors (N = 80) using four phases of CECT images	• Shape: 7
		
		 • 1st Order Statistics: 18
		
		 • 2nd Order Statistics: 53
		
		   – GLCM: 14
		
		   – GLDM: 22
		
		   – LBP: 10
		
		 • 1000-4000 dimensional deep features extracted from ImageNet pre-trained models (AlexNet, VGGNet, GoogleNet, and ResNet) with small renal mass image patches.
			• 2D ROI
			
			 • RF
			
			 • k-fold CV
				• Acc: range (0.75 - 0.77)
				
				 • Sen: range (0.73 - 0.79)
				
				 • Spe: range (0.75 - 0.77)
				
				 • AUC: range (0.79 - 0.82)
					The combined model that integrates hand-crafted Radiomics with deep Radiomics provided an enhanced diagnostic performance than individual models and thus; has the potential to distinguish AMLwvf from ccRCC.

Feng et al. [137] (Study 1)	Differentiation of small (≤ 4 cm) AMLwvf from RCC renal tumors (N = 58) using multi-phasic CECT images	• 1st Order Statistics: 8 • 2nd Order Statistics: 3 – GLCM: 3	• 2D ROI • RFE • SVM • SMOTE • 5-fold CV	• Acc: 0.94 • Sen: 0.88 • Spe: 1.00 • AUC: 0.96	Combination of SVM, RFE, and SMOTE can help selecting optimal Radiomics that could accurately distinguish AMLwvf from RCC

Feng et al. [117] (Study 2)	Grading of ccRCC renal tumors (N = 131) using three-phases of CECT images	• 1st Order Statistics: 5
		
		   – mean
		
		   – entropy
		
		   – STD
		
		   – skewness
		
		   – kurtosis
			• 2D ROI
			
			 • *t*-test (Statistical analysis only)
				• Acc: range (0.70 - 0.79)
				
				 • Sen: range (0.76 - 0.95)
				
				 • Spe: range (0.54 - 0.77)
				
				 • AUC: range (0.74 - 0.83)
					Entropy, STD, and kurtosis were statistically significant ($p < 0.05$) and are useful Radiomic markers to grade ccRCC renal tumors.

TABLE 7 – *Continued from previous page*

Study	Main Goal	Radiomics	Method	Results	Findings
Yan et al. [138]	Differentiation of AMLwvf from ccRCC and paRCC renal tumors (N = 50) using multi-phasic CECT images	• 1st Order Statistics: 11 • 2nd Order Statistics: 220 – GLCM: 220	• 2D ROI • NDA • kNN, ANN • 5-fold CV	• Acc: range (0.97 - 1.00) • Sen: — • Spe: — • AUC: —	Optimal Radiomics extracted from multi-phasic CT images have the power to distinguish AMLwvf from ccRCC and paRCC
Hodgdon et al. [92]	Differentiation of AMLwvf from RCC renal tumors (N = 100) using unenhanced CT images	• 1st Order Statistics: 2 • 2nd Order Statistics: 7 – GLCM: 5 – GLRLM: 2	• 2D ROI • Holm-P • SVM • 10-fold CV	• Acc: range (0.83 - 0.91) • Sen: — • Spe: — • AUC: range (0.73 - 0.90)	Radiomics extracted from unenhanced CT images can distinguish AMLwvf from RCC
Tanaka et al. [145]	Differentiation of benign from malignant renal tumors (N = 168) using four phases of CECT images	• 2D ROI images around the lesion (299 × 299) • Data augmentation was performed using rotation (90°, 180°, and 270°), mirroring, and the addition of gaussian noise (0.05, 0.10, and 0.15)	• 2D ROI • Augmentation • Inception-V3 CNN • 20% testing	• Acc: range (0.41 - 0.88) • Sen: range (0.29 - 0.96) • Spe: range (0.33 - 1.00) • AUC: range (0.49 - 0.85)	Deep learning has the potential to distinguish malignant from benign renal tumors especially in Phase 2 of CECT (corti-comedullary/Arterial)
kunapuli et al. [123]	Differentiation of benign from malignant renal tumors (N = 150) using four phases of CECT images	• 1st Order Statistics: 2 • 2nd Order Statistics: 8 – GLCM: 7 – GLDM: 1	• 2D/3D ROI • RFE • RFGB • 10-fold CV	• Acc: 0.82 • Sen: — • Spe: — • AUC: 0.83	RFGB machine learning classifier and Radiomic markers can be potentially used to distinguish malignant from benign renal tumors

TABLE 7 – *Continued from previous page*

Study	Main Goal	Radiomics	Method	Results	Findings
Ma et al. [139] (Study 1)	Differentiation of AMLwvf from ccRCC renal tumors (N = 84) using multi-phasic CECT images	• Total: 6 • 1st Order Statistics: — • 2nd Order Statistics: — – GLCM: —	• 3D ROI • LASSO • LR • 30% testing	• Acc: — • Sen: — • Spe: — • AUC: range (0.83 - 0.93)	Combined model integrating radiomics from different phases of CECT enhanced the diagnostic performance between AMLwvf and ccRCC when compared to individual models as well as the conventional CT
Ma et al. [165] (Study 2)	Differentiation of AMLwvf from ccRCC renal tumors (N = 230) using four phases of CECT images	• Total: 396 • Shape: — • 1st Order Statistics: — • 2nd Order Statistics: — – GLCM: — – GLRLM: — – GLSZM: —	• 3D ROI • LASSO • 30% validation	• Acc: range (0.69 - 0.80) • Sen: range (0.66 - 0.79) • Spe: range (0.76 - 0.85) • AUC: range (0.74 - 0.89)	The perirenal model using Radiomics from Phase 3 of CECT has superiority than other phases to distinguish AMLwvf from ccRCC.
Li et al. [146] (Study 1)	Differentiation between chrRCC and ONC renal tumors (N = 61) using four phases of CECT images	• 1st Order Statistics: 3 – Phase 2 & 3: 2 – Phase 4: 1 • 2nd Order Statistics: 5 – Phase 2 & 3: 3 (GLCM) – Phase 2 & 3: 2 (wavelet)	• 3D ROI • LASSO • SVM • 5-fold CV	• Acc: 0.95 • Sen: 0.99 • Spe: 0.80 • AUC: 0.85	Radiomics extracted from multi-phasic CECT can accurately differentiate chrRCC from ONC using SVM

TABLE 7 – *Continued from previous page*

Study	Main Goal	Radiomics	Method	Results	Findings

Li et al. [147] (Study 2)	Differentiation of ONC from ccRCC renal tumors (N = 122) using multi-phasic CECT images	• 1st Order Statistics: 5
		  – Phase 2: 2
		  – Phase 3: 3
		• 2nd Order Statistics: 6
		  – Phase 2: 2 (GLCM), 1 (GLSZM)
		  – Phase 3: 1 (GLCM)
		  – Phase 4: 2 (GLCM)
			• 3D ROI
			• LR, LASSO
			• Nomogram
			• Rad-score
			• 30% validation
				• Acc: 0.81
				• Sen: 0.86
				• Spe: 0.83
				• AUC: 0.84
					Radiomics extracted from multi-phasic CT can differentiate ONC from ccRCC. By integrating clinical factors, enhanced diagnosis is obtained (Acc = 0.87, Sen = 0.86, Spe = 0.87, and AUC = 0.90)

Li et al. [148] (Study 3)	Differentiation of ONC from chrRCC renal tumors with present central scar (N = 141) using multi-phasic CECT images	• 1st Order Statistics: 5
		  – Phase 2: 1
		  – Phase 3: 2
		  – Phase 4: 2
		• 2nd Order Statistics: 7
		  – Phase 2: 2 (GLCM), 1 (GLSZM)
		  – Phase 3: 2 (GLCM)
		  – Phase 4: 2 (GLCM)
			• 3D ROI
			• LR, LASSO
			• Nomogram
			• Radscore ≥ -0.55
			• 40% validation
				• Acc: 0.91
				• Sen: 0.84
				• Spe: 0.95
				• AUC: 0.96
					Radiomics extracted from multi-phasic CT can differentiate ONC from chrRCC. By integrating clinical factors, a Nomo-score ≥ 0.19 provides better diagnosis (Acc = 0.95, Sen = 0.90, Spe = 0.97, and AUC = 0.99)

Continued on next page

TABLE 7 – *Continued from previous page*

Study	Main Goal	Radiomics	Method	Results	Findings
Nassiri et al. [141]	Differentiation of benign from malignant renal tumors (N = 684) using multi-phasic CECT images	• Shape: — • 1st Order Statistics: — • 2nd Order Statistics: — – GLCM: — – GLDM: — – GLRLM: — – NGDTM: — – GLSZM: — • Higher Order Stats: — – DCT: — – FFT: — – LTE: —	• 3D ROI • RF, Adaboost • 10-fold CV	• Acc: range (0.74 - 0.79) • Sen: range (0.73 - 0.80) • Spe: 0.75 • AUC: range (0.77 - 0.84)	Radiomics from Phase 3 of CECT can potentially distinguish benign from malignant renal tumors. Integrating some clinical factors enhanced the diagnostic performance.
Uhlig et al. [116] (Study 1)	Differentiation of benign from malignant renal tumors (N = 94) using Phase 3 of CECT images	• Total: 120 • Shape: — • 1st Order Statistics: — • 2nd Order Statistics: — – GLCM: — – GLDM: — – GLRLM: — – NGDTM: — – GLSZM: —	• 3D ROI • RFE • RF • 10-fold CV	• Acc: 0.84 • Sen: 0.88 • Spe: 0.67 • AUC: 0.83	Radiomic markers Phase 3 of CECT and machine learning can potentially distinguish benign from malignant renal tumors.

TABLE 7 – *Continued from previous page*

Study	Main Goal	Radiomics	Method	Results	Findings
Uhlig et al. [152] (Study 2)	Renal tumors subtyping (N = 201) using Phase 3 of CECT images	• Total: 127 • Shape: — • 1st Order Statistics: — • 2nd Order Statistics: — – GLCM: — – GLDM: — – GLRLM: — – NGDTM: — – GLSZM: —	• 3D ROI • SMOTE, RFE • XGBoost, RF • 10-fold CV	• Acc: range (0.54 - 0.92) • Sen: range (0.05 - 0.80) • Spe: range (0.41 - 0.97) • AUC: range (0.45 - 0.85)	Radiomic markers Phase 3 of CECT and machine learning can potentially help distinguishing renal tumors subtypes. Differentiation of ONCs is still a challenging task.
Uhm et al. [166]	Subtyping of renal tumors (N = 308) using multi-phasic CECT images	• 3D Channel image of size 224×224 cropped from 2D ROI image with the largest segmented tumor at Phases 2, 3, &4 • ResNet-101 was initialized with weights obtained from a pre-trained ImageNet.	• 2D ROI • 16% validation • (N = 184) external test	• Acc: 0.72 • Sen: range (0.60 - 0.89) • Spe: range (0.87 - 0.97) • AUC: 0.89	Deep learning outperformed radiological diagnosis of renal tumors using multi-phasic CECT.
Zabihollahy et al. [149]	Differentiation of RCC from benign renal tumors (N = 315) using CECT images	• 2D ROI images around the tumor (512×512)	• 2D ROI • MJV • 2D & 3D CNN • 50% testing	• Acc: range (0.77 - 0.84) • Sen: range (0.84 - 0.92) • Spe: range (0.26 - 0.52) • AUC: —	Semi-automated MJV 2D-CNN demonstrated the best diagnostic performance in differentiating RCC from benign renal tumors using CECT.

TABLE 7 – *Continued from previous page*

Study	Main Goal	Radiomics	Method	Results	Findings
Yap et al. [142]	Differentiation between malignant and benign renal tumors (N = 735) using multi-phasic CECT images	• Total: top 10% (79) • Shape: — • 1st Order Statistics: — • 2nd Order Statistics: — – GLCM: — – GLDM: — • Higher Order Stats: — – FFT: —	• 3D ROI • RF, AdaBoost • 10-fold CV	• Acc: — • Sen: — • Spe: — • AUC: range (0.65 - 0.75)	The combined model integrating shape and texture Radiomic markers extracted from all phases of CECT enhanced the final diagnostic performance.
Yu et al. [150]	Differentiating benign from malignant renal tumors as well as subtyping (N = 119) using Phase 3 of CECT images	• 1st Order Statistics: 14 • 2nd Order Statistics: 20 – GLCM: 5 – GLRLM: 11 – GLGM: 4 • Higher Order Stats: 9 – LTE: 9	• 2D ROI • SVM • 5-fold CV	• Acc: — • Sen: — • Spe: — • AUC: range (0.86 - 0.92)	Machine learning and 1st Order Radiomic markers such as kurtosis, skewness, and median provides high diagnostic performance of different renal tumors' types.

TABLE 7 – *Continued from previous page*

Study	Main Goal	Radiomics	Method	Results	Findings
Shu et al. [118]	Differentiating low grade from high grade ccRCC (N = 260) using Phase 2 &3 of CECT images	• Shape: 5 – Phase 2: 1 – Phase 3: 4 • 1st Order Statistics: 9 – Phase 2: 3 – Phase 3: 6 • 2nd Order Statistics: 21 – Phase 2: 2 (GLCM), 3 (GLSZM), 2 (GLRLM) – Phase 3: 3 (GLCM), 8 (GLSZM), 3 (GLRLM)	• 3D ROI • ICC, LASSO • LR • 5-fold CV	• Acc: range (0.72 - 0.78) • Sen: range (0.60 - 0.69) • Spe: range (0.83 - 0.84) • AUC: range (0.77 - 0.82)	Radiomic markers extracted from combined Phases 2 & 3 of CECT could be potentially used for grading of ccRCC
Shu et al. [167]	Differentiating low grade from high grade ccRCC (N = 271) using Phase 2 &3 of CECT images	• 1st Order Statistics: 4 – Phase 2: 1 – Phase 3: 3 • 2nd Order Statistics: 8 – Phase 2: 1 (GLCM), 3 (GLRLM) – Phase 3: 2 (GLCM), 1 (GLRLM), 1 (GLSZM)	• 3D ROI • ICC, LASSO • SVM, RF, MLP • 40% validation	• Acc: range (0.92 - 0.94) • Sen: range (0.92 - 0.97) • Spe: range (0.86 - 0.95) • AUC: range (0.96 - 0.98)	Radiomic markers extracted from combined Phases 2 & 3 of CECT could be sufficiently used for grading of ccRCC using machine learning.

67

TABLE 7 – *Continued from previous page*

Study	Main Goal	Radiomics	Method	Results	Findings
Ding et al. [154]	Differentiating low grade from high grade ccRCC (N = 114) using Phase 2 &3 of CECT images	• 2nd Order Statistics: 4 – Phase 2: 1 (GLRLM) – Phase 3: 3 (GLCM)	• 2D ROI • LASSO • LR • (N = 92) external test	• Acc: — • Sen: — • Spe: — • AUC: ≥ 0.67	Radiomic markers extracted from Phases 2 & 3 of CECT could be potentially used for grading of ccRCC
Bektas et al. [156]	Differentiating low grade from high grade ccRCC (N = 54) using Phase 3 of CECT images	• 2nd Order Statistics: 8 – Phase 3: 5 (GLCM), 3 (GLRLM) • Higher Order Stats: 5 – Phase 3: 4 (wavelet), 1 (gradient)	• 2D ROI • wrapper, Nested 10-fold CV • SVM	• Acc: 0.85 • Sen: 0.91 • Spe: 0.80 • AUC: 0.86	Machine learning (e.g., SVM), and Radiomics extracted from Phases 3 provide a promising diagnostic tool to grade ccRCC renal tumors
kocak et al. [125]	Subtyping of RCC (N = 68) using Phase 1 &2 of CECT images	• 1st Order Statistics: 9 – Phase 1: 5 – Phase 2: 4 • 2nd Order Statistics: 16 – Phase 1: 3 (GLCM) – Phase 2: 13 (GLCM) • Higher Order Stats: 5 – Phase 1: 4 (wavelet), 1 (autoagressive)	• 2D ROI • wrapper, Nested 10-fold CV • SMOTE • SVM, ANN • (N = 26) external test	• Acc: range (0.69 - 0.85) • Sen: range (0.69 - 0.71) • Spe: 1.00 • AUC: —	Radiomics extracted and combined from Phases 1 & 2 (Phase 2 is superior) can distinguish nccRCC from ccRCC using machine learning. Distinguishing ccRCC, paRCC, chrRCC is challenging

TABLE 7 – *Continued from previous page*

Study	Main Goal	Radiomics	Method	Results	Findings
Sun et al. [168]	Differentiating low grade from high grade ccRCC (N = 227) using three phases of CECT images	• 1st Order Statistics: 1 – Phase 2 & 3: RMS • 2nd Order Statistics: 6 – Phase 2 & 3: 1 (GLCM), 3 (GLSZM), 2 (GLRLM)	• 2D ROI • ICC, LASSO • SVM • 20% validation	• Acc: 0.87 • Sen: 0.83 • Spe: 0.89 • AUC: 0.91	Radiomics extracted and combined from Phases 2 & 3 of CECT can sufficiently grade ccRCC renal tumors on SVM
Lin et al. [157]	Differentiating low grade from high grade ccRCC (N = 232) using three phases of CECT images	• 1st Order Statistics: 6 • 2nd Order Statistics: 16 – GLCM: 4 – GLDM: 4 – GLRLM: 4 – NGDTM: 1 – GLSZM: 3	• 2D ROI • CatBoost • GBDT • 5-fold CV	• Acc: 0.74 • Sen: 0.14 • Spe: 0.88 • AUC: 0.87	Radiomics extracted and combined from Phases 1, 2 & 3 of CECT can potentially grade ccRCC renal tumors using machine learning
Zhang et al. [115]	Differentiating ccRCC from nccRCC and classify nccRCC subtypes (N = 127) using multi-phasic CECT images	• 1st Order Statistics: 4 – mean – STD – entropy – kurtosis	• 2D ROI • CatBoost • SVM • 10-fold CV	• Acc: range (0.78 - 0.87) • Sen: range (0.87 - 0.89) • Spe: 0.92 • AUC: range (0.94 - 0.96)	Radiomics extracted from Phase 2 of CECT are sufficient for subtyping of RCC renal tumors using SVM

Continued on next page

TABLE 7 – *Continued from previous page*

Study	Main Goal	Radiomics	Method	Results	Findings
He et al. [162]	Grading of ccRCC renal tumors (N = 227) using multiphasic CECT images	• 1st Order Statistics: 6 – Phase 2: 4 – Phase 3: 2 • 2nd Order Statistics: 14 – Phase 2: 7 (GLCM), 3 (GLRLM) – Phase 3: 3 (GLCM), 1 (GLRLM) • Higher Order Stats: 9 – Phase 2: 1 (gradient), 4 (wavelet) – Phase 3: 1 (gradient), 3 (wavelet)	• 2D ROI • LASSO • ANN • 15% validation • 15% testing • 10-fold CV	• Acc: range (0.91 - 0.94) • Sen: — • Spe: — • AUC: —	Radiomics extracted and combined from Phases 2 & 3 of CECT are sufficient for grading of RCC renal tumors using ANN

TABLE 7 – *Continued from previous page*

Study	Main Goal	Radiomics	Method	Results	Findings
Momenian et al. [158]	Grading of ccRCC renal tumors (N = 103) using three phases of CECT images	• 1st Order Statistics: 18 – Phase 1: 6 – Phase 2: 6 – Phase 3: 6 • 2nd Order Statistics: 93 – Phase 1: 20 (GLCM), 11 (GLRLM) – Phase 2: 20 (GLCM), 11 (GLRLM) – Phase 3: 20 (GLCM), 11 (GLRLM)	• 2D ROI • RF • 10-fold CV	• Acc: 0.97 • Sen: — • Spe: — • AUC: —	1st Order Radiomics extracted from Phase 2 of CECT had shown the best grading performance of ccRCC renal tumors using RF outperforming the 2nd Order Radiomics alone and combined Radiomics.
Yin et al. [155]	Grading of ccRCC renal tumors (N = 78) using Phase 2 of CECT images	• 2nd Order Statistics: 10 – Phase 2: 7 (GLCM), 3 (GLRLM)	• 2D ROI • ICC, SMOTE • SVM • 32% testing • 10-fold CV	• Acc: 0.88 • Sen: 0.80 • Spe: 0.90 • AUC: 0.86	2nd Order Radiomics extracted from Phase 2 of CECT provided the best grading accuracy of ccRCC renal tumors on SVM
Chen et al. [153]	Differentiating of ccRCC from nccRCC renal tumors (N = 197) using multi-phasic CECT images	• 2nd Order Statistics: 9 – Phase 1: 3 (GLCM), 1 (GLRLM) – Phase 2: 1 (GLCM) – Phase 3: 1 (GLCM), 1 (GLSZM) – Phase 4: 2 (GLCM)	• 3D ROI • LASSO • SMOTE • LR	• Acc: range (0.82 - 0.88) • Sen: range (0.81 - 0.89) • Spe: range (0.81 - 0.88) • AUC: range (0.86 - 0.90)	2nd Order Radiomics when combined with non-texture markers extracted from Phase 3 of CECT, the best differentiation of ccRCC from nccRCC renal tumors(AUC = 0.9) was obtained

TABLE 7 – *Continued from previous page*

Study	Main Goal	Radiomics	Method	Results	Findings
Lai et al. [159]	Grading of ccRCC renal tumors (N = 137) using multi-phasic CECT images	• Shape: 5 – Phase 1: 5 • 1st Order Statistics: 5 – Phase 1: 5 mean, median, RMS, 10th Pctl, 90th Pctl	• 2D ROI • CMIM • SMOTE • Bagging • 5-fold CV	• Acc: — • Sen: — • Spe: — • AUC: 0.75	Shape and 1st Order Radiomics extracted from Phase 1 of CECT demonstrated the best ccRCC grading performance (AUC = 0.75) using Bagging classifier
Yi et al. [161]	Grading of ccRCC renal tumors (N = 264) using Phases 1 & 3 of CECT images	• 1st Order Statistics: 6 Phase 1: 6 • 2nd Order Statistics: 9 Phase 1: 9 (GLRLM) • Higher Order Stats: 4 Phase 1: 4 (wavelet)	• 2D ROI • ICC, LASSO • SVM • 25% validation	• Acc: 0.90 • Sen: 0.94 • Spe: 0.89 • AUC: 0.91	Radiomic markers extracted from Phase 1 of CECT can successfully grade ccRCC renal tumors (AUC = 0.91) using SVM
Xu et al. [163]	Grading of ccRCC renal tumors (N = 706) using Phase 2 of CECT images	• 2D ROI images (224 × 224 × 3) as input to VGG-16 pre-trained on ImageNet for segmentation. • Self-supervised pre-training using RegNetY400MF, RegNetY800MF, SE-ResNet50, ResNet101, and Ensamble.	• 2D ROI • VGG-16 • Ensamble • 16% validation	• Acc: 0.82 • Sen: 0.86 • Spe: 0.75 • AUC: 0.88	Deep learning applied on Phase 2 of CECT images can potentially grade ccRCC renal tumors (AUC = 0.88) using Ensamble/combined model outperforming all individual models.

TABLE 7 – *Continued from previous page*

Study	Main Goal	Radiomics	Method	Results	Findings
Luo et al. [160]	Grading of ccRCC renal tumors (N = 177) using four phases of CECT images	• Shape: 7 – Phase 1 & 4: 7 • 1st Order Statistics: 4 – Phase 1 & 4: 4 median, RMS, 10th Pctl, 90th Pctl	• 3D ROI • SMOTE • CIFE • RF • 5-fold CV	• Acc: 0.81 • Sen: 0.67 • Spe: 0.87 • AUC: 0.87	Shape and 1st Order Radiomics extracted from Phase 1 & 4 of CECT provided the best ccRCC grading accuracy (AUC = 0.87) using RF
Demirjian et al. [119]	Grading and staging of ccRCC renal tumors (N = 587) using four phases of CECT images	• Grading: – 1st Order Statistics: intensity – 2nd Order Statistics: 2D GLCM, 3D GLCM, 3D GLRLM • Staging: – 2nd Order Statistics: 2D GLCM, 3D GLCM, 2D GLDM, 3D GLDM	• 3D ROI • ICC • Gini index • RF • 32% testing	• Acc: — • Sen: — • Spe: — • AUC: 0.73 & 0.77	Radiomics extracted from multi-phasic CECT could be sufficiently used to grade and stage ccRCC (AUC = 0.73 and 0.77) using RF

Notes AMLwvf, angiomyolipoma without visible fat; RCC; renal cell carcinoma; CT, computed tomography; GLCM, grey-level co-occurrence matrix; GLRLM, grey-level run length matrix; GLSZM; grey-level size zone matrix; NGTDM, neighboring gray tone difference matrix; GLDM, grey-level dependence matrix; ROI, region of interest; SVM, support vector machine; Acc, accuracy, Sen, sensitivity, Spe, specificity, AUC, area under the curve; CECT, contrast-enhanced CT; std, standard deviation; Phase 1, unenhanced phase; Phase 2, corticomedullary phase, Phase 3, nephrographic phase, Phase 4, excretory phase; CP, cluster prominence; LRHGE, long-run high grey-level emphasis; SFS, sequential feature selection; ccRCC, clear-cell RCC; ONC, oncocytoma; TL, transfer learning;

GTf, Google Tensorflow; chrRCC, chromophobe RCC; Pctl, percentile; RMAD, robust mean absolute difference; MGLA, mean gray-level attenuation; LR, logistic regression; LSSF; Laplacian spatial scaling factor; FFT, fast Fourier transform; paRCC, papillary RCC, RF; random forests; SMOTE, synthetic minority oversampling technique; RFE, recursive feature elimination; kNN, k-nearest neighbor; NDA, nonlinear discriminant analysis; Holm-P, Holm-Bonferroni; RFGB, relational functional gradient boosting; LBP, local binary pattern; DCT; discrete cosine transform; LTE, Law's texture energy; XGB, extreme gradient boosting; MJV, majority voting; CNN, convolutional neural network; GLGM, grey-level gradient matrix; ICC, interclass correlation coefficient; RMS, root mean squared; MLP, multi-layer perceptron; GBDT, gradient boosting decision tree; CMIM, conditional mutual information maximization; CIFE, supervised feature selection methods;

In summary, the AI-based CAD systems that used CECT images have shown promising results in early diagnosis of RC, including differentiating malignant from benign tumors with an accuracy range of (41% - 97%) and AUC range of (0.49 - 0.97), subtyping of RCC tumors with an accuracy range of (47% - 92%) and AUC range of (0.49 - 0.92), grading and staging of RCC tumors with an accuracy range of (70% - 97%) and AUC range of (0.67 - 0.98). Entropy, a first order texture feature, has been named several times as one of the most important Radiomic marker that could be extracted from multiphasic CECT. Phase 3, namely; portal-venous/nephrographic phase was the most used and suggested among all other phases. In addition, SVM, RF, and ANNs classifiers had shown the best classification results. Although CECT has been proven sufficient for diagnosing RC, they are not preferred when the radiation exposure is contraindicated (i.e. patient is pregnant or a child). This motivated researchers to investigate the abilities of other imaging modalities such as MRIs to avoid such radiation exposures, if possible. However, during our search in the last decade, only limited number of studies were found and thus, they are discussed in details below.

For differentiating malignant from benign renal tumors, Xu et al. [109] investigated the power of DL and ML on T2-weighted MRI and DW-MRI. A total of 217 patients with renal tumors were included (training = 173 and testing = 44). After manual

labeling of ROIs, they developed three different DL ResNet-18 models and three different handcrafted-based RF models on a total of 96 Radiomics markers. The first model was for T2-weighted alone, the second model was for DW-MRI alone, and the third model was for the combination between both. They reported an accuracy of 77%, 80%, and 81.3% using the ResNet-18 models. For the handcrafted-based RF models, they achieved an accuracy of 77%, 71%, and 82%. Oostenburgge et al. [110] investigated the ability of texture features extracted from the 3D ADC maps of DW-MR images to differentiate benign ONC from malignant RCC renal tumors. Their study included a total of 39 tumors (RCC = 32 and ONC = 7). They have reported that entropy, STD, tumor volume, and gender were statistically significant between the different groups. They combined these features to create a logistic regression classification model, which achieved an AUC of 0.91, sensitivity of 86% and specificity of 84%. In addition, they have found that the $25^t h$ percentile and entropy are statistically significant when comparing healthy parts from cortex with the tumor. Li et al. [111] utilized DW-MRI to differentiate between malignant and benign renal tumors. Their study included a total of 92 renal tumors, of which malignant encompasses (ccRCC = 38, paRCC = 16, chrRCC = 18) and benign encompasses (AML = 13 and ONC = 7). They generated 3D ADC maps and then extracted 10 different first-order texture features. After making a statistical analysis to find the significant features, they performed a ROC curve analysis to assess the diagnostic performance. They found that mean, median, $75^t h$ percentile, $90^t h$ percentile, STD, and entropy ADCs of malignant tumors were significantly higher than benign ones. They reported an AUC of 0.85, sensitivity of 80%, and specificity of 86.1%. Razik et al. [101] investigated the differentiation between malignant and benign renal tumors using multi-parametric MRIs. Their study included 54 renal masses (RCC = 34, AML = 14, and ONC = 6) obtained from 42 patients. After placing 2D ROIs on the maximum area of the tumor, they extracted a total of six first-order texture features. Using ROC analysis, they found that mean of positive pixels (MPP) had the highest diagnostic performance in differentiating RCC from AML with an AUC of 0.89

75

on DW-MRI at b-values of 500 s/mm^2. While the mean value was the best feature in differentiating RCC from ONC achieving an AUC of 0.94 on DW-MRI at b-values of 1000 s/mm^2. Nikpanah et al. [169] investigated the power of deep CNNs on T2-weighted MRI, and multi-phasic CEMRI to differentiate ccRCC from ONC tumors. Their study included 74 patients with 243 renal masses (ccRCC = 203 and ONC = 40). They placed bounding box (2D ROIs) on the tumors and then feed them to an AlexNet CNN model for diagnosis. Using a 5-fold cross-validation, they reported an overall accuracy of 91% with an AUC of 0.9. Arita et al. [170] investigated the power of texture analysis on ADC maps extracted from DW-MRIs to differentiate benign AML from malignant nccRCC renal tumors. Their study included two datasets. The fist set included 67 tumor (AML = 46 and nccRCC - 21) and was used for developing the diagnostic model. While the second one included 39 tumors (AML = 24 and nccRCC = 15) for the validation. They extracted a total of 45 texture features on 3D ADC maps and used a RF classifier to obtain the final results. Their study reported that long-zone high grey-level emphasis as a second-order texture feature was the most important and dominant feature to identify AML. The RF classifier achieved an AUC of 0.82 and was comparable to the radiological assessment. Gunduz et al. [171] explored the potential of texture analysis on ADC maps extracted from DW-MRIs to differentiate benign ONC from malignant chrRCC renal tumors. They included only 14 patients (ONC = 6 and chrRCC = 8) in their analysis. Their study revealed a total of six texture features of which five were second-order (short run emphasis, run percentage, normalized run length nonuniformity, run variance, long run emphasis) and one was first-order (squared root of mean ADC). Using ROC analysis, they have reported 87.5% sensitivity and 83% specificity. Matsumoto et al. [112] investigated the utility of texture analysis on DW-MRIs to differentiate benign AML from malignant ccRCC renal tumors. Their study included two datasets. The fist set included 83 tumor (AML = 18 and ccRCC = 65) and was used for developing the diagnostic model. While the second one included 39 tumors (AML = 13 and ccRCC = 17) for the external validation. They extracted 39

texture features from ADC maps and then used a RF model to identify the importance of the features. Their study revealed that the mean ADC value as a first-order texture feature, and long-run low grey-level enhancement and grey-level run emphasis as second-order texture features were of the most dominant features in the diagnostic procedure with an obtained AUC of 0.87.

For subtyping and grading of RCC tumors, Goyal et al. [100] investigated the role of texture features extracted from multi-parametric MRIs such as multi-phasic CEMRI, T1-weighted MRI, T2-weighted MRI, and DW-MRI. Their study included 34 renal masses (ccRCC = 29 (low-grade = 19 and high-grade = 10) and nccRCC = 5). The 2D ROIs were placed on the maximum viable tumor. First-order texture features; namely: mean, STD, MPP, entropy, skewness, and kurtosis, were extracted from each MRI sequence for further analysis. In subtyping of RCCs and using ROC analysis, entropy achieved an AUC of 0.81 on T2-weighted, STD achieved an AUC of 0.81 and 0.88 on DW-MRI at b-values of 500 and 1000 s/mm^2, respectively, mean achieved an AUC of 0.848 on ADC, skewness achieved an AUC of 0.85 on T1-weighted an AUC of 0.91 on phase 2 of CEMRI. In grading of ccRCC renal tumors, entropy achieved an AUC of 0.82 on DW-MRI at b-value 1000 s/mm^2, mean achieved an AUC of 0.89 on phase 2 of CEMRI and MPP achieved an AUC of 0.87 on phase 3 of CEMRI. They concluded that several first order textural features extracted from multi-parametric MRIs can be helpful diagnostic tool in both subtyping and grading of renal tumors. Sun et al. [120] investigated the possibility of grading ccRCC tumors using texture analysis of susceptibility-weighted MR imaging (SW-MRI). Their study included a total of 45 patients (low-grade = 29 and high-grade = 16). They reduced the total of extracted texture features from 396 to 10. Then, they build their diagnostic model using a multivariable logistic regression, which achieved an accuracy of 77.3%, sensitivity of 80.5%, and specificity of 71.4%. Chen et al. [121] performed a study to grade ccRCC tumors using phase 2 of CEMRI. A total of 99 tumors (low-grade = 61

and high-grade = 38) were included in their study. After placing 2D ROIs, several first-, second-, and higher-order texture features were extracted and analyzed. The features were then reduced and selected using RF importance analysis resulting in a total of six texture features; namely: kurtosis, entropy, sum of entropy, horizontal grey-level nonuniformity, runlength nonuniformity, and grey-level nonuniformity. Then, they build a MLP-ANN classification model to obtain the final diagnosis, which achieved 86.2% accuracy, sensitivity of 72.7%, specificity of 94.4%, and an AUC of 0.76 on the validation dataset (N = 29). Although their system was specific, it was not sensitive enough, which can justified by the class imbalance. Choi et al. [172] investigated the ability of different Radiomic features including shape features and first- and second-order texture features extracted from T2-weighted and multi-phasic CEMRI to grade ccRCC renal tumors. Their study included 364 renal tumors (low-grade = 272 and high-grade = 92). Their RF classification model achieved an AUC of 0.89, accuracy of 98%, sensitivity of 72%, and specificity of 95%. Although they have achieved an overall good diagnostic performance, the low sensitivity can be justified by the data imbalance. Uyen et al. [173] investigated the role of multi-phasic MRI in the differentiation of RCC. Their study included 212 renal lesions from 36 patients (normal = 96, ccRCC = 87, paRCC = 8, and ONC = 11) of which the divided into two equal groups, one each for training and validation. After manual placement of 2D ROIs, they extracted first-order texture features (mean, STD, skewness, and kurtosis). Using a RF classification model, Phase 1 of CEMRI had shown the highest diagnostic accuracy of 79.1% among all other phases. However, after integrating different phases an enhanced diagnostic accuracy of 83.7% was obtained. Another study by the same group [113], investigated the utility of mult-phasic CEMRI to differentiate benign from malignant renal tumors as well as differentiating common subtypes of RCCs. Their study include 140 renal lesions from 41 patients (RCC = 90, paRCC = 22, and ONC = 30). They have placed three consecutive 2D ROIs on the slices encompasses the largest cross-section from each phase of CEMRI. Then, they extracted multiple first- and second-

order texture features using histogram analysis, GLCM, GLRLM, GLSZM, and NGTDM. Then, LASSO regression was applied to select the optimal features for classification purposes. They found that first-order texture features were informative in identifying the malignancy status, while adding the second-order texture features was beneficial in the subtyping problem. Using RF classification models, they achieved an accuracy of 77.9% in differentiating paRCC from ccRCC, 79.3% in distinguishing ONC from ccRCC, and 77.9% in differentiating ONC from paRCC.

Table 8 provides summary of the aforementioned AI-based CAD systems that have been developed, in the last decade, by utilizing different MRI modalities. The Table encompasses the following details: study, main goal, Radiomics, methods, results, and findings.

TABLE 8: Summary of studies utilized MRIs for renal cancer diagnosis in the last decade.

Study	Main Goal	Radiomics	Method	Results	Findings

Xu et al. [109]	Differentiation of malignant from benign renal tumors (N = 217) using T2-weighted MRI and DW-MRI	• Shape: —
		• 1st Order Statistics: 1
		• 2nd Order Statistics: 7
		  – GLCM: 2
		  – GLRLM: 3
		  – GLSZM: 1
		  – GLDM: 1
			• 2D ROI
			• ResNet-18
			• LASSO
			• RF
			• 10-fold CV
				• Acc: range (0.70 - 0.82)
				• Sen: range (0.81 - 0.94)
				• Spe: range (0.33 - 0.92)
				• AUC: range (0.74 - 0.93)
					Combined Radiomics extracted from multi-modal MRIs have the potential to accurately differentiate benign from malignant renal tumors by using handcrafted-based RFs or DL-based classification models.

Oostenburgge et al. [110]	Differentiation of benign ONC from malignant RCC renal tumors (N = 39) using 3D ADCs of DW-MRIs	• 1st Order Statistics: 2
		  – entropy
		  – STD
		• Tumor volume
			• 2D ROI
			• LR
				• Acc: 0.87
				• Sen: 0.86
				• Spe: 0.84
				• AUC: 0.91
					Radiomics extracted from 3D ADCs such as standard deviation and entropy when integrated with tumor volume and gender can discriminate ONC from RCC.

Li et al. [111]	Differentiation of benign from malignant renal tumors (N = 92) using 3D ADCs of DW-MRIs	• 1st Order Statistics: 6
		  – mean
		  – median
		  – STD
		  – entropy
		  – $75^{t}h$ pctl
		  – $90^{t}h$ pctl
			• 2D ROI
			• ANOVA
			• ROC analysis
				• Acc: 0.82
				• Sen: 0.80
				• Spe: 0.86
				• AUC: 0.85
					Radiomics extracted from 3D ADCs of DW-MRIs had shown significantly higher values in malignant tumors than benign ones ($p < 0.05$).

TABLE 8 – *Continued from previous page*

Study	Main Goal	Radiomics	Method	Results	Findings
Razik et al. [101]	Differentiation of benign from malignant renal tumors (N = 54) using multi-parametric MRIs	• 1st Order Statistics: 2 – mean – MPP	• 2D ROI • U-test (Statistical analysis only)	• Acc: range (0.79 - 0.95) • Sen: range (0.71 - 0.97) • Spe: range (0.80 - 1.00) • AUC: range (0.89 - 0.94)	MPP and the mean value can differentiate RCC from AML and RCC from ONC with an AUC of 0.89 and 0.94 at b_{500} s/mm^2 and b_{1000} s/mm^2 of DW-MRI, respectively.
Nikpanah et al. [169]	Differentiation of ccRCC from benign ONC renal tumors (N = 243) using T2-weighted MRI and multi-phasic CEMRI	• local ROI patch was automatically extracted, size of 100×100 mm. • RGB image patches were resized to 224×224 to fit the pre-trained AlexNet configuration.	• 2D ROI • AlexNet CNN • 5-fold CV	• Acc: 0.81 • Sen: 0.88 • Spe: 0.75 • AUC: 0.90	The DL-based system can potentially differentiate ccRCC from ONC renal tumors with high diagnostic performance on multi-phasic MRIs.
Arita et al. [170]	Differentiation of benign AML from malignant nccRCC renal tumors (N = 106) using 3D ADCs of DW-MRIs	• 1st Order Statistics: 7 • 2nd Order Statistics: 13 – GLCM: 4 – GLRLM: 4 – GLSZM: 4 – GLDM: 1	• 3D ROI • RFs • 37% validation	• Acc: 0.77 • Sen: 0.87 • Spe: 0.69 • AUC: 0.82	The long-zone high grey-level emphasis was the most important Radiomic marker to differentiate AML from nc-cRCC on a RF classifier with an AUC of 0.82

TABLE 8 – *Continued from previous page*

Study	Main Goal	Radiomics	Method	Results	Findings
Gunduz et al. [171]	Differentiation between malignant chrRCC and benign ONC (N = 14) using 3D ADCs of DW-MRIs	• 1st Order Statistics: 1 – squared root of mean ADC • 2nd Order Statistics: 5 – GLRLM: 5	• 3D ROI • ROC analysis	• Acc: 0.86 • Sen: 0.88 • Spe: 0.83 • AUC: 0.94	Squared root of mean ADC and GLRLM Radiomic markers of ADC maps can potentially differentiate ONC from chrRCC renal tumors.
Matsumoto et al. [112]	Differentiation between malignant ccRCC and benign AML (N = 122) using 3D ADCs of DW-MRIs	• 1st Order Statistics: 3 – mean ADC – skewness – entropy • 2nd Order Statistics: 9 – GLCM: 3 – GLRLM: 4 – GLZLM: 1 – GLDM: 1	• 3D ROI • RF • 32% validation	• Acc: — • Sen: — • Spe: — • AUC: 0.87	Mean ADC, long-run low grey-level, and grey-level run emphasis were the most dominant and important Radiomic markers in differentiating AML from ccRCC with an AUC of 0.87.
Goyal et al. [100]	Subtyping and grading of malignant renal tumors (N = 34) using Radiomic markers extracted from multi-parametric MRIs	• 1st Order Statistics: 6 – mean – STD – MPP – entropy – skewness – kutrosis	• 2D ROI • ROC analysis	• Subtyping: AUC range (0.81 - 0.91) • Grading: AUC range (0.82 - 0.89)	Several first order Radiomic markers extracted from multi-parametric MRIs can be helpful diagnostic tool in both subtyping and grading of renal tumors

TABLE 8 – *Continued from previous page*

Study	Main Goal	Radiomics	Method	Results	Findings

Sun et al. [120]	Grading of ccRCC renal tumors (N = 45) using susceptibility-weighted MR imaging (SW-MRI)	• Shape: 2
		• 2nd Order Statistics: 8
		  – GLCM: 2
		  – GLRLM: 1
		  – GLSZM: 2
		  – GLDM: 3
			• 2D ROI
			• U-test (Statistical analysis)
			• ROC analysis
			• LR
			• 30% validation
				• Acc: 0.77
				• Sen: 0.81
				• Spe: 0.71
				• AUC: 0.81
					Radiomic markers extracted from SW-MRI can provide a reliable differentiation between low and high grades of ccRCC

Chen et al. [121]	Grading of ccRCC renal tumors (N = 99) using Phase 2 of CEMRI	• 1st Order Statistics: 2
		  – entropy
		  – kurtosis
		• 2nd Order Statistics: 4
		  – GLCM: 1
		  – GLRLM: 3
			• 2D ROI
			• RF
			• MLP-ANN
			• 30% validation
				• Acc: 0.86
				• Sen: 0.73
				• Spe: 0.94
				• AUC: 0.76
					First- and second-order Radiomic markers extracted from phase 2 of CEMRI can potentially grade ccRCC renal tumors using MLP-ANN classification model

Choi et al. [172]	Grading of ccRCC renal tumors (N = 364) using T2-weighted MRI and multi-phasic CEMRI	• Shape: 5 • 2nd Order Statistics: 15 – GLDZM: 15	• 3D ROI • ANOVA • RF • 30% validation	• Acc: 0.98 • Sen: 0.72 • Spe: 0.95 • AUC: 0.89	Proper selection and integration of optimal Radiomic markers extracted from MRIs can potentially help in grading ccRCC renal tumors

Uyen et al. [173] (Study 1)	Differentiation of RCC renal tumors renal tumors (N = 212) using multi-phasic CEMRI images	• 1st Order Statistics: 4
		  – mean
		  – STD
		  – skewness
		  – kurtosis
			• 2D ROI
			• RF
			• 50% validation
				• Acc: 0.84
				• Sen: —
				• Spe: —
				• AUC: —
					Using a RF classification model, first-order Radiomic markers extracted from multi-phasic CEMRI could potentially identify RCC renal tumors.

TABLE 8 – *Continued from previous page*

Study	Main Goal	Radiomics	Method	Results	Findings

Uyen et al. [173] (Study 2)	Differentiation of benign from malignant renal tumors as well as subtyping of RCC (N = 140)	• 1st Order Statistics: 5
		
		• 2nd Order Statistics: 40
		
		  – GLCM: 9
		
		  – GLRLM: 13
		
		  – GLSZM: 13
		
		  – NGDTM: 5
			• 2D ROI
			
			• LASSO
			
			• RF
			
			• 5-fold CV
				• Acc: range (0.78 - 0.79)
				
				• Sen: range (0.67 - 0.70)
				
				• Spe: range (0.86 - 0.89)
				
				• AUC: —
					First-order Radiomic markers were informative in identifying the malignancy status, while adding second-order markers was beneficial in RCC subtyping

Notes ADCs, apparent diffusion coefficients; DW-MRIs, diffusion-weighted magnetic resonance images; MPP, mean positive pixels; GLZLM, grey-level zone length matrix; GLDM, grey-level dependence matrix; GLDZM, grey-level distance zone matrix;

In summary, these AI-based CAD systems that used different types of MRIs have shown promising results in early diagnosis of RC, including differentiating malignant from benign tumors with an accuracy range of (77% - 91%) and AUC range of (0.82 - 0.91) and subtyping and/or grading of RCC tumors with an accuracy range of (77% - 98%) and AUC range of (0.76 - 0.89). Entropy, mean, MPP, skewness, and kurtosis as first-order texture features, have been named several times as the most important Radiomic markers extracted from multi-parametric MRIs that could be beneficial to differentiate benign from malignant renal tumors. Additionally, second-order texture features extracted from GLRLM are important when added to the aforementioned first-order texture features. In particular, texture analysis of ADCs on DW-MRI was the most used technique among these MRI studies. In addition the RF classifiers had been nominated by most of these studies and shown the best classification results. Although MRIs has been proven sufficient for identifying the malignancy status, subtyping RCCs, grading RCCs, there were almost no studies investigated the staging of RCCs, which is very important for specifying the spread of the tumor, size, and location.

C.   Discussion and Conclusions

Comparing the number of studies performed on CTs to those performed on MRIs, one can easily justify that by the reduced cost of CTs when compared with MRIs ($\approx$ half the price of the scan). In both cases, they have been shown sufficient for accurate and early identification of renal tumors, including: malignancy status, subtyping, grading, and staging. Especially, when using the enhanced phase 3 (portal-venous/nephrographic phase). In addition, ADC maps of DW-MRIs have been widely used by researchers who studied texture differences instead of the functionality for RC diagnosis and have been showing promising results. Radiomics techniques have been proved successful to extract the most discriminating features that could help in the intended diagnostic problem. AI, ML, and DL have proved their diagnostic abilities when paired with good discriminatory features. Entropy, mean, skewness, kurtosis, STD, and median have been proven to be sufficient for differentiating benign from malignant renal tumors. However, it will not be the case if these benign tumors are fatpoor AML. Thus, the second-order texture features extracted from different constructed matrices (e.g., GLCM, GLRLM, GLSZM, GLDM, and NGDTM) have played an important role here to capture the spatial relationship between neighboring voxels, which might overcome the problem of noisy histogram/first-order texture features, and thus; might improve the low diagnostic sensitivity that most of the studies suffer from. Not many studies depended on neither morphological nor functional features, which if integrated will definitely enhance the diagnostic performance. Several hand-crafted AI-based CAD systems have been presented and a few depended on DL approaches. The hand-crafted ones have been proven efficient evidenced by high accuracy, sensitivity, and specificity are well-understood (i.e. explainable AI), and therefore are desirable and dependable. In particular, RFs, SVMs, and MLP-ANNs have provided impressive diagnostic results and had been accepted by many researchers in the field due to their ability to handle nonlinear and multi-class classification problems.

The success of early and accurate diagnosis of the malignancy status of renal tumors, the specific subtype, and the associated grade (I-IV) and stage (I-IV) is of immense clinical importance as it affects the decision of optimal treatment/management plan. According to the American Cancer Society [15], treatment plans could be one or more of the following options: Surgery (e.g., radical or partial nephroctomy), Active Surveillance, Ablation Therapy, Radiation Therapy, Adjuvant Therapy, Targeted Drug Therapy, Immunotherapy, Chemotherapy Therapy, etc. For a given renal tumour with high suspicious to be malignant, surgical intervention is considered the optimal management plan. Biopsy is essential to confirm the existence of RCC in the case of: patient is at high risk for surgery, tumor is locally advanced or became metastatic, before applying ablative therapy, the patient has a single kidney (original or allograft), or when other malignancy diagnoses present such as lymphoma or metastasis. In addition, treatment follow-up procedure is crucial to evaluate the clinical outcome/response, the recurrence rate, and the post-operative progression free-survival (PoPFs) rate as well.

To sum up, more investigative studies are still ongoing for both CTs and MRIs. Improvement in early diagnosis of renal tumors depend mainly on finding the optimal discriminating features for the intended diagnostic problem as well as finding the robust AI-based classification model that could be reproducible and generalizable. Hence, future research directions focus on building more comprehensive AI-based CAD systems that can integrate multiple types of features including morphological features to capture the complexity of the tumor surface and functional features that can describe the functionality through the wash-in/wash-out slopes quantified by the amount of enhancement in the case of using contrast-based imaging modalities such as CECT and CEMRI. In addition, functionality can be measured using ADC values in the case of using DW-MRIs. If not succeeded, multimodal imaging and even histopathology images and genomic markers might be other possible solutions to be integrated.

CHAPTER V

RENAL CANCER COMPUTER-AIDED DIAGNOSIS

A. Materials

Patients who had undergone renal biopsy for suspected cancer ($N = 140$) ranged from 15 to 87 years of age (mean = 50.5 years and standard deviation = 13.4 years). There were 72 patients who were males, while the remaining 68 were female. Informed consent was obtained from the patients themselves or their parents/legal guardians (age < 18 years) to participate in this study. Biopsy reports confirmed that 70 patients were malignant with renal cell carcinoma (RCC) (clear cell RCC (ccRCC) = 40 and non-ccRCC (nccRCC) = 30, of which 17 were papillary RCC and 13 were chromophobe RCC), while the other 70 had benign angiomyolipoma (AML) tumors. Study participants had undergone a multi-phase computed tomography (CT) examination prior to biopsy. Imaging was performed with a Brilliance CT 64 multislice scanner (Philips Medical Systems, Best, The Netherlands). A mechanical injector was used to administer contrast agent into an antecubital vein with a dose of 120 mL at a rate of 4.0 mL/s. The abdomen scanning included three main phases: a precontrast phase, a portal-venous phase, and a delayed-contrast phase acquired at $t = 0$, $t = 80$, and $t = 300$ s, respectively. All images were acquired using the following parameters: slice thickness = 2.5 mm; pitch = 0.984; rotation time = 0.75 s.

B.   Methods
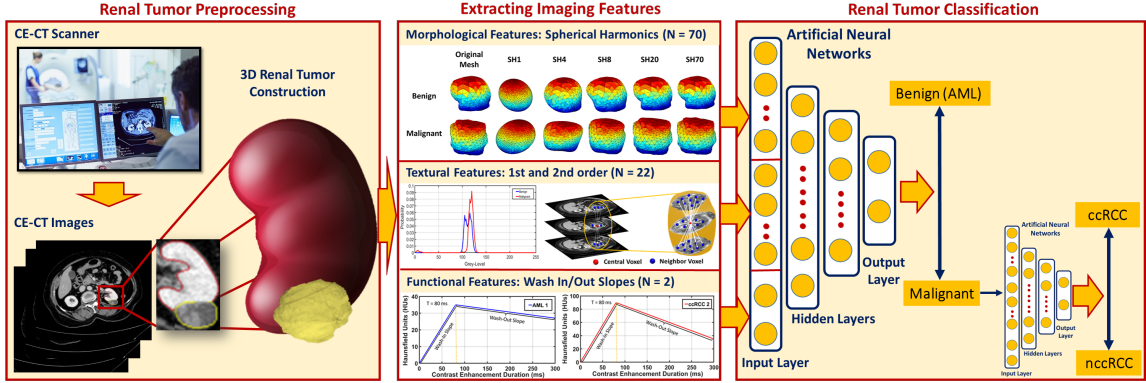
FIGURE 15: The proposed renal cancer computer-assisted diagnosis (RC-CAD) system.

The proposed RC-CAD system pipeline (see Figure 15) performs the following steps to obtain the final diagnosis: (1) constructs 3D models of renal tumors from manually segmented 2D ROIs, (2) applies applying a new parametric spherical harmonic technique to estimate the morphological features from the segmented renal tumors to capture the surface complexity/irregularity between different types of renal tumors, (3) constructs a rotation-invariant gray-level co-occurrence matrix (GLCM) to extract the textural features of the tumor volume, (4) estimates the wash-in/wash-out slopes inside the 3D region, and (5) integrates the estimated morphological features with the first- and second-order textural features and functional features and performs a two-stage classification using MLP-ANNs whose inputs comprise all aforementioned discriminant features. The first stage decides if the renal tumor is malignant (RCC) or benign (AML). In the former case, the second stage identifies the malignancy subtype as ccRCC or nccRCC. These steps are detailed below.

1.   Renal Tumor Preprocessing

To provide a more accurate extraction of morphological, textural, and functional discriminating imaging features, for each subject, each CT slice intersecting the renal tumor was accurately and manually segmented by expert radiologists to define the 2D ROI. Then, all 2D ROIs were stacked together to construct the 3D renal tumor object (3D ROI), as shown in Figure 16.
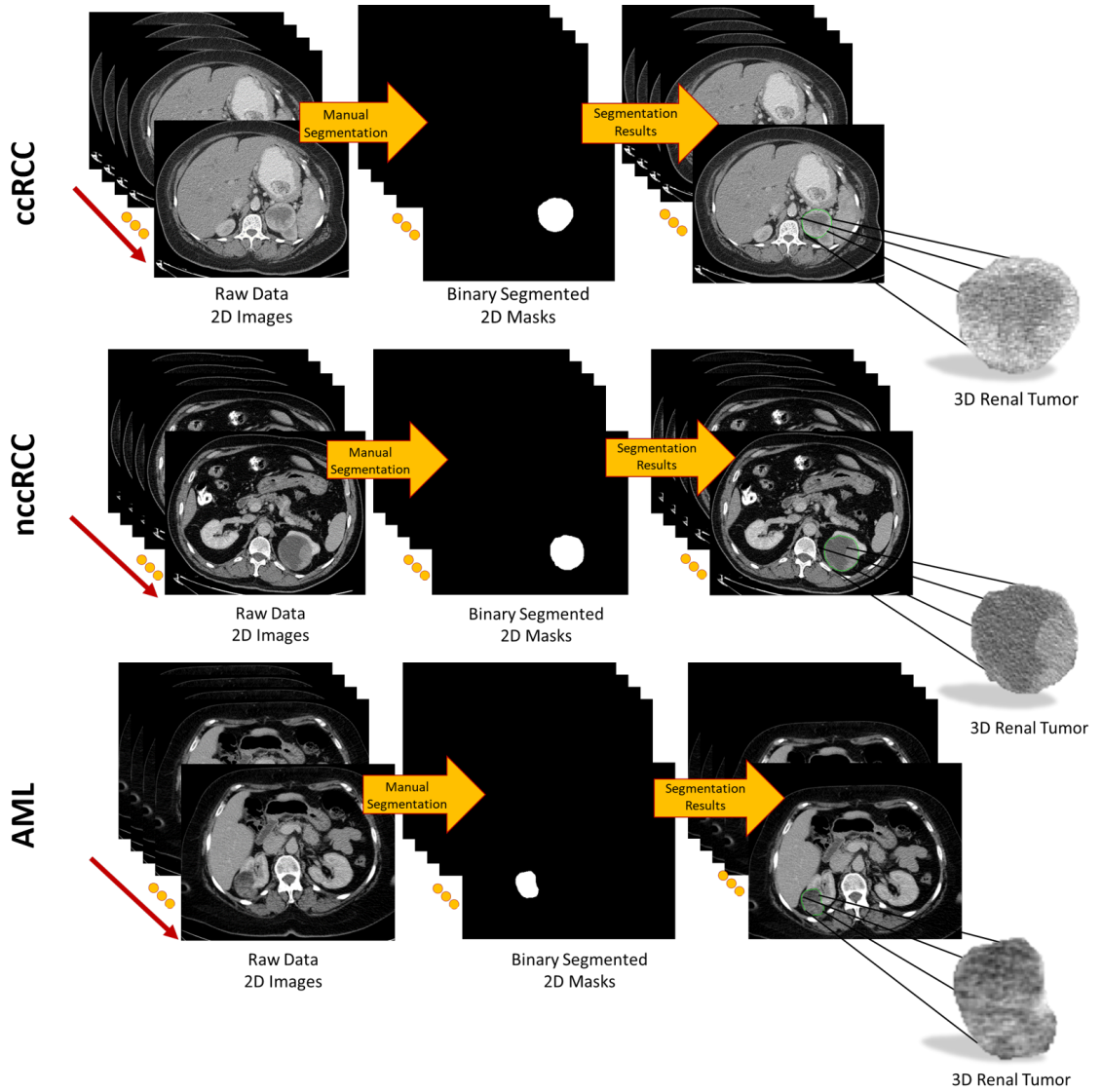
FIGURE 16: Visualization of the segmentation process to obtain 3D renal tumors.

89

2.   Extracting Imaging Features

For accurate identification of malignant renal tumors and the associated subtype, all 3D segmented volumes were characterized by their morphological, textural, and functional features, as described below.

Morphological features: To enhance both the sensitivity and specificity of early renal cancer diagnosis, morphological features of the tumor are incorporated into the algorithm. These features were designed to quantify the complex shape of the tumor boundary. This was motivated by the hypothesis that rapidly growing, malignant tumors develop more irregular/complex shapes relative to more slowly growing, benign tumors. Therefore, the utilization of such shape descriptors would enhance the performance of the automatic diagnosis. Examples of this phenomenon are illustrated in Figure 17.

Naturally, in order to measure the irregularity of the boundary, an accurate shape model of the tumor must be constructed. In this chapter, a state-of-the-art spectral decomposition was incorporated in terms of spherical harmonics (SHs) [174] to construct this shape model. An arbitrary point in the interior of the tumor, or more specifically, the interior of its convex kernel, was selected as the origin $(0, 0, 0)$. In this coordinate system, the tumor's surface may be considered a function of the polar and azimuthal angle, $f(\theta, \varphi)$, which can be expressed as a linear combination of basis functions $Y_{\tau\beta}$ defined on the unit sphere. Starting with a discrete approximation of the surface, i.e., a triangular mesh, the proposed algorithm uses an attraction–repulsion technique [175] to map this mesh to the unit sphere. The mapping fixes the image of each mesh vertex at the unit distance from the origin, while preserving the mesh topology and maintaining the distance between adjacent vertices as much as possible.
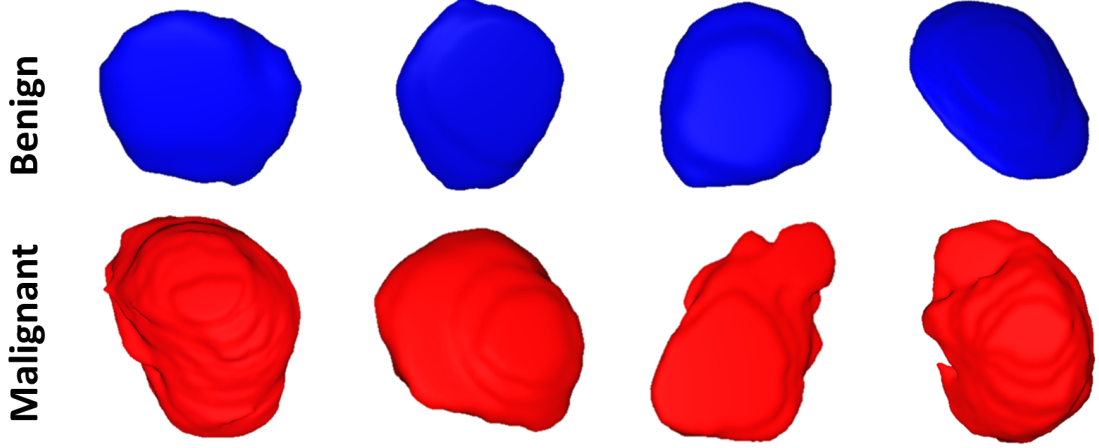
FIGURE 17: Visualizing 3D surface complexity differences between different renal tumors (benign are shown in blue, while malignant are shown in red).

Each iteration α of the attraction-repulsion works as follows. Let $\mathbf{C}_{\alpha,i}$ be the coordinates of the node on the unit sphere corresponding to mesh vertex i at the beginning of iteration α. Denote the vector from node i to node j by $\mathbf{d}_{\alpha,ji} = \mathbf{C}_{\alpha,j} - \mathbf{C}_{\alpha,i}$; then, the Euclidean distance between nodes i and j is $d_{\alpha,ji} = \left\| \mathbf{d}_{\alpha,ji} \right\|$. Finally, let J_i denote the index set of neighbors of vertex i in the triangulated mesh. Then, the attraction step updates the position of each node to keep it centered with respect to its neighbors:

$$\mathbf{C}'_{\alpha+1,i} = \mathbf{C}_{\alpha,i} + C_{A,1} \sum_{j \in J_i} \left(\mathbf{d}_{\alpha,ji} d^2_{\alpha,ji} + C_{A,2} \frac{\mathbf{d}_{\alpha,ji}}{d_{\alpha,ji}} \right), \tag{7}$$

The quantities $C_{A,1}$ and $C_{A,2}$ are implementation-defined parameters that determine the strength of the attractive force. The next step, repulsion, inflates the spherical mesh to prevent it from degenerating (the attraction step by itself would allow nodes to become arbitrarily close to one another).

$$\mathbf{C}''_{\alpha+1,i} = \mathbf{C}'_{\alpha+1,i} + \frac{C_R}{2I} \sum_{j=1; j \neq i}^{I} \frac{\mathbf{d}_{\alpha,ji}}{\mathbf{d}^2_{\alpha,ji}}, \tag{8}$$

Just as the attraction step, the repulsion step uses an implementation-defined parameter C_R

to set the strength of the repulsive force. Subsequently, the nodes are projected back onto the sphere by giving them the unit norm, and these are their coordinates at the beginning of the next iteration, $\mathbf{C}_{\alpha+1,i} = \mathbf{C}''_{\alpha+1,i}/\|\mathbf{C}''_{\alpha+1,i}\|$. At the terminal iteration α_f of the attraction–repulsion algorithm, the surface of the renal tumor is in a one-to-one correspondence with the unit sphere.

Each node $\mathbf{C}_i = (x_i, y_i, z_i)$ of the original mesh is mapped to a corresponding point $\mathbf{C}_{\alpha_f,i} = (\sin\theta_i \cos\phi_i, \sin\theta_i \sin\phi_i, \cos\theta_i)$ with polar angle $\theta_i \in [0, \pi]$ and azimuthal angle $\phi_i \in [0, 2\pi)$. Considering these points as samples of a continuous function $f(\theta, \varphi)$ defining the boundary, the tumor shape may be estimated by fitting an SH series to the sample nodes, since the SHs form an orthogonal basis for functions on a sphere. The SH $Y_{\tau\beta}$ of degree τ and order β is defined as:

$$
Y_{\tau\beta} = \begin{cases}
c_{\tau\beta} G_\tau^{|\beta|} \cos\theta \sin(|\beta|\,\varphi) & -\tau \leq \beta \leq -1 \\[2mm]
\frac{c_{\tau\beta}}{\sqrt{2}} G_\tau^{|\beta|} \cos\theta & \beta = 0 \\[2mm]
c_{\tau\beta} G_\tau^{|\beta|} \cos\theta \cos(|\beta|\,\varphi) & 1 \leq \beta \leq \tau
\end{cases}
\tag{9}
$$

where $c_{\tau\beta}$ is the SH factor and $G_\tau^{|\beta|}$ is the associated Legendre polynomial of degree τ and order β.

In practice, of course, the SH series is truncated by discarding harmonics above degree N, yielding an Nth order approximation. $N = 70$ suffices to accurately model the surface of renal tumors. Finally, the renal tumor object is reconstructed from the SHs of Equation (9). The first few harmonics describe the rough extent of the tumor, while higher degree harmonics provide the finer details of its surface. Therefore, benign tumors are accurately represented by a lower-order SH model, while malignant tumors, with their more complex morphology, require higher-order SH model to describe their shape.

Figure 18 shows the morphology approximation for three different renal tumors: malignant ccRCC, malignant nccRCC, and benign AML tumors. A summary of the attraction–repulsion algorithm is provided below.

	Original Mesh	SH1	SH4	SH8	SH20	SH70
Benign (AML)						
Malignant (ccRCC)						
Malignant (nccRCC)						
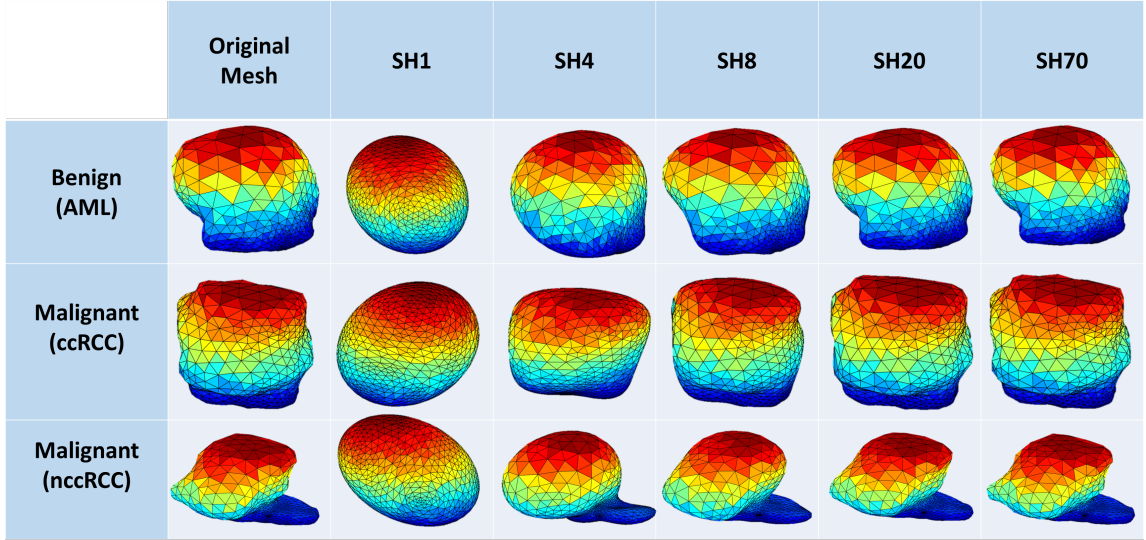
FIGURE 18: Renal tumors' reconstruction meshes showing the morphological differences among malignant ccRCC, malignant nccRCC, and benign AML tumors.

Initialization:

- Triangulate the surface of the tumor.

- Smooth the triangulated mesh with Laplacian filtering.

- Initialize the spherical parameterization with an arbitrary, topology-preserving map onto the unit sphere.

- Fix values of $C_{A,1}$, $C_{A,2}$, C_R, and threshold T.

Attraction–repulsion:

- **For** $\alpha = 0, 1, \ldots$

    - **For** $i = 1, \ldots, I$

- ∗ Calculate $\mathbf{C}'_{\alpha+1,i}$ using Equation (7)

- **For** $i = 1, \ldots, I$

    - ∗ Calculate $\mathbf{C}''_{\alpha+1,i}$ using Equation (8)

    - ∗ Let $\mathbf{C}_{\alpha+1,i} = \mathbf{C}''_{\alpha+1,i}/\|\mathbf{C}''_{\alpha+1,i}\|$

- **If** $\max_i \|\mathbf{C}_{\alpha+1,i} - \mathbf{C}_{\alpha,i}\| \leq T$ **Then**, let $\alpha_f = \alpha + 1$, and **Stop**.

Textural features: Recently, TA has become a popular research topic, particularly in the field of medical imaging. New techniques of TA provide different quantitative patterns/descriptors by combining the grey values of each pixel/voxel in a tumor image/volume. As a result of these abilities, TA has been used in the diagnosis of several tumors and their related subtypes with encouraging classification abilities [104, 105, 176–182]. Therefore, in this chapter, TA techniques were applied on the segmented 3D renal tumor volumes to precisely extract first- and second-order textural features that best describe the homogeneity/heterogeneity between renal tumors with different diagnoses. The use of such comprehensive textural features relies on the fact that malignant tumors mostly show high textural heterogeneity when compared to benign ones. The success of these findings would enhance the sensitivity and the specificity towards an early identification of renal cancer tumors. Figure 19 demonstrates the lesion texture differences of two malignant ccRCC subjects, two malignant nccRCC subjects, and two benign (AML) subjects.
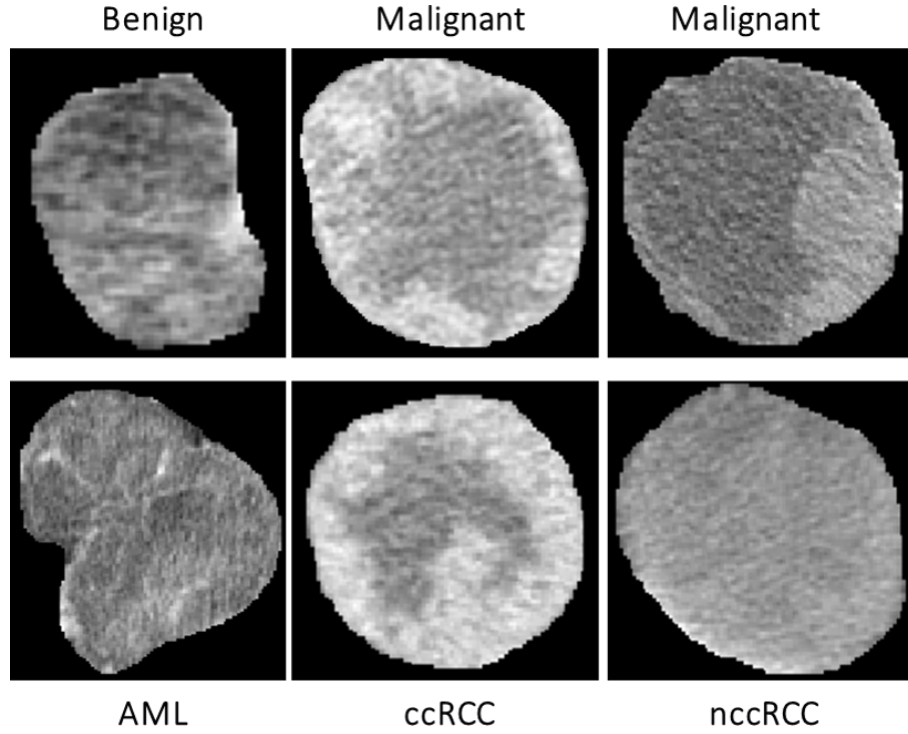
FIGURE 19: An illustrative example showing differences in texture between various renal tumor types.

First-order textural features: These textural features include any quantity that can be derived from the gray-level histogram of the tumor volume. In particular, mean, variance, standard deviation, entropy, skewness, kurtosis, cumulative distribution functions, and the grey-level percentiles [183] were extracted.

Figure 20 shows the average normalized histogram curves for all benign subjects (blue) vs. malignant (red). To construct these curves, the grey-level range was normalized first by dividing by the maximum grey-level value obtained from all subjects. Then, all histograms were constructed for all subjects within the new normalized grey-level range from 0 to 255. For each subject, the individual grey-level probability was obtained by dividing the histogram values by the corresponding number of voxels. Then, all normalized histograms from a particular group (malignant or benign) were averaged pointwise to obtain the final curve.
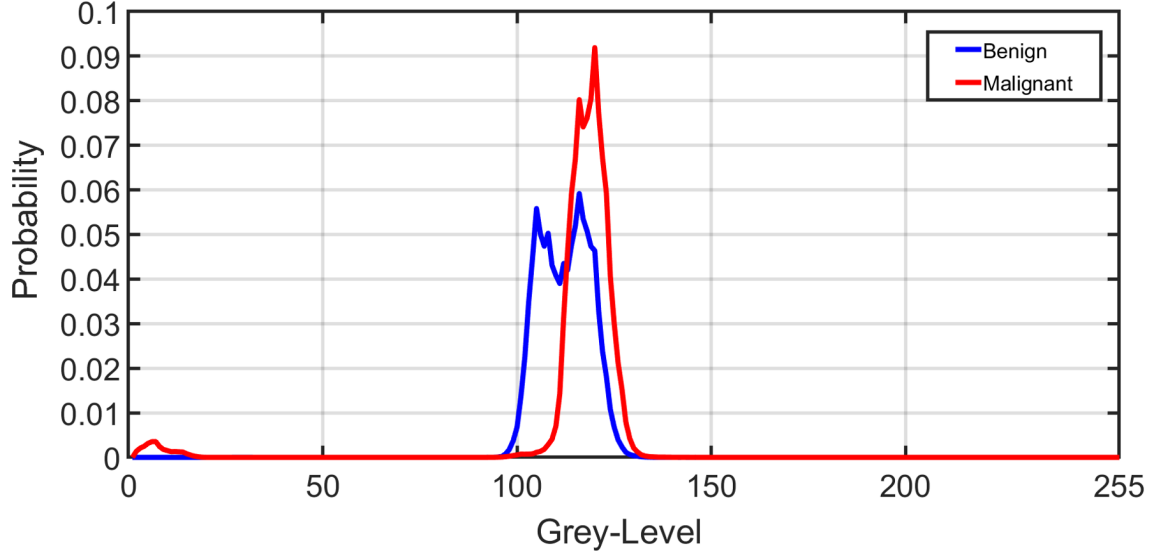
FIGURE 20: A visualization of the average normalized histogram curves for all benign subjects (blue) vs. malignant (red).

Second-order textural features: Since the first-order textural features might not be sufficient, with their range of values exhibiting significant overlap across classes, especially between subtypes of malignant tumor, second-order textural features were incorporated into the system. These features describe the joint distribution of gray values in multiple voxels that are considered to be neighbors of each other. In particular, the grey-level co-occurrence matrix (GLCM) [184] was used to capture the heterogeneous appearance of renal tumors.

To construct the GLCM, the number of times an ordered pair of two grey values occurs in two neighboring voxels within the renal tumor object must be counted. This technique is continued until all conceivable occurrence frequencies within the grey-level range of the renal tumor item are found, which covers all possible pairs of neighbors. For this, the renal tumor object's original grey-level range was first first contrast stretched to fit the desired span 0–255, yielding a GLCM matrix with a size of 256 × 256. Then, all feasible pair combinations were identified to construct the GLCM matrix (i.e., neigh-

bors with gray levels i and j contribute to row i, column j of the GLCM). To define the neighborhoods, a distance criterion that voxels must be separated by $\leq \sqrt{2}$ mm was used, making the calculations rotation invariant (see Figure 21). The resultant GLCM was then normalized and used to extracting the following second-order texture features [183, 184]: contrast, dissimilarity, homogeneity, angular second moment (ASM), energy, and correlation.
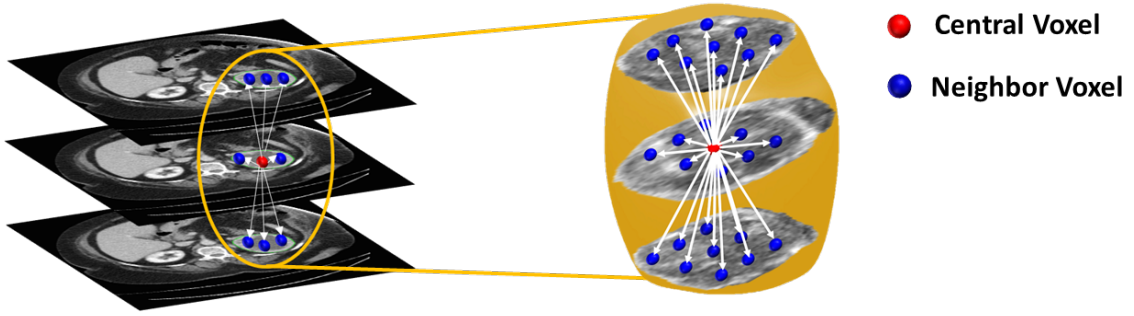
FIGURE 21: Visualization of the rotation-invariant neighborhood calculation system used to construct the grey-level co-occurrence matrix (GLCM). The GLCM can be constructed by counting the occurrence frequency of different grey-level pairs in-plane and in adjacent planes accounting for the 26-neighbor voxels (blue) of the central voxel (red).

The definitions of all first- and second-order textural features are provided in Tables 9 and 16 in Appendix .A.

Functional features: Discriminating RCC from AML, as well as ccRCC from nccRCC might be achieved using time-dependent characteristics of CE-CT imaging. The most relevant CE-CT findings for this purpose are generally homogenous and prolonged enhancement patterns [185]. The time dependency can be expressed by the slopes of wash-in and wash-out. Wash-in is described as the rate of increasing attenuation (in HU) from the precontrast to portal-venous phase. Similarly, wash-out is the rate of decrease in attenuation between the portal-venous and delayed-contrast phase [186]. Higher slopes of wash-in and wash-out are typically associated with malignancy. Moreover, nccRCC demonstrates wash-in and wash-out slopes intermediate between those of AML and those of ccRCC [187]. Therefore, both wash-in and wash-out slopes were constructed for all renal tumor subjects for the classification of the renal tumor status. Examples of wash-in/-out slopes showing the differences across ccRCC, nccRCC, and AML are shown in Figure 22.
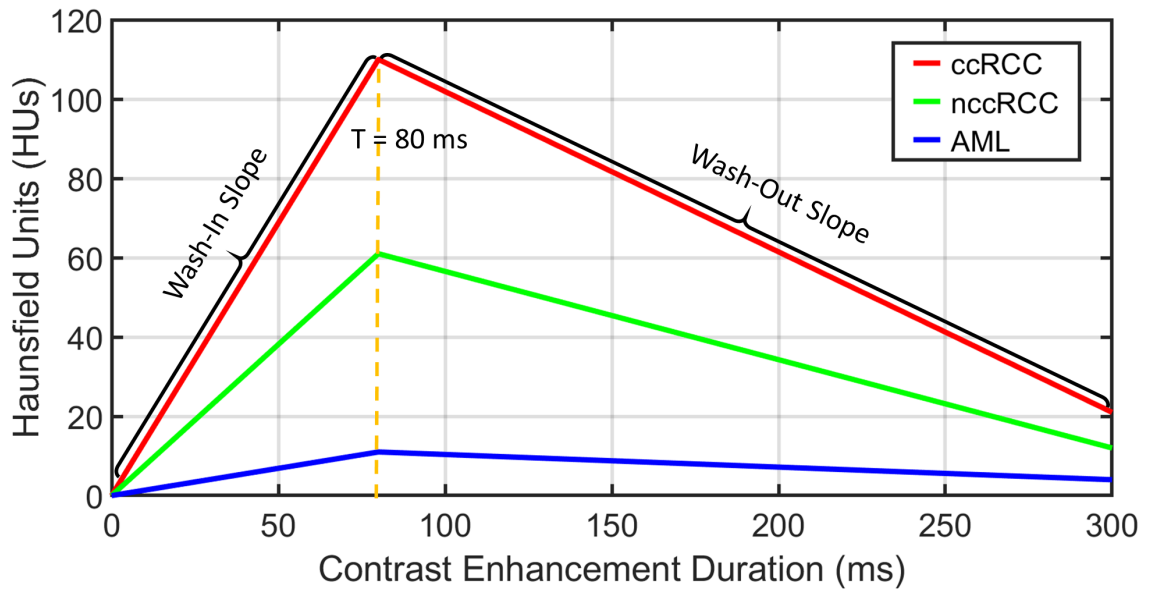
FIGURE 22: Example of the wash-in and wash-out slopes construction process for various types of renal tumors. When compared to nccRCC (green) and AML (blue), ccRCC tumors exhibit higher and faster wash-in/-out slopes (red).

TABLE 9: Definition of first- and second-order textural features.

Textural Feature	Definition
First Order	
Mean	The average grey value of voxels within the tumor.
Variance	Second central moment of gray values.
Standard deviation	Square root of variance.
Skewness (Skew)	Asymmetry of the distribution of gray values about the mean. If Skew < 0, that means the grey-level spreads out more to the left of the mean than to the right and if Skew > 0, that means the grey-level spreads out more to the right of the mean than to the left. Skew will equal to zero in the case of normal distributions.
Kurtosis (Kurt)	Measures the tail weight, or tendency to extreme values, of the object grey-level distribution. The normal distribution has Kurt $= 3$; distributions with heavier tails have Kurt > 3, and distributions with less weight in the tails have Kurt < 3.
Entropy	A measure of randomness of grey values with in an input image.
CDFs	A distribution function that accumulates voxel-wise grey values from the whole tumor with minimum value $= 0$ and maximum value $= 1$.
Percentiles	Grey values percentiles corresponding to the CDFs (from 10% to 100%)
Second Order	
Contrast	Measures the disparity in grey-level values between neighbors.
Dissimilarity	Finds to what extent voxels are different from their neighbors.
Homogeneity	Expresses the inverse difference moment among neighbors.
Angular second moment (ASM)	Determines the gray-levels local uniformity (orderliness).
Energy	The square root of the ASM.
Correlation	Determines the grey-level linear dependency in neighborhood blocks.

3.   Feature Integration and Renal Tumor Classification

Following the extraction of morphological, textural, and functional features from all given renal tumors, RC-CAD proceeds with two-stage diagnostic classification. The first stage aims to differentiate malignant (RCC) from benign (AML) tumors. In the case of malignancy, the second stage provides the classification of RCC tumors as ccRCC or nccRCC.

The multilayer perceptron (MLP) artificial neural network (ANN) consists of at least three layers: an input layer, one or more hidden layers, and an output layer, each with arbitrarily many activation/processing units, known as nodes/neurons. Each layer is fully connected to the next layer in sequence. Neurons use nonlinear activation functions to give the MLP-ANN the capability to divide the feature space into arbitrarily complex regions. The MLP-ANN mainly utilizes supervised backpropagation learning technique in the training phase, in which gradient descent methods are utilized to update the connection weights and additive biases in order to minimize the loss function. To achieve the goal, the MLP-ANN was optimized in both classification stages to obtain the final diagnosis. Classifier performance was assessed using five different feature sets (Table 10) as the ANN input in both stages. Feature Set 1 includes first-order histogram textural features ($N = 6$; mean, variance, standard deviation, skewness, kurtosis, and entropy); Feature Set 2 includes first-order percentile textural features ($N = 10$; from the 10th to the 100th percentile in 10% point steps); Feature Set 3 includes second-order GLCM textural features ($N = 6$; contrast, dissimilarity, homogeneity, ASM, energy, and correlation); Feature Set 4 includes SH reconstruction error (SHRE) morphological features ($N = 70$); and Feature Set 5 includes functional features ($N = 2$; wash-in slope and wash-out slope). At each classification stage, the individual feature sets were concatenated to obtain the combined features ($N = 94$) and were fed to a MLP-ANN to obtain the final diagnosis.

100

TABLE 10: Details of the extracted feature-sets used in the two-stage renal tumor classification.

Texture features	
Feature-Set 1: First order (Histogram features)	6 features
Feature-Set 2: First order (Percentiles)	10 features
Feature-Set 3: Second order (GLCM)	6 features
Shape features	
Feature-Set 4: Spherical Harmonics Reconstruction Errors	70 features
Functional features	
Feature-Set 5: Wash-In/Out slopes	2 features
Combined Features	
Feature-Sets 1, 2, 3, 4, and 5	94 features

C. Results

The diagnostic performance of the RC-CAD system on the dataset of 140 renal tumors was assessed using leave-one-subject-out (LOSO) cross-validation. The system's diagnostic capabilities were assessed, evaluated, and compared in both classification stages using the individual feature sets, as well as the combined features. Each classification process was repeated 10 times, and the results were tabulated in terms of the mean ± the standard deviation to provide a more quantitative expression of the diagnostic performance.

The first stage classification (RCC vs. AML) performance for the RC-CAD system was first evaluated using individual Feature Sets 1, 2, 3, 4, and 5 (see Table 10) along with different MLP-ANN classification models. Then, the RC-CAD system was evaluated using the combined features, resulting in a noticeably enhanced diagnostic performance.

A summary of the first stage performance in terms of the sensitivity, specificity, and Dice similarity coefficient (DSC) [188, 189] is presented in Table 11.

TABLE 11: Diagnostic performance results of the first stage classification (RCC vs. AML) using different individual feature-sets along with multi-layer perceptron artificial neural network (MLP-ANN) classification models. The RC-CAD system diagnostic performance using the combined features outperformed the diagnostic abilities using individual feature-sets. Sens: sensitivity, Spec: specificity, DSC: Dice coefficient of similarity, hl_n: size of hidden layer n.

RCC vs. AML Classification Performance (Mean±SD ≈)				
Feature-Set	**Sens%**	**Spec%**	**DSC**	**MLP-ANN**
Set 1	94.1±1.5	97.9±1.5	0.96±0.01	hl_1 = 10 nodes
Set 2	92.4±2.9	95.1±3.5	0.94±0.02	hl_1 = 10 nodes
Set 3	94.9±2.2	95.3±2.5	0.95±0.02	hl_1 = 10 nodes
Set 4	92.0±2.4	96.6±2.0	0.94±0.02	hl_1 = 10 nodes, hl_2 = 5 nodes
Set 5	82.7±4.1	91.7±2.0	0.87±0.02	hl_1 = 10 nodes
RC-CAD	**95.3±2.0**	**99.9±0.4**	**0.98±0.01**	**hl_1 = 50 nodes, hl_2 = 25 nodes**

Hyper-parameters: MLP-ANN (optimization function: trainlm, max epochs = 500, goal = 0, max validation failure = 6, min gradient = 10^{-7}, training gain (μ): initial μ = 0.001, μ decrease factor = 0.1, μ increase factor = 10, max μ = $1e^{10}$).

The diagnostic performance of the second stage classification (ccRCC vs. nc-cRCC) of the RC-CAD system was evaluated using the same LOSO cross-validation approach. As before, specially tailored MLP-ANN models were used with different feature sets. The best second stage classifier performance was obtained using the concatenated feature set (Table 12).

TABLE 12: Results from the second stage classification (ccRCC vs. nccRCC) using individual feature-sets (1, 2, 3, 4, and 5) along with multi-layer perceptron artificial neural networks (MLP-ANN) classification models. The RC-CAD system diagnostic performance using the combined features outperformed the diagnostic abilities using individual feature-sets. Acc: accuracy, hl_n: size of hidden layer n.

ccRCC vs. nccRCC classification Performance (Mean±SD ≈)		
Feature-Set	**Acc%**	**MLP-ANN Architecture**
Set 1	76.8±2.6	hl_1 = 10 nodes
Set 2	75.7±3.8	hl_1 = 10 nodes
Set 3	83.3±5.6	hl_1 = 10 nodes
Set 4	81.4±5.1	hl_1 = 10 nodes, hl_2 = 5 nodes
Set 5	76.2±2.33	hl_1 = 10 nodes
RC-CAD	**89.6±5.0**	**hl_1 = 50 nodes, hl_2 = 25 nodes**

Hyper-parameters: MLP-ANN (optimization function: trainlm, max epochs = 500, goal = 0, max validation failure = 6, min gradient = 10^{-7}, training gain (μ): initial μ = 0.001, μ decrease factor = 0.1, μ increase factor = 10, max μ = $1e^{10}$).

Figure 23 demonstrates a difficult case presentation for two ccRCC, two nccRCC, and two AML renal tumors. This figure visualizes the texture differences, wash-in and wash-out slope differences, and morphological differences between the different types of renal tumors, which emphasizes the potential power of the integration process of such features in providing a precise identification of a given renal tumor.
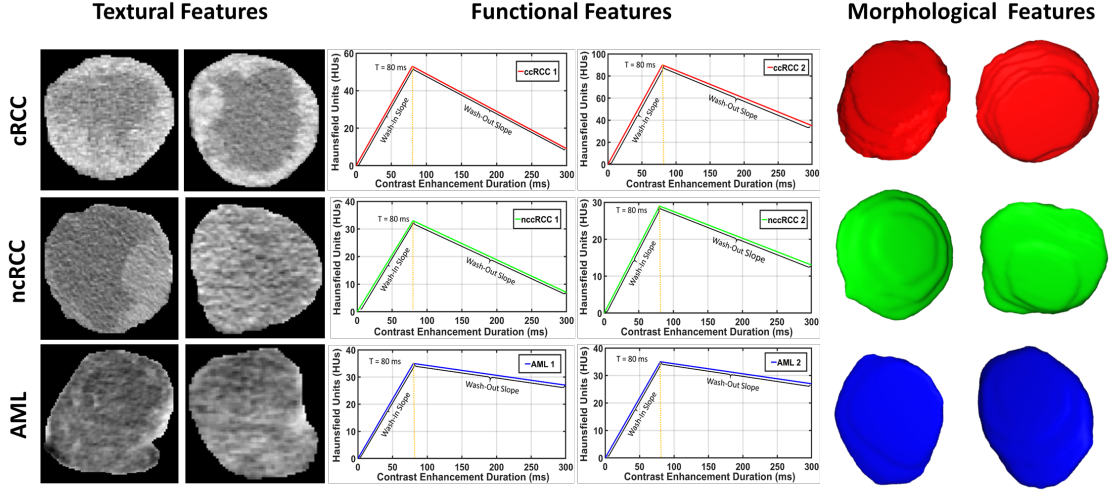
FIGURE 23: A difficult case presentation showing the textural differences, wash-in and wash-out slope differences, and shape differences between two ccRCC, two nccRCC, and two AML renal tumors.

To ensure that the developed system is not prone to overfitting and to validate the reproducibility and robustness of the RC-CAD, a randomly stratified 10-fold cross-validation approach was employed in both stages using the combined features. Likewise, the classification process was repeated 10 times using the same MLP-ANN classification model, and results are tabulated in terms of the mean ± the standard deviation (Table 13).

To highlight the advantages of using MLP-ANN classifier, the diagnostic performance of the RC-CAD was compared with other, well-known machine learning classifiers (e.g., SVM$_{Quad}$ and RF). As documented in Table 13, the diagnostic performance obtained by the RC-CAD system outperformed all other classifiers in both classification stages, which justifies the potential of such MLP-ANN classifiers being utilized for the developed RC-CAD system. It is worth mentioning that, in each classification stage, a grid search algorithm was employed to find the optimal set of hyperparameters, with the classification accuracy optimization criterion, for each of the classifier techniques being evaluated. The results of the hyperparameter optimization are appended to Table 13.

TABLE 13: Diagnostic performance comparison for both classification stages between the developed RC-CAD system and other classification approaches (e.g., random forest (RF) and support vector machine (SVM)). Using leave-one-subject-out (LOSO) and a randomly stratified 10-fold cross-validation approach, the diagnostic abilities of the RC-CAD outperformed others. Let Sens: sensitivity, Spec: Specificity, DSC: Dice similarity coefficient, and Acc: Accuracy.

First Stage Classification (RCC vs. AML) Performance (Mean±SD ≈)				
Method	**Validation**	**Sens%**	**Spec%**	**DSC**
RC-CAD (Proposed)	**LOSO**	**95.3±2.0**	**99.9±0.4**	**0.98±0.01**
	10-fold	**89.0±3.4**	**91.0±2.7**	**0.90±0.02**
RFs	LOSO	89.0±1.7	92.7±2.7	0.91±0.02
	10-fold	88.4±1.0	90.7±3.0	0.89±0.01
SVM$_{Quad}$	LOSO	82.9±0.0	88.6±0.0	0.85±0.00
	10-fold	81.9±2.2	87.7±2.5	0.84±0.02

Second Stage Classification (ccRCC vs. nccRCC) Performance (Mean±SD ≈)		
Method	**Validation**	**Acc%**
RC-CAD (Proposed)	**LOSO**	**89.6±5.0**
	10-fold	**78.6±5.7**
RFs	LOSO	53.7±3.7
	10-fold	51.9±2.6
SVM$_{Quad}$	LOSO	52.9±0.0
	10-fold	54.3±3.0

Hyper-parameters: MLP-ANN (optimization function: trainlm, max epochs = 500, hidden layers: $hl_1 = 50$ nodes, $hl_2 = 25$ nodes, goal = 0, max validation failure = 6, min gradient = 10^{-7}, training gain (μ): initial μ = 0.001, μ decrease factor = 0.1, μ increase factor = 10, max μ = $1e^{10}$); RF (method: Bag, number of learning cycles = 30); SVM (kernel function: quadratic, box constraint = 1).

For the comparison with the RC-CAD, the existing state-of-the-art approach [123] was applied using a total of 10 textural markers extracted from the portal-venous phase only along with the gradient boosting classification technique. In addition, the state-of-the-art deep learning CNN approaches proposed by Lee et al. [128] and Oberai et al. [133] were applied on the same datasets (first stage: N = 140; second stage: N = 70). To highlight the advantages of the RC-CAD system, all results are compared in Table 14. The diagnostic performance of RC-CAD exceeded that of other approaches in both classification stages.

TABLE 14: Diagnostic performance comparison for both classification stages between the developed RC-CAD system and other state-of-the-art approaches. The diagnostic abilities of the RC-CAD outperformed all other methods in both classification stages. Let Sens: sensitivity, Spec: Specificity, DSC: Dice similarity coefficient, and Acc: Accuracy.

First Stage Classification (RCC vs. AML) Performance (Mean±SD ≈)			
Method	**Sens%**	**Spec%**	**DSC**
RC-CAD (Proposed)	**95.3±2.0**	**99.9±0.4**	**0.98±0.01**
Kunapuli [123]	81.4±0.0	95.7±0.0	0.88±0.00
Oberai [133]	88.9±1.7	87.4±1.4	0.91±0.01
Lee [128] AlexNet	84.0±1.7	93.4±1.9	0.88±0.02
GoogleNet	88.3±1.7	95.1±1.9	0.91±0.01
ResNet	88.0±3.5	95.7±0.9	0.91±0.02
VGGNet	86.9±0.6	91.4±2.4	0.89±0.01

Second Stage Classification (ccRCC vs. nccRCC) Performance (Mean±SD ≈)			
Method	**Acc%**	**ccRCC/40**	**nccRCC/30**
RC-CAD (Proposed)	**89.6±5.0**	**35±2**	**28±3**
Kunapuli [123]	60.6±2.7	28±1	15±1
Oberai [133]	84.3±3.1	34±1	25±2
Lee [128] AlexNet	71.7±1.9	31±2	19±2
GoogleNet	68.0±1.5	32±1	15±1
ResNet	70.3±2.5	32±0	17±2
VGGNet	72.6±2.3	33±1	18±1

Hyper-parameters: MLP-ANN (optimization function: trainlm, max epochs = 500, hidden layers: hl_1 = 50 nodes, hl_2 = 25 nodes, goal = 0, max validation failure = 6, min gradient = 10^{-7}, training gain (μ): initial μ = 0.001, μ decrease factor = 0.1, μ increase factor = 10, max μ = $1e^{10}$).

D.   Discussion and Conclusions

The developed RC-CAD system demonstrated high diagnostic performance in terms of accuracy, sensitivity, specificity, and DSC in discrimination between benign (AML) and malignant (RCC) and in classification of the RCC subtype into ccRCC or nccRCC. This early and precise identification of the malignancy status of a given renal tumor and its associated subtype can enable clinicians to provide the appropriate early intervention/treatment plan and improve the outcomes. CE-CT was utilized as it is an imaging modality with the ability to provide different aspects of features, including but not limited to, morphological features, textural features, and functional features. The integration of these features is effective in determining the malignancy status of a given renal tumor when combined with a powerful machine learning classifier such as the MLP-ANN.

The grade of malignancy of a given renal tumor largely specifies the morphology of the tumor. Typically, malignant tumors demonstrate a more complex morphology than benign ones. Therefore, morphological features based on using spherical harmonics were utilized to capture possible surface complexity differences between malignant and benign renal tumors, as well as differences between different subtypes of malignancy.

First- and second-order textural features have been widely utilized to identify a given renal tumor status as malignant or benign, as well as to describe the malignancy subtype [122, 123, 125, 127, 128, 134]. These features capture all possible textural homogeneity/heterogeneity across renal tumors with different diagnoses. In line with these studies, the extracted textural features provided high diagnostic performance in discriminating malignant ccRCC and nccRCC from benign (AML) renal tumors.

Additionally, functionality was utilized to identify the malignancy status renal tumors. The wash-in and wash-out slopes can capture existing differences in the enhance-

ment characteristics [185, 186]. In this study, the results obtained by functionality metrics demonstrated the efficacy of such features in discriminating between benign (AML) and malignant (RCC) and identifying the malignancy subtype as ccRCC or nccRCC.

Although individual features have provided a reasonable diagnostic performance, they are not sufficient to rule out surgical intervention in (what may turn out to be) benign lesions. Therefore, the integration process of these features is critical to enhance the diagnostic accuracy to the point of clinical utility. The integration process produced a reliable and accurate RC-CAD system with an enhanced diagnostic performance in both classification stages as documented in Tables 11–13.

To sum up, the developed RC-CAD system demonstrated a high classification sensitivity of 95.29% ± 2.03%, a specificity of 99.86% ± 0.43%, an ad DSC of 0.98 ± 0.01 in differentiating benign AML from malignant RCC renal tumors. In addition, the RC-CAD achieved an overall classification accuracy of 89.57% ± 5.03% in distinguishing ccRCC from nccRCC to provide the proper management plan. Integrating accurate morphological features with functional features and multiple first-order and second-order textural features was adequate to significantly enhance the diagnostic capabilities.

CHAPTER VI

CONCLUSIONS AND FUTURE WORK

This dissertation presented a new computer-assisted diagnostic (Renal-CAD) system to precisely diagnose acute rejection (AR) post kidney transplantation at an early stage. The Renal-CAD system demonstrated 93.3% accuracy, 90.0% sensitivity, and 95.0% specificity in differentiating AR from non-rejection (NR). Robustness of the Renal-CAD system was also confirmed by the area under the curve value of 0.92. In addition, a new renal cancer CAD (RC-CAD) system for precise diagnosis of RC at an early stage was developed. The RC-CAD achieved a sensitivity of 95.3% ± 2.0%, a specificity of 99.9% ± 0.4%, and Dice similarity coefficient of 0.98 ± 0.01 in differentiating malignant from benign renal tumors, as well as an overall accuracy of 89.6% ± 5.0% in the subtyping of renal cell carcinomas (RCCs). The results obtained outperformed other machine learning classifiers as well as other different approaches from the literature. Machine learning and deep learning approaches have shown potential abilities to be utilized to build such AI-based CAD systems. This is evidenced by the promising diagnostic performance obtained by both Renal-CAD and RC-CAD systems. For the Renal-CAD, the integration of functional markers extracted from multimodal MRIs with clinical biomarkers using deep learning-based stacked autoencoder (SAE) classification model, potentially improved the final diagnostic results evidenced by high accuracy, sensitivity, and specificity. The developed Renal-CAD demonstrated high feasibility and efficacy for early, accurate, and non-invasive identification of AR. For the RC-CAD, integrating morphological, textural, and functional features extracted from CE-CT images using a machine learning-based

110

multi-layer perceptron artificial neural network (MLP-ANN) classification model eventually enhanced the final results in terms of accuracy, sensitivity, and specificity, making the proposed RC-CAD a reliable noninvasive diagnostic tool for renal cancer (RC). The early and accurate diagnosis of AR and/or RC will help physicians to provide early intervention with the appropriate treatment plan to prolong the life span of the diseased kidney, increase the survival chance of the patient, and thus improve the healthcare outcome in the U.S. and worldwide.

A.   Summary of Contributions

Main contributions of this dissertation are summarized in the following pullets:

- A new AI-based CAD system was developed to precisely diagnose AR post kidney transplantation at an early stage. The developed system was named Renal-CAD and encompasses the following contributions:

  - Extraction of DW-MR image markers, namely: voxel-wise apparent diffusion coefficients (ADCs) are calculated from the segmented kidneys at 11 different low and high b-values and then mapped to their cumulative distribution functions (CDFs) for better representation.

  - Extraction of BOLD-MR image markers, namely: the transverse relaxation rate (R2*) values from the segmented kidneys at four different echotimes and then R2* curves were constructed for better representation.

  - Integrating the extracted multimodal MR image markers with the associated clinical biomarkers serum creatinine (SCr) and creatinine clearance (CrCl). These integrated biomarkers are then fed to the developed DL classification model built on SAEs to diagnose the kidney transplant as NR or AR.

111

- A new AI-based CAD system for precise diagnosis of RC at an early stage was developed. The developed system was named RC-CAD and incorporates the following major contributions:

    – Integrating the morphological features the best describe the surface complexity of a given renal tumor, with first and second order appearance-based features that can capture the texture heterogeneity of a given renal tumor, and with the functional features by constructing wash-in/wash-out slopes to quantify the enhancement variations across different CE-CT phases.

    – Modeling a two-stage MLP-ANN classifier using the aforementioned integrated features to diagnose the renal tumor as benign or malignant and identify the malignancy subtype.

B. Future Avenues

The success of both AI-based CAD systems (Renal-CAD and RC-CAD) presented in this dissertation opens research pathway and thoughts towards some future avenues:

- Increasing the number of kidney transplant patients who had both types of scans (i.e. DW-MRI and BOLD-MRI). In this study, only the DW-MRI analysis pipeline included data from different geographical areas; and thus, more data could be collected for further validation, optimization, and fine tuning.

- The abilities of the Renal-CAD system could be extended (see Fig. 24 by adding genomic markers and proteomic markers to identify different types of AR post kidney transplantation as T-cell mediated rejection (TMR) or antibody mediated rejection (AMR). These specific identification will enhance the Renal-CAD diagnostic abilities, help in administering a timely intervention with the appropriate

112

treatment/management plan, prolong the survival rate of the transplanted kidney, improve the patient outcomes, and thus, improve the healthcare in the U.S. and worldwide.
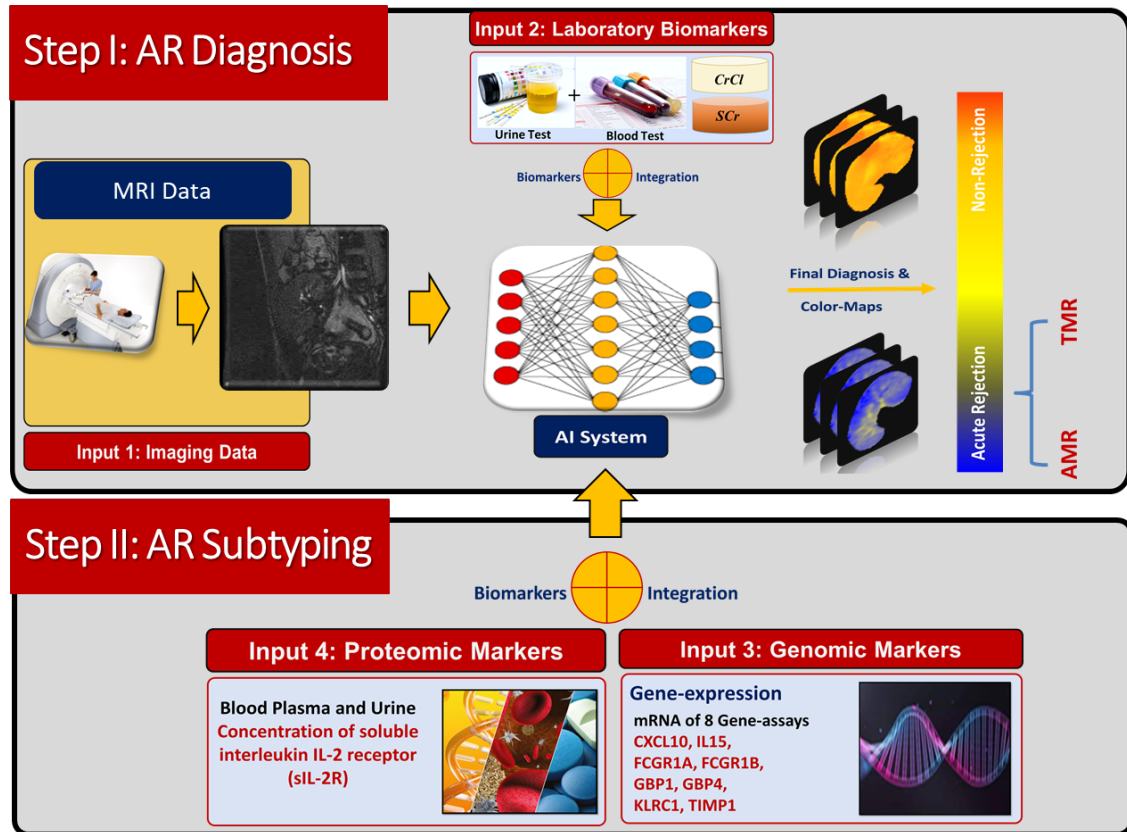
FIGURE 24: Suggested pipeline for identifying the AR subtype as TMR or AMR.

- The abilities of the Renal-CAD could also be investigated to identify additional renal dysfunction conditions such as nephrotic syndrome, acute tubular necrosis, tubular inflammation, acute kidney injury, and other chronic kidney diseases that might affect either the native or the transplanted. Integration of histopathology images, DNA, and RNA analysis could potentially help.

- Investigate the abilities of the RC-CAD system in identifying other tumors such as oncocytomas. Although they are benign tumors, they usually have a central scar

and showing similar characteristics of malignant tumors, specifically chromophobe RCC, which in turn make the differentiating between oncocytomas and chromophobe a challenging task.

- The abilities of the RC-CAD system to differentiate papillary RCC from chromophobe RCC will be investigated.

- Automatic detection, localization, and segmentation of renal tumors is very challenging for many reasons, including: (1) the wide variety in renal tumors size, some of them are very small ($\leq$ 4 cm) and some of them are very large and can cover large portions of the abdomen and (2) different locations, they could be on the right side, left side, different locations of the kidney (upper, middle, or lower) portion. Thus; most of the studies still depend on expert knowledge to segment the renal tumor manually using some segmentation tools before the handcrafted features are extracted.

- Development of an end-to-end AI-based CAD system is an ongoing research. Such systmes utilize deep learning techniques (e.g., convolutional neural networks (CNNs)) and could be one of the solutions that can provide the final diagnosis from an input image without the need for manual segmentation or hand-crafted features.

- Multi-parametric MRIs are other imaging modalities that could be used for diagnosing RC, especially in the cases when the patient is pregnant or a child, then there is no need to expose them to radiation.

- Potential investigation of an AI-based CAD system that integrate multi-modal imaging Radiomic makers extracted from CTs and MRIs could be helpful in accurate grading (I-IV) and staging (I-IV) of renal tumors to determine how aggressive the tumor is and the exact location of the tumor. These findings will help administering appropriate intervention and treatment plans in a timely manner.

- The abilities of the RC-CAD systems could be extended (see Fig. 25) to predict the treatment response such as recurrence rate, post-operative progression free-survival rate, or good response. This prediction will help physicians/oncologists in determining the treatment outcome and thus, recommend the change of therapy course or not.
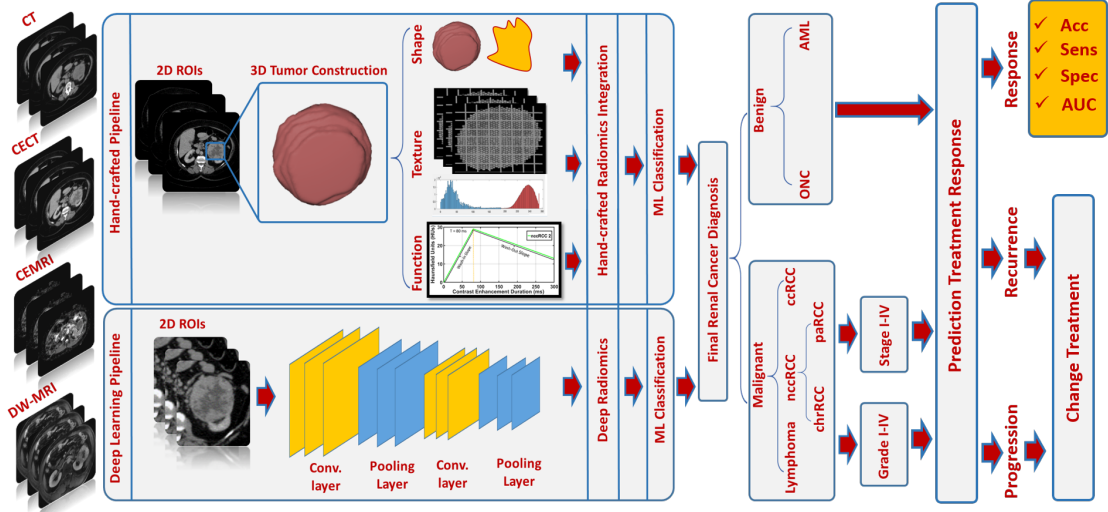
FIGURE 25: Suggested pipeline for: (1) identifying the malignancy status of a given renal tumors, malignancy subtyping, grading (I-IV), and staging (I-IV) and (2) prediction of treatment response.

- This work could also be applied to various other applications in medical imaging, such as the prostate [190–216], the kidney [33, 72, 217–244, ?–258], the heart [259–294], the lung [174, 295–348], the brain [349–432], the retina [433–448], the bladder [449–455], the liver [456–458], head and neck [459–462], and injury prediction [463] as well as several non-medical applications [464–471].

REFERENCES

[1] M. N. Wernick, Y. Yang, J. G. Brankov, G. Yourganov, and S. C. Strother. Machine learning in medical imaging. *IEEE Signal Processing Magazine*, 27(4):25–38, July 2010.

[2] Y. LeCun, Y. Bengio, and G. Hinton. Deep learning. *Nature*, 521(7553):436, 2015.

[3] J. Ker, L. Wang, J. Rao, and T. Lim. Deep learning applications in medical image analysis. *IEEE Access*, 6:9375–9389, 2018.

[4] Y. Bengio et al. Greedy layer-wise training of deep networks. *Advances in Neural Information Processing Systems*, 19:153, 2007.

[5] Y. Bengio, A. Courville, and P. Vincent. Representation learning: A review and new perspectives. *IEEE Transactions on Pattern Analysis and Machine Intelligence*, 35(8):1798–1828, 2013.

[6] M. Tariq, S. Iqbal, H. Ayesha, I. Abbas, K. T. Ahmad, and M. F. K. Niazi. Medical image based breast cancer diagnosis: State of the art and future directions. *Expert Systems with Applications*, 167:114095, 2021.

[7] Different types of kidney diseases. https://www.niddk.nih.gov/health-information/kidney-disease. Accessed: 2022-07-01.

[8] National chronic kidney disease fact sheet, 2021.

[9] Organ donation and transplantation statistics, Jan 2016.

[10] National Kidney Foundation. Organ donation and transplantion statistics. 2016.

[11] Centers for Disease Control and Prevention et al. National chronic kidney disease fact sheet. *Atlanta, GA: US Department of Health and Human Services*, 2017.

[12] A. J. Collins, R. N. Foley, B. Chavers, D. Gilbertson, C. Herzog, K. Johansen, B. Kasiske, N. Kutner, J. Liu, W. S. Peter, and et al. Us Renal Data System 2011 Annual Data Report. *American Journal of Kidney Diseases*, 59(1), 2012.

[13] E. Hollis, M. Shehata, F. Khalifa, M. A. El-Ghar, T. El-Diasty, and A. El-Baz. Towards non-invasive diagnostic techniques for early detection of acute renal transplant rejection: A review. *The Egyptian Journal of Radiology and Nuclear Medicine*, 48(1):257–269, 2017.

[14] B. L. Kasiske et al. Kdigo clinical practice guideline for the care of kidney transplant recipients: A summary. *Kidney International*, 77(4):299–311, 2010.

[15] American Cancer Society. Key statistics about kidney cancer. https://www.cancer.org/cancer/kidney-cancer/about/key-statistics.html/. Accessed: 2022-07-01.

[16] Kidney cancer facts. https://www.mayoclinic.org/tests-procedures/kidney-biopsy/about/pac-20394494. Accessed: 2022-07-01.

[17] G. Low, G. Huang, W. Fu, Z. Moloo, and S. Girgis. Review of renal cell carcinoma and its common subtypes in radiology. *World journal of radiology*, 8(5):484, 2016.

[18] T. J. van Oostenbrugge, J. J. Fütterer, and P. F. Mulders. Diagnostic imaging for solid renal tumors: a pictorial review. *Kidney Cancer*, 2(2):79–93, 2018.

[19] E. P. Widmaier, H. Raff, and K. T. Strang. *Vander's human physiology*, volume 5. McGraw-Hill New York, NY, 2006.

[20] G. Tortora and N. Anagnostakos. Maintenance of the human body. *Principles of Anatomy and Physiology. New York, NY: Harper and Row*, pages 441–695, 1981.

[21] R. Saran, B. Robinson, K. C. Abbott, L. Y. Agodoa, N. Bhave, J. Bragg-Gresham, R. Balkrishnan, X. Dietrich, A. Eckard, P. W. Eggers, et al. US renal data system 2017 annual data report: Epidemiology of kidney disease in the united states. *American Journal of Kidney Diseases: The Official Journal of The National Kidney Foundation*, 71(3 Suppl 1):A7, 2018.

[22] G. L. Myers et al. Recommendations for improving serum creatinine measurement: A report from the laboratory working group of the national kidney disease education program. *Clin. Chem.*, 52(1):5–18, 2006.

[23] E. Hodneland et al. In vivo estimation of glomerular filtration in the kidney using DCE-MRI. *IEEE Proceedings of International Symposium on Image and Signal Processing and Analysis*, 7th:755–761, 2011.

[24] F. G. Zöllner et al. Assessment of 3D DCE-MRI of the kidneys using non-rigid image registration and segmentation of voxel time courses. *Comput. Med. Imaging Graph.*, 33(3):171–181, 2009.

[25] D. Zikic, S. Sourbron, X. Feng, H. J. Michaely, A. Khamene, and N. Navab. Automatic alignment of renal DCE-MRI image series for improvement of quantitative tracer kinetic studies. In *Proceedings of SPIE, Medical Imaging: Image Processing*, volume 6914, pages 1–8. International Society for Optics and Photonics, 2008.

[26] B. D. de Senneville, I. A. Mendichovszky, S. Roujol, I. Gordon, C. Moonen, and N. Grenier. Improvement of MRI-functional measurement with automatic movement correction in native and transplanted kidneys. *Journal of Magnetic Resonance Imaging*, 28(4):970–978, 2008.

[27] A. Farag et al. A framework for the detection of acute rejection with Dynamic Contrast Enhanced Magnetic Resonance Imaging. In *IEEE Int. Symp. Biomed. Imaging*, pages 418–421, 2006.

[28] M. Aslan, H. A. El Munim, A. Farag, and M. Abou El-Ghar. Assessment of kidney function using dynamic contrast enhanced MRI techniques. *Biomedical Image Analysis and Machine Learning Technologies: Applications and Techniques: Applications and Techniques*, page 214, 2009.

[29] A. Wentland, E. Sadowski, A. Djamali, T. Grist, B. Becker, and S. Fain. Quantitative MR measures of intrarenal perfusion in the assessment of transplanted kidneys: initial experience. *Academic radiology*, 16(9):1077–1085, 2009.

[30] M. Abou El-Ghar, A. Farag, T. El-Diasty, A. Shokeir, H. Refaie, Y. Osman, T. Mohsen, and M. Ghoneim. Computer aided detection of acute renal allograft dysfunction using dynamic contrast enhanced MRI. *The Egyptian Journal of Radiology and Nuclear Medicine*, 42(3):443–449, 2011.

[31] A. Yamamoto, J. Zhang, H. Rusinek, H. Chandarana, P.-H. Vivier, J. Babb, T. Diflo, D. John, J. Benstein, L. Barisoni, et al. Quantitative evaluation of acute renal transplant dysfunction with low-dose three-dimensional MR renography. *Radiology*, 260(3):781–789, 2011.

[32] F. Khalifa, A. El-Baz, G. Gimel'farb, and M. A. El-Ghar. Non-invasive image-based approach for early detection of acute renal rejection. In *Proceedings of Int. Conf. Med. Image Comput. Comput.-Assist. Interv.*, pages 10–18, Beijing, China, September 20–24, 2010.

[33] F. Khalifa, G. M. Beache, M. A. El-Ghar, T. El-Diasty, G. Gimel'farb, M. Kong, and A. El-Baz. Dynamic contrast-enhanced MRI-based early detection of acute renal transplant rejection. *IEEE Transactions on Medical Imaging*, 32(10):1910–1927, 2013.

[34] A. El-Baz et al. New motion correction models for automatic identification of renal transplant rejection. pages 235–243, 2007.

[35] A. Sharfuddin. Renal relevant radiology: imaging in kidney transplantation. *Clinical Journal of American Society of Nephrology*, 9(2):416–429, 2014.

[36] K. Hueper, A. A. Khalifa, J. H. Bräsen, V. D. Vo Chieu, M. Gutberlet, S. Wintterle, F. Lehner, N. Richter, M. Peperhove, S. Tewes, et al. Diffusion-weighted imaging and diffusion tensor imaging detect delayed graft function and correlate with allograft fibrosis in patients early after kidney transplantation. *Journal of Magnetic Resonance Imaging*, 44(1):112–121, 2016.

[37] G. Liu et al. Detection of renal allograft rejection using blood oxygen level-dependent and diffusion weighted magnetic resonance imaging: A retrospective study. *BMC Nephrology*, 15(1):158, 2014.

[38] M. Abou-El-Ghar, T. El-Diasty, A. El-Assmy, H. Refaie, A. Refaie, and M. Ghoneim. Role of diffusion-weighted MRI in diagnosis of acute renal allograft dysfunction: a prospective preliminary study. *The British Journal of Radiology*, 85(1014):e206–e211, 2014.

[39] A. Kaul et al. Assessment of allograft function using diffusion-weighted magnetic resonance imaging in kidney transplant patients. *Saudi Journal of Kidney Diseases and Transplantation*, 25(6):1143, 2014.

[40] K. Wypych-Klunder et al. Diffusion-weighted MR imaging of transplanted kidneys: Preliminary report. *Polish J. Radiol.*, 79:94–98, 2014.

[41] U. Eisenberger et al. Evaluation of renal allograft function early after transplantation with diffusion-weighted MR imaging. *European Radiology*, 20(6):1374–1383, 2010.

[42] F. Han et al. The significance of BOLD MRI in differentiation between renal transplant rejection and acute tubular necrosis. *Nephrology Dialysis Transplantation*, 23(8):2666–2672, 2008.

[43] E. A. Sadowski et al. Blood oxygen level-dependent and perfusion magnetic resonance imaging: Detecting differences in oxygen bioavailability and blood flow in transplanted kidneys. *Magnetic Resonance Imaging*, 28(1):56–64, 2010.

[44] A. Djamali et al. Noninvasive assessment of early kidney allograft dysfunction by blood oxygen level-dependent magnetic resonance imaging. *Transplantation*, 82(5):621–628, 2006.

[45] M. Pruijm et al. Renal blood oxygenation level-dependent magnetic resonance imaging to measure renal tissue oxygenation: a statement paper and systematic review. *Nephrology Dialysis Transplantation*, 33(suppl_2):ii22–ii28, 2018.

[46] M. E. Hall et al. Bold magnetic resonance imaging in nephrology. *International Journal of Nephrology and Renovascular Disease*, 11:103, 2018.

[47] M. Seif et al. Renal blood oxygenation level–dependent imaging in longitudinal follow-up of donated and remaining kidneys. *Radiology*, 279(3):795–804, 2016.

[48] J. Zhang et al. Blood-oxygenation-level-dependent-(bold-) based r2â€² MRI study in monkey model of reversible middle cerebral artery occlusion. *Journal of Biomedicine and Biotechnology*, 2011, 2011.

[49] H. Michaely et al. Functional renal imaging: Nonvascular renal disease. *Abdominal Imaging*, 32(1):1–16, 2007.

[50] G. S. Chilla, C. H. Tan, C. Xu, and C. L. Poh. Diffusion weighted magnetic resonance imaging and its recent trend: A survey. *Quantitative imaging in medicine and surgery*, 5(3):407, 2015.

[51] J. Xu et al. Value of diffusion-weighted mr imaging in diagnosis of acute rejection after renal transplantation. *Journal of Zhejiang University. Medical sciences*, 39(2):163–167, 2010.

[52] S. Palmucci et al. Magnetic resonance with diffusion-weighted imaging in the evaluation of transplanted kidneys: Preliminary findings. In *Transplantation Proceedings*, volume 43, pages 960–966, 2011.

[53] S. Palmucci et al. Magnetic resonance with diffusion-weighted imaging in the evaluation of transplanted kidneys: Updating results in 35 patients. *Transplantation Proceedings*, 44(7):1884–8, 2012.

[54] K. Wypych-Klunder, A. Adamowicz, A. Lemanowicz, W. Szczesny, Z. Włodarczyk, and Z. Serafin. Diffusion-weighted MR imaging of transplanted kidneys: Preliminary report. *Polish Journal of Radiology*, 79:94, 2014.

[55] S. Y. Park et al. Assessment of early renal allograft dysfunction with blood oxygenation level-dependent MRI and diffusion-weighted imaging. *European Journal of Radiology*, 83(12):2114–2121, 2014.

[56] P. Steiger, S. Barbieri, A. Kruse, M. Ith, and H. C. Thoeny. Selection for biopsy of kidney transplant patients by diffusion-weighted MRI. *European Radiology*, 27(10):4336–4344, 2017.

[57] Y. Xie, Y. Li, J. Wen, X. Li, Z. Zhang, J. Li, Y. Zhao, P. Wang, J. Zhang, Y. Tian, et al. Functional evaluation of transplanted kidneys with reduced field-of-view diffusion-weighted imaging at 3T. *Korean Journal of Radiology*, 19(2):201–208, 2018.

[58] W. Xiao, J. Xu, Q. Wang, Y. Xu, and M. Zhang. Functional evaluation of transplanted kidneys in normal function and acute rejection using BOLD MR imaging. *European Journal of Radiology*, 81(5):838–845, 2012.

[59] G. F. Mendes, P. M. Falsarella, R. G. Garcia, L. G. Sanches, and R. H. Baroni. Evaluation of the blood-oxygen-level-dependent (BOLD) sequence with 3 tesla device in renal transplant patients in the assessment of early allograft dysfunction, correlated with biopsy. *Einstein (São Paulo)*, 19, 2021.

[60] P. Vermathen et al. Three-year follow-up of human transplanted kidneys by diffusion-weighted MRI and blood oxygenation level-dependent imaging. *Journal of Magnetic Resonance Imaging*, 35(5):1133–1138, 2012.

[61] D. Gray, A. Daar, H. Shepherd, D. Oliver, and P. Morris. Oral versus intravenous high-dose steroid treatment of renal allograft rejection: The big shot or not? *The Lancet*, 311(8056):117–118, 1978.

[62] C. Shinn, D. Malhotra, L. Chan, R. L. Cosby, and J. I. Shapiro. Time course of response to pulse methylprednisolone therapy in renal transplant recipients with acute allograft rejection. *American journal of kidney diseases*, 34(2):304–307, 1999.

[63] A. C. Webster, T. Pankhurst, F. Rinaldi, J. R. Chapman, and J. C. Craig. Monoclonal and polyclonal antibody therapy for treating acute rejection in kidney transplant recipients: A systematic review of randomized trial data. *Transplantation*, 81(7):953–965, 2006.

[64] F. Qureshi, H. Rabb, and B. L. Kasiske. Silent acute rejection during prolonged delayed graft function reduces kidney allograft survival. *Transplantation*, 74(10):1400–1404, 2002.

[65] W.-j. Fan, T. Ren, Q. Li, P.-l. Zuo, M.-m. Long, C.-b. Mo, L.-h. Chen, L.-x. Huang, and W. Shen. Assessment of renal allograft function early after transplantation with isotropic resolution diffusion tensor imaging. *European Radiology*, 26(2):567–575, 2016.

[66] H. C. Thoeny and F. De Keyzer. Diffusion-weighted MR imaging of native and transplanted kidneys. *Radiology*, 259(1):25–38, 2011.

[67] J. L. Zhang et al. Variability of renal apparent diffusion coefficients: limitations of the monoexponential model for diffusion quantification. *Radiology*, 254(3):783–792, 2010.

[68] H.-J. Wittsack, R. S. Lanzman, C. Mathys, H. Janssen, U. Mödder, and D. Blondin. Statistical evaluation of diffusion-weighted imaging of the human kidney. *Magnetic resonance in medicine*, 64(2):616–622, 2010.

[69] L. Lu, J. R. Sedor, V. Gulani, J. R. Schelling, A. O'Brien, C. A. Flask, and K. M. Dell. Use of diffusion tensor MRI to identify early changes in diabetic nephropathy. *American journal of nephrology*, 34(5):476–482, 2011.

[70] Y.-T. Wang, Y.-C. Li, L.-L. Yin, H. Pu, and J.-Y. Chen. Functional assessment of transplanted kidneys with magnetic resonance imaging. *World journal of radiology*, 7(10):343, 2015.

[71] K. Hueper, B. Hensen, M. Gutberlet, R. Chen, D. Hartung, A. Barrmeyer, M. Meier, W. Li, M.-S. Jang, M. Mengel, et al. Kidney transplantation: Multiparametric functional magnetic resonance imaging for assessment of renal allograft pathophysiology in mice. *Investigative Radiology*, 51(1):58–65, 2016.

[72] M. Shehata, A. Mahmoud, A. Soliman, F. Khalifa, M. Ghazal, M. A. El-Ghar, M. El-Melegy, and A. El-Baz. 3d kidney segmentation from abdominal diffusion MRI using an appearance-guided deformable boundary. *PloS one*, 13(7):e0200082, 2018.

[73] N. J. Tustison et al. N4ITK: Improved N3 bias correction. *IEEE Tansactions on Medical imaging*, 29(6):1310–1320, 2010.

[74] B. Glocker et al. Non-rigid registration using discrete MRFs: Application to thoracic CT images. *Workshop Evaluation of Methods for Pulmonary Image Registration, MICCAI 2010*, 13th:147–154, 2010.

[75] D. Le Bihan and E. Breton. Imagerie de diffusion in-vivo par résonance magnétique nucléaire. *Comptes-Rendus de l'Académie des Sciences*, 93(5):27–34, 1985.

[76] E. Hosseini-Asl et al. Deep learning of part-based representation of data using sparse autoencoders with nonnegativity constraints. *IEEE Transactions on Neural Networks and Learning Systems*, 27(12):2486–2498, 2015.

[77] N. Srivastava, G. Hinton, A. Krizhevsky, I. Sutskever, and R. Salakhutdinov. Dropout: A simple way to prevent neural networks from overfitting. *The Journal of Machine Learning Research*, 15(1):1929–1958, 2014.

[78] S. Wang and C. Manning. Fast dropout training. In *International Conference on Machine Learning*, pages 118–126, 2013.

[79] T. Fawcett. An introduction to ROC analysis. *Pattern Recognition Letters*, 27(8):861–874, 2006.

[80] ASCO. Kidney cancer. https://www.cancer.net/cancer-types/kidney-cancer/statistics/. Accessed: 2022-07-15.

[81] National Cancer Institute. Cancer prevalence and cost of care projections. https://costprojections.cancer.gov/graph.php, 2018. Accessed: 03-January-2018.

[82] R. L. Siegel, K. D. Miller, and A. Jemal. Cancer statistics, 2015. *CA: a cancer journal for clinicians*, 65(1):5–29, 2015.

[83] W. Chen, R. Zheng, P. D. Baade, S. Zhang, H. Zeng, F. Bray, A. Jemal, X. Q. Yu, and J. He. Cancer statistics in china, 2015. *CA: a cancer journal for clinicians*, 66(2):115–132, 2016.

[84] H. Moch, A. L. Cubilla, P. A. Humphrey, V. E. Reuter, and T. M. Ulbright. The 2016 WHO classification of tumours of the urinary system and male genital organs—part A: renal, penile, and testicular tumours. *European urology*, 70(1):93–105, 2016.

[85] B. Delahunt, P. B. Bethwaite, and J. N. Nacey. Outcome prediction for renal cell carcinoma: evaluation of prognostic factors for tumours divided according to histological subtype. *Pathology*, 39(5):459–465, 2007.

[86] J. C. Cheville, C. M. Lohse, H. Zincke, A. L. Weaver, and M. L. Blute. Comparisons of outcome and prognostic features among histologic subtypes of renal cell carcinoma. *The American journal of surgical pathology*, 27(5):612–624, 2003.

[87] R. A. Rendon. Active surveillance as the preferred management option for small renal masses. *Canadian Urological Association Journal*, 4(2):136, 2010.

[88] A. C. Mues and J. Landman. Small renal masses: current concepts regarding the natural history and reflections on the american urological association guidelines. *Current opinion in urology*, 20(2):105–110, 2010.

[89] R. Heuer, I. S. Gill, G. Guazzoni, Z. Kirkali, M. Marberger, J. P. Richie, and J. J. de la Rosette. A critical analysis of the actual role of minimally invasive surgery and active surveillance for kidney cancer. *European urology*, 57(2):223–232, 2010.

[90] J. Xipell. The incidence of benign renal nodules (a clinicopathologic study). *The Journal of urology*, 106(4):503–506, 1971.

[91] I. S. Gill, M. Aron, D. A. Gervais, and M. A. Jewett. Small renal mass. *New England journal of medicine*, 362(7):624–634, 2010.

[92] T. Hodgdon, M. D. McInnes, N. Schieda, T. A. Flood, L. Lamb, and R. E. Thornhill. Can quantitative CT texture analysis be used to differentiate fat-poor renal angiomyolipoma from renal cell carcinoma on unenhanced CT images? *Radiology*, 276(3):787–796, 2015.

[93] S. R. Mindrup, J. S. Pierre, L. Dahmoush, and B. R. Konety. The prevalence of renal cell carcinoma diagnosed at autopsy. *BJU international*, 95(1):31–33, 2005.

[94] American Cancer Society. Test for kidney cancer. https://www.cancer.org/cancer/kidney-cancer/detection-diagnosis-staging/how-diagnosed.html. Accessed: 2020-04-10.

[95] R. S. Lim et al. Renal angiomyolipoma without visible fat: Can we make the diagnosis using CT and MRI? *European Radiology*, 28(2):542–553, 2018.

[96] H. Chandarana, A. B. Rosenkrantz, T. C. Mussi, S. Kim, A. A. Ahmad, S. D. Raj, J. McMenamy, J. Melamed, J. S. Babb, B. Kiefer, et al. Histogram analysis of whole-lesion enhancement in differentiating clear cell from papillary subtype of renal cell cancer. *Radiology*, 265(3):790–798, 2012.

[97] X. Zhou et al. Characterization and diagnostic confidence of contrast-enhanced ultrasound for solid renal tumors. *Ultrasound in medicine & biology*, 37(6):845–853, 2011.

[98] R. Dyer, D. J. DiSantis, and B. L. McClennan. Simplified imaging approach for evaluation of the solid renal mass in adults. *Radiology*, 247(2):331–343, 2008.

[99] J. Zhang, R. A. Lefkowitz, N. M. Ishill, L. Wang, C. S. Moskowitz, P. Russo, H. Eisenberg, and H. Hricak. Solid renal cortical tumors: differentiation with ct. *Radiology*, 244(2):494–504, 2007.

[100] A. Goyal, A. Razik, D. Kandasamy, A. Seth, P. Das, B. Ganeshan, and R. Sharma. Role of MR texture analysis in histological subtyping and grading of renal cell carcinoma: a preliminary study. *Abdominal Radiology*, 44(10):3336–3349, 2019.

[101] A. Razik, A. Goyal, R. Sharma, D. Kandasamy, A. Seth, P. Das, and B. Ganeshan. MR texture analysis in differentiating renal cell carcinoma from lipid-poor angiomyolipoma and oncocytoma. *The British journal of radiology*, 93(1114):20200569, 2020.

[102] J. R. Young, D. Margolis, S. Sauk, A. J. Pantuck, J. Sayre, and S. S. Raman. Clear cell renal cell carcinoma: discrimination from other renal cell carcinoma subtypes and oncocytoma at multiphasic multidetector ct. *Radiology*, 267(2):444–453, 2013.

[103] J. K. Kim, T. K. Kim, H. J. Ahn, C. S. Kim, K.-R. Kim, and K.-S. Cho. Differentiation of subtypes of renal cell carcinoma on helical ct scans. *American Journal of Roentgenology*, 178(6):1499–1506, 2002.

[104] M. G. Lubner, A. D. Smith, K. Sandrasegaran, D. V. Sahani, and P. J. Pickhardt. Ct texture analysis: definitions, applications, biologic correlates, and challenges. *Radiographics*, 37(5):1483–1503, 2017.

[105] R. J. Gillies, P. E. Kinahan, and H. Hricak. Radiomics: images are more than pictures, they are data. *Radiology*, 278(2):563–577, 2016.

[106] C. Scapicchio, M. Gabelloni, A. Barucci, D. Cioni, L. Saba, and E. Neri. A deep look into radiomics. *La radiologia medica*, 126(10):1296–1311, 2021.

[107] R. Yang, J. Wu, L. Sun, S. Lai, Y. Xu, X. Liu, Y. Ma, and X. Zhen. Radiomics of small renal masses on multiphasic CT: accuracy of machine learning–based classification models for the differentiation of renal cell carcinoma and angiomyolipoma without visible fat. *European radiology*, 30(2):1254–1263, 2020.

[108] M.-W. You, N. Kim, and H. Choi. The value of quantitative CT texture analysis in differentiation of angiomyolipoma without visible fat from clear cell renal cell carcinoma on four-phase contrast-enhanced CT images. *Clinical Radiology*, 74(7):547–554, 2019.

[109] Q. Xu, Q. Zhu, H. Liu, L. Chang, S. Duan, W. Dou, S. Li, and J. Ye. Differentiating benign from malignant renal tumors using T2-and diffusion-weighted images: A comparison of deep learning and radiomics models versus assessment from radiologists. *Journal of Magnetic Resonance Imaging*, 55(4):1251–1259, 2022.

[110] T. J. van Oostenbrugge, I. M. Spenkelink, L. Bokacheva, H. Rusinek, M. J. van Amerongen, J. F. Langenhuijsen, P. F. Mulders, and J. J. Fütterer. Kidney tumor diffusion-weighted magnetic resonance imaging derived ADC histogram parameters combined with patient characteristics and tumor volume to discriminate oncocytoma from renal cell carcinoma. *European Journal of Radiology*, 145:110013, 2021.

[111] A. Li, W. Xing, H. Li, Y. Hu, D. Hu, Z. Li, and I. R. Kamel. Subtype differentiation of small (≤ 4 cm) solid renal mass using volumetric histogram analysis of DWI at 3-T MRI. *American Journal of Roentgenology*, 211(3):614–623, 2018.

[112] S. Matsumoto, Y. Arita, S. Yoshida, H. Fukushima, K. Kimura, I. Yamada, H. Tanaka, F. Yagi, M. Yokoyama, Y. Matsuoka, et al. Utility of radiomics features of diffusion-weighted magnetic resonance imaging for differentiation of fat-poor angiomyolipoma from clear cell renal cell carcinoma: model development and external validation. *Abdominal Radiology*, 47(6):2178–2186, 2022.

[113] U. N. Hoang, S. Mojdeh Mirmomen, O. Meirelles, J. Yao, M. Merino, A. Metwalli, W. Marston Linehan, and A. A. Malayeri. Assessment of multiphasic contrast-enhanced mr textures in differentiating small renal mass subtypes. *Abdominal Radiology*, 43(12):3400–3409, 2018.

[114] Y. Deng, E. Soule, A. Samuel, S. Shah, E. Cui, M. Asare-Sawiri, C. Sundaram, C. Lall, and K. Sandrasegaran. CT texture analysis in the differentiation of major renal cell carcinoma subtypes and correlation with fuhrman grade. *European radiology*, 29(12):6922–6929, 2019.

[115] G.-M.-Y. Zhang, B. Shi, H.-D. Xue, B. Ganeshan, H. Sun, and Z.-Y. Jin. Can quantitative CT texture analysis be used to differentiate subtypes of renal cell carcinoma? *Clinical radiology*, 74(4):287–294, 2019.

[116] J. Uhlig, L. Biggemann, M. M. Nietert, T. Beißbarth, J. Lotz, H. S. Kim, L. Trojan, and A. Uhlig. Discriminating malignant and benign clinical T1 renal masses on computed tomography: A pragmatic radiomics and machine learning approach. *Medicine*, 99(16), 2020.

[117] Z. Feng, Q. Shen, Y. Li, and Z. Hu. CT texture analysis: a potential tool for predicting the fuhrman grade of clear-cell renal carcinoma. *Cancer Imaging*, 19(1):1–7, 2019.

[118] J. Shu, Y. Tang, J. Cui, R. Yang, X. Meng, Z. Cai, J. Zhang, W. Xu, D. Wen, and H. Yin. Clear cell renal cell carcinoma: CT-based radiomics features for the prediction of fuhrman grade. *European journal of radiology*, 109:8–12, 2018.

[119] N. L. Demirjian, B. A. Varghese, S. Y. Cen, D. H. Hwang, M. Aron, I. Siddiqui, B. K. Fields, X. Lei, F. Y. Yap, M. Rivas, et al. CT-based radiomics stratification of tumor grade and TNM stage of clear cell renal cell carcinoma. *European Radiology*, 32(4):2552–2563, 2022.

[120] J. Sun, L. Pan, T. Zha, W. Xing, J. Chen, and S. Duan. The role of MRI texture analysis based on susceptibility-weighted imaging in predicting fuhrman grade of clear cell renal cell carcinoma. *Acta Radiologica*, 62(8):1104–1111, 2021.

[121] X.-Y. Chen, Y. Zhang, Y.-X. Chen, Z.-Q. Huang, X.-Y. Xia, Y.-X. Yan, M.-P. Xu, W. Chen, X.-l. Wang, and Q.-L. Chen. MRI-based grading of clear cell renal cell carcinoma using a machine learning classifier. *Frontiers in Oncology*, 11:708655, 2021.

[122] Y. Deng, E. Soule, E. Cui, A. Samuel, S. Shah, C. Lall, C. Sundaram, and K. Sandrasegaran. Usefulness of CT texture analysis in differentiating benign and malignant renal tumours. *Clinical radiology*, 75(2):108–115, 2020.

[123] G. Kunapuli, B. A. Varghese, P. Ganapathy, B. Desai, S. Cen, M. Aron, I. Gill, and V. Duddalwar. A decision-support tool for renal mass classification. *Journal of Digital Imaging*, 31(6):929–939, 2018.

[124] I. Guyon, J. Weston, S. Barnhill, and V. Vapnik. Gene selection for cancer classification using support vector machines. *Machine Learning*, 46(1-3):389–422, 2002.

[125] B. Kocak, A. H. Yardimci, C. T. Bektas, M. H. Turkcanoglu, C. Erdim, U. Yucetas, S. B. Koca, and O. Kilickesmez. Textural differences between renal cell carcinoma subtypes: Machine learning-based quantitative computed tomography texture analysis with independent external validation. *European Journal of Radiology*, 107:149–157, 2018.

[126] P. M. Szczypiński, M. Strzelecki, A. Materka, and A. Klepaczko. MaZda—a software package for image texture analysis. *Computer methods and programs in biomedicine*, 94(1):66–76, 2009.

[127] X.-Y. Sun, Q.-X. Feng, X. Xu, J. Zhang, F.-P. Zhu, Y.-H. Yang, and Y.-D. Zhang. Radiologic-radiomic machine learning models for differentiation of benign and malignant solid renal masses: Comparison with expert-level radiologists. *American Journal of Roentgenology*, 214(1):W44–W54, 2020.

[128] H. Lee, H. Hong, J. Kim, and D. C. Jung. Deep feature classification of angiomyolipoma without visible fat and renal cell carcinoma in abdominal contrast-enhanced CT images with texture image patches and hand-crafted feature concatenation. *Medical physics*, 45(4):1550–1561, 2018.

[129] A. Krizhevsky, I. Sutskever, and G. E. Hinton. Imagenet classification with deep convolutional neural networks. In *Advances in neural information processing systems*, pages 1097–1105, 2012.

[130] K. Simonyan and A. Zisserman. Very deep convolutional networks for large-scale image recognition. *arXiv preprint arXiv:1409.1556*, 2014.

[131] C. Szegedy, W. Liu, Y. Jia, P. Sermanet, S. Reed, D. Anguelov, D. Erhan, V. Vanhoucke, and A. Rabinovich. Going deeper with convolutions. In *Proceedings of the IEEE conference on computer vision and pattern recognition*, pages 1–9, 2015.

[132] K. He, X. Zhang, S. Ren, and J. Sun. Deep residual learning for image recognition. In *Proceedings of the IEEE conference on computer vision and pattern recognition*, pages 770–778, 2016.

[133] A. Oberai, B. Varghese, S. Cen, T. Angelini, D. Hwang, I. Gill, M. Aron, C. Lau, and V. Duddalwar. Deep learning based classification of solid lipid-poor contrast enhancing renal masses using contrast enhanced CT. *The British journal of radiology*, 93(1111):20200002, 2020.

[134] L. Zhou, Z. Zhang, Y.-C. Chen, Z.-Y. Zhao, X.-D. Yin, and H.-B. Jiang. A deep learning-based radiomics model for differentiating benign and malignant renal tumors. *Translational oncology*, 12(2):292–300, 2019.

[135] E.-M. Cui, F. Lin, Q. Li, R.-G. Li, X.-M. Chen, Z.-S. Liu, and W.-S. Long. Differentiation of renal angiomyolipoma without visible fat from renal cell carcinoma by machine learning based on whole-tumor computed tomography texture features. *Acta Radiologica*, 60(11):1543–1552, 2019.

[136] H. S. Lee, H. Hong, D. C. Jung, S. Park, and J. Kim. Differentiation of fat-poor angiomyolipoma from clear cell renal cell carcinoma in contrast-enhanced MDCT images using quantitative feature classification. *Medical physics*, 44(7):3604–3614, 2017.

[137] Z. Feng, P. Rong, P. Cao, Q. Zhou, W. Zhu, Z. Yan, Q. Liu, and W. Wang. Machine learning-based quantitative texture analysis of CT images of small renal masses: Differentiation of angiomyolipoma without visible fat from renal cell carcinoma. *European radiology*, 28(4):1625–1633, 2018.

[138] L. Yan, Z. Liu, G. Wang, Y. Huang, Y. Liu, Y. Yu, and C. Liang. Angiomyolipoma with minimal fat: differentiation from clear cell renal cell carcinoma and papillary renal cell carcinoma by texture analysis on CT images. *Academic Radiology*, 22(9):1115–1121, 2015.

[139] Y. Ma, F. Cao, X. Xu, and W. Ma. Can whole-tumor radiomics-based CT analysis better differentiate fat-poor angiomyolipoma from clear cell renal cell caricinoma: compared with conventional CT analysis? *Abdominal Radiology*, 45(8):2500–2507, 2020.

[140] Z. Tang, D. Yu, T. Ni, T. Zhao, Y. Jin, and E. Dong. Quantitative analysis of multiphase contrast-enhanced CT images: a pilot study of preoperative prediction of fat-poor angiomyolipoma and renal cell carcinoma. *American Journal of Roentgenology*, 214(2):370–382, 2020.

[141] N. Nassiri, M. Maas, G. Cacciamani, B. Varghese, D. Hwang, X. Lei, M. Aron, M. Desai, A. A. Oberai, S. Y. Cen, et al. A radiomic-based machine learning algorithm to reliably differentiate benign renal masses from renal cell carcinoma. *European Urology Focus*, 2021.

[142] F. Y. Yap, B. A. Varghese, S. Y. Cen, D. H. Hwang, X. Lei, B. Desai, C. Lau, L. L. Yang, A. J. Fullenkamp, S. Hajian, et al. Shape and texture-based radiomics signature on CT effectively discriminates benign from malignant renal masses. *European Radiology*, 31(2):1011–1021, 2021.

[143] H. Coy, K. Hsieh, W. Wu, M. B. Nagarajan, J. R. Young, M. L. Douek, M. S. Brown, F. Scalzo, and S. S. Raman. Deep learning and radiomics: the utility of google tensorflow™ inception in classifying clear cell renal cell carcinoma and oncocytoma on multiphasic CT. *Abdominal Radiology*, 44(6):2009–2020, 2019.

[144] N. Y. Kim, M. G. Lubner, J. T. Nystrom, J. F. Swietlik, E. J. Abel, T. C. Havighurst, S. G. Silverman, J. P. McGahan, and P. J. Pickhardt. Utility of CT texture analysis

in differentiating low-attenuation renal cell carcinoma from cysts: a bi-institutional retrospective study. *American Journal of Roentgenology*, 213(6):1259–1266, 2019.

[145] T. Tanaka, Y. Huang, Y. Marukawa, Y. Tsuboi, Y. Masaoka, K. Kojima, T. Iguchi, T. Hiraki, H. Gobara, H. Yanai, et al. Differentiation of small (4 cm) renal masses on multiphase contrast-enhanced CT by deep learning. *American journal of roentgenology*, 214(3):605–612, 2020.

[146] Y. Li, X. Huang, Y. Xia, and L. Long. Value of radiomics in differential diagnosis of chromophobe renal cell carcinoma and renal oncocytoma. *Abdominal Radiology*, 45(10):3193–3201, 2020.

[147] X. Li, Q. Ma, C. Tao, J. Liu, P. Nie, and C. Dong. A CT-based radiomics nomogram for differentiation of small masses (¡ 4 cm) of renal oncocytoma from clear cell renal cell carcinoma. *Abdominal Radiology*, 46(11):5240–5249, 2021.

[148] X. Li, Q. Ma, P. Nie, Y. Zheng, C. Dong, and W. Xu. A CT-based radiomics nomogram for differentiation of renal oncocytoma and chromophobe renal cell carcinoma with a central scar-matched study. *The British Journal of Radiology*, 95(1129):20210534, 2022.

[149] F. Zabihollahy, N. Schieda, S. Krishna, and E. Ukwatta. Automated classification of solid renal masses on contrast-enhanced computed tomography images using convolutional neural network with decision fusion. *European Radiology*, 30(9):5183–5190, 2020.

[150] H. Yu, J. Scalera, M. Khalid, A.-S. Touret, N. Bloch, B. Li, M. M. Qureshi, J. A. Soto, and S. W. Anderson. Texture analysis as a radiomic marker for differentiating renal tumors. *Abdominal Radiology*, 42(10):2470–2478, 2017.

[151] B. A. Varghese, F. Chen, D. H. Hwang, S. Y. Cen, B. Desai, I. S. Gill, and V. A. Duddalwar. Differentiation of predominantly solid enhancing lipid-poor renal cell masses by use of contrast-enhanced CT: evaluating the role of texture in tumor subtyping. *American Journal of Roentgenology*, 211(6):W288–W296, 2018.

[152] J. Uhlig, A. Leha, L. M. Delonge, A.-M. Haack, B. Shuch, H. S. Kim, F. Bremmer, L. Trojan, J. Lotz, and A. Uhlig. Radiomic features and machine learning for the discrimination of renal tumor histological subtypes: a pragmatic study using clinical-routine computed tomography. *Cancers*, 12(10):3010, 2020.

[153] M. Chen, F. Yin, Y. Yu, H. Zhang, and G. Wen. CT-based multi-phase radiomic models for differentiating clear cell renal cell carcinoma. *Cancer Imaging*, 21(1):1–13, 2021.

[154] J. Ding, Z. Xing, Z. Jiang, J. Chen, L. Pan, J. Qiu, and W. Xing. CT-based radiomic model predicts high grade of clear cell renal cell carcinoma. *European journal of radiology*, 103:51–56, 2018.

[155] R.-H. Yin, Y.-C. Yang, X.-Q. Tang, H.-F. Shi, S.-F. Duan, and C.-J. Pan. Enhanced computed tomography radiomics-based machine-learning methods for predicting the fuhrman grades of renal clear cell carcinoma. *Journal of X-ray Science and Technology*, (Preprint):1–12, 2021.

[156] C. T. Bektas, B. Kocak, A. H. Yardimci, M. H. Turkcanoglu, U. Yucetas, S. B. Koca, C. Erdim, and O. Kilickesmez. Clear cell renal cell carcinoma: machine learning-based quantitative computed tomography texture analysis for prediction of fuhrman nuclear grade. *European radiology*, 29(3):1153–1163, 2019.

[157] F. Lin, E.-M. Cui, Y. Lei, and L.-p. Luo. CT-based machine learning model to predict the fuhrman nuclear grade of clear cell renal cell carcinoma. *Abdominal Radiology*, 44(7):2528–2534, 2019.

[158] S. Haji-Momenian, Z. Lin, B. Patel, N. Law, A. Michalak, A. Nayak, J. Earls, and M. Loew. Texture analysis and machine learning algorithms accurately predict histologic grade in small (¡ 4 cm) clear cell renal cell carcinomas: a pilot study. *Abdominal Radiology*, 45(3):789–798, 2020.

[159] S. Lai, L. Sun, J. Wu, R. Wei, S. Luo, W. Ding, X. Liu, R. Yang, and X. Zhen. Multiphase contrast-enhanced CT-based machine learning models to predict the fuhrman nuclear grade of clear cell renal cell carcinoma. *Cancer Management and Research*, 13:999, 2021.

[160] S. Luo, R. Wei, S. Lu, S. Lai, J. Wu, Z. Wu, X. Pang, X. Wei, X. Jiang, X. Zhen, et al. Fuhrman nuclear grade prediction of clear cell renal cell carcinoma: influence of volume of interest delineation strategies on machine learning-based dynamic enhanced CT radiomics analysis. *European Radiology*, 32(4):2340–2350, 2022.

[161] X. Yi, Q. Xiao, F. Zeng, H. Yin, Z. Li, C. Qian, C. Wang, G. Lei, Q. Xu, C. Li, et al. Computed tomography radiomics for predicting pathological grade of renal cell carcinoma. *Frontiers in oncology*, 10:570396, 2021.

[162] X. He, Y. Wei, H. Zhang, T. Zhang, F. Yuan, Z. Huang, F. Han, and B. Song. Grading of clear cell renal cell carcinomas by using machine learning based on artificial neural networks and radiomic signatures extracted from multidetector computed tomography images. *Academic Radiology*, 27(2):157–168, 2020.

[163] L. Xu, C. Yang, F. Zhang, X. Cheng, Y. Wei, S. Fan, M. Liu, X. He, J. Deng, T. Xie, et al. Deep learning using CT images to grade clear cell renal cell carcinoma: Development and validation of a prediction model. *Cancers*, 14(11):2574, 2022.

[164] P. Nie, G. Yang, Z. Wang, L. Yan, W. Miao, D. Hao, J. Wu, Y. Zhao, A. Gong, J. Cui, et al. A CT-based radiomics nomogram for differentiation of renal angiomyolipoma without visible fat from homogeneous clear cell renal cell carcinoma. *European radiology*, 30(2):1274–1284, 2020.

[165] Y. Ma, X. Xu, P. Pang, and Y. Wen. A CT-based tumoral and mini-peritumoral radiomics approach: Differentiate fat-poor angiomyolipoma from clear cell renal cell carcinoma. *Cancer Management and Research*, 13:1417, 2021.

[166] K.-H. Uhm, S.-W. Jung, M. H. Choi, H.-K. Shin, J.-I. Yoo, S. W. Oh, J. Y. Kim, H. G. Kim, Y. J. Lee, S. Y. Youn, et al. Deep learning for end-to-end kidney cancer diagnosis on multi-phase abdominal computed tomography. *NPJ Precision Oncology*, 5(1):1–6, 2021.

[167] J. Shu, D. Wen, Y. Xi, Y. Xia, Z. Cai, W. Xu, X. Meng, B. Liu, and H. Yin. Clear cell renal cell carcinoma: Machine learning-based computed tomography radiomics analysis for the prediction of WHO/ISUP grade. *European journal of radiology*, 121:108738, 2019.

[168] X. Sun, L. Liu, K. Xu, W. Li, Z. Huo, H. Liu, T. Shen, F. Pan, Y. Jiang, and M. Zhang. Prediction of ISUP grading of clear cell renal cell carcinoma using support vector machine model based on CT images. *Medicine*, 98(14), 2019.

[169] M. Nikpanah, Z. Xu, D. Jin, F. Farhadi, B. Saboury, M. W. Ball, R. Gautam, M. J. Merino, B. J. Wood, B. Turkbey, et al. A deep-learning based artificial intelligence (AI) approach for differentiation of clear cell renal cell carcinoma from oncocytoma on multi-phasic MRI. *Clinical Imaging*, 77:291–298, 2021.

[170] Y. Arita, S. Yoshida, T. C. Kwee, H. Akita, S. Okuda, Y. Iwaita, K. Mukai, S. Matsumoto, R. Ueda, R. Ishii, et al. Diagnostic value of texture analysis of apparent diffusion coefficient maps for differentiating fat-poor angiomyolipoma from non-clear-cell renal cell carcinoma. *European Journal of Radiology*, 143:109895, 2021.

[171] N. Gündüz, M. Eser, A. Yıldırım, and A. Kabaalioğlu. Radiomics improves the utility of ADC for differentiation between renal oncocytoma and chromophobe renal cell carcinoma: Preliminary findings. *Actas Urológicas Españolas (English Edition)*, 46(3):167–177, 2022.

[172] J. W. Choi, R. Hu, Y. Zhao, S. Purkayastha, J. Wu, A. J. McGirr, S. W. Stavropoulos, A. C. Silva, M. C. Soulen, M. B. Palmer, et al. Preoperative prediction of the stage, size, grade, and necrosis score in clear cell renal cell carcinoma using MRI-based radiomics. *Abdominal Radiology*, 46(6):2656–2664, 2021.

[173] U. N. Hoang, A. A. Malayeri, N. S. Lay, R. M. Summers, and J. Yao. Texture analysis of common renal masses in multiple mr sequences for prediction of pathology. In *Medical Imaging 2017: Computer-Aided Diagnosis*, volume 10134, pages 917–929. SPIE, 2017.

[174] A. Shaffie, A. Soliman, M. Ghazal, F. Taher, N. Dunlap, B. Wang, A. Elmaghraby, G. Gimel'farb, and A. El-Baz. A new framework for incorporating appearance and shape features of lung nodules for precise diagnosis of lung cancer. In *Image Processing (ICIP), 2017 IEEE International Conference on*, pages 1372–1376. IEEE, 2017.

[175] M. J. Nitzken. *Shape analysis of the human brain*. PhD thesis, University of Louisville, 2015.

[176] L. Moya, H. Zakeri, F. Yamazaki, W. Liu, E. Mas, and S. Koshimura. 3d gray level co-occurrence matrix and its application to identifying collapsed buildings. *ISPRS journal of photogrammetry and remote sensing*, 149:14–28, 2019.

[177] R. C. Gonzales and R. E. Woods. Digital image processing, 2002.

[178] A. S. Kurani, D.-H. Xu, J. Furst, and D. S. Raicu. Co-occurrence matrices for volumetric data. *Heart*, 27:25, 2004.

[179] N. Tustison and J. Gee. Run-length matrices for texture analysis. *Insight J*, 1:1–6, 2008.

[180] B. Barry, K. Buch, J. A. Soto, H. Jara, A. Nakhmani, and S. W. Anderson. Quantifying liver fibrosis through the application of texture analysis to diffusion weighted imaging. *Magnetic resonance imaging*, 32(1):84–90, 2014.

[181] G. Castellano, L. Bonilha, L. Li, and F. Cendes. Texture analysis of medical images. *Clinical radiology*, 59(12):1061–1069, 2004.

[182] S. W. Anderson, H. Jara, A. Ozonoff, M. O'Brien, J. A. Hamilton, and J. A. Soto. Effect of disease progression on liver apparent diffusion coefficient and t2 values in a murine model of hepatic fibrosis at 11.7 tesla MRI. *Journal of Magnetic Resonance Imaging*, 35(1):140–146, 2012.

[183] J. J. Van Griethuysen, A. Fedorov, C. Parmar, A. Hosny, N. Aucoin, V. Narayan, R. G. Beets-Tan, J.-C. Fillion-Robin, S. Pieper, and H. J. Aerts. Computational radiomics system to decode the radiographic phenotype. *Cancer research*, 77(21):e104–e107, 2017.

[184] R. M. Haralick. Statistical and structural approaches to texture. *Proceedings of the IEEE*, 67(5):786–804, 1979.

[185] J. K. Kim, S.-Y. Park, J.-H. Shon, and K.-S. Cho. Angiomyolipoma with minimal fat: differentiation from renal cell carcinoma at biphasic helical ct. *Radiology*, 230(3):677–684, 2004.

[186] X.-D. Ye, J.-D. Ye, Z. Yuan, S. Dong, and X.-S. Xiao. Characterization of solitary pulmonary nodules: Use of washout characteristics at contrast-enhanced computed tomography. *Oncology letters*, 3(3):672–676, 2012.

[187] P. Xie, Z. Yang, and Z. Yuan. Lipid-poor renal angiomyolipoma: Differentiation from clear cell renal cell carcinoma using wash-in and washout characteristics on contrast-enhanced computed tomography. *Oncology letters*, 11(3):2327–2331, 2016.

131

[188] L. R. Dice. Measures of the amount of ecologic association between species. *Ecology*, 26(3):297–302, 1945.

[189] A. Carass, S. Roy, A. Gherman, J. C. Reinhold, A. Jesson, T. Arbel, O. Maier, H. Handels, M. Ghafoorian, B. Platel, et al. evaluating white matter lesion segmentations with refined sørensen-dice analysis. *Scientific Reports*, 10(1):1–19, 2020.

[190] I. Reda, M. Ghazal, A. Shalaby, M. Elmogy, A. AbouEl-Fetouh, B. O. Ayinde, M. AbouEl-Ghar, A. Elmaghraby, R. Keynton, and A. El-Baz. A novel adcs-based cnn classification system for precise diagnosis of prostate cancer. In *2018 24th International Conference on Pattern Recognition (ICPR)*, pages 3923–3928. IEEE, 2018.

[191] I. Reda, A. Khalil, M. Elmogy, A. Abou El-Fetouh, A. Shalaby, M. Abou El-Ghar, A. Elmaghraby, M. Ghazal, and A. El-Baz. Deep learning role in early diagnosis of prostate cancer. *Technology in cancer research & treatment*, 17:1533034618775530, 2018.

[192] I. Reda, B. O. Ayinde, M. Elmogy, A. Shalaby, M. El-Melegy, M. A. El-Ghar, A. A. El-fetouh, M. Ghazal, and A. El-Baz. A new cnn-based system for early diagnosis of prostate cancer. In *2018 IEEE 15th International Symposium on Biomedical Imaging (ISBI 2018)*, pages 207–210. IEEE, 2018.

[193] S. M. Ayyad, M. A. Badawy, M. Shehata, A. Alksas, A. Mahmoud, M. Abou El-Ghar, M. Ghazal, M. El-Melegy, N. B. Abdel-Hamid, L. M. Labib, H. A. Ali, and A. El-Baz. A new framework for precise identification of prostatic adenocarcinoma. *Sensors*, 22(5), 2022.

[194] K. Hammouda, F. Khalifa, M. El-Melegy, M. Ghazal, H. E. Darwish, M. A. El-Ghar, and A. El-Baz. A deep learning pipeline for grade groups classification using digitized prostate biopsy specimens. *Sensors*, 21(20):6708, 2021.

[195] I. Reda, A. Shalaby, M. Abou El-Ghar, F. Khalifa, M. Elmogy, A. Aboulfotouh, E. Hosseini-Asl, A. El-Baz, and R. Keynton. A new NMF-autoencoder based CAD system for early diagnosis of prostate cancer. In *Proceedings of IEEE 13th International Symposium on Biomedical Imaging (ISBI'16)*, pages 1237–1240. IEEE, 2016.

[196] M. Abou El-Ghar, A. El-Baz, F. Khalifa, A. Elnakib, A. Firjani, and T. El-Diasty. Non-invasive image-based approach for early diagnosis of prostate cancer. In *Proceedings of 18th Symposium of the European Society of Urogenital Radiology, (ESUR'11)*, Dubrovnik, Croatia, October 13–16, 2011.

[197] A. Firjani, A. Elmaghraby, and A. El-Baz. MRI-based diagnostic system for early detection of prostate cancer. In *Biomedical Sciences and Engineering Conference (BSEC), 2013*, pages 1–4, 2013.

[198] A. Firjani, A. Elnakib, F. Khalifa, A. El-Baz, G. Gimel'farb, M. Abou El-Ghar, and A. Elmaghraby. A novel 3D segmentation approach for segmenting the prostate from dynamic contrast enhanced MRI using current appearance and learned shape prior. In *Proceedings of IEEE International Symposium on Signal Processing and Information Technology, (ISSPIT'10)*, pages 137–143, Luxor, Egypt, December 15–18, 2010.

[199] A. Firjani, A. Elnakib, F. Khalifa, G. Gimel'farb, M. A. El-Ghar, A. Elmaghraby, and A. El-Baz. A new 3D automatic segmentation framework for accurate extraction of prostate from diffusion imaging. In *Proceedings of Biomedical Science and Engineering Conference–Image Informatics and Analytics in Biomedicine, (BSEC'11)*, pages 1306–1309, 2011.

[200] A. Firjani, A. Elnakib, F. Khalifa, G. Gimel'farb, M. A. El-Ghar, J. Suri, A. Elmaghraby, and A. El-Baz. A new 3D automatic segmentation framework for accurate extraction of prostate from DCE-MRI. In *Proceedings of IEEE International Symposium on Biomedical Imaging: From Nano to Macro, (ISBI'11)*, pages 1476–1479, Chicago, Illinois, March 30–April 2, 2011.

[201] A. Firjani, A. Elnakib, F. Khalifa, G. Gimelâ€™farb, M. Abou El-Ghar, A. Elmaghraby, and A. El-Baz. A diffusion-weighted imaging based diagnostic system for early detection of prostate cancer. *Journal of Biomedical Science and Engineering*, 6(3A):346–356, 2013.

[202] A. Firjani, F. Khalifa, A. Elnakib, G. Gimel'farb, M. A. El-Ghar, A. Elmaghraby, and A. El-Baz. Non-invasive image-based approach for early detection of prostate cancer. In *Proceedings of Fourth International Conference on Developments in eSystems Engineering, (DeSE'11)*, pages 172–177, Dubai, UAE, December 6–8, 2011.

[203] A. Firjani, F. Khalifa, A. Elnakib, G. Gimel'farb, M. A. El-Ghar, A. Elmaghraby, and A. El-Baz. 3D automatic approach for precise segmentation of the prostate from diffusion-weighted magnetic resonance imaging. In *Proceedings of IEEE International Conference on Image Processing, (ICIP'11)*, pages 2285–2288, Brussels, Belgium, September 11–14, 2011.

[204] A. Firjani, F. Khalifa, A. Elnakib, G. Gimel'farb, M. Abou El-Ghar, A. Elmaghraby, and A. El-Baz. A novel image-based approach for early detection of prostate cancer using DCE-MRI. In K. Suzuki, editor, *Computational Intelligence in Biomedical Imaging*, pages 55–82. Springer New York, 2014.

[205] A. Firjani, F. Khalifa, A. Elnakib, G. Gimel'farb, A. Elmaghraby, and A. El-Baz. A novel image-based approach for early detection of prostate cancer. In *Proceedings of IEEE International Conference on Image Processing, (ICIP'12)*, pages 2849–2852, Lake Buena Vista, Florida, September 30–October 3, 2012.

133

[206] A. Firjany, A. Elnakib, A. El-Baz, G. Gimel'farb, M. Abou El-Ghar, and A. El-magharby. Novel stochastic framework for accurate segmentation of prostate in dynamic contrast enhanced MRI. In A. Madabhushi, J. Dowling, P. Yan, A. Fenster, P. Abolmaesumi, and N. Hata, editors, *Prostate Cancer Imaging. Computer-Aided Diagnosis, Prognosis, and Intervention*, volume 6367 of *Lecture Notes in Computer Science*, pages 121–130. Springer Berlin Heidelberg, 2010.

[207] A. Firjany, A. Elnakib, A. El-Baz, G. Gimelâ€™farb, M. Abou El-Ghar, and A. El-magharby. Novel stochastic framework for accurate segemntation of prostate in dynamic contrast-enhanced MRI. In *Proceedings of the International Wokshop on Prostate Cancer Imaging: Computer-Aided Diagnosis, Prognosis, and Intervention*, pages 121–130, Beijing, China, Sptember 24, 2010.

[208] P. McClure, F. Khalifa, A. Soliman, M. Abou El-Ghar, G. Gimelfarb, A. Elmagraby, and A. El-Baz. A novel nmf guided level-set for dwi prostate segmentation. *Journal of Computer Science and Systems Biology*, 7:209–216, 2014.

[209] R. Alkadi, F. Taher, A. El-Baz, and N. Werghi. A deep learning-based approach for the detection and localization of prostate cancer in t2 magnetic resonance images. *Journal of digital imaging*, 32(5):793–807, 2019.

[210] S. M. Ayyad, M. Shehata, A. Shalaby, M. Abou El-Ghar, M. Ghazal, M. El-Melegy, N. B. Abdel-Hamid, L. M. Labib, H. A. Ali, and A. El-Baz. Role of ai and histopathological images in detecting prostate cancer: a survey. *Sensors*, 21(8):2586, 2021.

[211] R. Alkadi, F. Taher, A. El-Baz, and N. Werghi. Early diagnosis and staging of prostate cancer using magnetic resonance imaging: State of the art and perspectives. *Prostate Cancer Imaging*, pages 165–188, 2018.

[212] F. Khalifa, A. Shalaby, M. Abou El-Ghar, J. S. Suri, and A. El-Baz. A dce-mri-based noninvasive cad system for prostate cancer diagnosis. In *Prostate Cancer Imaging*, pages 189–217. CRC Press, 2018.

[213] I. Reda, A. Shalaby, M. Elmogy, A. Aboulfotouh, M. Abou El-Ghar, A. El-magharaby, and A. El-Baz. Diagnosing prostate cancer based on deep learning with a stacked nonnegativity constraint autoencoder. In *Prostate Cancer Imaging*, pages 325–347. CRC Press, 2018.

[214] I. Reda, P. McClure, A. Shalaby, M. Elmogy, A. Aboulfotouh, M. Abou El-Ghar, M. El-Melegy, J. S. Suri, and A. El-Baz. Prostate segmentation from dw-mri using level-set guided by nonnegative matrix factorization. In *Prostate Cancer Imaging*, pages 219–241. CRC Press, 2018.

[215] I. Reda, M. Elmogy, A. Aboulfotouh, M. Ismail, A. El-Baz, and R. Keynton. Prostate segmentation using deformable model-based methods. *Biomedical Image Segmentation: Advances and Trends*, page 293, 2016.

[216] A. Firjani, F. Khalifa, A. Elnakib, G. Gimelâ€™farb, M. A. El-Ghar, A. El-maghraby, and A. El-Baz. A novel image-based approach for early detection of prostate cancer using dce-mri. In *Computational intelligence in biomedical imaging*, pages 55–82. Springer, 2014.

[217] M. Shehata, A. Shalaby, A. E. Switala, M. El-Baz, M. Ghazal, L. Fraiwan, A. Khalil, M. A. El-Ghar, M. Badawy, A. M. Bakr, et al. A multimodal computer-aided diagnostic system for precise identification of renal allograft rejection: Preliminary results. *Medical physics*, 47(6):2427–2440, 2020.

[218] M. Shehata, F. Khalifa, A. Soliman, M. Ghazal, F. Taher, M. Abou El-Ghar, A. C. Dwyer, G. Gimel'farb, R. S. Keynton, and A. El-Baz. Computer-aided diagnostic system for early detection of acute renal transplant rejection using diffusion-weighted MRI. *IEEE Transactions on Biomedical Engineering*, 66(2):539–552, 2018.

[219] E. Hollis, M. Shehata, M. Abou El-Ghar, M. Ghazal, T. El-Diasty, M. Merchant, A. E. Switala, and A. El-Baz. Statistical analysis of adcs and clinical biomarkers in detecting acute renal transplant rejection. *The British journal of radiology*, 90(1080):20170125, 2017.

[220] M. Shehata, A. Alksas, R. T. Abouelkheir, A. Elmahdy, A. Shaffie, A. Soliman, M. Ghazal, H. Abu Khalifeh, R. Salim, A. A. K. Abdel Razek, et al. A comprehensive computer-assisted diagnosis system for early assessment of renal cancer tumors. *Sensors*, 21(14):4928, 2021.

[221] F. Khalifa, M. A. El-Ghar, B. Abdollahi, H. Frieboes, T. El-Diasty, and A. El-Baz. A comprehensive non-invasive framework for automated evaluation of acute renal transplant rejection using DCE-MRI. *NMR in Biomedicine*, 26(11):1460–1470, 2013.

[222] F. Khalifa, A. Elnakib, G. M. Beache, G. Gimel'farb, M. A. El-Ghar, G. Sokhadze, S. Manning, P. McClure, and A. El-Baz. 3D kidney segmentation from CT images using a level set approach guided by a novel stochastic speed function. In *Proceedings of International Conference Medical Image Computing and Computer-Assisted Intervention, (MICCAI'11)*, pages 587–594, Toronto, Canada, September 18–22, 2011.

[223] M. Shehata, F. Khalifa, E. Hollis, A. Soliman, E. Hosseini-Asl, M. A. El-Ghar, M. El-Baz, A. C. Dwyer, A. El-Baz, and R. Keynton. A new non-invasive approach for early classification of renal rejection types using diffusion-weighted MRI. In *IEEE International Conference on Image Processing (ICIP), 2016*, pages 136–140. IEEE, 2016.

[224] F. Khalifa, A. Soliman, A. Takieldeen, M. Shehata, M. Mostapha, A. Shaffie, R. Ouseph, A. Elmaghraby, and A. El-Baz. Kidney segmentation from CT images using a 3D NMF-guided active contour model. In *IEEE 13th International Symposium on Biomedical Imaging (ISBI), 2016*, pages 432–435. IEEE, 2016.

[225] M. Shehata, F. Khalifa, A. Soliman, A. Takieldeen, M. A. El-Ghar, A. Shaffie, A. C. Dwyer, R. Ouseph, A. El-Baz, and R. Keynton. 3d diffusion MRI-based CAD system for early diagnosis of acute renal rejection. In *Biomedical Imaging (ISBI), 2016 IEEE 13th International Symposium on*, pages 1177–1180. IEEE, 2016.

[226] M. Shehata, F. Khalifa, A. Soliman, R. Alrefai, M. Abou El-Ghar, A. C. Dwyer, R. Ouseph, and A. El-Baz. A novel framework for automatic segmentation of kidney from DW-MRI. In *2015 IEEE 12th International Symposium on Biomedical Imaging (ISBI)*, pages 951–954. IEEE, 2015.

[227] M. Shehata, F. Khalifa, A. Soliman, R. Alrefai, M. A. El-Ghar, A. C. Dwyer, R. Ouseph, and A. El-Baz. A level set-based framework for 3d kidney segmentation from diffusion mr images. In *IEEE International Conference on Image Processing (ICIP), 2015*, pages 4441–4445. IEEE, 2015.

[228] M. Shehata, F. Khalifa, A. Soliman, M. A. El-Ghar, A. C. Dwyer, G. Gimel'farb, R. Keynton, and A. El-Baz. A promising non-invasive cad system for kidney function assessment. In *International Conference on Medical Image Computing and Computer-Assisted Intervention*, pages 613–621. Springer, 2016.

[229] F. Khalifa, A. Soliman, A. Elmaghraby, G. Gimel'farb, and A. El-Baz. 3d kidney segmentation from abdominal images using spatial-appearance models. *Computational and mathematical methods in medicine*, 2017:1–10, 2017.

[230] M. Shehata, F. Khalifa, A. Soliman, M. A. El-Ghar, A. C. Dwyer, and A. El-Baz. Assessment of renal transplant using image and clinical-based biomarkers. In *Proceedings of 13th Annual Scientific Meeting of American Society for Diagnostics and Interventional Nephrology (ASDIN'17), New Orleans, LA, USA, February 10-12, 2017*, 2017.

[231] F. Khalifa, M. Shehata, A. Soliman, M. Abou El-Ghar, T. El-Diasty, A. C. Dwyer, M. El-Melegy, G. Gimel'farb, R. Keynton, and A. El-Baz. A generalized MRI-based CAD system for functional assessment of renal transplant. In *2017 IEEE 14th International Symposium on Biomedical Imaging (ISBI 2017)*, pages 758–761. IEEE, 2017.

[232] M. Shehata, M. Ghazal, G. Beache, M. Abou EI-Ghar, A. Dwyer, H. Hajjdiab, A. Khalil, and E.-B. Ayman. Role of integrating diffusion MR image-markers with clinical-biomarkers for early assessment of renal transplants. In *2018 25th IEEE International Conference on Image Processing (ICIP)*, pages 146–150. IEEE, 2018.

[233] H. Abdeltawab, M. Shehatal, A. Shalaby, S. Mesbah, M. El-Baz, M. Ghazal, Y. AlKhali, M. AbouEl-Ghar, A. C. Dwyer, M. El-Melegy, et al. A new 3D CNN-based CAD system for early detection of acute renal transplant rejection. In *2018 24th International Conference on Pattern Recognition (ICPR)*, pages 3898–3903. IEEE Computer Society, 2018.

[234] M. Shehata, M. Ghazal, F. Khalifa, M. Abou El-Ghar, A. Khalil, A. C. Dwyer, A. El-giziri, M. El-Melegy, and A. El-Baz. A novel CAD system for detecting acute rejection of renal allografts based on integrating imaging-markers and laboratory biomarkers. In *2018 IEEE International Conference on Imaging Systems and Techniques (IST)*, pages 1–6. IEEE, 2018.

[235] M. Shehata, F. Taher, M. Ghazal, A. Mahmoud, G. Beache, M. Abou El-Ghar, A. C. Dwyer, A. Elmaghraby, and A. El-Baz. Early assessment of acute renal rejection post-transplantation: a combined imaging and clinical biomarkers protocol. In *2018 IEEE International Symposium on Signal Processing and Information Technology (ISSPIT)*, pages 297–302. IEEE, 2018.

[236] M. Shehata, F. Khalifa, A. Soliman, M. A. El-Ghar, A. C. Dwyer, and A. El-Baz. Early assessment of acute renal rejection. In *Proceedings of 12th Annual Scientific Meeting of American Society for Diagnostics and Interventional Nephrology (ASDIN'16), Pheonix, AZ, USA, February 19-21, 2016*, 2016.

[237] H. Abdeltawab, M. Shehata, A. Shalaby, F. Khalifa, A. Mahmoud, M. A. El-Ghar, A. C. Dwyer, M. Ghazal, H. Hajjdiab, R. Keynton, et al. A novel cnn-based cad system for early assessment of transplanted kidney dysfunction. *Scientific reports*, 9(1):5948, 2019.

[238] H. A. Abdeltawab, F. A. Khalifa, M. A. Ghazal, L. Cheng, A. S. El-Baz, and D. D. Gondim. A deep learning framework for automated classification of histopathological kidney whole-slide images. *Journal of Pathology Informatics*, 13:100093, 2022.

[239] M. Shehata, A. Shalaby, M. Ghazal, M. Abou El-Ghar, M. Badawy, G. Beache, A. Dwyer, M. El-Melegy, G. Giridharan, R. Keynton, et al. Early assessment of renal transplants using BOLD-MRI: Promising results. In *2019 IEEE International Conference on Image Processing (ICIP)*, pages 1395–1399. IEEE, 2019.

[240] M. Shehata, F. Khalifa, A. Soliman, A. T. Eldeen, M. Abou El-Ghar, T. El-Diasty, A. El-Baz, and R. Keynton. An appearance-guided deformable model for 4D kidney segmentation using diffusion MRI. In *Biomedical Image Segmentation*, pages 291–312. CRC Press, 2016.

[241] M. Mostapha, F. Khalifa, A. Alansary, A. Soliman, J. Suri, and A. S. El-Baz. Computer-aided diagnosis systems for acute renal transplant rejection: Challenges and methodologies. In *Abdomen and Thoracic Imaging*, pages 1–35. Springer, 2014.

[242] M. Shehata, M. Ghazal, H. A. Khalifeh, A. Khalil, A. Shalaby, A. C. Dwyer, A. M. Bakr, R. Keynton, and A. El-Baz. A deep learning-based cad system for renal allograft assessment: Diffusion, bold, and clinical biomarkers. In *2020 IEEE International Conference on Image Processing (ICIP)*, pages 355–359. IEEE, 2020.

[243] M. Shehata, A. Alksas, R. T. Abouelkheir, A. Elmahdy, A. Shaffie, A. Soliman, M. Ghazal, H. A. Khalifeh, A. A. Razek, and A. El-Baz. A new computer-aided diagnostic (CAD) system for precise identification of renal tumors. In *2021 IEEE 18th International Symposium on Biomedical Imaging (ISBI)*, pages 1378–1381. IEEE, 2021.

[244] M. Shehata, H. Abdeltawab, M. Ghazal, A. Khalil, S. Shaker, A. Shalaby, A. Mahmoud, M. Abou El-Ghar, A. C. Dwyer, M. El-Melegy, et al. Accurate identification of renal transplant rejection: convolutional neural networks and diffusion MRI. In *State of the Art in Neural Networks and their Applications*, pages 91–115. Elsevier, 2021.

[245] M. Shehata, F. Taher, M. Ghazal, S. Shaker, M. Abou El-Ghar, M. Badawy, A. Shalaby, M. El-Baz, A. Mahmoud, A. C. Dwyer, et al. Early identification of acute rejection for renal allografts: a machine learning approach. In *State of the Art in Neural Networks and their Applications*, pages 197–218. Elsevier, 2021.

[246] M. Shehata, F. Khalifa, A. Soliman, S. Shaker, A. Shalaby, M. El-Baz, A. Mahmoud, A. C. Dwyer, M. Abou El-Ghar, M. Ghazal, et al. Early classification of renal rejection types: A deep learning approach. In *Machine Learning in Medicine*, pages 257–280. Chapman and Hall/CRC, 2021.

[247] M. Shehata, A. Shalaby, A. Mahmoud, M. Ghazal, H. Hajjdiab, M. A. Badawy, M. Abou El-Ghar, A. M. Bakr, A. C. Dwyer, R. Keynton, et al. Towards big data in acute renal rejection, 2019.

[248] M. Mostapha, F. Khalifa, A. Alansary, A. Soliman, J. Suri, and A. S. El-Baz. Computer-aided diagnosis systems for acute renal transplant rejection: Challenges and methodologies. In *Abdomen and Thoracic Imaging*, pages 1–35. Springer, 2014.

[249] A. S. El-Baz, A. Dwyer, R. Ouseph, F. Khalifa, A. Soliman, and M. Shehata. Computer aided diagnostic system for classifying kidneys, March 27 2018. US Patent 9,928,347.

[250] A. S. El-Baz, A. Dwyer, R. Ouseph, F. Khalifa, A. Soliman, and M. Shehata. Computer aided diagnostic system for classifying kidneys, October 22 2019. US Patent 10,453,569.

[251] A. S. El-Baz, A. Dwyer, A. Soliman, M. Shehata, H. Abdeltawab, and F. Khalifa. Computer aided diagnosis system for classifying kidneys, February 1 2022. US Patent 11,238,975.

[252] A. El-Baz, A. A. Farag, S. E. Yuksel, M. E. El-Ghar, T. A. Eldiasty, and M. A. Ghoneim. Application of deformable models for the detection of acute renal rejection. In *Deformable models*, pages 293–333. Springer, 2007.

138

[253] M. Shehata, M. Ghazal, A. Shalaby, M. Badawy, M. Abou El-Ghar, G. Beache, et al. A big data computer-aided diagnostic system for assessing renal allografts. In *Biomedical Engineering Society Annual Scientific Meeting (BMES19), Philadelphia, Pennsylvania, USA*, 2019.

[254] M. Shehata, M. Abou El-Ghar, T. Eldiasty, and A. El-Baz. An integrated cad system of dwi-mri and laboratory biomarkers in diagnosis of kidney transplant dysfunction. In *European Congress of Radiology (ECR 2018), Austria Center Vienna, Bruno-Kreisky-Platz*, volume 11220, 2018.

[255] M. Shehata, M. Abou El-Ghar, T. Eldiasty, and A. El-Baz. Integrating clinical with diffusion image markers as a noninvasive alternative to renal biopsy. In *European Congress of Radiology (ECR 2019), Austria Center Vienna, Bruno-Kreisky-Platz*, volume 11220, 2019.

[256] M. Shehata, E. Hollis, M. Abou El-Ghar, M. Ghazal, T. Eldiasty, M. Merchant, A. Switala, A. Dwyer, and A. El-Baz. Possible role of diffusion MRI in diagnosing acute renal rejection. In *Proceedings of 14th Annual Scientific Meeting of American Society for Diagnostics and Interventional Nephrology (ASDIN'18), Salt Lake City, UT, USA, February 16À18*, 2018.

[257] M. Shehata, M. Abou El-Ghar, T. Eldiasty, and A. El-Baz. Deep learning in classification of kidney transplant dysfunction: combined imaging and clinical biomarkers. In *European Symposium of Urogenital Radiology (ESUR 2018), Barcelona, Spain, September*, volume 13, page 16, 2018.

[258] M. N. M. I. Shehata. A non-invasive diagnostic system for early assessment of acute renal transplant rejection. 2016.

[259] A. Elnakib, G. M. Beache, G. Gimelâ€™farb, and A. El-Baz. Intramyocardial strain estimation from cardiac cine mri. *International journal of computer assisted radiology and surgery*, 10(8):1299–1312, 2015.

[260] G. Beache, F. Khalifa, G. Gimel'farb, and A. El-Baz. Fully automated framework for the analysis of myocardial first-pass perfusion MR images. *Medical Physics*, 41(10):1–18, 2014.

[261] A. Elnakib, G. M. Beache, G. Gimel'farb, and A. El-Baz. A new framework for automated segmentation of left ventricle wall from contrast enhanced cardiac magnetic resonance images. In *Proceeding of International Conference on Image Processing (ICIP'2011)*, pages 2289–2292. IEEE, 2011.

[262] A. Elnakib, G. Beache, G. G. T. Inanc, and A. El-Baz. Validating a new methodology for strain estimation from cardiac cine MRI. In *Proceedings of International Symposium on Computational Models for Life Science (CMLS'13)*, 2013.

[263] A. Elnakib, G. Beache, M. Nitzken, G. Gimel'farb, and A. El-Baz. A new framework for automated identification of pathological tissues in contrast enhanced cardiac magnetic resonance images. In *Proceedings of IEEE International Symposium on Biomedical Imaging: From Nano to Macro (ISBI'2011)*, pages 1272–1275. IEEE, 2011.

[264] A. Elnakib, G. Beache, H. Sliman, G. Gimel'farb, T. Inanc, and A. El-Baz. A novel Laplace-based method to estimate the strain from cine cardiac magnetic resonance images. In *Proceedings of IEEE International Conference on Image Processing (ICIP'2013)*. IEEE, 2013.

[265] K. Hammouda, F. Khalifa, H. Abdeltawab, A. Elnakib, G. Giridharan, M. Zhu, C. Ng, S. Dassanayaka, M. Kong, H. Darwish, et al. A new framework for performing cardiac strain analysis from cine MR imaging in mice. *Scientific reports*, 10(1):1–15, 2020.

[266] H. Abdeltawab, F. Khalifa, K. Hammouda, J. M. Miller, M. M. Meki, Q. Ou, A. El-Baz, and T. Mohamed. Artificial intelligence based framework to quantify the cardiomyocyte structural integrity in heart slices. *Cardiovascular Engineering and Technology*, pages 1–11, 2021.

[267] F. Khalifa, G. M. Beache, A. Elnakib, H. Sliman, G. Gimel'farb, K. C. Welch, and A. El-Baz. A new shape-based framework for the left ventricle wall segmentation from cardiac first-pass perfusion MRI. In *Proceedings of IEEE International Symposium on Biomedical Imaging: From Nano to Macro, (ISBI'13)*, pages 41–44, San Francisco, CA, April 7–11, 2013.

[268] F. Khalifa, G. M. Beache, A. Elnakib, H. Sliman, G. Gimel'farb, K. C. Welch, and A. El-Baz. A new nonrigid registration framework for improved visualization of transmural perfusion gradients on cardiac first–pass perfusion MRI. In *Proceedings of IEEE International Symposium on Biomedical Imaging: From Nano to Macro, (ISBI'12)*, pages 828–831, Barcelona, Spain, May 2–5, 2012.

[269] F. Khalifa, G. M. Beache, A. Firjani, K. C. Welch, G. Gimel'farb, and A. El-Baz. A new nonrigid registration approach for motion correction of cardiac first-pass perfusion MRI. In *Proceedings of IEEE International Conference on Image Processing, (ICIP'12)*, pages 1665–1668, Lake Buena Vista, Florida, September 30–October 3, 2012.

[270] F. Khalifa, G. M. Beache, G. Gimel'farb, and A. El-Baz. A novel CAD system for analyzing cardiac first-pass MR images. In *Proceedings of IAPR International Conference on Pattern Recognition (ICPR'12)*, pages 77–80, Tsukuba Science City, Japan, November 11–15, 2012.

[271] F. Khalifa, G. M. Beache, G. Gimel'farb, and A. El-Baz. A novel approach for accurate estimation of left ventricle global indexes from short-axis cine MRI. In *Proceedings of IEEE International Conference on Image Processing, (ICIP'11)*, pages 2645–2649, Brussels, Belgium, September 11–14, 2011.

[272] F. Khalifa, G. M. Beache, G. Gimel'farb, G. A. Giridharan, and A. El-Baz. A new image-based framework for analyzing cine images. In A. El-Baz, U. R. Acharya, M. Mirmedhdi, and J. S. Suri, editors, *Handbook of Multi Modality State-of-the-Art Medical Image Segmentation and Registration Methodologies*, volume 2, chapter 3, pages 69–98. Springer, New York, 2011.

[273] F. Khalifa, G. M. Beache, G. Gimel'farb, G. A. Giridharan, and A. El-Baz. Accurate automatic analysis of cardiac cine images. *IEEE Transactions on Biomedical Engineering*, 59(2):445–455, 2012.

[274] F. Khalifa, G. M. Beache, M. Nitzken, G. Gimel'farb, G. A. Giridharan, and A. El-Baz. Automatic analysis of left ventricle wall thickness using short-axis cine CMR images. In *Proceedings of IEEE International Symposium on Biomedical Imaging: From Nano to Macro, (ISBI'11)*, pages 1306–1309, Chicago, Illinois, March 30–April 2, 2011.

[275] M. Nitzken, G. Beache, A. Elnakib, F. Khalifa, G. Gimel'farb, and A. El-Baz. Accurate modeling of tagged cmr 3D image appearance characteristics to improve cardiac cycle strain estimation. In *Image Processing (ICIP), 2012 19th IEEE International Conference on*, pages 521–524, Orlando, Florida, USA, September 2012. IEEE.

[276] M. Nitzken, G. Beache, A. Elnakib, F. Khalifa, G. Gimel'farb, and A. El-Baz. Improving full-cardiac cycle strain estimation from tagged cmr by accurate modeling of 3D image appearance characteristics. In *Biomedical Imaging (ISBI), 2012 9th IEEE International Symposium on*, pages 462–465, Barcelona, Spain, May 2012. IEEE. (Selected for oral presentation).

[277] M. J. Nitzken, A. S. El-Baz, and G. M. Beache. Markov-gibbs random field model for improved full-cardiac cycle strain estimation from tagged cmr. *Journal of Cardiovascular Magnetic Resonance*, 14(1):1–2, 2012.

[278] H. Sliman, A. Elnakib, G. Beache, A. Elmaghraby, and A. El-Baz. Assessment of myocardial function from cine cardiac MRI using a novel 4D tracking approach. *J Comput Sci Syst Biol*, 7:169–173, 2014.

[279] H. Sliman, A. Elnakib, G. M. Beache, A. Soliman, F. Khalifa, G. Gimel'farb, A. Elmaghraby, and A. El-Baz. A novel 4D PDE-based approach for accurate assessment of myocardium function using cine cardiac magnetic resonance images. In *Proceedings of IEEE International Conference on Image Processing (ICIP'14)*, pages 3537–3541, Paris, France, October 27–30, 2014.

[280] H. Sliman, F. Khalifa, A. Elnakib, G. M. Beache, A. Elmaghraby, and A. El-Baz. A new segmentation-based tracking framework for extracting the left ventricle cavity from cine cardiac MRI. In *Proceedings of IEEE International Conference on Image Processing, (ICIP'13)*, pages 685–689, Melbourne, Australia, September 15–18, 2013.

[281] H. Sliman, F. Khalifa, A. Elnakib, A. Soliman, G. M. Beache, A. Elmaghraby, G. Gimel'farb, and A. El-Baz. Myocardial borders segmentation from cine MR images using bi-directional coupled parametric deformable models. *Medical Physics*, 40(9):1–13, 2013.

[282] H. Sliman, F. Khalifa, A. Elnakib, A. Soliman, G. M. Beache, G. Gimel'farb, A. Emam, A. Elmaghraby, and A. El-Baz. Accurate segmentation framework for the left ventricle wall from cardiac cine MRI. In *Proceedings of International Symposium on Computational Models for Life Science, (CMLS'13)*, volume 1559, pages 287–296, Sydney, Australia, November 27–29, 2013.

[283] H. Abdeltawab, F. Khalifa, F. Taher, M. Ghazal, A. H. Mahmoud, A. El-Baz, and J. S. Suri. Left ventricle segmentation for cine mr using deep learning. In *Diabetes and Cardiovascular Disease*, pages 37–57. Elsevier, 2021.

[284] A. Elnakib, M. Ghazal, F. Taher, A. H. Mahmoud, and A. El-Baz. Computational methods for identifying left ventricle heart pathologies. In *Diabetes and Cardiovascular Disease*, pages 59–93. Elsevier, 2021.

[285] Y. Gebru, G. Giridharan, M. Ghazal, A. Mahmoud, A. Shalaby, and A. El-Baz. Detection of cerebrovascular changes using magnetic resonance angiography. In *Cardiovascular Imaging and Image Analysis*, pages 1–22. CRC Press, 2018.

[286] A. El-Baz, A. Elnakib, F. Khalifa, M. Abou El-Ghar, P. McClure, A. Soliman, and G. Gimelrfarb. Precise segmentation of 3-d magnetic resonance angiography. *IEEE Transactions on Biomedical Engineering*, 59(7):2019–2029, 2012.

[287] A. Mahmoud, A. Shalaby, F. Taher, M. El-Baz, J. S. Suri, and A. El-Baz. Vascular tree segmentation from different image modalities. In *Cardiovascular Imaging and Image Analysis*, pages 43–70. CRC Press, 2018.

[288] A. Shalaby, A. Mahmoud, S. Mesbah, M. El-Baz, J. S. Suri, and A. El-Baz. Accurate unsupervised 3d segmentation of blood vessels using magnetic resonance angiography. In *Cardiovascular Imaging and Image Analysis*, pages 71–94. CRC Press, 2018.

[289] M. Ghazal, Y. Al Khalil, and A. El-Baz. An unsupervised parametric mixture model for automatic cerebrovascular segmentation. In *Cardiovascular Imaging and Image Analysis*, pages 95–108. CRC Press, 2018.

[290] S. Salahat, A. Soliman, H. Bhaskar, T. McGloughlin, A. El-Baz, and N. Werghi. Detection of calcification from abdominal aortic aneurysm. In *Cardiovascular Imaging and Image Analysis*, pages 173–196. CRC Press, 2018.

[291] Y. Wang, L. Liang, W. Wang, Z. Tan, P. Sethu, A. S. El-Baz, and G. A. Giridharan. Basis of artificial heart technologies. In *Artificial Hearts*, pages 31–52. Springer, 2020.

[292] R. R. Abouleisa, A. B. M. Salama, Q. Ou, X.-L. Tang, M. Solanki, Y. Guo, Y. Nong, L. McNally, P. K. Lorkiewicz, K. M. Kassem, et al. Transient cell cycle induction in cardiomyocytes to treat subacute ischemic heart failure. *Circulation*, 145(17):1339–1355, 2022.

[293] Q. Ou, Z. Jacobson, R. R. Abouleisa, X.-L. Tang, S. M. Hindi, A. Kumar, K. N. Ivey, G. Giridharan, A. El-Baz, K. Brittian, et al. Physiological biomimetic culture system for pig and human heart slices. *Circulation research*, 125(6):628–642, 2019.

[294] A. Naglah, F. Khalifa, N. Singam, B. Aladili, M. Ghazal, G. Giridharan, A. Khalil, A. Elmaghraby, A. El-Baz, and A. DeFilippis. Computer-aided diagnosis of acute myocardial infarction using time-dependent plasma metabolites. In *2019 IEEE International Conference on Imaging Systems and Techniques (IST)*, pages 1–5. IEEE, 2019.

[295] A. Sharafeldeen, M. Elsharkawy, N. S. Alghamdi, A. Soliman, and A. El-Baz. Precise segmentation of covid-19 infected lung from ct images based on adaptive first-order appearance model with morphological/anatomical constraints. *Sensors*, 21(16):5482, 2021.

[296] M. Elsharkawy, A. Sharafeldeen, F. Taher, A. Shalaby, A. Soliman, A. Mahmoud, M. Ghazal, A. Khalil, N. S. Alghamdi, A. A. K. A. Razek, et al. Early assessment of lung function in coronavirus patients using invariant markers from chest x-rays images. *Scientific Reports*, 11(1):1–11, 2021.

[297] B. Abdollahi, A. C. Civelek, X.-F. Li, J. Suri, and A. El-Baz. PET/CT nodule segmentation and diagnosis: A survey. In L. Saba and J. S. Suri, editors, *Multi Detector CT Imaging*, chapter 30, pages 639–651. Taylor , Francis, 2014.

[298] B. Abdollahi, A. El-Baz, and A. A. Amini. A multi-scale non-linear vessel enhancement technique. In *Engineering in Medicine and Biology Society, EMBC, 2011 Annual International Conference of the IEEE*, pages 3925–3929. IEEE, 2011.

[299] B. Abdollahi, A. Soliman, A. Civelek, X.-F. Li, G. Gimel'farb, and A. El-Baz. A novel gaussian scale space-based joint MGRF framework for precise lung segmentation. In *Proceedings of IEEE International Conference on Image Processing, (ICIP'12)*, pages 2029–2032. IEEE, 2012.

[300] B. Abdollahi, A. Soliman, A. Civelek, X.-F. Li, G. Gimel'farb, and A. El-Baz. A novel 3D joint MGRF framework for precise lung segmentation. In *Machine Learning in Medical Imaging*, pages 86–93. Springer, 2012.

[301] A. M. Ali, A. S. El-Baz, and A. A. Farag. A novel framework for accurate lung segmentation using graph cuts. In *Proceedings of IEEE International Symposium on Biomedical Imaging: From Nano to Macro, (ISBI'07)*, pages 908–911. IEEE, 2007.

[302] A. El-Baz, G. M. Beache, G. Gimel'farb, K. Suzuki, and K. Okada. Lung imaging data analysis. *International journal of biomedical imaging*, 2013:1–2, 2013.

[303] A. El-Baz, G. M. Beache, G. Gimel'farb, K. Suzuki, K. Okada, A. Elnakib, A. Soliman, and B. Abdollahi. Computer-aided diagnosis systems for lung cancer: Challenges and methodologies. *International Journal of Biomedical Imaging*, 2013:1–46, 2013.

[304] A. El-Baz, A. Elnakib, M. Abou El-Ghar, G. Gimel'farb, R. Falk, and A. Farag. Automatic detection of 2D and 3D lung nodules in chest spiral CT scans. *International Journal of Biomedical Imaging*, 2013:1–11, 2013.

[305] A. El-Baz, A. A. Farag, R. Falk, and R. La Rocca. A unified approach for detection, visualization, and identification of lung abnormalities in chest spiral CT scans. In *International Congress Series*, volume 1256, pages 998–1004. Elsevier, 2003.

[306] A. El-Baz, A. A. Farag, R. Falk, and R. La Rocca. Detection, visualization and identification of lung abnormalities in chest spiral CT scan: Phase-I. In *Proceedings of International conference on Biomedical Engineering, Cairo, Egypt*, volume 12, 2002.

[307] A. El-Baz, A. Farag, G. Gimel'farb, R. Falk, M. A. El-Ghar, and T. Eldiasty. A framework for automatic segmentation of lung nodules from low dose chest CT scans. In *Proceedings of International Conference on Pattern Recognition, (ICPR'06)*, volume 3, pages 611–614. IEEE, 2006.

[308] A. El-Baz, A. Farag, G. Gimel'farb, R. Falk, and M. A. El-Ghar. A novel level set-based computer-aided detection system for automatic detection of lung nodules in low dose chest computed tomography scans. *Lung Imaging and Computer Aided Diagnosis*, 10:221–238, 2011.

[309] A. El-Baz, G. Gimel'farb, M. Abou El-Ghar, and R. Falk. Appearance-based diagnostic system for early assessment of malignant lung nodules. In *Proceedings of IEEE International Conference on Image Processing, (ICIP'12)*, pages 533–536. IEEE, 2012.

[310] A. El-Baz, G. Gimel'farb, and R. Falk. A novel 3D framework for automatic lung segmentation from low dose CT images. In A. El-Baz and J. S. Suri, editors, *Lung Imaging and Computer Aided Diagnosis*, chapter 1, pages 1–16. Taylor , Francis, 2011.

[311] A. El-Baz, G. Gimel'farb, R. Falk, and M. El-Ghar. Appearance analysis for diagnosing malignant lung nodules. In *Proceedings of IEEE International Symposium on Biomedical Imaging: From Nano to Macro (ISBI'10)*, pages 193–196. IEEE, 2010.

[312] A. El-Baz, G. Gimel'farb, R. Falk, and M. A. El-Ghar. A novel level set-based CAD system for automatic detection of lung nodules in low dose chest CT scans.

In A. El-Baz and J. S. Suri, editors, *Lung Imaging and Computer Aided Diagnosis*, volume 1, chapter 10, pages 221–238. Taylor , Francis, 2011.

[313] A. El-Baz, G. Gimel'farb, R. Falk, and M. A. El-Ghar. A new approach for automatic analysis of 3D low dose CT images for accurate monitoring the detected lung nodules. In *Proceedings of International Conference on Pattern Recognition, (ICPR'08)*, pages 1–4. IEEE, 2008.

[314] A. El-Baz, G. Gimel'farb, R. Falk, and M. A. El-Ghar. A novel approach for automatic follow-up of detected lung nodules. In *Proceedings of IEEE International Conference on Image Processing, (ICIP'07)*, volume 5, pages V–501. IEEE, 2007.

[315] A. El-Baz, G. Gimel'farb, R. Falk, and M. A. El-Ghar. A new CAD system for early diagnosis of detected lung nodules. In *Image Processing, 2007. ICIP 2007. IEEE International Conference on*, volume 2, pages II–461. IEEE, 2007.

[316] A. El-Baz, G. Gimel'farb, R. Falk, M. A. El-Ghar, and H. Refaie. Promising results for early diagnosis of lung cancer. In *Proceedings of IEEE International Symposium on Biomedical Imaging: From Nano to Macro, (ISBI'08)*, pages 1151–1154. IEEE, 2008.

[317] A. El-Baz, G. L. Gimel'farb, R. Falk, M. Abou El-Ghar, T. Holland, and T. Shaffer. A new stochastic framework for accurate lung segmentation. In *Proceedings of Medical Image Computing and Computer-Assisted Intervention, (MICCAI'08)*, pages 322–330, 2008.

[318] A. El-Baz, G. L. Gimel'farb, R. Falk, D. Heredis, and M. Abou El-Ghar. A novel approach for accurate estimation of the growth rate of the detected lung nodules. In *Proceedings of International Workshop on Pulmonary Image Analysis*, pages 33–42, 2008.

[319] A. El-Baz, G. L. Gimel'farb, R. Falk, T. Holland, and T. Shaffer. A framework for unsupervised segmentation of lung tissues from low dose computed tomography images. In *Proceedings of British Machine Vision, (BMVC'08)*, pages 1–10, 2008.

[320] A. El-Baz, G. Gimel'farb, R. Falk, and M. A. El-Ghar. 3D MGRF-based appearance modeling for robust segmentation of pulmonary nodules in 3D LDCT chest images. In *Lung Imaging and Computer Aided Diagnosis*, chapter 3, pages 51–63. chapter, 2011.

[321] A. El-Baz, G. Gimel'farb, R. Falk, and M. A. El-Ghar. Automatic analysis of 3D low dose CT images for early diagnosis of lung cancer. *Pattern Recognition*, 42(6):1041–1051, 2009.

[322] A. El-Baz, G. Gimel'farb, R. Falk, M. A. El-Ghar, S. Rainey, D. Heredia, and T. Shaffer. Toward early diagnosis of lung cancer. In *Proceedings of Medical Image Computing and Computer-Assisted Intervention, (MICCAI'09)*, pages 682–689. Springer, 2009.

[323] A. El-Baz, G. Gimel'farb, R. Falk, M. A. El-Ghar, and J. Suri. Appearance analysis for the early assessment of detected lung nodules. In *Lung Imaging and Computer Aided Diagnosis*, chapter 17, pages 395–404. chapter, 2011.

[324] A. El-Baz, F. Khalifa, A. Elnakib, M. Nitkzen, A. Soliman, P. McClure, G. Gimel'farb, and M. A. El-Ghar. A novel approach for global lung registration using 3D Markov Gibbs appearance model. In *Proceedings of International Conference Medical Image Computing and Computer-Assisted Intervention, (MICCAI'12)*, pages 114–121, Nice, France, October 1–5, 2012.

[325] A. El-Baz, M. Nitzken, A. Elnakib, F. Khalifa, G. Gimel'farb, R. Falk, and M. A. El-Ghar. 3D shape analysis for early diagnosis of malignant lung nodules. In *Proceedings of International Conference Medical Image Computing and Computer-Assisted Intervention, (MICCAI'11)*, pages 175–182, Toronto, Canada, September 18–22, 2011.

[326] A. El-Baz, M. Nitzken, G. Gimel'farb, E. Van Bogaert, R. Falk, M. A. El-Ghar, and J. Suri. Three-dimensional shape analysis using spherical harmonics for early assessment of detected lung nodules. In *Lung Imaging and Computer Aided Diagnosis*, chapter 19, pages 421–438. chapter, 2011.

[327] A. El-Baz, M. Nitzken, F. Khalifa, A. Elnakib, G. Gimel'farb, R. Falk, and M. A. El-Ghar. 3D shape analysis for early diagnosis of malignant lung nodules. In *Proceedings of International Conference on Information Processing in Medical Imaging, (IPMI'11)*, pages 772–783, Monastery Irsee, Germany (Bavaria), July 3–8, 2011.

[328] A. El-Baz, M. Nitzken, E. Vanbogaert, G. Gimel'Farb, R. Falk, and M. Abo El-Ghar. A novel shape-based diagnostic approach for early diagnosis of lung nodules. In *Biomedical Imaging: From Nano to Macro, 2011 IEEE International Symposium on*, pages 137–140. IEEE, 2011.

[329] A. El-Baz, P. Sethu, G. Gimel'farb, F. Khalifa, A. Elnakib, R. Falk, and M. A. El-Ghar. Elastic phantoms generated by microfluidics technology: Validation of an imaged-based approach for accurate measurement of the growth rate of lung nodules. *Biotechnology journal*, 6(2):195–203, 2011.

[330] A. El-Baz, P. Sethu, G. Gimel'farb, F. Khalifa, A. Elnakib, R. Falk, and M. A. El-Ghar. A new validation approach for the growth rate measurement using elastic phantoms generated by state-of-the-art microfluidics technology. In *Proceedings of IEEE International Conference on Image Processing, (ICIP'10)*, pages 4381–4383, Hong Kong, September 26–29, 2010.

[331] A. El-Baz, P. Sethu, G. Gimel'farb, F. Khalifa, A. Elnakib, R. Falk, and M. A. E.-G. J. Suri. Validation of a new imaged-based approach for the accurate estimating of the growth rate of detected lung nodules using real CT images and elastic phantoms generated by state-of-the-art microfluidics technology. In A. El-Baz and J. S. Suri,

editors, *Handbook of Lung Imaging and Computer Aided Diagnosis*, volume 1, chapter 18, pages 405–420. Taylor & Francis, New York, 2011.

[332] A. El-Baz, A. Soliman, P. McClure, G. Gimel'farb, M. A. El-Ghar, and R. Falk. Early assessment of malignant lung nodules based on the spatial analysis of detected lung nodules. In *Proceedings of IEEE International Symposium on Biomedical Imaging: From Nano to Macro, (ISBI'12)*, pages 1463–1466. IEEE, 2012.

[333] A. El-Baz, S. E. Yuksel, S. Elshazly, and A. A. Farag. Non-rigid registration techniques for automatic follow-up of lung nodules. In *Proceedings of Computer Assisted Radiology and Surgery, (CARS'05)*, volume 1281, pages 1115–1120. Elsevier, 2005.

[334] A. S. El-Baz and J. S. Suri. *Lung Imaging and Computer Aided Diagnosis*. CRC Press, 2011.

[335] A. Soliman, F. Khalifa, N. Dunlap, B. Wang, M. El-Ghar, and A. El-Baz. An iso-surfaces based local deformation handling framework of lung tissues. In *Biomedical Imaging (ISBI), 2016 IEEE 13th International Symposium on*, pages 1253–1259. IEEE, 2016.

[336] A. Soliman, F. Khalifa, A. Shaffie, N. Dunlap, B. Wang, A. Elmaghraby, and A. El-Baz. Detection of lung injury using 4d-ct chest images. In *Biomedical Imaging (ISBI), 2016 IEEE 13th International Symposium on*, pages 1274–1277. IEEE, 2016.

[337] A. Soliman, F. Khalifa, A. Shaffie, N. Dunlap, B. Wang, A. Elmaghraby, G. Gimel'farb, M. Ghazal, and A. El-Baz. A comprehensive framework for early assessment of lung injury. In *Image Processing (ICIP), 2017 IEEE International Conference on*, pages 3275–3279. IEEE, 2017.

[338] A. Soliman, F. Khalifa, A. Shaffie, N. Liu, N. Dunlap, B. Wang, A. Elmaghraby, G. Gimel'farb, and A. El-Baz. Image-based cad system for accurate identification of lung injury. In *Image Processing (ICIP), 2016 IEEE International Conference on*, pages 121–125. IEEE, 2016.

[339] A. Soliman, A. Shaffie, M. Ghazal, G. Gimel'farb, R. Keynton, and A. El-Baz. A novel cnn segmentation framework based on using new shape and appearance features. In *2018 25th IEEE International Conference on Image Processing (ICIP)*, pages 3488–3492. IEEE, 2018.

[340] A. Shaffie, A. Soliman, H. A. Khalifeh, M. Ghazal, F. Taher, R. Keynton, A. Elmaghraby, and A. El-Baz. On the integration of ct-derived features for accurate detection of lung cancer. In *2018 IEEE International Symposium on Signal Processing and Information Technology (ISSPIT)*, pages 435–440. IEEE, 2018.

[341] A. Shaffie, A. Soliman, H. A. Khalifeh, M. Ghazal, F. Taher, A. Elmaghraby, R. Keynton, and A. El-Baz. Radiomic-based framework for early diagnosis of lung

cancer. In *2019 IEEE 16th International Symposium on Biomedical Imaging (ISBI 2019)*, pages 1293–1297. IEEE, 2019.

[342] A. Shaffie, A. Soliman, M. Ghazal, F. Taher, N. Dunlap, B. Wang, V. Van Berkel, G. Gimelfarb, A. Elmaghraby, and A. El-Baz. A novel autoencoder-based diagnostic system for early assessment of lung cancer. In *2018 25th IEEE International Conference on Image Processing (ICIP)*, pages 1393–1397. IEEE, 2018.

[343] A. Shaffie, A. Soliman, L. Fraiwan, M. Ghazal, F. Taher, N. Dunlap, B. Wang, V. van Berkel, R. Keynton, A. Elmaghraby, et al. A generalized deep learning-based diagnostic system for early diagnosis of various types of pulmonary nodules. *Technology in cancer research & treatment*, 17:1533033818798800, 2018.

[344] A. Shaffie, A. Soliman, A. Eledkawy, X.-A. Fu, M. H. Nantz, G. Giridharan, V. van Berkel, and A. El-Baz. Lung cancer diagnosis system based on volatile organic compounds (VOCs) profile measured in exhaled breath. *Applied Sciences*, 12(14):7165, 2022.

[345] J. S. Suri, S. Agarwal, B. Jena, S. Saxena, A. El-Baz, V. Agarwal, M. K. Kalra, L. Saba, K. Viskovic, M. Fatemi, et al. Five strategies for bias estimation in artificial intelligence-based hybrid deep learning for acute respiratory distress syndrome covid-19 lung infected patients using AP (ai) Bias 2.0: A systematic review. *IEEE Transactions on Instrumentation and Measurement*, 2022.

[346] I. S. Farahat, A. Sharafeldeen, M. Elsharkawy, A. Soliman, A. Mahmoud, M. Ghazal, F. Taher, M. Bilal, A. A. K. Abdel Razek, W. Aladrousy, et al. The role of 3D CT imaging in the accurate diagnosis of lung function in coronavirus patients. *Diagnostics*, 12(3):696, 2022.

[347] A. Shaffie, A. Soliman, A. Eledkawy, V. van Berkel, and A. El-Baz. Computer-assisted image processing system for early assessment of lung nodule malignancy. *Cancers*, 14(5):1117, 2022.

[348] F. Taher, N. Prakash, A. Shaffie, A. Soliman, and A. El-Baz. An overview of lung cancer classification algorithms and their performances. *IAENG International Journal of Computer Science*, 48(4), 2021.

[349] A. A. K. Abdel Razek, A. Alksas, M. Shehata, A. AbdelKhalek, K. Abdel Baky, A. El-Baz, and E. Helmy. Clinical applications of artificial intelligence and radiomics in neuro-oncology imaging. *Insights into Imaging*, 12(1):1–17, 2021.

[350] Y. ElNakieb, M. T. Ali, O. Dekhil, M. E. Khalefa, A. Soliman, A. Shalaby, A. Mahmoud, M. Ghazal, H. Hajjdiab, A. Elmaghraby, et al. Towards accurate personalized autism diagnosis using different imaging modalities: sMRI, fMRI, and DTI. In *2018 IEEE International Symposium on Signal Processing and Information Technology (ISSPIT)*, pages 447–452. IEEE, 2018.

[351] Y. ElNakieb, A. Soliman, A. Mahmoud, O. Dekhil, A. Shalaby, M. Ghazal, A. Khalil, A. Switala, R. S. Keynton, G. N. Barnes, et al. Autism spectrum disorder diagnosis framework using diffusion tensor imaging. In *2019 IEEE International Conference on Imaging Systems and Techniques (IST)*, pages 1–5. IEEE, 2019.

[352] R. Haweel, O. Dekhil, A. Shalaby, A. Mahmoud, M. Ghazal, R. Keynton, G. Barnes, and A. El-Baz. A machine learning approach for grading autism severity levels using task-based functional MRI. In *2019 IEEE International Conference on Imaging Systems and Techniques (IST)*, pages 1–5. IEEE, 2019.

[353] O. Dekhil, M. Ali, R. Haweel, Y. Elnakib, M. Ghazal, H. Hajjdiab, L. Fraiwan, A. Shalaby, A. Soliman, A. Mahmoud, et al. A comprehensive framework for differentiating autism spectrum disorder from neurotypicals by fusing structural MRI and resting state functional MRI. In *Seminars in Pediatric Neurology*, page 100805. Elsevier, 2020.

[354] R. Haweel, O. Dekhil, A. Shalaby, A. Mahmoud, M. Ghazal, A. Khalil, R. Keynton, G. Barnes, and A. El-Baz. A novel framework for grading autism severity using task-based FMRI. In *2020 IEEE 17th International Symposium on Biomedical Imaging (ISBI)*, pages 1404–1407. IEEE, 2020.

[355] A. El-Baz, G. Gimel'farb, R. Falk, M. A. El-Ghar, V. Kumar, and D. Heredia. A novel 3D joint Markov-gibbs model for extracting blood vessels from PC–mra images. In *Medical Image Computing and Computer-Assisted Intervention–MICCAI 2009*, volume 5762, pages 943–950. Springer, 2009.

[356] A. Elnakib, M. Nitzken, M. Casanova, H. Park, G. Gimel'farb, and A. El-Baz. Quantification of age-related brain cortex change using 3D shape analysis. In *Pattern Recognition (ICPR), 2012 21st International Conference on*, pages 41–44. IEEE, 2012.

[357] F. E.-Z. A. El-Gamal, M. M. Elmogy, M. Ghazal, A. Atwan, G. N. Barnes, M. F. Casanova, R. Keynton, and A. S. El-Baz. A novel cad system for local and global early diagnosis of alzheimer's disease based on pib-pet scans. In *2017 IEEE International Conference on Image Processing (ICIP)*, pages 3270–3274. IEEE, 2017.

[358] A. Alansary, M. Ismail, A. Soliman, F. Khalifa, M. Nitzken, A. Elnakib, M. Mostapha, A. Black, K. Stinebruner, M. F. Casanova, et al. Infant brain extraction in t1-weighted mr images using bet and refinement using lcdg and mgrf models. *IEEE journal of biomedical and health informatics*, 20(3):925–935, 2016.

[359] E. H. Asl, M. Ghazal, A. Mahmoud, A. Aslantas, A. Shalaby, M. Casanova, G. Barnes, G. Gimel'farb, R. Keynton, and A. El-Baz. Alzheimer's disease diagnostics by a 3d deeply supervised adaptable convolutional network. *Frontiers in bioscience (Landmark edition)*, 23:584–596, 2018.

[360] O. Dekhil, M. Ali, Y. El-Nakieb, A. Shalaby, A. Soliman, A. Switala, A. Mahmoud, M. Ghazal, H. Hajjdiab, M. F. Casanova, A. Elmaghraby, R. Keynton, A. El-Baz,

and G. Barnes. A personalized autism diagnosis cad system using a fusion of structural MRI and resting-state functional MRI data. *Frontiers in Psychiatry*, 10:392, 2019.

[361] O. Dekhil, A. Shalaby, A. Soliman, A. Mahmoud, M. Kong, G. Barnes, A. El-maghraby, and A. El-Baz. Identifying brain areas correlated with ados raw scores by studying altered dynamic functional connectivity patterns. *Medical Image Analysis*, 68:101899, 2021.

[362] Y. A. Elnakieb, M. T. Ali, A. Soliman, A. H. Mahmoud, A. M. Shalaby, N. S. Alghamdi, M. Ghazal, A. Khalil, A. Switala, R. S. Keynton, et al. Computer aided autism diagnosis using diffusion tensor imaging. *IEEE Access*, 8:191298–191308, 2020.

[363] M. T. Ali, Y. A. Elnakieb, A. Shalaby, A. Mahmoud, A. Switala, M. Ghazal, A. Khelifi, L. Fraiwan, G. Barnes, and A. El-Baz. Autism classification using SMRI: A recursive features selection based on sampling from multi-level high dimensional spaces. In *2021 IEEE 18th International Symposium on Biomedical Imaging (ISBI)*, pages 267–270. IEEE, 2021.

[364] M. T. Ali, Y. ElNakieb, A. Elnakib, A. Shalaby, A. Mahmoud, M. Ghazal, J. Yousaf, H. Abu Khalifeh, M. Casanova, G. Barnes, et al. The role of structure MRI in diagnosing autism. *Diagnostics*, 12(1):165, 2022.

[365] Y. ElNakieb, M. T. Ali, A. Elnakib, A. Shalaby, A. Soliman, A. Mahmoud, M. Ghazal, G. N. Barnes, and A. El-Baz. The role of diffusion tensor mr imaging (dti) of the brain in diagnosing autism spectrum disorder: Promising results. *Sensors*, 21(24):8171, 2021.

[366] M. M. Ismail, R. S. Keynton, M. M. Mostapha, A. H. ElTanboly, M. F. Casanova, G. L. Gimel'farb, and A. El-Baz. Studying autism spectrum disorder with structural and diffusion magnetic resonance imaging: a survey. *Frontiers in human neuroscience*, 10:211, 2016.

[367] M. Ismail, A. Soliman, A. ElTanboly, A. Switala, M. Mahmoud, F. Khalifa, G. Gimel'farb, M. F. Casanova, R. Keynton, and A. El-Baz. Detection of white matter abnormalities in mr brain images for diagnosis of autism in children. In *Proceedings of IEEE 13th International Symposium on Biomedical Imaging (ISBI'16)*, pages 6–9. IEEE, 2016.

[368] A. Alansary, A. Soliman, F. Khalifa, A. Elnakib, M. Mostapha, M. Nitzken, M. Casanova, and A. El-Baz. MAP-based framework for segmentation of MR brain images based on visual appearance and prior shape. *MIDAS J*, 1:1, 2013.

[369] A. Alansary, A. Soliman, M. Nitzken, F. Khalifa, A. Elnakib, M. Mostapha, M. Casanova, and A. El-Baz. An integrated geometrical and stochastic approach for accurate infant brain extraction. In *Proceedings of IEEE International Conference on Image Processing (ICIP'14)*, pages 3542–3546. IEEE, 2014.

[370] M. Casanova, A. El-Baz, M. Mott, G. Mannheim, H. Hassan, R. Fahmi, J. Giedd, J. Rumsey, A. Switala, and A. Farag. Reduced gyral window and corpus callosum size in autism: Possible macroscopic correlates of a minicolumnopathy. *Journal of Autism and Developmental Disorders*, 39(5):751–764, 2009.

[371] M. Casanova, A. El-Baz, and A. Switala. Laws of conservation as related to brain growth, aging, and evolution: symmetry of the minicolumn. *Frontiers in Neuroanatomy*, 5, 2011.

[372] M. Casanova, A. El-Baz, E. Vanbogaert, P. Narahari, and A. Switala. A topographic study of minicolumnar core width by lamina comparison between autistic subjects and controls: Possible minicolumnar disruption due to an anatomical element incommon to multiple laminae. *Brain Pathology*, 20(2):451–458, 2010.

[373] M. Casanova, A. El-Baz, E. Vanbogaert, P. Narahari, and J. Trippe. Minicolumnar width: comparison between supragranular and infragranular layers. *Journal of Neuroscience Methods*, 184(1):19–24, 2009.

[374] M. Casanova, A. El-Baz, S. Kamat, B. Dombroski, F. Khalifa, A. Elnakib, A. Soliman, A. Allison-McNutt, and A. Switala. Focal cortical dysplasias in autism spectrum disorders. *Acta Neuropathologica Communications*, 1(1):67, 2013.

[375] M. Casanova, A. El-Baz, and J. Suri. *Imaging the Brain in Autism*. Springer, 2013.

[376] M. Casanova, A. Farag, E.-B. Ayman, M. Meghan, H. Hassan, R. Fahmi, and A. Switala. Abnormalities of the gyral window in autism: A macroscopic correlate to a putative minicolumnopathy. *Journal of Special Education and Rehabilitation*, 7(1-2), 2006.

[377] A. Chowdhury, A. Rudra, M. Sen, A. Elnakib, and A. El-Baz. Cerebral white matter segmentation from MRI using probabilistic graph cuts and geometric shape priors. In *ICIP*, pages 3649–3652, 2010.

[378] B. Dombroski, A. Switala, A. El-Baz, and M. Casanova. Gyral window mapping of typical cortical folding using MRI. *Translational neuroscience*, 2(2):142–147, 2011.

[379] B. Dombroski, M. Nitzken, A. Elnakib, F. Khalifa, A. El-Baz, and M. Casanova. Cortical surface complexity in a population-based normative sample. *Translational Neuroscience*, 5(1):17–24, 2014.

[380] A. El-Baz, M. Casanova, G. Gimel'farb, M. Mott, and A. Switala. An MRI-based diagnostic framework for early diagnosis of dyslexia. *International Journal of Computer Assisted Radiology and Surgery*, 3(3-4):181–189, 2008.

[381] A. El-Baz, M. Casanova, G. Gimel'farb, M. Mott, A. Switala, E. Vanbogaert, and R. McCracken. A new CAD system for early diagnosis of dyslexic brains. In *Proceedings of International Conference on Image Processing (ICIP'2008)*, pages 1820–1823. IEEE, 2008.

[382] A. El-Baz, M. Casanova, G. Gimel'farb, M. Mott, and A. Switala. Autism diagnostics by 3D texture analysis of cerebral white matter gyrifications. In *Proceedings of International Conference on Medical Image Computing and Computer-Assisted Intervention (MICCAI'2007)*, pages 882–890. Springer, 2007.

[383] A. El-Baz, M. Casanova, G. Gimel'farb, M. Mott, and A. Switwala. A new image analysis approach for automatic classification of autistic brains. In *Proceedings of IEEE International Symposium on Biomedical Imaging: From Nano to Macro (ISBI'2007)*, pages 352–355. IEEE, 2007.

[384] A. El-Baz, A. Elnakib, F. Khalifa, M. A. El-Ghar, P. McClure, A. Soliman, and G. Gimel'farb. Precise segmentation of 3-D magnetic resonance angiography. *IEEE Transactions on Biomedical Engineering*, 59(7):2019–2029, 2012.

[385] A. El-Baz, A. Farag, G. Gimel'farb, M. Abou El-Ghar, and T. Eldiasty. Probabilistic modeling of blood vessels for segmenting mra images. In *ICPR (3)*, pages 917–920, 2006.

[386] A. El-Baz, A. Farag, G. Gimelâ€™farb, M. Abou El-Ghar, and T. Eldiasty. A new adaptive probabilistic model of blood vessels for segmenting mra images. In *Proceedings of Medical Image Computing and Computer-Assisted Intervention (MICCAI'06)*, volume 4191, pages 799–806. Springer, 2006.

[387] A. El-Baz, A. Farag, G. Gimelâ€™farb, and S. Hushek. Automatic cerebrovascular segmentation by accurate probabilistic modeling of tof-mra images. In *Medical Image Computing and Computer-Assisted Intervention (MICCAI'05)*, pages 34–42. Springer, 2005.

[388] A. El-Baz, A. Farag, A. Elnakib, M. F. Casanova, G. Gimel'farb, A. E. Switala, D. Jordan, and S. Rainey. Accurate automated detection of autism related corpus callosum abnormalities. *Journal of Medical Systems*, 35(5):929–939, 2011.

[389] A. El-Baz, A. G. G. M. Casanova G. Gimel'farb M. Mott El-Baz, M. Mott, A. Switala, E. Vanbogaert, and R. McCracken. Dyslexia diagnostics by 3D texture analysis of cerebral white matter gyrifications. In *Proceedings of International Conference on Pattern Recognition (ICPR'2008)*, pages 1–4. IEEE, 2008.

[390] G. G.-M. M. A. El-Baz, M. Casanova and A. Switala. A new image-based diagnostic framework for early diagnosis of dyslexic brains. In *Proceedings of of Computer Assisted Radiology and Surgery (CARS'08)*, pages 46–47, 2008.

[391] A. Elnakib, A. El-Baz, M. F. Casanova, G. Gimel'farb, and A. E. Switala. Image-based detection of corpus callosum variability for more accurate discrimination between dyslexic and normal brains. In *Proc. IEEE International Symposium on Biomedical Imaging: From Nano to Macro (ISBI'2010)*, pages 109–112. IEEE, 2010.

[392] A. Elnakib, A. El-Baz, M. F. Casanova, G. Gimel'farb, and A. Switala. Image-based detection of corpus callosum variability for more accurate discrimination between autistic and normal brains. In *Proceedings of IEEE International Conference on Image Processing (ICIP'2010)*, pages 4337–4340. IEEE, 2010.

[393] A. Elnakib, A. El-Baz, M. Casanova, and A. Switala. Dyslexia diagnostics by centerline-based shape analysis of the corpus callosum. In *Proceedings of International Conference on Pattern Recognition (ICPR'2010)*, pages 261–264. IEEE, 2010.

[394] A. Elnakib, M. Casanova, G. Gimel'farb, A. Switala, and A. El-Baz. Dyslexia diagnostics by 3-D shape analysis of the corpus callosum. *IEEE Transactions on Information Technology in Biomedicine*, 16(4):700–708, 2012.

[395] A. Elnakib, M. F. Casanova, G. Gimel'farb, A. E. Switala, and A. El-Baz. Autism diagnostics by centerline-based shape analysis of the corpus callosum. In *Proc. IEEE International Symposium on Biomedical Imaging: From Nano to Macro (ISBI'2011)*, pages 1843–1846. IEEE, 2011.

[396] A. Elnakib, M. Casanova, G. Gimel'farb, and A. El-Baz. Autism diagnostics by 3D shape analysis of the corpus callosum. In K. Suzuki, editor, *Machine Learning in Computer-aided Diagnosis: Medical Imaging Intelligence and Analysis*, chapter 15, pages 315–335. IGI Global, Berlin, 2012.

[397] R. Fahmi, A. Elbaz, H. Hassan, A. Farag, and M. Casanova. Structural MRI-based discrimination between autistic and typically developing brain. In *Proceedings of Computer Assisted Radiology and Surgery (CARS'2007)*, pages 24–26, 2007.

[398] A. Farag, R. Fahmi, M. Casanova, A. Abdel-Hakim, H. Abd El-Munim, and A. El-Baz. Robust neuroimaging-based classification techniques of autistic vs. typically developing brain. In *Deformable Models*, chapter 16, pages 535–566. Springer, 2007.

[399] M. Casanova, A. El-Baz, A. Elnakib, A. Switala, E. Williams, D. Williams, N. Minshew, and T. Conturo. Quantitative analysis of the shape of the corpus callosum in patients with autism and comparison individuals. *Autism*, 15(2):223–238, 2011.

[400] M. Casanova, A. El-Baz, A. Elnakib, J. Giedd, J. Rumsey, E. Williams, and A. Switala. Corpus callosum shape analysis with application to dyslexia. *Translational Neuroscience*, 1(2):124–130, 2010.

[401] M. Casanova, A. El-Baz, J. Giedd, J. Rumsey, and A. Switala. Increased white matter gyral depth in dyslexia: Implications for corticocortical connectivity. *Journal of Autism and Developmental Disorders*, 40(1):21–29, 2010.

[402] M. Mostapha, A. Alansary, A. Soliman, F. Khalifa, M. Nitzken, R. Khodeir, M. Casanova, and A. El-Baz. Atlas-based approach for the segmentation of infant DTI MR brain images. In *Proceedings of IEEE 11th International Symposium on Biomedical Imaging (ISBI'14)*, pages 1255–1258. IEEE, 2014.

[403] M. Mostapha, A. Soliman, F. Khalifa, A. Elnakib, A. Alansary, M. Nitzken, M. F. Casanova, and A. El-Baz. A statistical framework for the classification of infant DT images. In *Proceedings of IEEE International Conference Image Processing (ICIP'14)*, pages 2222–2226. IEEE, 2014.

[404] M. Nitzken, M. Casanova, G. Gimel'farb, A. Elnakib, F. Khalifa, A. Switala, and A. El-Baz. 3D shape analysis of the brain cortex with application to dyslexia. In *Image Processing (ICIP), 2011 18th IEEE International Conference on*, pages 2657–2660, Brussels, Belgium, September 2011. IEEE. (Selected for oral presentation. Oral acceptance rate is 10 percent and the overall acceptance rate is 35 percent).

[405] M. Nitzken, M. Casanova, G. Gimel'farb, F. Khalifa, A. Elnakib, A. Switala, and A. El-Baz. 3D shape analysis of the brain cortex with application to autism. In *Proceedings of IEEE International Symposium on Biomedical Imaging: From Nano to Macro (ISBI'13)*, pages 1847–1850, Chicago, Illinois, USA, March 2011. IEEE.

[406] M. Nitzken, M. Casanova, F. Khalifa, G. Sokhadze, and A. El-Baz. Shape-based detection of cortex variability for more accurate discrimination between autistic and normal brains. In A. El-Baz, R. Acharya, A. Laine, and J. Suri, editors, *Handbook of Multi-Modality State-of-the-Art Medical Image Segmentation and Registration Methodologies*, volume 2, chapter 7, pages 161–185. Springer Verlag, New York, March 2011.

[407] M. Nitzken, M. Casanova, and A. El-Baz. Spharm analysis of the brain cortex for diagnosing dyslexia. In *Proceedings of IEEE 11th International Symposium on Biomedical Imaging (ISBI'14)*, Beijing, China, April 2014. IEEE.

[408] M. Nitzken, G. Casanova, Mand Gimelfarb, T. Inanc, J. Zurada, and A. El-Baz. Shape analysis of the human brain: a brief survey. *Journal of Biomedical and Health Informatics*, 18(4):1337–1354, 2014.

[409] A. Rudra, M. Sen, A. Chowdhury, A. Elnakib, and A. El-Baz. 3D graph cut with new edge weights for cerebral white matter segmentation. *Pattern Recognition Letters*, 32(7):941–947, 2011.

[410] E. Williams, A. El-Baz, M. Nitzken, A. Switala, and M. Casanova. Spherical harmonic analysis of cortical complexity in autism and dyslexia. *Translational Neuroscience*, 3(1):36–40, 2012.

[411] Y. J. Li, E. M. Sokhadze, H. I. Luo, A. S. El-Baz, and A. S. Elmaghraby. Affective virtual reality gaming for autism. In *Modern Approaches to Augmentation of Brain Function*, pages 575–606. Springer, 2021.

[412] E. M. Sokhadze, I. Opris, L. Sears, A. S. El-Baz, A. Tasman, and M. F. Casanova. Effects of rtms on behavioral and electrocortical measures of error monitoring and correction function in children with autism spectrum disorder. In *Modern Approaches to Augmentation of Brain Function*, pages 551–573. Springer, 2021.

[413] M. F. Casanova, M. Shaban, M. Ghazal, A. S. El-Baz, E. L. Casanova, I. Opris, and E. M. Sokhadze. Effects of transcranial magnetic stimulation therapy on evoked and induced gamma oscillations in children with autism spectrum disorder. *Brain sciences*, 10(7):423, 2020.

[414] Y. ElNakieb, M. T. Ali, A. Soliman, A. Mahmoud, A. Shalaby, A. Switala, M. Ghazal, A. Khalil, L. Fraiwan, G. Barnes, et al. Identifying brain pathological abnormalities of autism for classification using diffusion tensor imaging. In *Neural Engineering Techniques for Autism Spectrum Disorder*, pages 361–376. Elsevier, 2021.

[415] M. T. Ali, A. Shalaby, A. Mahmoud, M. Ghazal, J. Yousaf, M. AlHalabi, G. Barnes, J. S. Suri, and A. S. El-Baz. Extract image markers of autism using hierarchical feature selection technique. In *Neural Engineering Techniques for Autism Spectrum Disorder*, pages 333–343. Elsevier, 2021.

[416] R. Haweel, A. Shalaby, A. Mahmoud, M. Ghazal, A. Khelifi, G. Barnes, J. S. Suri, and A. El-Baz. Early autism analysis and diagnosis system using task-based fmri in a response to speech task. In *Neural Engineering Techniques for Autism Spectrum Disorder*, pages 345–359. Elsevier, 2021.

[417] R. Haweel, O. Dekhil, A. Shalaby, A. Mahmoud, M. Ghazal, H. Hajjdiab, S. Ghniemy, R. Keynton, J. S. Suri, G. N. Barnes, et al. Autism diagnosis using task-based functional mri.

[418] O. Dekhil, A. Mahmoud, A. Shalaby, A. Soliman, F. Taher, H. Hajjdiab, A. Khalil, M. Ghazal, R. Keynton, G. Barnes, et al. Computational analysis techniques: A case study on fmri for autism spectrum disorder. 2019.

[419] A. Mahmoud, Y. ElNakieb, A. Shalaby, A. Soliman, F. Taher, H. Hajjdiab, A. Khalil, M. Ghazal, R. Keynton, J. S. Suri, et al. Towards a robust cad system for early diagnosis of autism using structural mri. 2019.

[420] Y. ElNakieb, A. Shalaby, A. Mahmoud, H. Hajjdiab, A. Khalil, M. Ghazal, F. Taher, A. Soliman, R. Keynton, G. Barnes, et al. A noninvasive image-based approach toward an early diagnosis of autism. 2019.

[421] F. E.-Z. A. El-Gamal, M. M. Elmogy, H. Hajjdiab, A. Khalil, M. Ghazal, A. Mahmoud, H. Soliman, and A. Atwan. A local/regional computer aided system for the diagnosis of mild cognitive impairment.

[422] E. M. Sokhadze, M. F. Casanova, D. L. Kelly, G. E. Sokhadze, Y. Li, A. S. Elmaghraby, and A. S. El-Baz. Virtual reality with psychophysio logical monitoring as an approach to evaluate emotional reactivity, social skills, and joint attention in autism spectrum disorder. In *Autism Imaging and Devices*, pages 387–412. CRC Press, 2017.

[423] E. M. Sokhadze, A. S. El-Baz, A. Tasman, G. E. Sokhadze, H. E. M. Farag, and M. F. Casanova. Repetitive transcranial magnetic stimulation (rtms) effects on evoked and induced gamma frequency eeg oscillations in autism spectrum disorder. In *Autism Imaging and Devices*, pages 513–552. CRC Press, 2017.

[424] E. M. Sokhadze, L. Sears, A. S. El-Baz, A. Tasman, and M. F. Casanova. Clinical applications of electrophysiological approaches based on cortical modularity in autism. In *Recent Advances on the Modular Organization of the Cortex*, pages 239–269. Springer, 2015.

[425] E. M. Sokhadze, J. Frederick, Y. Wang, M. Kong, A. S. El-Baz, A. Tasman, and M. F. Casanova. Event-related potential (erp) study of facial expression processing deficits in autism. *Journal of Communications Research*, 7(4):391–412, 2015.

[426] M. F. Casanova, J. Baruth, A. S. El-Baz, G. E. Sokhadze, M. Hensley, and E. M. Sokhadze. Evoked and induced gamma-frequency oscillations in autism. In *Imaging the brain in autism*, pages 87–106. Springer, 2013.

[427] A. Elnakib, M. F. Casanova, G. Gimelâ€™farb, and A. El-Baz. Autism diagnostics by 3d shape analysis of the corpus callosum. In *Machine Learning in Computer-aided Diagnosis: Medical Imaging Intelligence and Analysis*, pages 315–335. IGI Global, 2012.

[428] A. Elnakib, M. F. Casanova, A. Soliman, G. Gimel'farb, and A. El-Baz. Analysis of 3d corpus callosum images in the brains of autistic individuals. In *Handbook of Research on Trends in the Diagnosis and Treatment of Chronic Conditions*, pages 159–184. IGI Global, 2016.

[429] M. Nitzken, M. F. Casanova, F. Khalifa, G. Sokhadze, and A. El-Baz. Shape-based detection of cortex variability for more accurate discrimination between autistic and normal brains. In *Multi Modality State-of-the-Art Medical Image Segmentation and Registration Methodologies*, pages 161–185. Springer, 2011.

[430] A. A. Farag, R. Fahmi, M. F. Casanova, A. E. Abdel-Hakim, H. A. El-Munim, and A. El-Baz. Robust neuroimaging-based classification techniques of autistic vs. typically developing brain. In *Deformable Models*, pages 535–566. Springer, 2007.

[431] I. Yasser, F. Khalifa, H. Abdeltawab, M. Ghazal, H. S. Sandhu, and A. El-Baz. Automated diagnosis of optical coherence tomography angiography (octa) based on machine learning techniques. *Sensors*, 22(6):2342, 2022.

[432] R. Jagadapillai, X. Qiu, K. Ojha, Z. Li, A. El-Baz, S. Zou, E. Gozal, and G. N. Barnes. Potential cross talk between autism risk genes and neurovascular molecules: A pilot study on impact of blood brain barrier integrity. *Cells*, 11(14):2211, 2022.

[433] M. Elsharkawy, A. Sharafeldeen, A. Soliman, F. Khalifa, M. Ghazal, E. El-Daydamony, A. Atwan, H. S. Sandhu, and A. El-Baz. A novel computer-aided

diagnostic system for early detection of diabetic retinopathy using 3d-oct higher-order spatial appearance model. *Diagnostics*, 12(2):461, 2022.

[434] M. Elsharkawy, M. Elrazzaz, A. Sharafeldeen, M. Alhalabi, F. Khalifa, A. Soliman, A. Elnakib, A. Mahmoud, M. Ghazal, E. El-Daydamony, et al. The role of different retinal imaging modalities in predicting progression of diabetic retinopathy: A survey. *Sensors*, 22(9):3490, 2022.

[435] M. Elsharkawy, M. Elrazzaz, M. Ghazal, M. Alhalabi, A. Soliman, A. Mahmoud, E. El-Daydamony, A. Atwan, A. Thanos, H. S. Sandhu, et al. Role of optical coherence tomography imaging in predicting progression of age-related macular disease: A survey. *Diagnostics*, 11(12):2313, 2021.

[436] H. S. Sandhu, M. Elmogy, A. T. Sharafeldeen, M. Elsharkawy, N. El-Adawy, A. Eltanboly, A. Shalaby, R. Keynton, and A. El-Baz. Automated diagnosis of diabetic retinopathy using clinical biomarkers, optical coherence tomography, and optical coherence tomography angiography. *American journal of ophthalmology*, 216:201–206, 2020.

[437] A. Sharafeldeen, M. Elsharkawy, F. Khalifa, A. Soliman, M. Ghazal, M. AlHalabi, M. Yaghi, M. Alrahmawy, S. Elmougy, H. Sandhu, et al. Precise higher-order reflectivity and morphology models for early diagnosis of diabetic retinopathy using oct images. *Scientific Reports*, 11(1):1–16, 2021.

[438] A. A. Sleman, A. Soliman, M. Elsharkawy, G. Giridharan, M. Ghazal, H. Sandhu, S. Schaal, R. Keynton, A. Elmaghraby, and A. El-Baz. A novel 3d segmentation approach for extracting retinal layers from optical coherence tomography images. *Medical Physics*, 48(4):1584–1595, 2021.

[439] A. A. Sleman, A. Soliman, M. Ghazal, H. Sandhu, S. Schaal, A. Elmaghraby, and A. El-Baz. Retinal layers oct scans 3-d segmentation. In *2019 IEEE International Conference on Imaging Systems and Techniques (IST)*, pages 1–6. IEEE, 2019.

[440] N. Eladawi, M. Elmogy, M. Ghazal, O. Helmy, A. Aboelfetouh, A. Riad, S. Schaal, and A. El-Baz. Classification of retinal diseases based on oct images. *Front Biosci (Landmark Ed)*, 23:247–264, 2018.

[441] H. S. Sandhu, A. El-Baz, and J. M. Seddon. Progress in automated deep learning for macular degeneration. *JAMA ophthalmology*, 2018.

[442] M. Ghazal, S. S. Ali, A. H. Mahmoud, A. M. Shalaby, and A. El-Baz. Accurate detection of non-proliferative diabetic retinopathy in optical coherence tomography images using convolutional neural networks. *IEEE Access*, 8:34387–34397, 2020.

[443] W. Furtado, A. Shalaby, A. H. Mahmoud, A. Khallaf, A. Khalil, M. Ghazal, F. Taher, J. S. Suri, G. Giridharan, and A. El-Baz. A noninvasive approach for the early detection of diabetic retinopathy. In *Diabetes and Retinopathy*, pages 205–228. Elsevier, 2020.

[444] M. Shaban, A. H. Mahmoud, A. Shalaby, M. Ghazal, H. Sandhu, and A. El-Baz. Low-complexity computer-aided diagnosis for diabetic retinopathy. *Diabetes and retinopathy*, pages 133–149, 2020.

[445] M. Ghazal, Y. Al Khalil, M. Alhalabi, L. Fraiwan, and A. El-Baz. Early detection of diabetics using retinal oct images. In *Diabetes and Retinopathy*, pages 173–204. Elsevier, 2020.

[446] H. Mahmoud, N. Eladawi, M. Elmogy, M. Ghazal, M. T. Alhalabi, A. H. Mahmoud, A. Aboelfetouh, A. Riad, S. Schaal, and A. El-Baz. Retinal diseases diagnosis based on optical coherence tomography angiography. In *Diabetes and Fundus OCT*, pages 159–190. Elsevier, 2020.

[447] N. Eladawi, M. Elmogy, M. Ghazal, H. Mahmoud, A. H. Mahmoud, A. Khalil, A. Aboelfetouh, A. Riad, R. Keynton, and A. El-Baz. Computer-aided diagnosis system based on a comprehensive local features analysis for early diabetic retinopathy detection using octa. In *Diabetes and Fundus OCT*, pages 1–23. Elsevier, 2020.

[448] N. Eladawi, A. ElTanboly, M. Elmogy, M. Ghazal, A. Mahmoud, A. Aboelfetouh, A. Riad, M. El-Azab, J. S. Suri, G. Giridharan, et al. Automatic detection of early signs of diabetic retinopathy based on feature fusion from OCT and OCTA scans. In *Big Data in Multimodal Medical Imaging*, pages 263–280. CRC Press, 2019.

[449] K. Hammouda, F. Khalifa, A. Soliman, M. Ghazal, M. Abou El-Ghar, A. Haddad, M. Elmogy, H. Darwish, A. Khalil, A. Elmaghraby, et al. A CNN-based framework for bladder wall segmentation using MRI. In *2019 Fifth International Conference on Advances in Biomedical Engineering (ICABME)*, pages 1–4. IEEE, 2019.

[450] K. Hammouda, F. Khalifa, A. Soliman, M. Ghazal, M. Abou El-Ghar, A. Haddad, M. Elmogy, H. Darwish, R. Keynton, and A. El-Baz. A deep learning-based approach for accurate segmentation of bladder wall using mr images. In *2019 IEEE International Conference on Imaging Systems and Techniques (IST)*, pages 1–6. IEEE, 2019.

[451] K. Hammouda, F. Khalifa, A. Soliman, H. Abdeltawab, M. Ghazal, M. Abou El-Ghar, A. Haddad, H. E. Darwish, R. Keynton, and A. El-Baz. A 3d cnn with a learnable adaptive shape prior for accurate segmentation of bladder wall using mr images. In *2020 IEEE 17th International Symposium on Biomedical Imaging (ISBI)*, pages 935–938. IEEE, 2020.

[452] K. Hammouda, F. Khalifa, A. Soliman, M. Ghazal, M. Abou El-Ghar, M. Badawy, H. Darwish, A. Khelifi, and A. El-Baz. A multiparametric MRI-based CAD system for accurate diagnosis of bladder cancer staging. *Computerized Medical Imaging and Graphics*, 90:101911, 2021.

[453] K. Hammouda, F. Khalifa, A. Soliman, M. Ghazal, M. Abou El-Ghar, M. Badawy, H. Darwish, and A. El-Baz. A CAD system for accurate diagnosis of bladder cancer

staging using a multiparametric MRI. In *2021 IEEE 18th International Symposium on Biomedical Imaging (ISBI)*, pages 1718–1721. IEEE, 2021.

[454] R. F. Hoey, D. Medina-Aguiñaga, F. Khalifa, B. Ugiliweneza, D. Wang, S. Zdunowski, J. Fell, A. Naglah, A. S. El-Baz, A. N. Herrity, et al. Thoracolumbar epidural stimulation effects on bladder and bowel function in uninjured and chronic transected anesthetized rats. *Scientific reports*, 12(1):1–18, 2022.

[455] R. F. Hoey, D. Medina-Aguiñaga, F. Khalifa, B. Ugiliweneza, S. Zdunowski, J. Fell, A. Naglah, A. S. El-Baz, A. N. Herrity, S. J. Harkema, et al. Bladder and bowel responses to lumbosacral epidural stimulation in uninjured and transected anesthetized rats. *Scientific reports*, 11(1):1–21, 2021.

[456] A. Alksas, M. Shehata, G. A. Saleh, A. Shaffie, A. Soliman, M. Ghazal, H. A. Khalifeh, A. A. Razek, and A. El-Baz. A novel computer-aided diagnostic system for early assessment of hepatocellular carcinoma. In *2020 25th International Conference on Pattern Recognition (ICPR)*, pages 10375–10382. IEEE, 2021.

[457] A. Alksas, M. Shehata, G. A. Saleh, A. Shaffie, A. Soliman, M. Ghazal, A. Khelifi, H. A. Khalifeh, A. A. Razek, G. A. Giridharan, et al. A novel computer-aided diagnostic system for accurate detection and grading of liver tumors. *Scientific reports*, 11(1):1–18, 2021.

[458] A. Naglah, F. Khalifa, A. El-Baz, and D. Gondim. Conditional GANs based system for fibrosis detection and quantification in hematoxylin and eosin whole slide images. *Medical Image Analysis*, page 102537, 2022.

[459] A. A. K. A. Razek, R. Khaled, E. Helmy, A. Naglah, A. AbdelKhalek, and A. El-Baz. Artificial intelligence and deep learning of head and neck cancer. *Magnetic Resonance Imaging Clinics*, 30(1):81–94, 2022.

[460] A. Sharafeldeen, M. Elsharkawy, R. Khaled, A. Shaffie, F. Khalifa, A. Soliman, A. A. k. Abdel Razek, M. M. Hussein, S. Taman, A. Naglah, et al. Texture and shape analysis of diffusion-weighted imaging for thyroid nodules classification using machine learning. *Medical physics*, 2021.

[461] A. Naglah, F. Khalifa, R. Khaled, A. A. K. Abdel Razek, M. Ghazal, G. Giridharan, and A. El-Baz. Novel MRI-based CAD system for early detection of thyroid cancer using multi-input CNN. *Sensors*, 21(11):3878, 2021.

[462] A. Naglah, F. Khalifa, R. Khaled, A. El-Baz, et al. Thyroid cancer computer-aided diagnosis system using mri-based multi-input CNN model. In *2021 IEEE 18th International Symposium on Biomedical Imaging (ISBI)*, pages 1691–1694. IEEE, 2021.

[463] A. Naglah, F. Khalifa, A. Mahmoud, M. Ghazal, P. Jones, T. Murray, A. S. El-maghraby, and A. El-Baz. Athlete-customized injury prediction using training load statistical records and machine learning. In *2018 IEEE International Symposium*

on Signal Processing and Information Technology (ISSPIT), pages 459–464. IEEE, 2018.

[464] A. H. Mahmoud. *Utilizing radiation for smart robotic applications using visible, thermal, and polarization images.* PhD thesis, University of Louisville, 2014.

[465] A. Mahmoud, A. El-Barkouky, J. Graham, and A. Farag. Pedestrian detection using mixed partial derivative based his togram of oriented gradients. In *2014 IEEE International Conference on Image Processing (ICIP)*, pages 2334–2337. IEEE, 2014.

[466] A. El-Barkouky, A. Mahmoud, J. Graham, and A. Farag. An interactive educational drawing system using a humanoid robot and light polarization. In *2013 IEEE International Conference on Image Processing*, pages 3407–3411. IEEE, 2013.

[467] A. H. Mahmoud, M. T. El-Melegy, and A. A. Farag. Direct method for shape recovery from polarization and shading. In *2012 19th IEEE International Conference on Image Processing*, pages 1769–1772. IEEE, 2012.

[468] M. A. Ghazal, A. Mahmoud, A. Aslantas, A. Soliman, A. Shalaby, J. A. Benediktsson, and A. El-Baz. Vegetation cover estimation using convolutional neural networks. *IEEE Access*, 7:132563–132576, 2019.

[469] M. Ghazal, A. Mahmoud, A. Shalaby, and A. El-Baz. Automated framework for accurate segmentation of leaf images for plant health assessment. *Environmental monitoring and assessment*, 191(8):491, 2019.

[470] M. Ghazal, A. Mahmoud, A. Shalaby, S. Shaker, A. Khelifi, and A. El-Baz. Precise statistical approach for leaf segmentation. In *2020 IEEE International Conference on Image Processing (ICIP)*, pages 2985–2989. IEEE, 2020.

[471] M. Shaban, R. Salim, H. Abu Khalifeh, A. Khelifi, A. Shalaby, S. El-Mashad, A. Mahmoud, M. Ghazal, and A. El-Baz. A deep-learning framework for the detection of oil spills from SAR data. *Sensors*, 21(7):2351, 2021.

APPENDIX1

A.   Mathematical Formulas for Textural Features

In this appendix, we are going to detail the mathematical formulas used to extract the textural features:

Basic Notation

- μ: Mean.

- n: Total number of Voxels in the object.

- v_i: Gray-level value of Voxel i.

- σ^2: Variance.

- σ: Standard deviation.

- N_g: The normalized grey-levels.

- p: The normalized histogram counts.

- ϵ: An initial random small number.

- N_g: Grey-levels (normalized 0–255).

- G_N: The GLCM (normalized 0–1).

TABLE 15: First order texture features formulas.

Feature	Formula	
Mean (μ)	$\dfrac{1}{n}\sum\limits_{i=1}^{n} v_i = \dfrac{v_1 + v_2 + \cdots + v_n}{n}$	(10)
Variance (σ^2)	$\dfrac{\sum_{i=1}^{n}(v_i - \mu)^2}{n}$	(11)
Entropy (Ent)	$-\sum\limits_{i=1}^{N_g} p(i)\log_2\left(p(i) + \epsilon\right)$	(12)
Skewness (Skew)	$\dfrac{1}{n}\sum\limits_{i=1}^{n}\left(\dfrac{v_i - \mu}{\sigma}\right)^3$	(13)
Kurtosis (Kurt)	$\dfrac{1}{n}\sum\limits_{i=1}^{n}\left(\dfrac{v_i - \mu}{\sigma}\right)^4$	(14)

- $\bar{x}$, $\sigma_x(i)$: The row margins (mean and standard deviation).

- $\bar{y}$, $\sigma_y(i)$: The column margins (mean and standard deviation).

TABLE 16: Second order texture features formulas.

Feature	Formula	
Contrast	$$\sum_{i=0}^{N_g} \sum_{j=0}^{N_g} (i-j)^2 G_N(i,j)$$	(15)
Dissimilarity	$$\sum_{i=0}^{N_g} \sum_{j=0}^{N_g} |i-j| G_N(i,j)$$	(16)
Homogeneity	$$\sum_{i=0}^{N_g} \sum_{j=0}^{N_g} \frac{G_N(i,j)}{1+(i-j)^2}$$	(17)
ASM	$$\sum_{i=0}^{N_g} \sum_{j=0}^{N_g} (G_N(i,j))^2$$	(18)
Energy	$$\sqrt{ASM}$$	(19)
Correlation	$$\frac{\sum_{i=0}^{N_g} \sum_{j=0}^{N_g} G_N(i,j) i j - \bar{x}\bar{y}}{\sigma_x(i)\sigma_y(j)}$$	(20)

CURRICULUM VITAE

Mohamed Nazih Shehata
Paul C. Lutz Hall, Room # 309
BioImaging Laboratory
Department of Bioengineering
University of Louisville, Louisville, KY, USA
University E-mail:*mnsheh01@louisville.edu*
Personal E-mail:*eng.mohamednazeeh@hotmail.com*
Office: (502) 852–4032
Cell: (502) 797–1805

Current Research Interest

I am a graduate Ph.D student at Computer Science and Engineering Department at the
University of Louisville, Louisville, KY, USA since Summer 2016. I have finished my
M.Sc. at Electrical and Computer Engineering Department in Summer 2016. My general research interests are in digital image processing, medical imaging, machine learning,
Big Data, and computer vision. In August 2014, I have joined the BioImaging Lab and
have actively been working on developing innovative computer-aided diagnostic (CAD)
systems for early detection of different kidney diseases.

Education

2016–Pres.	Ph.D Student, Computer Science and Engineering Department, Speed School of Engineering, University of Louisville, Louisville, KY 40292 Ph.D Candidate, since 2017, GPA = 3.984/4.0.
2016	M.Sc., Electrical and Computer Engineering Department, Speed School of Engineering, University of Louisville, Louisville, KY 40292 **M.Sc. Thesis:** *A Non-Invasive Diagnostic System for Early Assessment of Acute Renal Transplant Rejection*- Prof. Ayman S. El-Baz, Thesis Advisor. GPA = 4.0 (*Graduation date: Summer 2016*)
2009	B.Sc., Computers Engineering and Control Systems, Mansoura University, Mansoura 35516, Egypt. **Sr. Project:** *Remote Controlling of Moving Objects Via Mobile or Fixed Phones*- Prof. Aly El-Desouky, Project Supervisor. GPA = 3.87 (*Graduated with **excellence with honor** and ranked the **first** in a class of 200*)

Experience

Fall'14–Pres.	Graduate Research Assistant, BioImaging laboratory, Department of Bioengineering, University of Louisville, Louisville, KY 40292, USA.
2010–2014	Graduate Research Assistant, Department of Computers Engineering and Control Systems, Mansoura University, Mansoura 35516, Egypt.

Teaching/Administration Experience

Assist in teaching, laboratory demonstration, conducting tutorials, grading, and senior graduation projects of the following Electrical Engineering undergraduate courses:

Place	Course Subject	Semester/Year
Mansoura University	Artificial Neural Networks Artificial Intelligence Machine Learning Fuzzy Control Systems Advanced Control Systems Digital Control Systems Computer Architecture Computer Maintenance	2010-2014
Mansoura University	Supervision support for an undergraduate final project (Smart Modern Automatic Control Restaurant Trend) using PAC	2012-2013
Mansoura University	Summer trainer for undergraduate student on Matlab basic tools and PAC controller	2011-2012
Mansoura University	Supervision support for an undergraduate final project (Smart Gate) using image processing techniques; specifically, face recognition	2010-2011

Professional Affiliations and Memberships

- Student Member, Biomedical Engineering Society (BMES).

- Young Professional Member, Biomedical Engineering Society (IEEE).

- Young Professional Member, Institute of Electrical and Electronics Engineers (IEEE).

- Member, IEEE Signal Processing (SPS) Society.

- Member, IEEE Engineering in Medicine and Biology (EMBS) Society.

- Member, IEEE Biometrics Council.

- Member, IEEE Sensors Council.

- Member, IEEE Nanotechnology Council.

- Member, IEEE Electronic Design Automation Council.

- Member, IEEE Cloud Computing Community.

- Member, IEEE Systems Council.

- Member, Egyptian Engineers Syndicate, Electrical Engineering.

Awards and Recognition (Total = 21)

- *Exemplary Research Scholarship Award* in the Bioengineeing Department, Speed school of Engineering, University of Louisville, 2022.

- *MIT Technology Review MENA IU35 Award* MIT Technology Review Innovators under 35 Yrs in the Middle East and North Africa for the year 2021

- 2nd **place winner** *Research Louisville 2021, Doctoral Engineering Category at The UofL*

- *Doctoral Dissertation Completion Award for Summer 2021 at The UofL*

- *CSE Arthur M Riehl Award for Spring 2021 at The UofL*

- *Exemplary Research Scholarship Award* in the Bioengineeing Department, Speed school of Engineering, University of Louisville, 2021.

- *EPIC Inventor Awards 2020 at The UofL*

- *Cover Article of the Volume 47, Issue 6 of Medical Physics Journal 2020*

- 2nd *place winner* at the 16th annual American Society for Diagnostic and Interventional Nephrology (ASDIN) meeting, Las Vegas, Nevada, USA, Feb 21–23, 2020 (ASDIN'20).

- *Exemplary Research Scholarship Award* in the Bioengineeing Department, Speed school of Engineering, University of Louisville, 2020.

- *EPIC Inventor Awards 2019 at The UofL*

- *Exemplary Research Scholarship Award* in the Bioengineeing Department, Speed school of Engineering, University of Louisville, 2019.

- *International Student Tuition Support Award 2018, 2019, and 2021*.

- 2nd *place winner* at the 13th annual American Society for Diagnostic and Interventional Nephrology (ASDIN) meeting, New Orleans, Louisiana, USA, Feb 10–12, 2017 (ASDIN'17).

- *Merit of Excellence Certificate* from Graduate Student Council (GSC) at the Uni-

versity of Louisville, in the area of community engagement in Graduate Student Regional Research Conference (GSRRC), April 2016.

- *One of The Best 39 papers* in the International Symposium on Biomedical Imaging: From Nano to Macro, Prague, Czech Republic, April 16–20, 2016 (ISBI'16).

- *IEEE Signal Processing Society (SPS) Travel Award 2015 and 2018* to attend the IEEE International Conference on Image processing, Quebec City, Canada, September 27–30, 2015 (ICIP'15).

- *GSC at the University of Louisville Travel Award 2015, 2018, 2019, and 2021*.

- *Theobald Scholarship Award* in the Electrical and Computer Engineering Department, Speed school of Engineering, University of Louisville, 2015.

- *Discretionary Certificate* for distinct participation in student activities (Robocon Competition supervision), 2009–2010.

- *Higher Education Enhancement Project Fund Discretionary Certificate* for distinct students in the Department of Communications and Electronics Engineering for Excellent grade ranked **third** in the second undergraduate year of education, Mansoura University , 2005–2006.

Class Work Grade

A total of *72* credit hours in Computer Science and Engineering, Electrical and Computer Engineering, and Bioengineering subjects with a cumulative *GPA of 3.984*. Particular course concentration has been in medical image analysis and machine learning.

Research Activities

- Image modeling, 2D, 3D, and 4D image segmentation and registration.
- Development of computer-aided diagnostic (CAD) system by integrating diffusion-

weighted magnetic resonance imaging (DW-MRI), BOLD-MRI, and clinical biomarkers for the early assessment of acute renal transplant rejection.

- Development of a CAD system for the early detection of different types of kidney rejection using DW-MRIs.

- Development of a cascaded two-stage CAD system for differentiating nonrejection renal transplants from transplanted kidneys with abnormalities using DW-MRIs and then, classifying abnormal kidney transplants into early rejection and other kidney diseases including: tubular inflammation, acute tubular injury, graft amyloidosis, and acute tubular necrosis.

- Development of computer-aided diagnostic (CAD) system by integrating morphological markers, texture markers, and functional markers for the accurate identification of renal cancer tumors.

- Development of computer-aided diagnostic (CAD) system by integrating morphological markers, texture markers, and functional markers for the accurate grading of Liver cancer tumors.

- Development of computer-aided prediction (CAP) system for precise evaluation of favorable response to pre-operative chemotherapy of Wilm's tumors in children by estimating tumor size reduction and functionality.

- Development of computer-aided diagnostic (CAD) system for precise grading of brain cancer tumors (Glioma).

- Development of computer-aided diagnostic (CAD) system for detecting and grading spine cancer tumors.

- Development of a new scoring system to accurately detect and grade prostate cancer.

- Development of a new scoring system for the early and precise identification of breast cancer using histopathological images.

- Assisted in grants writing and preparing primary results for the BioImaging Lab, University of Louisville.

Out of Reach Connectivity

- I am currently working with three undergraduate student for their summer training of 2022.

- I am currently working with two of the summer graduate students in summer 2022 and we are working together to prepare two publications.

- I have worked closely with one of the summer graduate students in summer 2021 and she was able to win the $2^{n}d$ place award in KAS poster competition at Berea college.

- I have trained one of the summer graduate students in summer 2021 and we are close to submit a journal article together.

- I have trained one of the undergraduate students from Fall 2019 to Fall of 2020 and we had one published conference papers and three book chapters.

- I have trained one of the high school students during Fall and Spring of 2015 and we had two published conference papers.

- I have trained one of the middle school students during Fall and Spring of 2016 and we had one published conference paper.

Publications

During Fall 2014–Summer 2022, I have authored or co-authored 15 journal articles, 9 book chapter, 16 peer-reviewed conference papers, 19 abstract in proceedings, and 4 patents/disclosures. The articles have been published in very prestigious journals such as Scientific Reports: Nature Journal (5-year impact factor 5.516), IEEE Transaction on Biomedical Engineering (IEEE TBME) Journal (5-year impact factor 5.674), Medical Physics Journal (5-year impact factor 4.354), Insights into Imaging (5-year impact factor 5.964), Public Library of Science (PLOS) One Journal (5-year impact factor 3.788), Sensors (5-year impact factor 4.069), the British Journal of Radiology (BJR) (5-year impact factor 3.456), etc. The conference papers were reported as top-rank international conferences in medical imaging, image processing, and pattern recognition e.g., MICCAI, ISBI, ICIP, and ICPR with acceptance rate less than 30%.

- **Journal Articles (Total = 15)**

    1. H. Magdy Balaha, M. Elgendy, A. Alksas, M. Shehata, N. Alghamdi, F. Taher, M. Ghazal, M. Ghoneim, E. Hamed, F. Sherif, A. Elgarayhi, M. Sallah, M. Salem, E. Kamal, and A. El-Baz,"A Novel, Non-Invasive, AI-Based System for Precise Grading of Anosmia in COVID-19 using Neuroimaging," *Scientific Reports: Nature,* 2022. (Under-review).

    2. M. El-Melegy, R. Kamal, M. Abou El-Ghar, M. Shehata, F. Khalifa, and A. El-Baz, "Kidney segmentation from DCE-MRI converging level set methods, fuzzy clustering and Markov random field modeling," *Scientific Reports: Nature,* 2022. (Under-review).

    3. M. Elgendy, H. Magdy Balaha, M. Shehata, A. Alksas, M. Ghoneim, F. Sherif, A. Mahmoud, A. Elgarayhi, F. Taher, M. Sallah, M. Ghazal, and A. El-Baz,"Role of Imaging and AI in the Evaluation of COVID-19 Infection: A Comprehensive

Survey," *Frontiers in Bioscience-Landmark,* 2022. (Accepted with major revision).

4. A. Alksas, M. Shehata, H. Atef, F. Sherif, M. Ghazal, A. Abdel Razek, L. Elsorogy, and A. El-Baz,"A Novel System for Precise Grading of Glioma," *Medical Physics,* 2022. (Accepted with major revision).

5. S. Ayyad, M. Badawy, M. Shehata, A. Alksas, A. Mahmoud, M. Abou El-Ghar, M. Ghazal, M. El-Melegy, N. B. Abdel-Hamid, L. M. Labib, H. A. Ali, and A. El-Baz,"A New Framework for Precise Identification of Prostatic Adenocarcinoma," *Sensors,* 2022, vol. 22(5),pp. 1848, 2022.

6. A. Abdel Razek, A. Alksas, M. Shehata, A. AbdelKhalek, K. Abdel Baky, A. El-Baz, and E. Helmy, "Clinical applications of artificial intelligence in neuro-oncology imaging," *Insights into Imaging,* 2021, vol. 12(152), pp. 1-17.

7. S. Ayyad, M. Shehata, A. Shalaby, M. Abou El-Ghar, M. Ghazal, M. El-Melegy, N. B. Abdel-Hamid, L. M. Labib, H. A. Ali, and A. El-Baz,"Role of AI and Histopathological Images in Detecting Prostate Cancer: A Survey," *Sensors,* 2021, vol. 21(8),pp. 2586, 2021.

8. M. Shehata*, A. Alksas*, R. T. Abouelkheir*, A. Almahdy, A. Shaffie, A. Soliman, M. Ghazal, H. Abu Khalifeh, R. Salim, A. Abdel Razek, N. S. Alghamdi, and A. El-Baz,"A Comprehensive Computer-Assisted Diagnosis System for Early Assessment of Renal Cancer Tumors," *Sensors,* 2021, vol. 21(14), pp. 4928.

9. A. Alksas*, M. Shehata*, G. Saleh*, A. Shaffie, A. Soliman, M. Ghazal, A. Khelifi, H. Abu Khalifeh, A. Abdel Razek, G. Giridharan, and A. El-Baz,"A Novel Computer-Aided Diagnostic System for Accurate Detection and Grading of Liver Tumors," *Scientific Reports: Nature,* 2021, vol. 11(1), pp. 1-18.

10. M. Shehata, A. Shalaby, A. E. Switala, M. El-Baz, M. Ghazal, L. Fraiwan, A. Khalil, M. Abou El-Ghar, M. Badawy, A. M. Bakr, A. C. Dwyer, A. Elmagraby, G. Giridharan, R. Keynton, and A. El-Baz,"A multimodal computer-aided diagnostic system for precise identification of renal allograft rejection: Preliminary results,"

Medical Physics, vol. 47(6),pp. 2427-2440, 2020. *(Selected the Cover Article in its Issue)*

11. H. Abdeltawab*, **M. Shehata***, A. Shalaby, F. Khalifa, A. Mahmoud, M. Abou El-Ghar, A. C. Dwyer, M. Ghazal, H. Hajjdiab, R. Keynton, and A. El-Baz,"A Novel CNN-Based CAD System for Early Assessment of Transplanted Kidney Dysfunction," *Scientific Reports: Nature,* vol. 9(1),pp. 5948, 2019.

12. **M. Shehata**, F. Khalifa, A. Soliman, M. Ghazal, F. Taher, M. Abou El-Ghar, A. C. Dwyer, G. Gimel'farb, R. Keynton, and A. El-Baz, "Computer-Aided Diagnostic System for Early Detection of Acute Renal Transplant Rejection Using Diffusion-Weighted MRI," *IEEE Transaction on Biomedical Engineering,* vol. 66(2), pp.539–552, 2019.

13. **M. Shehata**, A. Mahmoud, A. Soliman, F. Khalifa, M. Ghazal, M. Abou El-Ghar, M. El-Melegy, and A. El-Baz, "3D Kidney Segmentation from Abdominal Diffusion MRI Using an Appearance-Guided Deformable Boundary," *PLOS One,* vol. 13(7), pp. e02000822018, 2018.

14. E. Hollis*, **M. Shehata***, M. Abou El-Ghar, M. Ghazal, T. El-Diasty, M. Merchant, A. Switala, and A. El-Baz, "Statistical Analysis of ADCs and Clinical Biomarkers in Detecting Acute Renal Transplant Rejection ," *The British Journal of Radiology,*vol. 90(1080), pp.20170125, 2017.

15. E. Hollis, **M. Shehata**, F. Khalifa, M. Abou El-Ghar, T. El-Diasty, G. Gimel'farb, and A. El-Baz, "Towards Non-invasive Diagnostic Techniques for Early Detection of Acute Renal Rejection: A Review," *The Egyptian Journal of Radiology and Nuclear Medicine,* vol. 48(1), pp. 257–269, 2017.

- **Book Chapters (Total = 9)**

1. **M. Shehata**, A. Elmahdy, A. Alksas, R. Abouelkheir, A. Mahmoud, M. abou El-Ghar, M. Ghazal, and A. El-Baz "Role of AI and Radiomics in Diagnosing Renal

174

Tumors: A Survey," *State of the Art in Neural Networks and Their Applications, Volume 2*, A. El-Baz, and J. Suri, Eds, Elsevier, 2022, Chapter 11, eBook ISBN: 9780128218495, (in press).

2. S. Ayyad, M. Shehata, A. Mahmoud, M. Ghazal, and A. El-Baz "Cloud Computing in Healthcare and Medical Imaging: A Brief Overview," *Cloud Computing in Medical Imaging, Healthcare Technologies and Services, Volume 1*, A. El-Baz, and J. Suri, Eds, NYC: Chapman and Hall/CRC, 2022, (in press).

3. S. Ayyad, M. Shehata, A. Alksas, M. Badawy, A. Mahmoud, M. abou El-Ghar, M. Ghazal, M. El-Melegy, N. Abdel-Hamid, L. Labib, H. Arafat, and A. El-Baz "A Multimodal MR-based CAD System for Precise Assessment of Prostatic Adenocarcinoma," *Texture Analysis in Image Processing, Volume 2*, A. El-Baz, and J. Suri, Eds, NYC: Chapman and Hall/CRC, 2022, (in press).

4. S. Ayyad, M. Shehata, A. Shalaby, M. abou El-Ghar, M. Ghazal, M. El-Melegy, A. mahmoud, N. Abdel-Hamid, L. Labib, H. Arafat, and A. El-Baz "Prostate Cancer Detection Using Histopathology Images Analysis," *Artificial Intelligence in Cancer Diagnosis, Volume 3: Brain and Prostate Cancer*, A. El-Baz, and J. Suri, Eds, IOP publisher, ISBN13 9780750336017, 2021, (in press).

5. M. Shehata, F. Khalifa, A. Soliman, M. Abou El-Ghar, S. Shaker, A. Shalaby, M. El-Baz, A. Mahmoud, M. Ghazal, A. C. Dwyer, and A. El-Baz "Early Classification of Renal Rejection Types: A Deep Learning Approach," *Machine Learning in Medicine*, A. El-Baz, and J. Suri, Eds, CRC Press, 2021, pp. 257-280.

6. M. Shehata, H. Abdeltawab, M. Ghazal, A. Khalil, S. Shaker, A. Shalaby, A. Mahmoud, M. Abou El-Ghar, A. C. Dwyer, M. El-Melegy, A. M. Bakr, J. Suri, and A. El-Baz "Accurate Identification of Renal Transplant Rejection: Convolutional Neural Networks and Diffusion MRI," *State-of-the-Art in Neural Networks and its Applications: Volume 1*, A. El-Baz, and J. Suri, Eds, Elsevier, 2021, pp. 91-115.

7. M. Shehata, F. Taher, M. Ghazal, S. Shaker, M. Abou El-Ghar, M. Badawy, A.

Shalaby, M. El-Baz, A. Mahmoud, A. C. Dwyer, A. M. Bakr, J. Suri, and A. El-Baz. "Early Identification of Acute Rejection for Renal Allografts: A Machine Learning Approach," *State-of-the-Art in Neural Networks and its Applications: Volume 1*, A. El-Baz, and J. Suri, Eds, Elsevier, 2021, pp. 197-218.

8. M. Shehata, A. Shalaby, A. Mahmoud, M. Ghazal, H. Hajjdiab, M. A. Badawy, M. Abou El-Ghar, A. M. Bakr, A. C. Dwyer, R. Keynton, A. Elmaghraby, and A. El-Baz, "Towards Big Data in Acute Renal Rejection," *Big Data in Multimodal Medical Imaging* , A. El-Baz, and J. Suri, Eds, Taylor & Francis, 2019, ch. 9, pp. 205–223.

9. M. Shehata, F. Khalifa, A. Soliman, A. Taki Eldeen, M. Abou El-Ghar, T. El-Diasty, A. El-Baz, and R. Keynton, "An appearance-guided deformable model for 4D kidney segmentation using diffusion MRI," *Biomedical Image Segmentation: Advances and Trends*, A. El-Baz, X. Jiang, and J. Suri, Eds, Taylor & Francis, 2016, ch. 12, pp. 269–283.

- **Peer-Reviewed Conference Proceedings (Total = 16)**

1. M. Shehata, F. Khalifa, A. Soliman, R. Alrefai, M. Abou El-Ghar, A. C. Dwyer, R. Ouseph, and A. El-Baz, "A Novel Framework for Automatic Segmentation of Kidney from DW-MRI," In: *Proceedings of IEEE International Symposium on Biomedical Imaging: From Nano to Macro (ISBI'15)*, New York, USA, April 16–19, 2015, pp. 951–954.

2. M. Shehata, F. Khalifa, A. Soliman, R. Alrefai, M. Abou El-Ghar, A. C. Dwyer, R. Ouseph, and A. El-Baz, "A Level Set-Based Framework for 3D Kidney Segmentation from Diffusion MR Images," In: *Proceedings of International Conference on Image Processing (ICIP'15)*, Quebec, Canada, September 27–30, 2015, pp. 4441–4445.

3. M. Shehata, F. Khalifa, A. Soliman, A. Takieldeen, M. Abou El-Ghar, A. Shaffie,

A. C. Dwyer, R. Ouseph, A. El-Baz, and R. Keynton, "3D Diffusion MRI-Based CAD System for Early Diagnosis of Acute Renal Rejection," In: *Proceedings of IEEE International Symposium on Biomedical Imaging: From Nano to Macro (ISBI'16)*, Prague, Czech Republic, April 13–16, 2016, pp. 1177–1180. *(Selected as One of the Best 39 papers from around 340 accepted papers)*.

4. F. Khalifa, A. Soliman, A. Takieldeen, M. Shehata, M. Mostapha, A. Shaffie, R. Ouseph, A. Elmaghraby, and A. El-Baz, "Kidney Segmentation from CT Images Using A 3D NMF-Guided Active Contour Model," In: *Proceedings of IEEE International Symposium on Biomedical Imaging: From Nano to Macro (ISBI'16)*, Prague, Czech Republic, April 13–16, 2016, pp. 432–435.

5. M. Shehata, F. Khalifa, E. Hollis, A. Soliman, E. Hosseini-Asl, M. Abou El-Ghar, M. El-Baz, A. C. Dwyer, A. El-Baz, and R. Keynton, "A New Non-Invasive Approach for Early Classification of Renal Rejection Types Using Diffusion-Weighted MRI," In: *Proceedings of International Conference on Image Processing (ICIP'16)*, Phoenix, Arizona, USA, September 25–28, 2016, pp. 136–140. *(Selected for Oral Presentation)*.

6. M. Shehata, F. Khalifa, A. Soliman, M. Abou El-Ghar, A. C. Dwyer, G. Gimel'farb, R. Keynton, and A. El-Baz, "A Promising Non-Invasive CAD System for Kidney Function Assessment," In: *Proceedings of Medical Image Computing and Computer Assisted Intervention (MICCAI'16)*, Athens, Greece, October 17–21, vol (9902), 2016, pp. 613–621.

7. F. Khalifa, M. Shehata, A. Soliman, M. Abou El-Ghar, T. El-Diasty, A. C. Dwyer, M. El-Melegy, R. Keynton, and A. El-Baz, "A Generalized MRI-Based CAD System for Functional Assessment of Renal Transplant," In: *Proceedings of IEEE International Symposium on Biomedical Imaging: From Nano to Macro (ISBI'17)*, Melbourne, Australia, April 18–21, 2017, pp. 758–761. *(Selected for Oral Presentation)*.

177

8. **M. Shehata**, M. Ghazal, G. M. Beache, M. Abou El-Ghar, A. C. Dwyer, A. Khalil, and A. El-Baz, "Role of Integrating Diffusion mR Image-Markers with Clinical-Biomarkers for Early Assessment of Renal Transplants," In: *Proceedings of International Conference on Image Processing (ICIP'18)*, Athens, Greece, October 7–10, 2018, pp. 146–150. *(Selected for Oral Presentation)*.

9. H. Abdeltawab*, **M. Shehata***, A. Shalaby, S. Mesbah, M. El-Baz, M. Ghazal, Y. Al Khalil, M. Abou El-Ghar, A. C. Dwyer, M. El-Melegy, G. Giridharan, and A. El-Baz, "A New 3D CNN-based CAD System for Early Detection of Acute Renal Transplant Rejection," In: *Proceedings of International Conference on Pattern recognition (ICPR'18)*, Beijing, China, August 20–24, 2018, pp. 3898–3903.

10. **M. Shehata**, M. Ghazal, F. Khalifa, M. Abou El-Ghar, A. C. Dwyer, A. El-giziri, M. El-Melegy, and A. El-Baz, "A Novel CAD System for Detecting Acute Rejection of Renal Allografts Based on Integrating Imaging-markers and Laboratory Biomarkers," In: *Proceedings of International Conference on Imaging Systems and Techniques (IST'18)*, Krakow, Poland, October 16–18, 2018, pp. 1–6. *(Selected for Oral Presentation)*.

11. **M. Shehata**, F. Taher, M. Ghazal, A. Mahmoud, G. Beache, M. Abou El-Ghar, A. C. Dwyer, A. Elmaghraby, and A. El-Baz, "Early Assessment of Acute Renal Rejection Post-transplantation: A Combined Imaging and Clinical Biomarkers Protocol," In: *Proceedings of International Symposium on Signal Processing and Information Technology (ISSPIT'18)*, Louisville, KY, USA December 9–12, 2018, pp. 297–302. *(Selected for Oral Presentation)*.

12. **M. Shehata**, A. Shalaby, M. Ghazal, M. Abou El-Ghar, M. A. Badawy, G. M. Beache, A. C. Dwyer, M. El-Melegy, G. Giridharan, R. Keynton, and A. El-Baz, "Early Assessment of Renal Transplants using BOLD-MRI: Promising Results," In: *Proceedings of International Conference on Image Processing (ICIP'19)*, Taipei, Taiwan, September 22–25, 2019, pp. 1395-1399.

13. **M. Shehata**, M. Ghazal, H. Abu Khalifeh, A. Khalil, A. Shalaby, A. C. Dwyer, A. M. Bakr, R. Keynton, and A. El-Baz, "A Deep Learning-Based CAD System for Renal Allograft Assessment: Diffusion, BOLD, and Clinical Biomarkers," In: *Proceedings of International Conference on Image Processing (ICIP'20)*, AbuDhabi, UAE, October 25–28, 2020, pp. 355-359.

14. A. Alksas*, **M. Shehata***, G. Saleh*, A. Shaffie, A. Soliman, M. Ghazal, H. Abu Khalifeh, A. Abdel Razek, and A. El-Baz, "A Novel Computer-Aided Diagnostic System for Early Assessment of Hepatocellular Carcinoma," In: *Proceedings of International Conference on Pattern recognition (ICPR'20)*, Milan, Italy, January 10–15, 2020, pp. 10375–10382.

15. **M. Shehata***, A. Alksas*, R. T. Abouelkheir*, A. Almahdy, A. Shaffie, A. Soliman, M. Ghazal, H. Abu Khalifeh, A. Abdel Razek, and A. El-Baz, "A New Computer-aided Diagnostic (CAD) System for Precise Identification of Renal Tumors," In: *Proceedings of IEEE International Symposium on Biomedical Imaging: From Nano to Macro (ISBI'21)*, Nice, France, April 13–16, 2021, pp. 1378–1381.

16. A. Alksas*, **M. Shehata***, H. Atef, F. Sherif, M. Yaghi, M. Alhalabi, M. Ghazal, L. El Serougy, and A. El-Baz, "A Comprehensive Non-Invasive System for Early Grading of Gliomas," In: *Proceedings of International Conference on Pattern recognition (ICPR'22)*, Montreal Quebec, Canada, August 21–25, 2022, (inpress).

- **Abstracts Published in Proceedings (Total = 19)**

  1. M. Abou El-Ghar, S. Ayyad, **M. Shehata**, A. Alksas, M. Badawy, M. El-Melegy, and A. El-Baz, "Role of MRI Imaging Markers and Clinical Biomarkers for accurate assessment of Prostate Cancer: A Machine Learning Approach", In: *European Congress of Radiology 2022*, Vienna, Austria, July 13 – 17, 2022. *(Selected for EPOS)*

  2. M. Abou El-Ghar, S. Ayyad, A. Elmahdy, **M. Shehata**, M. El-Melegy, and A. El-

Baz, "Machine learning based algorithm for intravoxel incoherent motion in diagnosis of prostate cancer: Preliminary Results", In: *The 58th Scientific Conference of Egyptian Society of Radiology 2022*, Tolip Elforsan, Ismailia, Egypt, March 10 - 11, 2022. *(Selected for Oral Presentation)*

3. **M. Shehata***, M. Abou El-Ghar, M. Badawy, and A. El-Baz, "A Deep-Learning Based CAD System That Integrates Diffusion and BOLD MR Image Markers with Laboratory-Based Biomarkers for Precise Evaluation of Acute Renal Allografts", In: *International Society for Magnetic Resonance in Medicine (ISMRM'21)* Workshop on Kidney MRI Biomarkers: The Route to Clinical Adoption, Philadelphia, PA, USA (and Lisbon, Portugal, and online), Sep. 10 - 12, 2021. *(Selected for Oral Presentation)*.

4. A. Alksas, **M. Shehata**, H. Atef, M. Ghazal, A. Abdel Razek, and A. El-Baz, "Applying Machine Learning over Multimodal MRI Imaging for Early Grading of Gliomas", In: *Biomedical Engineering Society Annual Scientific Meeting (BMES'21)*, Orlando, FL, USA, October 6–9, 2021.

5. **M. Shehata**, M. Ghazal, M. Abou El-Ghar, M. Badawy, M. El-Baz, A. C. Dwyer, and A. El-Baz, "Precise Identification of Renal Transplant Status Using BOLD-MRIs", In: *Proceedings of 16th Annual Scientific Meeting of American Society for Diagnostics and Interventional Nephrology (ASDIN'20)*, Las Vegas, Nevada, February 21–23, 2020. *(Second Place Winner, Oral Session)*.

6. **M. Shehata***, A. Alksas*, R. T. Abouelkheir, A. Elmahdy, A. Shaffie, A. Soliman, M. Ghazal, H. Abu Khalifeh, A. Abdel Razek, and A. El-Baz, "A Machine Learning-Based CAD System for Early Detection and Classification of Renal Tumors", In: *Biomedical Engineering Society Annual Scientific Meeting (BMES'20)*, Virtual Meeting, USA, October 14–17, 2020.

7. A. Alksas*, **M. Shehata***, G. Saleh*, A. Shaffie, A. Soliman, M. Ghazal, H. Abu Khalifeh, A. Abdel Razek, and A. El-Baz, "Applying Machine Learning Over Mul-

tiphase Contrast-Enhanced MRI for Detecting and Staging HCC", In: *Biomedical Engineering Society Annual Scientific Meeting (BMES'20)*, Virtual Meeting, USA, October 14–17, 2020.

8. M. Shehata, A. Shalaby, M. Ghazal, M. Abou El-Ghar, M. A. Badawy, G. M. Beache, A. C. Dwyer, M. El-Melegy, G. Giridharan, R. Keynton, and A. El-Baz, "Evaluating Renal Transplants using BOLD-MRI: Preliminary Results", In: *Biomedical Engineering Society Annual Scientific Meeting (BMES'19)*, Philadelphia, Pennsylvania, USA, October 16–19, 2019.

9. M. Shehata, M. Ghazal, A. Shalaby, M. A. Badawy, M. Abou El-Ghar, G. M. Beache, A. C. Dwyer, F. taher, G. Giridharan, A. Bakr, R. Keynton, and A. El-Baz, "A Big Data Computer-aided Diagnostic System for Assessing Renal Allografts", In: *Biomedical Engineering Society Annual Scientific Meeting (BMES'19)*, Philadelphia, Pennsylvania, USA, October 16–19, 2019.

10. M. Shehata, M. Abou El-Ghar, T. Eldiasty, and A. El-Baz, "Integrating Clinical with Diffusion Image Markers as a Noninvasive Alternative to Renal Biopsy," In: *European Congress of Radiology (ECR 2019)*, Austria Center Vienna, Bruno-Kreisky-Platz 11220, Vienna, Austria, February 27 – March 3, 2019. *(Selected for Oral Session)*.

11. M. Shehata, M. Ghazal, G. Beache, M. Abou El-Ghar, A. Dwyer, A. Khalil, A. Elmaghraby, and A. El-Baz, "Fusion of Image and Clinical Markers for Renal Transplant Rejection Assessment: A Pilot Study", In: *Biomedical Engineering Society Annual Scientific Meeting (BMES'18)*, Atlanta, Georgia, USA, October 17–20, 2018. *(Selected for Oral Session)*.

12. H. Abdeltawab, M. Shehata, A. Shalaby, S. Mesbah, M. El-Baz, M. Ghazal, Y. Al Khalil, M. Abou El-Ghar, A. Dwyer, M. El-Melegy, A. Elmaghraby, and A. El-Baz, "Deep Learning Based Framework for Early Detection of Acute Renal Transplant Rejection", In: *Biomedical Engineering Society Annual Scientific Meeting*

(BMES'18), Atlanta, Georgia, USA, October 17–20, 2018. *(Oral Session)*.

13. **M. Shehata**, E. Hollis, M. Abou El-Ghar, M. Ghazal, T. Eldiasty, M. Merchant, A. Switala, A. C. Dwyer, and A. El-Baz, "Possible Role of Diffusion MRI in Diagnosig Acute Renal Rejection," In: *Proceedings of* 14th *Annual Scientific Meeting of American Society for Diagnostics and Interventional Nephrology (ASDIN'18)*, Salt Lake City, UT, USA, February 16–18, 2018. *(Published in Journal of Vascular Access 2018; vol. 19(5); NP1–NP15)*.

14. **M. Shehata**, M. Abou El-Ghar, T. Eldiasty, and A. El-Baz, "An integrated CAD system of DWI MRI and laboratory biomarkers in diagnosis of kidney transplant dysfunction," In: *European Congress of Radiology (ECR 2018)*, Austria Center Vienna, Bruno-Kreisky-Platz 11220, Vienna, Austria, February 28 – March 4, 2018. *(Selected for Oral Session)*.

15. **M. Shehata**, M. Abou El-Ghar, T. Eldiasty, and A. El-Baz, "Deep learning in classification of kidney transplant dysfunction: combined imaging and clinical biomarkers," In: *European Symposium of Urogenital Radiology (ESUR 2018)*, Barcelona, Spain, September 13 – 16, 2018.

16. **M. Shehata**, F. Khalifa, A. Soliman, M. Abou El-Ghar, A. C. Dwyer, and A. El-Baz, "Assessment of Renal Transplant Using Image and Clinical-based Biomarkers," In: *Proceedings of* 13th *Annual Scientific Meeting of American Society for Diagnostics and Interventional Nephrology (ASDIN'17)*, New Orleans, Louisiana, USA, February 10–12, 2017. *(Published in Journal of Vascular Access 2017; vol. 18(5); e78–e87, Second Place Winner)*.

17. **M. Shehata**, A. Soliman, M. Abou El-Ghar, F. Khalifa, D. Bhutto, M. Elmelegy, A. Elmaghraby, and A. El-Baz, "A Geometric Deformable Model-Based Framework For Kidney Segmentation Using 3D Diffusion MRI", In: *Biomedical Engineering Society Annual Scientific Meeting (BMES'17)*, Phoenix, Arizona, USA, October 11–14, 2017.

18. **M. Shehata**, M. Abou El-Ghar, and A. El-Baz, "Role of Image and Clinical-based Biomarkers in Renal Transplant Assessment," In: *Proceedings of 2nd International Symposium on Functional Renal Imaging: Where Physiology, Nephrology, Radiology and Physics Meet*, October 11th - 13th 2017, Max Delbrück Center for Molecular Medicine, Robert-Rössle Str. 10, Berlin 13125, Germany. *(Selected for Power Poster Session)*.

19. **M. Shehata**, F. Khalifa, A. Soliman, M. Abou El-Ghar, A. C. Dwyer, R. Ouseph, and A. El-Baz, "Early Assessment of Acute Renal Rejection," In: *Proceedings of 12th Annual Scientific Meeting of American Society for Diagnostics and Interventional Nephrology (ASDIN'16)*, Phoenix, Arizona, USA, February 19–21, 2016.

- **Patents and Disclosures (Total = 4)**

  1. A. El-Baz, A. C. Dwyer, A. Soliman, **M. Shehata**, H. Abdeltawab, F. Khalifa "COMPUTER AIDED DIAGNOSIS SYSTEM FOR CLASSIFYING KIDNEYS," *US Patent Publication No. 11,238,975,* February 1st, 2022. *(Patent Grant)*.

  2. A. El-Baz, A. Alksas, **M. Shehata**, A. Shaffie, A. Soliman, "A Comprehensive CAD System for Early Identification of Liver and Renal Cancer by Integrating Morphological, Textural, and Functional Imaging Markers,"*US Patent Disclosure 21051,* March 5th, 2021. *(Disclosure)*.

  3. A. El-Baz, A. C. Dwyer, R. Ouseph, F. Khalifa, A. Soliman, **M. Shehata**, "COMPUTER AIDED DIAGNOSTIC SYSTEM FOR CLASSIFYING KIDNEYS," *US Patent Publication No. 10,453,569,* October 22nd, 2019. *(Patent Grant)*.

  4. A. El-Baz, A. C. Dwyer, R. Ouseph, F. Khalifa, A. Soliman, **M. Shehata**, "COMPUTER AIDED DIAGNOSTIC SYSTEM FOR CLASSIFYING KIDNEYS," *US Patent Publication No. 9,928,347,* March 27th, 2018. *(Patent Grant)*.

Reviewer

- *Journals*

  1. Computational and Structural Biotechnology Journal

  2. IEEE Journal of Biomedical and Health Informatics

  3. IEEE Access

  4. Cancers

  5. Frontiers Oncology

  6. Sensors

  7. Diagnostics

  8. Electronics

  9. Frontiers in Neuroscience

  10. Cancers in Medicine

  11. Computer Methods and Programs in Biomedicine

  12. Egyptian Journal of Radiology and Nuclear Medicine

- *Conferences*

  1. International Conference on Medical Image Computing and Computer Assisted Intervention (MICCAI)

  2. International Conference on Pattern recognition (ICPR)

  3. IEEE International Conference on Imaging Processing (ICIP)

  4. IEEE International Symposium on Biomedical Imaging (ISBI)

  5. IEEE International Conference on Biomedical and Health Informatics (BHI)

  6. IEEE International Conference on Imaging Systems and Techniques (IST)

  7. IEEE International Symposium on Signal Processing and Information Technology (ISSPIT)

  8. IEEE Canadian Conference on Electrical and Computer Engineering (CCECE)

Graduate Advisor

Doctorate of Philosophy in Computer Science and Engineering:

1. Dr. Ayman El-Baz, Department of Bioengineering, University of Louisville, KY, USA.

2. Dr. Adel Elmaghraby, Department of Computer Science and Engineering, University of Louisville, KY, USA.

Master of Science in Electrical Engineering:

1. Dr. Ayman El-Baz, Department of Bioengineering, University of Louisville, KY, USA.

Referrals

1. Dr. Ayman El-Baz, Department of Bioengineering, University of Louisville, KY, USA, *ayman.elbaz@louisville.edu*

2. Dr. Adel Elmaghraby, Department of Computer Science and Engineering, University of Louisville, KY, USA, *adel.elmaghraby@louisville.edu*

3. Dr. Amy Dwyer, Kidney Disease Program, Department of Nephrology, University of Louisville, KY, USA. *amy.dwyer@louisville.edu*

4. Dr. Guruprasad Giridharan, Department of Bioengineering, University of Louisville, KY, USA, *guruprasad.giridharan@louisville.edu*